Czech Technical University in Prague
Faculty of Electrical Engineering
Department of Radioelectronics

Hyperspectral Imaging in VIS – IR

Doctoral Thesis

Ing. Lukáš Krauz

Prague, June 2023

Ph.D. programme: Electrical Engineering and Information Technology (P2612)
Branch of study: Radioelectronics (2601V010)

Supervisor: Prof. Mgr. Petr Páta, Ph.D.

Supervisor:
Prof. Mgr. Petr Páta, Ph.D.
Department of Radioelectronics
Faculty of Electrical Engineering
Czech Technical University in Prague
Technická 2
160 00 Prague 6
Czech Republic

Declaration

I hereby declare that I worked out the presented thesis independently and I quoted all sources used in this thesis in accord with methodical instructions about ethical principles for writing academic theses.

Prague, June 28, 2023 Lukáš Krauz

Acknowledgments

First of all, I would like to thank my supervisor Prof. Mgr. Petr Páta, Ph.D. for all the help, support, and guidance throughout my Ph.D. studies and related research. Besides that, I would also like to thank Prof. Ing. Miloš Klíma, CSc. for his support during our countless consultations and also for all his advice during my studies.

Additional thanks are forwarded to my colleagues at the Department of Radioelectronics for everyday encouragement, valuable comments, motivation but also fun. In particular, I would like to express my gratitude to Doc. Ing. Stanislav Vítek, Ph.D., Ing. Karel Fliegel, Ph.D. and Ing. Václav Navrátil, Ph.D. for all the advice and support, but also to my fellow doctoral students Ing. Martin Urban, Ing. Ondřej Nentvich, Ing. Adam Zizien, and many others. Thanks also go to the Ph.D. colleagues who have already defended their work.

I would also like to acknowledge the Czech Science Foundation and the Grant Agency of Czech Technical University in Prague. This work and the results presented within have been partially supported by grants GA 20-10907S: "*Meteor clusters: An evidence for fragmentation of meteoroids in interplanetary space*", SGS18/141/OHK3/2T/13 *Analysis and advanced algorithms for ultra-wide imaging systems*, SGS20/179/OHK3/3T/13 "*Modern Optical Imaging Systems with Non-linear Point Spread Function and Advanced Algorithms for Image Data Processing*", and SGS23/186/OHK3/3T/13 *Acquisition, processing, and display techniques for extended multidimensional imaging modalities.*

In addition, a huge thanks belongs to my beloved family and friends who have supported me throughout my studies and life in general. Without them, none of this would not have been possible.

Last but not least, I would like to thank my wonderful wife Anička for her endless support during all the difficult moments of my studies and for the fact that together we are achieving all the planned goals in our career and personal life.

Prague, June 28, 2023 Lukáš Krauz

Copyright

Abstract

Hyperspectral imaging (HSI) represents a highly advanced field within optical imaging techniques that integrates standard imaging and spectroscopy methods across a wide range of spectral bands, including visible and infrared. In general, the domain of HSI encompasses a number of technical aspects such as instrument design, data preprocessing, data compression, spectral pattern analysis, target detection, and cutting-edge machine learning techniques. In the field of instrumentation, there is currently a strong demand for new devices that can enable HSI in the thermal infrared region with high spectral resolution. At the same time, there is an ongoing search for areas where HSI or multispectral imaging (exploiting the spectral characteristics of real objects) can be applied or enhance existing solutions to increase their efficiency. This thesis provides a comprehensive overview of the HSI topic with an emphasis on advanced HSI techniques and the study of spectral properties for potential real-world applications. The core of the work is a collection of journal publications, two of which have a key role in the investigation of a novel spatio-spectral hyperspectral system based on an acousto-optic tunable filter (AOTF). In particular, the research focuses on optimizing the design of a novel quasi-collinear AOTF and Wollaston polarizer. These designs take advantage of the promising anisotropic mercurous halide-based crystals that allow the spatio-spectral system to operate in the thermal spectral region. The next core publications examined two diverse applications where the spectral characteristics of different objects of interest obtained from hyperspectral or multispectral imagery can be exploited. The first of these studies focused on ground-based remote sensing, investigating the segmentation of clouds based on their spectral (color) characteristics using image data from WILLIAM (WIde-field aLL-sky Image Analyzing Monitoring system). In particular, significant progress has been made in identifying color variations among different cloud types within a specific color space. This finding could lead to an automated method of classifying cloud types based on their color characteristics. The second promising application investigated the spectral variations among diverse hyperspectrally captured inkjet photo prints, and thus the variations among the diverse inks themselves. This was done using principal component analysis and spectral similarity measures, parts of which were also exploited in the previous publication to assess cloud color characteristics. The results showed significant differences between professional pigment-based prints and hobby dye-based prints implying the possibility of using the hyperspectral system as a simple tool for their identification and potentially for detecting printed artwork forgeries.

Keywords: Hyperspectral Imaging (HSI), Hyperspectral Systems, Spatio-spectral Imaging, Quasi-collinear Acousto-optic Tunable Filter (AOTF), Crystal Polarizers, Mercurous Halides, Visible Band, Infrared Band, Spectral Similarity Analysis, WILLIAM, Clouds Color Analysis, Inkjet Print Analysis, Counterfeit Detection, Principal Component Analysis (PCA).

Abstrakt

Hyperspektrální zobrazování (HSI) představuje vysoce pokročilou oblast optických zobrazovacích technik, která integruje standardní metody zobrazování a spektroskopie v širokém rozsahu spektrálních pásem, včetně viditelného a infračerveného. Obecně oblast HSI zahrnuje řadu technických aspektů, jako je konstrukce přístrojů, předzpracování dat, komprese dat, analýza spektrálních vzorů, detekce objektů a moderních technik strojového učení. V oblasti instrumentace existuje v současné době silná poptávka po nových zařízeních, která by umožňovala HSI v tepelné infračervené oblasti s vysokým spektrálním rozlišením. Současně probíhá hledání oblastí, kde lze HSI nebo multispektrální zobrazování (využívající spektrální charakteristiky reálných objektů) použít nebo vylepšit stávající řešení a zvýšit tak jejich účinnost. Tato práce poskytuje ucelený přehled tématu HSI s důrazem na pokročilé techniky HSI a studium spektrálních vlastností pro potenciální aplikace v reálném světě. Jádrem práce je soubor časopiseckých publikací, z nichž dvě mají klíčovou roli při zkoumání nového prostorověspektrálního hyperspektrálního systému založeného na akusticko-optickém laditelném filtru (AOTF). Výzkum se zaměřuje zejména na optimalizaci návrhu nového kvazikolineárního AOTF a Wollastonova polarizátoru. Tyto návrhy využívají perspektivní anizotropní krystaly na bázi halogenidů rtuti, které umožňují provozovat prostorový spektrální systém v tepelné spektrální oblasti. V dalších publikacích byly zkoumány dvě rozdílné aplikace, kde lze využít spektrální charakteristiky různých zájmových objektů získaných z hyperspektrálních nebo multispektrálních snímků. První z těchto studií se zaměřila na pozemní dálkový průzkum a zkoumala segmentaci oblak na základě jejich spektrálních (barevných) charakteristik s využitím obrazových dat ze systému WILLIAM (WIde-field aLL-sky Image Analyzing Monitoring system). Významného pokroku bylo dosaženo zejména při identifikaci barevných rozdílů mezi různými typy oblak v rámci určitého barevného prostoru. Toto zjištění by mohlo vést k automatické metodě klasifikace typů oblaků na základě jejich barevných charakteristik. Druhá slibná aplikace zkoumala spektrální rozdíly mezi hyperspektrálně zachycenými inkoustovými fotografickými výtisky, a tedy rozdíly mezi samotnými inkousty. K tomu byla použita analýza hlavních komponent a spektrální metriky, z nichž některé jejich části byly také využity v předchozí publikaci posuzování barevných charakteristik oblak. Výsledky ukázaly významné rozdíly mezi profesionálními výtisky na bázi pigmentu a hobby výtisky na bázi barviv, což naznačuje možnost využití hyperspektrálního systému jako jednoduchého nástroje pro jejich identifikaci a potenciálně i pro odhalování padělků tištěných uměleckých děl.

Klíčová slova: Hyperspektrální zobrazování (HSI), hyperspektrální systémy, prostorově spektrální zobrazování, kvazikolineární akusticko-optický laditelný filtr (AOTF), krystalové polarizátory, halogenidy rtuti, viditelné pásmo, infračervené pásmo, analýza spektrální podobnosti, WILLIAM, analýza barev oblak, analýza inkoustového tisku, detekce padělků, analýza hlavních komponent (PCA).

Contents

Abbreviations

2D	Two-dimensional
3D	Three-dimensional
AO	Acousto-Optic
AOTF	Acousto-Optic Tunable Filter
AVIRIS	Airborne Visible / Infrared Imaging Spectrometer
BEO	Backend Optics
BC	Bhattacharyya Coefficient
BD	Bhattacharyya distance
ESA	European Space Agency
FEE	Faculty of Electrical Engineering
FEO	Frontend Optics
FOV	Field of View
FP	Fabry–Perot
FWHM	Full Width Half Maximum
HSI	Hyperspectral Imaging
IR	Infrared
JMD	Jeffries–Matusita Distance
JMSAM	Jeffries–Matusita Spectral Angle Mapper
LC	Liquid Crystal
LCTF	Liquid Crystal Tunable Filter
LVF	Linear Variable filter
LWIR	Long-wave Infrared
MWIR	Mid-wave Infra-Red
NASA	National Aeronautics and Space Administration
NIR	Near Infra-Red
PC	Principal Component
PCA	Principal Component Analysis
PSF	Point Spread Function
PVT	Physical Vapor Transport
SAM	Spectral Angle Mapper
SCA	Spectral Correlation Angle
SCM	Spectral Correlation Mapper
SID	Spectral Information Divergence
SIDSAM	Spectral Information Divergence Spectral Angle Mapper
SNR	Signal-to-Noise Ratio

RGB	Red Green Blue
THETIS	Thermal Hyperspectral Imaging System
TIR	Thermal Infra-Red
UV	Ultra Violet
UAV	Unmanned Aerial Vehicles
VIS	Visible Spectral Band
VNIR	Visible Near-infrared
WILLIAM	WIde-field aLL-sky Image Analyzing Monitoring system
WMD	WILLIAM Meteo Database
WMO	World Meteorological Organization

1

Introduction

Hyperspectral imaging (HSI), often referred to as imaging spectroscopy, is an emerging field of science that combines two broad scientific and technical areas: standard imaging and spectroscopy [1]. This unique combination allows the acquisition of standard two-dimensional (2D) image information of the imaged scene, but at the same time, each of the imaged pixels (image points) is enriched with continuous spectral information. Thus, a third additional dimension with spectral information is added to the acquired 2D spatial information of the scene, resulting in extensive three-dimensional (3D) data. This type of data is usually called a hyperspectral cube or hypercube and consists of multiple 2D image slices depending on the number of channels (corresponding to specific wavelengths) captured. An example of a hypercube constructed in this way is shown in Figure 1.1, where x and y denote the two spatial coordinates and λ denotes the spectral coordinate.

Fundamentally, considering the imaging part, HSI builds upon its predecessors [3], such as monochromatic imaging (capturing only intensities), the well-known red, green, blue (RGB) imaging (considered as limited multispectral imaging), and standard multispectral imaging. As the name of each imaging technique suggests, the main difference between the approaches lies in the number of spectral channels captured during imaging. Whilst HSI allows obtaining continuous spectral information from tens to thousands of spectral channels for each spatial pixel, multispectral imaging operates only with a decreased number of spectral channels, usually up to 10. In comparison, monochromatic imaging captures only an intensity channel/profile of the captured scene, and the differentiation from the RGB imaging is apparent. Although standard RGB imaging can be considered as multispectral, it is limited to three captured channels – red, green, and blue. Nevertheless, as already mentioned, if one looks at all the presented sensing techniques, it is true for all of them that the more advanced ones (with more spectral channels) always build on the foundations of the previous ones, both in sensing and in subsequent image processing. The comparison between all the mentioned types of imaging is illustrated in Figure 1.2.

HSI typically operates in many possible, often different, but sometimes overlapping spectral bands, depending on the design of the HSI system [4]. The width of the operational spectral band also highly depends on the design and used dispersive components. Sorting the spectral bands from lower to higher wavelengths of the electromagnetic spectrum, HSI typically ranges

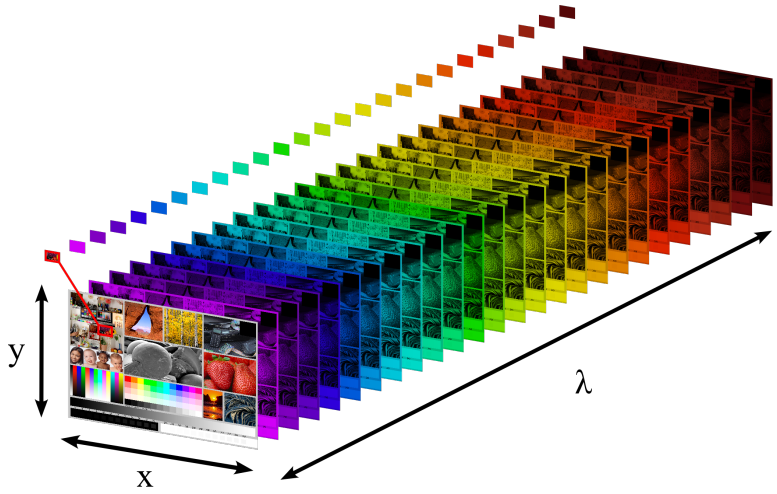

Figure 1.1: An example of a hyperspectral image (hypercube). This image shows the division of the captured image into a large number of spectral images, each corresponding to one captured spectral channel. The same spectral division is shown for the single-pixel example from the sample image, which is bounded by the red rectangle. The spatial coordinates are denoted as x and y, and the spectral coordinate corresponds to the symbol λ. The test pattern designed by ©Bill Atkinson, Jack Flesher, and Uwe Steinmueller [2], which is widely used in the print quality assessment community, serves as the template for this and several other hyperspectral image examples in the thesis.

from the ultraviolet (UV) spectral band to the thermal-infrared (TIR) part of the long-wave infrared (LWIR) spectral band. The division of spectral bands with indicated wavelengths for hyperspectral imaging is shown in Figure 1.3.

Although UV HSI systems have become increasingly popular in recent years [5–7], their construction and parameter optimization are still highly challenging. Evaluating the use of hyperspectral sensing in the past years, it can be concluded that most systems operate in the visible (VIS) and infrared (IR) regions [8–11]. A very common combination of hyperspectral systems are those that operate in the visible near-infrared (VNIR) spectral band [12–15]. In addition, systems operating only in the near-infrared (NIR) [16–18], short-wave infrared (SWIR) [19–22], mid-wave infrared (MWIR) [23–25], and the already mentioned LWIR bands [26–32] are also often used. The farther away from the visible spectral range, the more challenging (due to low photon fluxes in natural illumination conditions) it is to design hyperspectral systems and to supply and use optical elements in them. These systems are often limited by the spectral bandwidth in which they operate, spectral resolution, signal-to-noise ratio (SNR), and many other parameters [33–36]. New systems that improve these parameters, expand their potential applicability, and introduce new HSI approaches are both valuable and desirable. A very recent and promising concept of a hyperspectral system that could operate in several spectral bands (from VIS to LWIR) is the Thermal Hyperspectral Imaging System (THETIS) project initiated by European Space Agency (ESA). Some of its operating principles have been described in more detail in [37, 38]. A major advantage of the THETIS system is the planned integration of optical devices (polarizers and acousto-optic tunable filters) based on promising optical materials such as mercurous halides [39–41]. These optical materials offer enormous potential for use as substrate materials for optical devices useful (not only) in

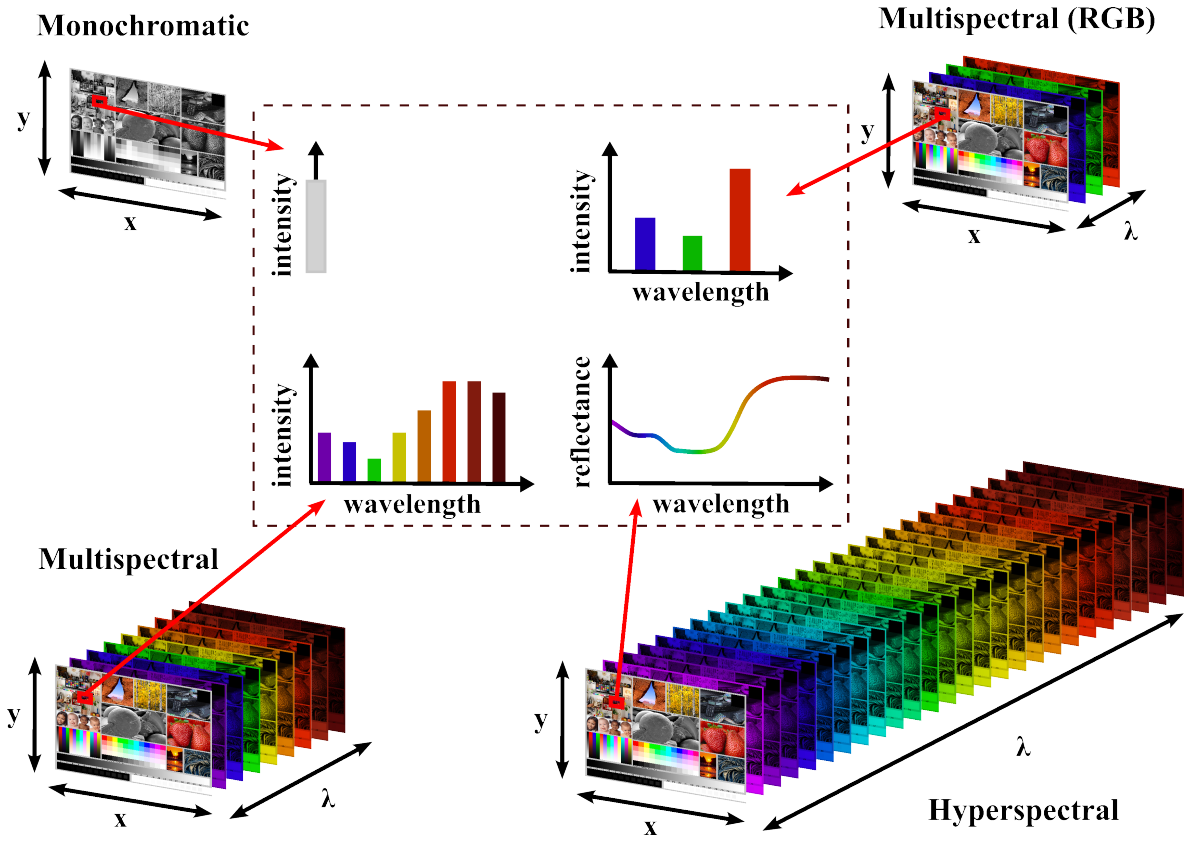

Figure 1.2: A comparison of types of imaging techniques. Similar to the previous Figure 1.1, the spatial coordinates are denoted as x and y, and the spectral coordinate corresponds to the symbol λ. An example of obtained image pixel values is given for each specific technique.

hyperspectral systems operating in multiple spectral bands. However, the optimization and the overall development of these optical devices is still in the research phase. More about the properties of these materials, their current research, and their use in hyperspectral imaging will be presented in later sections of this thesis.

Returning to the use of HSI, the choice of hyperspectral system, and therefore the spectral region of interest, depends primarily on the application and research being conducted. The immense potential of HSI is reflected in the enormous list of applications that grows every year. Over the past years, many new applications of HSI have emerged in various fields of science and technology. Nevertheless, at least some of the most important ones can be mentioned in this thesis. For example, among the significant applications of HSI with high impact on everyday life can be mentioned food quality inspection [17, 42–48], especially focused on meat of various kinds [12, 13, 16, 49–55] or fruits and vegetables [19, 56–61]. These more or less laboratory applications are also related to the involvement of HSI in agriculture [35, 62–66], both for monitoring of crops health and condition [67–70], but also for measuring moisture content [71–73] and assessing soil quality or contaminants [74–78]. Similarly, HSI is used for the biology of plants [79–82] or inspecting of vegetation [83–85]. The vegetation inspection and soil evaluation bring us to HSI applications in geology [86–89] but most importantly to a remote inspection of the Earth, in general. Remote sensing is one of the most exploited and original applications of HSI [63, 85, 90–93]. Many systems are currently located on various satellites

[94–96], and more are coming [97]. Leaving aside standard airborne HSI systems [98, 99], unmanned aerial vehicles (UAV) are also used more and more frequently [84, 100–103]. Apart from previously mentioned vegetation, agriculture, and geological applications, many such UAV systems then serve, for example, for military surveillance purposes [104]. Returning to more down-to-earth use cases, HSI plays an important role among forensic tools [105–108], but also in the assessment of cultural heritage [109–111] and evaluation of the authenticity of works of art [112–114]. Nevertheless, some of the most deserving and advanced HSI applications are in biological imaging [115–117], biomedicine [118–121], or medicine in general [10, 122–125]. Thus, HSI finds its use as a surgical or clinical tool [126–128] and the acquired medical data can then be used as an input for a variety of image processing tools, and classification or recognition models [125, 129, 130].

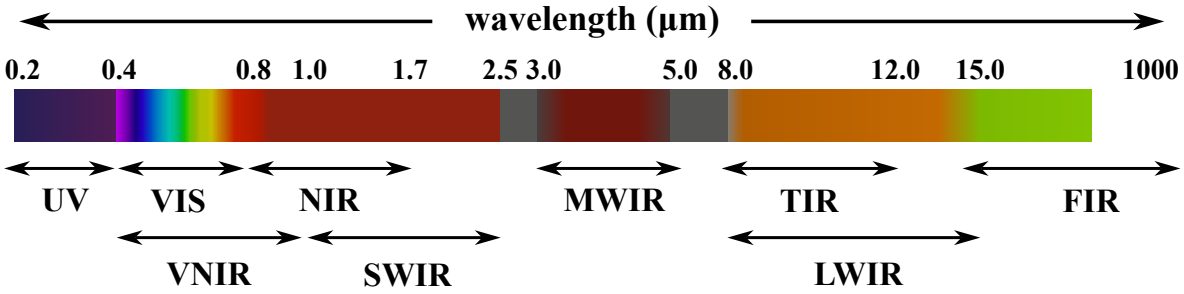

Figure 1.3: A selection of electromagnetic spectra relevant to HSI. The range is given from the UV to the FIR (far infrared) spectral band.

One can see the endless possibilities for new applications of HSI, and new trends are constantly emerging [131]. The same is true for the individual processes involved in HSI, each of which can be considered a separate scientific and technical discipline. A simplified list of processes and tasks integrated within a technical field of HSI is shown in Figure 1.4. The figure can also show a step-by-step or task-by-task flowchart (pipeline or chain) covering all major HSI disciplines from the photonic system design of the hyperspectral system through calibration, image data preprocessing, data preparation, and postprocessing. This flowchart is an extended version of the technical workflow diagram presented in [81]. At first glance at Figure 1.4, the multidisciplinary nature of HSI is evident. In general, HSI can be divided into three main areas or parts, which are:

- **Imaging part**,
- **Image data preprocessing part**,
- **Data exploitation and processing part**.

The imaging part involves the overall photonic design of the HSI camera system and its optimization, followed by the actual acquisition of hyperspectral images. The overall design (optical and electronic parts) determines the operational spectral bands, the spectral and spatial resolution, and thus the final quality of the output image data [4, 96]. The output image parameters are then influenced by the system setup, its settings, and the adjustment of the scanning mode. The acquired hyperspectral data then enters the image data processing pipeline. At this stage, image calibration is applied to remove the effects of illumination, aberrations, and instrument noise, while taking into account the transfer function of the

imaging system to produce a calibrated data output. The next phase is the initial data preprocessing involving image and signal processing tasks [132–135] such as normalization, filtering and smoothing, position and distance correction, fusion or masking. The adjusted hyperspectral image data is then explored and further preprocessed in terms of dimension reduction and selection of the most significant wavelengths due to the high redundancy between spectral channels. The patterns and features can then be explored and extracted from the reduced image data. Subsequently, the spectral unmixing [136] can be applied, or the features can proceed to the final data exploitation stage. In the final stage of the HSI pipeline, the preprocessed data are taken and prepared for the specified postprocessing algorithms and models [137–142], which are then optimized. The output results are then interpreted and used for identification, detection, prediction, or quantification, depending on the previous task definition.

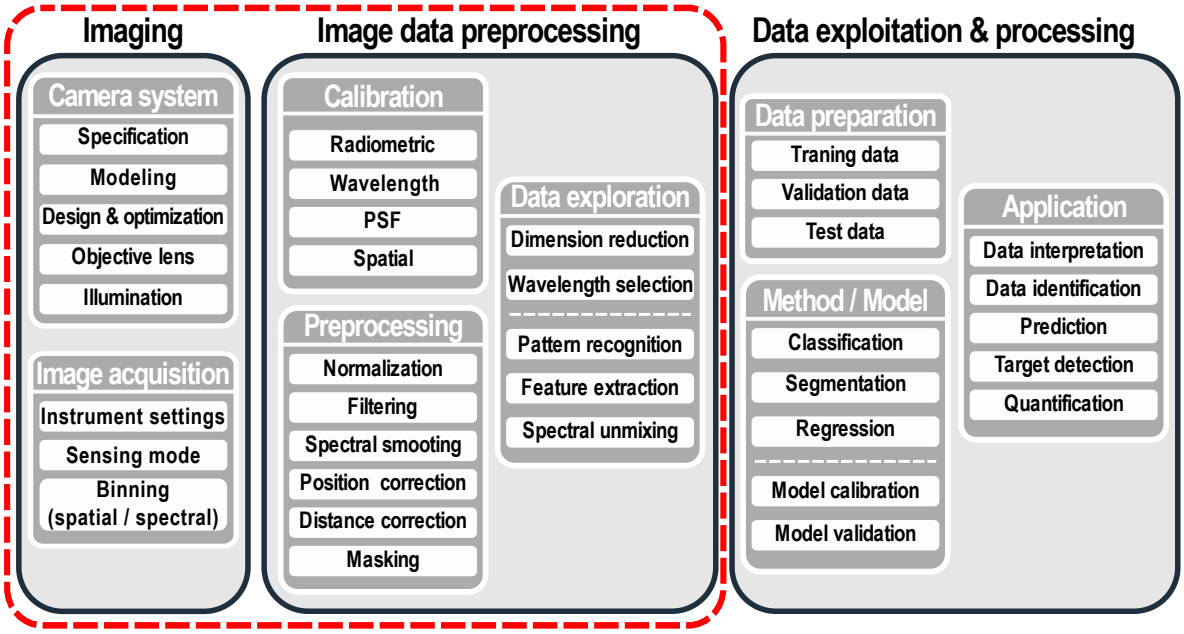

Figure 1.4: Disciplines and processes related to HSI. The red dashed rectangle defines the main focus areas of the thesis.

The HSI pipeline, or parts of it, can then be used in a variety of applications, as the text above illustrates, each with its own challenges and problems. This thesis primarily focuses on two selected major areas of the HSI pipeline: the imaging and image preprocessing parts. More specifically, this thesis aims to contribute to these areas or, more precisely, to some disciplines in the mentioned areas of the HSI pipeline. The two HSI areas of focus of the thesis are also highlighted within Figure 1.4.

1.1 Objectives of the thesis

Within the selected areas of the HSI pipeline, there are many challenges that need to be investigated and addressed. In particular, the topic of investigating new hyperspectral approaches and systems operating in farther infrared bands, such as the LWIR band, continues to gain popularity in the research community. Moreover, there are still many important applications

and problems that can be more efficiently or accurately solved via imaging by incorporating more spectral channels, or even different spectral bands than in standard visible imaging. These applications require the proper study and exploration of the spectral characteristics of the captured objects of interest. From the overview of the topics, two main specific objectives of the thesis focus on HSI emerge:

[G.1] **Propose a design and optimization analysis of optical devices based on mercurous halides, exploitable and applicable for infrared (e.g., thermal) acousto-optic-based hyperspectral imaging.**

[G.2] **Investigate and evaluate spectral feature discrimination methods for different objects of interest acquired via multispectral and hyperspectral systems.**

Nevertheless, these two main and broad objectives are also linked to a number of specific sub-objectives and milestones.

The first goal [G.1] is related to the design of specific optical components for the development of a polarization-sensitive thermal hyperspectral imaging system and includes these specific milestones:

- Investigate the optical and acousto-optic (AO) properties of mercurous halides and compare them against different optical materials.
- Propose a model of an acousto-optic tunable filter (AOTF) applicable to thermal HSI.
- Analyze the parameters of the AOTF model based on mercurous halides and verify its possible hyperspectral operation.
- Propose an optimization scheme of a mercurous halide-based polarizer necessary for the mercurous halide-based AOTF operation within the LWIR region.
- Optimize and discuss the polarizer model for a broadband (VIS–LWIR) operation.

For the second goal [G.2], the appropriate applications of spectral feature exploration and analysis need to be defined. In particular, two main specific applications have been identified as very promising. The first one uses daily image data from all-sky meteorological multispectral imaging systems. The second one is based on hyperspectral systems capable of capturing fine art prints. Both identified applications are highly suitable for exploring the spectral properties of the selected object of interest and subsequently evaluating their potential use in practice (more details are given in the next chapter). Regarding the second goal of this thesis, the first key application is focused on the ground-based spectral (color) investigation of cloud phenomena for meteorological purposes. Ideal for this investigation is multispectral (RGB) data of the all-sky monitoring system, the WIde-field aLL-sky Image Analyzing Monitoring (WILLIAM) system. The second pre-selected application involves a VNIR hyperspectral system SPECIM PFD4K-65-V10E (available at the Department of Radioelectronics, Faculty of Electrical Engineering, Czech Technical University in Prague). This system can be easily utilized for the hyperspectral capturing of fine art prints with the goal of forgery identification. Thus, the second goal [G.2] brings together these specific milestones:

- Extract the cloud color-based signatures (features) from available all-sky image data from the WILLIAM system.
- Assess the color spaces suitable for the feature extraction.
- Investigate the properties of color features for different cloud types.
- Extract the spectral feature of diverse inks using VNIR hyperspectral system with subsequent data processing.
- Investigate and compare the spectral features of diverse fine art ink prints.
- Evaluate the suitability of the VNIR hyperspectral system for possible fine art print forgery identification.

The elaboration of these defined objectives, focusing on HSI topics in different spectral regions, is presented in the main part of this thesis through the author's four core publications [A.1, A.2, A.3, A.4]. Before that, however, the proposed topics, which are in line with the aims of the thesis, are presented in more detail in the following chapter on contributions and state of the art.

1.2 Thesis outline

The thesis is divided into six main chapters. After introducing the HSI topics and the aims of the thesis in Chapter 1, the author's contributions and the related state of the art are described in Chapter 2. The next two chapters, Chapter 3 and Chapter 4, then present the core of the thesis, based on a compilation of the author's journal publications, within which each publication is also described in terms of its relevance and relation to the thesis topic. The results are then summarized and discussed in Chapter 5, along with opportunities for future follow-up research and other challenges. The thesis is then concluded in Chapter 6.

2

Contributions & related state of the art

Following the defined objectives of the thesis, which deal with the use of mercurous halide-based optical devices for HSI and with the exploration of spectral properties (features) in predefined applications, this chapter presents, in several sections, the current progress and state-of-the-art areas related to these objectives. Some parts of this chapter have been adopted and modified from the author's core publications [A.1, A.2, A.3, A.4], which are incorporated into the main body of this thesis. The purpose of including these excerpts is twofold: first, to introduce the author's specific contributions, and second, to provide a contextual framework for the selected topics while clarifying their fundamental concepts. The chapter is divided into five main sections. The first section introduces the current hyperspectral systems and techniques used for HSI in general. The next section is focused on the highly promising optical materials - mercurous halides, their properties, and their possible utilization for hyperspectral systems. In the following section, the focus shifts from hyperspectral systems to acquired hyperspectral data and analysis of spectral properties of objects of interest for predefined applications. Therefore, these sections describe selected hyperspectral and multispectral application cases and methods for spectral feature analysis.

2.1 Hyperspectral imaging techniques and instrumentation

Regarding the HSI topic, one of the first steps is the selection, or in some cases, the sole optoelectronic design of the imaging system and acquisition technique. The design must match the intended application and the operational spectral band. In addition to the operational band, the spectral and spatial resolution of the system should be considered.

In general terms, the construction of the hyperspectral imaging system can be divided into four main parts - the imaging part, the illumination part, the sample stage part, and the electronic (computer) driving part [48]. The most technique-determining is definitely the imaging part of the hyperspectral system, or more precisely, the construction of a dispersion unit (spectrograph/spectral separation unit/diffractive device) used within the system. Dispersive

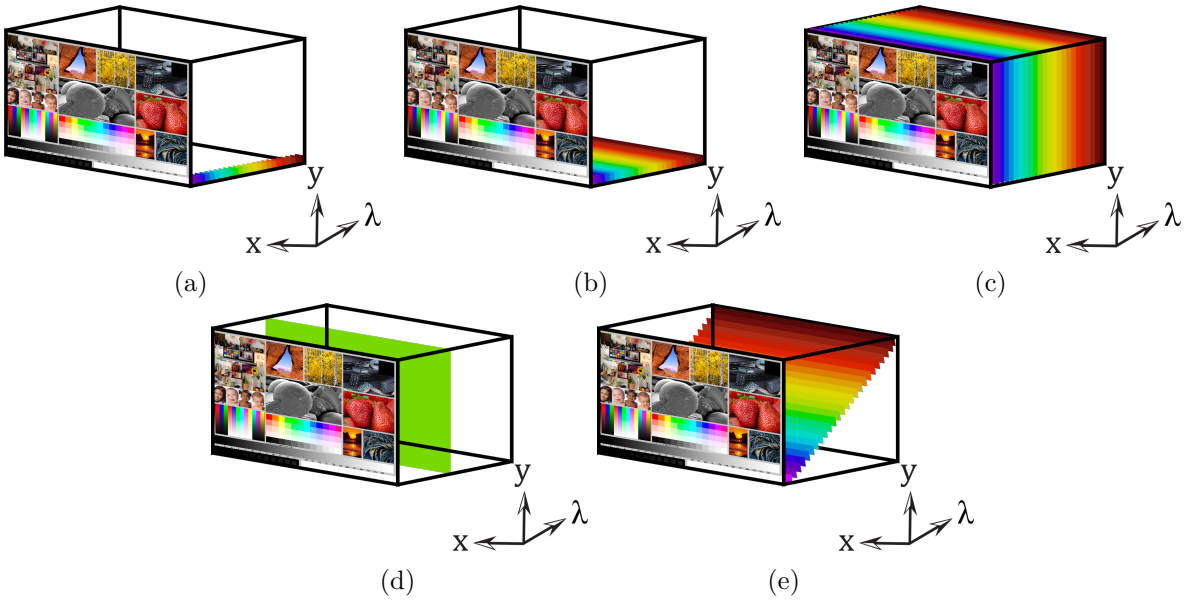

Figure 2.1: An illustration of hyperspectral techniques and their fundamental principles. Figure 2.1a represents the whisk-broom (point-scanning) technique. Figure 2.1b corresponds to the push-broom (line-scanning) technique. Figure 2.1c represents the snapshot (non-scanning) technique. Figure 2.1d shows the staring (spectral scanning) technique. Figure 2.1e illustrates the hybrid spatio-spectral technique.

units can take the form of prisms, gratings, interference-based standard filters, linear variable filters (LVF), Fabry–Perot (FP) type filters, and electronically tunable filters. The other elements of the imaging part, such as frontend optics (FEO), backend optics (BEO), polarizers, and sensors, are mostly selected and designed to be compatible with the used dispersion unit. The use of the optical elements must also be consistent with the planned operational spectral band since not all the materials used for the devices are applicable for broadband operation.

Nowadays, there are several techniques used to obtain a hyperspectral image. The most common are currently three main approaches [96]: spatial scanning principle, snapshot principle, and spectral scanning (staring) principle. The fourth, relatively new principle that combines the previous techniques is the spatio-spectral scanning [37, 143, 144], which was also the subject of interest in [A.2]. The principle example of operation for each one of them can be seen in Figure 2.1.

The choice of hyperspectral technique depends heavily on the application. The two common spatial scanning techniques are the whisk-broom or point-scanning mode and the push-broom or line-scanning mode. The push-broom technique is currently the most widely used solution for commercial applications. However, as the name implies, a hyperspectral image is acquired using the spatial scanning principle, either in one or two spatial directions, which is time-consuming. Therefore, capturing the entire instantaneous hyperspectral image at once, or the snapshot technique, is of great interest to system designers. On the contrary, the snapshot technique is constrained by a highly complex design and limitations in spectral and spatial resolution. Frequently exploited is also the spectral scanning (staring) principle, but with limitations in spectral channel acquisition (using standard interference filters) or complicated design and optimization (using electronically tunable filters). Probably the most

recent, and still under investigation, is the spatial-spectral principle. This technique spreads different spatial parts of the scene into different spectral channels, which are displayed on the detector/sensor. For its functionality, it needs scanning through space or changing the parameters of the dispersive element, which enables the tunable filters [A.2]. More details on selected HSI techniques are provided in the following sections. The additional comprehensive list of hyperspectral approaches and systems can be found in [3, 97].

2.1.1 Whisk-broom

The whisk-broom mode is the most simplistic among the hyperspectral systems. As the name suggests, the captured scene is scanned point by point, which is limited by the sampling pixel point size of the used system sensor. For the purpose of whisk-broom mode operation, some kind of line-type detector is usually used. Each of the scanned pixels of the scene is then dispersed on the line detector. Thus, to obtain a final hyperspectral image $I_{HS}(x, y, \lambda)$, the scene must be scanned in both orthogonal spatial coordinates x, and y while keeping the wavelength dispersion constant, which is very time-consuming.

On the contrary, the great advantage of the whisk-broom system is a simple design, no keystone distortion [145, 146], and a wide field of view (FOV) not limited by a standard 2D sensor composition. The most famous among the whisk-broom systems is undoubtedly the Airborne Visible / Infrared Imaging Spectrometer (AVIRIS) system introduced by the National Aeronautics and Space Administration (NASA) in [147]. The usage of the whisk-broom system has also been found in confocal microscopy [148] but also in cultural heritage [149].

However, due to the impracticality of long-term scene acquisition while aiming at very high spectral and spatial resolution, the need for a mechanical scanner with moving parts for its operation, and the possible spatial dissimilarity (incongruence) of the final image, the whisk-broom systems have been gradually replaced by the push-broom mode.

2.1.2 Push-broom

The majority of the current hyperspectral systems operate in a push-broom mode. The reason for this is that it offers several advantages over other hyperspectral approaches. The push-broom system is optimized for a line-scanning principle while dispersing the captured line of the scene into a whole spectrum with parameters defined by the system imaging properties. For this purpose, the slit is integrated into the system. This allows the system to use standard 2D sensors for line spectral dispersion over the entire sensor area. Movement of the system is therefore only required in one direction. Compared to a whisk-broom system, the push-broom mode is faster (100 times [9]), allows longer integration time (improved SNR), and improves the possible spatial dissimilarity (incongruence) that may occur.

Moreover, it does not really matter whether the system is satellite-based [97], UAV-based [103] or used for laboratory measurements [81]. The push-broom systems are suitable for each of these applications. In addition, the push-broom systems usually do not require moving parts for satellite- and UAV-based applications. The situation is different for laboratory (bench-top) or industrial applications. These systems almost always need to incorporate some sort of moving table or conveyor belt that is connected to the camera (to set the imaging parameters), or the camera itself has to be mounted on some moving parts (also aligned with camera drivers). An example of a laboratory push-broom system used in [A.3] for the analysis of inkjet photo prints is shown in Figure 2.2.

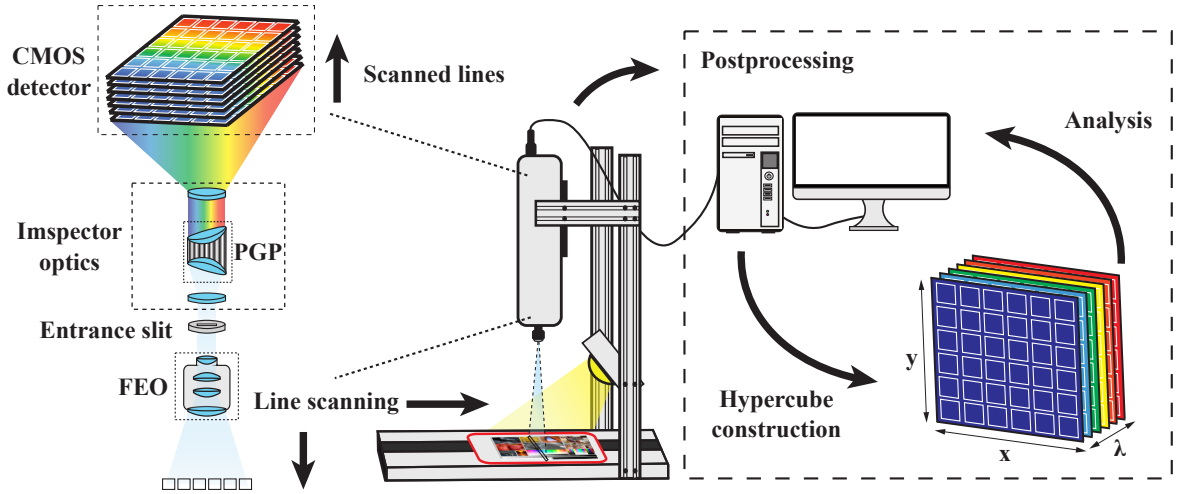

Figure 2.2: Laboratory (bench-top) line-scanning (push-broom) system. Adopted from [A.3] and modified.

However, the push-broom mode also introduces some other disadvantages. The overall optical design of the system is much more complicated, and the systems require correction for the spatial and spectral distortions (keystone and smile) [145]. In addition, the FOV of the system is limited by the finite number of pixels of the sensor. Although the push-broom system mitigates the temporal limitation [150] of the scanning system, new hyperspectral approaches are being tested and developed to overcome this problem.

2.1.3 Snapshot principle

An interesting topic regarding the principles of hyperspectral imaging is the snapshot approach. This type of imaging focuses on the direct acquisition of the hyperspectral image (3D hypercube) in a single capture (snapshot) [151]. This approach does not involve any kind of scanning, and the image can be obtained in a single integration time of a sensor or detector array. However, it usually requires a detector with a significant number of pixels. Therefore, special optical devices are usually required for the snapshot system. A snapshot system typically includes multiple prisms, diffraction gratings, or microlenses that form different types of spectral images at different positions on a detector. The software processing is then used to reconstruct the hyperspectral image.

According to [152] the snapshot systems can be divided into several groups: spectral filter array methods, coded aperture methods, speckle-based methods, and dispersion-based methods, each with pros and cons. The general advantages and disadvantages of snapshot systems are apparent. The very positive aspect is the time it takes to acquire an image. Moreover, these systems can achieve high sensitivity and light collection. On the contrary, the snapshot systems often suffer from lower resolution and could be limited in terms of spectral resolution, number of captured channels, and operational bandwidth. Therefore, the greatest potential of these types of systems is the ability to acquire images at high speed and to capture rapidly changing scenes, for example, in the form of hyperspectral or multispectral video.

Regarding applications, snapshot systems find their usage, for example, in medicine [153] and ophthalmology [154], but also in fluorescence microscopy [155] and many other disciplines

[156]. However, due to the aforementioned system complexity and lower resolution, snapshot hyperspectral imaging can still be considered at an early stage, and the technology is still under development.

2.1.4 Staring systems

The last commonly used hyperspectral technique is staring, sometimes called the spectral scanning principle. To obtain a hyperspectral image, some sort of filter device is needed to select the specific transmitted wavelengths (channels). These spectral filters can take the form of an interference filter, which is attached to some kind of filter wheel, or an electronically tunable type of filter such as an AOTF, or a liquid crystal tunable filter (LCTF) [157, 158]. The whole spatial dimension of the scene can be captured instantly, and the spectral part of the final hyperspectral image is obtained step by step by changing the filters or tuning the filter to pass only a certain wavelength. In particular, research on hyperspectral systems based on LCTF and AOTF has become increasingly popular in a variety of applications [159–161].

In general, LCTF filters use tunable liquid crystal (LC) elements that allow a specific wavelength to pass while blocking the others. The standard principle is based on the Lyot-Ohman approach [162], which involves the transmission of radiation through a sequence of nematic liquid crystals and polarizers [163]. The arrangement of the LC elements is determined by the applied electric field, resulting in a transmitted spectrum with a central peak at one wavelength and near-zero transmission at other wavelengths. By stacking multiple polarization and LC elements, the width of the transmitted wavelength peak can be reduced, and other wavelengths can be more strongly suppressed. In practical implementations, the speed of the LCTF device depends on the thickness of the LC elements and the temperature. The main advantage is the ease of integration into optical systems. The disadvantage is the relatively high loss of transmitted radiation due to multiple propagations through polarizing elements. Among the most important applications of LCTF-based hyperspectral systems can be considered, for example, food inspection [164] and medicine [159].

The AOTF devices, sometimes called Bragg cells, are mostly based on a Bragg diffraction AO phenomenon [165] (more on that in Section 2.2.1). The AOTF device usually consists of an electronically driven piezoelectric transducer that emits the acoustic wave into an anisotropic (typically) optical crystal material (substrate material), where the AO interaction between the incident radiation and the acoustic wave proceeds. The acoustic wave deforms the optical material. This creates a grating that diffracts the incident radiation into different directions. The diffraction characteristics of the AOTF depend on the frequency of the acoustic wave. Tuning the acoustic wave frequency within the filter changes the wavelength of the diffracted radiation. Since the frequency tuning speed of the acoustic wave within the AOTF is relatively fast, it is possible to change the properties of the AOTF instantaneously to obtain a complete hyperspectral or multispectral image. However, the image quality depends on several aspects, such as the quality of the optical material, the diffraction efficiency of the AO interaction, and the overall fulfillment of the AO interaction conditions.

There are several modes of operation for the AOTF devices. The two standard modes are the original collinear [166] and non-collinear [167] interactions and one hybrid mode called close-to-collinear or quasi-collinear interaction [168], each with its own advantages.

As mentioned above, a number of studies on AOTF-based hyperspectral imaging have been carried out in recent years [158, 169–176]. However, the operational spectral band of such AOTF-based systems is severely limited by the properties of the optical substrate materials,

mainly by their optical transparency. Therefore, it is of great interest to investigate new materials that are transparent, for example, in the LWIR spectral band, and suitable for AOTF operation. Mercurous halides are at the forefront of the new materials under investigation due to their high anisotropy and optical transparency from the VIS to the TIR spectral band and beyond. Therefore, the following section is devoted to their basic introduction and the recent research that has been conducted with an emphasis on these materials.

2.2 Mercurous halides - promising optical materials and their usage for VIS - IR hyperspectral imaging

Mercurous halides Hg_2X_2 belong to the family of dielectric crystals with tetragonal lattice (I4/mmm) [40, 177]. Their high optical anisotropy and photoelasticity result from the convenient structure of parallel chains of linear X-Hg-Hg-X molecules arranged in the direction of the crystallographic C axis, where the intramolecular bond is mainly covalent, and the adjacent molecules are bound by van der Waals forces [178, 179].

Three specific members of the mercurous halide group are almost always considered: mercurous chloride (Hg_2Cl_2), also known as calomel, mercurous bromide (Hg_2Br_2), also known as kuzminite, and mercurous iodide (Hg_2I_2), also known as moschelite. These optical crystals hold great promise for the construction of a variety of optical devices. In particular, acousto-optic devices [180–186], [A.2], polarizers [187, 188], [A.4], or radiation detectors [189–191].

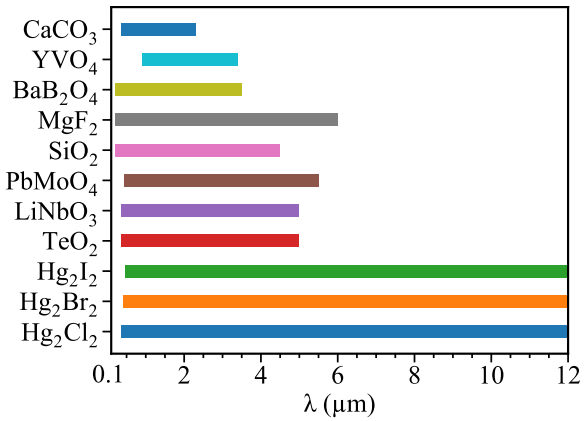

Figure 2.3: An example of the optical transmission or transparency range of several selected common optical materials and a comparison with mercurous halides [39, 192]. The λ symbol represents the wavelength.

The most competitive advantage of mercurous halides is the unique transmission range from VIS (sometimes even UV is reported) to LWIR and parts of the FIR spectral bands. Compared to other commercially available optical materials, the transmission bandwidth of mercurous halides is enormous and offers considerable application possibilities. According to the handbook [192] the transmission range of Hg_2Cl_2 extends over a spectral band that spans from 0.35 µm to 20 µm. The transparency range of Hg_2Br_2 and Hg_2I_2 is even wider, ranging from 0.4 µm to 30 µm and from 0.45 µm to 40 µm, respectively. The general transmission comparison between the other optical materials and mercurous halides is outlined in Figure 2.3.

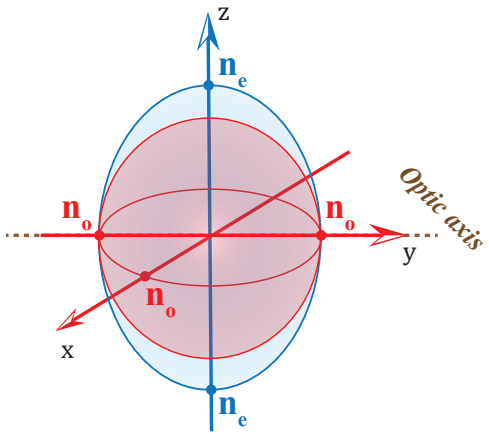

Figure 2.4: The index ellipsoid of uniaxial mercurous chloride Hg_2Cl_2. Adopted from [A.4].

In terms of optics, mercurous halides are classified as anisotropic or birefringent crystals. As such, they interact with incident polarized electromagnetic radiation. Their optical polarization behavior can be evaluated by studying their interaction with the electric field of electromagnetic radiation. In general, the electric field within a linear dielectric anisotropic material can be expressed as [193]

$$\mathbf{E} = \boldsymbol{\epsilon}^{-1}\mathbf{D}, \tag{2.1}$$

where $\mathbf{D}$ represents the vector of electrical induction, $\mathbf{E}$ represents the vector of electrical intensity, and $\boldsymbol{\epsilon}^{-1}$ denotes the tensor of electrical impermeability. The tensor $\boldsymbol{\epsilon}^{-1}$ fully characterizes the dielectric properties of the material. For an anisotropic material with a specific symmetry in a principal coordinate system (xyz), the above equation can be further expressed as

$$\begin{pmatrix} E_x \\ E_y \\ E_z \end{pmatrix} = \begin{pmatrix} 1/n_1^2 & 0 & 0 \\ 0 & 1/n_2^2 & 0 \\ 0 & 0 & 1/n_3^2 \end{pmatrix} \begin{pmatrix} D_x \\ D_y \\ D_z \end{pmatrix}. \tag{2.2}$$

.

Here $1/n_1^2$, $1/n_2^2$, and $1/n_3^2$ represent the principal values of the electrical impermeability tensor. The tensor can be visualized as an index ellipsoid in the xyz-coordinate system, described by the equation

$$\frac{x^2}{n_1^2} + \frac{y^2}{n_2^2} + \frac{z^2}{n_3^2} = 1, \tag{2.3}$$

where n_1, n_2, and n_3 correspond to the refractive indices of the anisotropic crystal. In the case of mercurous halides, which are classified as uniaxial optical crystals, the refractive indices are represented as $n_1 = n_2 = n_\mathrm{o}$ and $n_3 = n_\mathrm{e}$, where n_o and n_e correspond to the ordinary and extraordinary refractive indices, respectively. An important direction within the uniaxial optical material is determined by the optic axis of the crystal. The optic axis designates a direction along which the material behaves as isotropic for both parallel and perpendicular polarized input radiation. Therefore, only an ordinary index of refraction applies

in this direction. The illustration of the index ellipsoid for the Hg_2Cl_2 crystal, which serves as a representative member of the mercurous halide family, is shown in Figure 2.4.

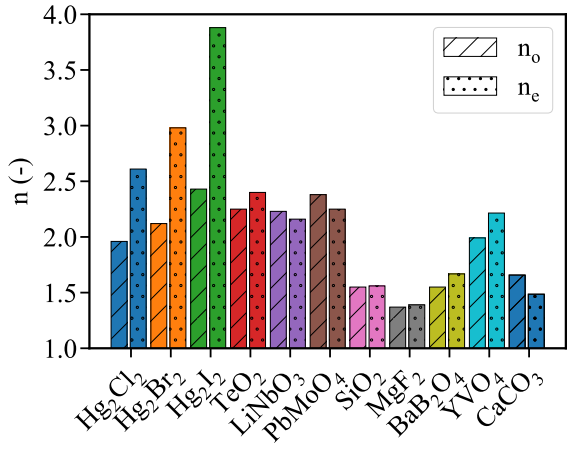

Figure 2.5: An example of the refractive indices (n) of several selected common optical materials and comparison with mercurous halides. The refractive indices correspond to the wavelength (0.633 µm) [39, 192]. The n_o symbol represents the ordinary refractive index. The n_e symbol corresponds to the extraordinary refractive index.

The above leads to the important and already mentioned optical property that makes mercurous halides unique, which is a significant positive birefringence Δn. The birefringence can be expressed as a function of wavelength λ as follows

$$\Delta n(\lambda) = |n_e(\lambda) - n_o(\lambda)|. \tag{2.4}$$

The refractive index dispersion can be approximated, for example, by Cauchy's formula [194] denoted as

$$n\,(\lambda) = A + \frac{B}{\lambda^2} + \frac{C}{\lambda^4} + \frac{D}{\lambda^6} + \dots\ . \tag{2.5}$$

The coefficients A, B, C, D vary with the selected material. For mercurous halides and their most used competitor for acousto-optic devices TeO_2, the coefficients were taken from [A.2]. By choosing the standard wavelength corresponding to the HeNe laser radiation (0.633 µm), the refractive indices Hg_2Cl_2, Hg_2Br_2, Hg_2I_2 can be estimated as $n_o = 1.96$, $n_e = 2.61$; $n_o = 2.12$, $n_e = 2.98$; and $n_o = 2.43$, $n_e = 3.88$, respectively. A comparison of the refractive indices of common optical materials with mercurous halides can be seen in Figure 2.5. In addition, the evolution of the refractive index as a function of wavelength can be seen in Figure 2.6, for all mercurous halides and TeO_2.

Taking into account the refractive index values obtained in this way, one can easily evaluate the birefringence of the selected optical materials according to the previous equation (2.4). For the wavelength 0.633 µm the birefringence is then for Hg_2Cl_2 approximately 0.66; for Hg_2Br_2 approximately 0.86; and Hg_2I_2 approximately 1.48. The birefringence of mercurous halides and TeO_2 against the wavelength in the range from 0.4 µm to 12 µm is shown in Figure 2.7.

Another very important parameter of mercurous halides, with respect to optical applications, is the acousto-optic figure of merit M_2 and the very low acoustic wave velocity for the shear

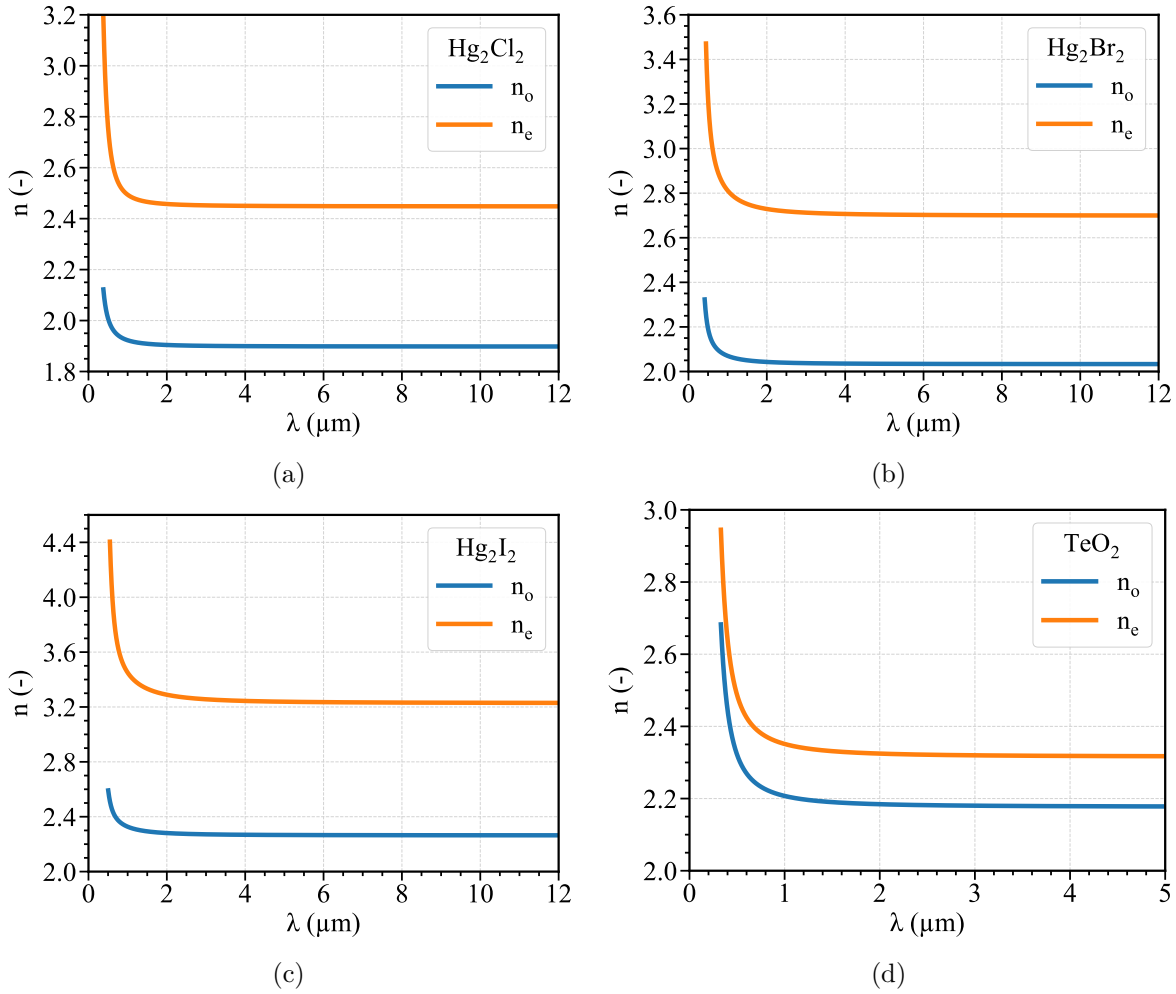

Figure 2.6: Estimated refractive indices (n_o, blue - ordinary; n_e - extraordinary) of mercurous halides: Hg_2Cl_2 (Figure 2.6a), Hg_2Br_2 (Figure 2.6b) Hg_2I_2 (Figure 2.6c), and paratellurite TeO_2 (Figure 2.6d). The λ symbol represents the wavelength. Redrawn from [A.2].

mode, which is directly related to M_2. Simplistically, M_2 is given by [195]

$$M_2 = \frac{N^6 p_{\text{eff}}^2}{\rho V^3}. \tag{2.6}$$

Note that the acousto-optic figure of merit depends strongly on the crystallographic orientation and thus on the polarization. Within the expression (2.6), N represents the refractive index expression (dependent on the incident polarization and acousto-optic diffraction), p_{eff} is the effective elastic-optic coefficient (highly dependent on the crystallographic orientation, the direction of the radiation, and the acoustic wave propagation within the crystal), ρ is the density of the crystalline material, and V is the velocity of the induced acoustic wave (depending on the crystallographic orientation, the mode of the acoustic wave, and the propagation direction).

There are various crystallographic planes that can be annotated by Miller indices and considered for AO operation. For mercurous halides, the most promising plane with a very low shear acoustic wave velocity propagation is the crystallographic plane [110], [001] [40]. The

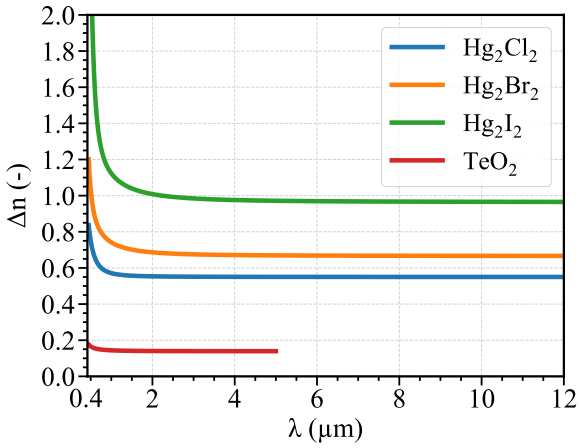

Figure 2.7: Birefringence Δn of mercurous halides Hg_2Cl_2 - blue, Hg_2Br_2 - orange, Hg_2I_2 - green, and TeO_2 - red, against wavelenght λ. Partially redrawn from [A.4].

minimal acoustic wave velocities can be reached in a direction [110], where V_{110} for Hg_2Cl_2 can be considered as $V_{110} < 350\,\mathrm{m\,s^{-1}}$, for Hg_2Br_2 as $V_{110} < 285\,\mathrm{m\,s^{-1}}$, and for Hg_2I_2 as $V_{110} < 255\,\mathrm{m\,s^{-1}}$. In comparison, for TeO_2 is the $V_{110} < 620\,\mathrm{m\,s^{-1}}$. It is worth mentioning that for the direction [001], the acoustic wave velocities are much higher - $V_{001} \approx 1000\,\mathrm{m\,s^{-1}}$, and for TeO_2 - $V_{001} \approx 2100\,\mathrm{m\,s^{-1}}$. Standardly, the estimates for the M_2 (considering the slow acoustic shear wave mode) reach values around $1000 \times 10^{-15}\,\mathrm{s^3\,kg^{-1}}$ for Hg_2Cl_2, around $2600 \times 10^{-15}\,\mathrm{s^3\,kg^{-1}}$ for Hg_2Br_2, and around $3200 \times 10^{-15}\,\mathrm{s^3\,kg^{-1}}$ for Hg_2I_2 [196], compared to the TeO_2 with M_2 around $800 \times 10^{-15}\,\mathrm{s^3\,kg^{-1}}$.

However, there is an important issue with these values of M_2 for mercurous halides. These values are only qualified estimates for the crystallographic plane [110], [001]. For this plane the p_{eff} can be expressed as [197, 198]

$$p_{\mathrm{eff}} = p_{44} \cos\theta_i \sin\theta_a - \frac{(p_{11} - p_{12})}{2} \sin\theta_i \cos\theta_a, \tag{2.7}$$

where θ_i and θ_a describe the propagation of incident radiation and acoustic waves in the material (specifically within the crystallographic plane). The symbols p_{44}, p_{11}, p_{12} represent elasto-optic coefficients obtained from the fourth-rank elasto-optic tensor. These coefficients depend strongly on the material properties and are different for each anisotropic material. This is where the problem arises in determining the values of these elasto-optic coefficients for mercurous halides. For Hg_2Cl_2 only the coefficients p_{11}, p_{12} have been measured and confirmed ($p_{11} = 0.0551$, $p_{12} = 0.44$) [192]. The crucial coefficient p_{44} still remains unknown during the writing of this thesis. The same applies to the remaining mercurous halides Hg_2Br_2 and Hg_2I_2, except that neither p_{11} nor p_{12} are known. For this reason, the manuscript [A.2] attempted to refine the estimate and show how the value of p_{44} affects M_2 for Hg_2Cl_2.

This brings us to the fundamental limiting factor of mercurous halides and the complication for their widespread use in the design of standard and commercially available optical devices, which is the problematic and time-consuming growth, crystal quality, and various chemical reactions with selected compounds. For this reason, the missing elasto-optic coefficients are very difficult to determine today and will continue to be so until genuinely functional AO

devices (with successful and reliable transducer bonding) are constructed, and these coefficients can then be measured.

Several research institutes around the world are now working on the growth of mercurous halides. Currently, the mercurous halide crystals (bulks, bouls) are primarily grown via the Physical Vapor Transport (PVT) method. It is driven by a dynamic temperature field and corresponding axial and radial temperature gradients. The entire process must be carefully maintained within narrow physical constraints, making it highly complex (see more in [189, 199–204]). A related problem is crystal processing and precise polishing. Nowadays, polished crystals of mercurous halides (mostly Hg_2Cl_2 and Hg_2Br_2) reach sizes in the order of tens of mm [205, 206], a few tens of cm at most[1]. The limiting factor is the achievable size of high-quality crystals without bubbles, cracks, scratches, scatter, striae, and other inhomogeneities [207].

For this reason, it is nowadays essential to optimize the design of mercurous halide-based optical devices so that their grown crystals can be properly processed and thus prepared for testing optical applications. The inaccurate and suboptimal design of these devices will result in inadequate fabrication, which is time-consuming and costly. At the same time, it is critical to come up with new designs and applications for mercurous halide-based devices to clearly demonstrate the potential of these materials, which could then lead to pressure to expand research into their improved growth and processing. This is a way to achieve the transfer from basic research to flawless manufacturing processes leading to optimum quality of processed crystals and hence the quality of designed optical devices in the future.

In general, from the perspective of HSI, polarization devices and mercurous halide-based AOTFs have been identified as very promising devices, especially as building blocks for a possible unconventional hyperspectral system operating in the thermal (or other infrared) spectral band, with the promise of high spectral resolution and no moving integral parts. Therefore, the following sections are dedicated to the introduction of this novel hyperspectral concept and to the optimization of mercurous halide-based devices. These research areas are also placed in the context of the current state of the art and the results presented in Chapter 3.

2.2.1 Spatio-spectral hyperspectral system based on quasi-collinear AOTF

The possibilities and approaches of using acousto-optic filters for HSI have been discussed in the above Section 2.1.4. In particular, the selection of an operational spectral band is important for the design of the AOTF. Historically, AOTF-based HSI has been limited to approximately 5 µm (the transmission range of the most widely used AOTF optical material TeO_2), and this is where the scope for mercurous halides opens up, as they are transparent from VIS to TIR. In the past years, a number of approaches of mercurous halide-based AOTF designs were investigated [186, 198, 208–214]. However, their exploitation within the complete imaging system is often limited or not considered in detail.

A completely new approach has been selected by Maksimenka in [37], where the spatio-spectral AOTF-based hyperspectral system has been introduced. An example of its operation can be seen in Figure 2.8. The original system was designed for MWIR and LWIR operation with a collinear-based AOTF. Two breadboard prototypes were built as a proof of concept. However, it was concluded that the physical properties of the AOTF were identified as the main limitation of the presented spatio-spectral hyperspectral system. Therefore, a new design

[1] "Advertised by BBT-Materials Processing, Ltd.", `http://calomel.cz`, (2023)

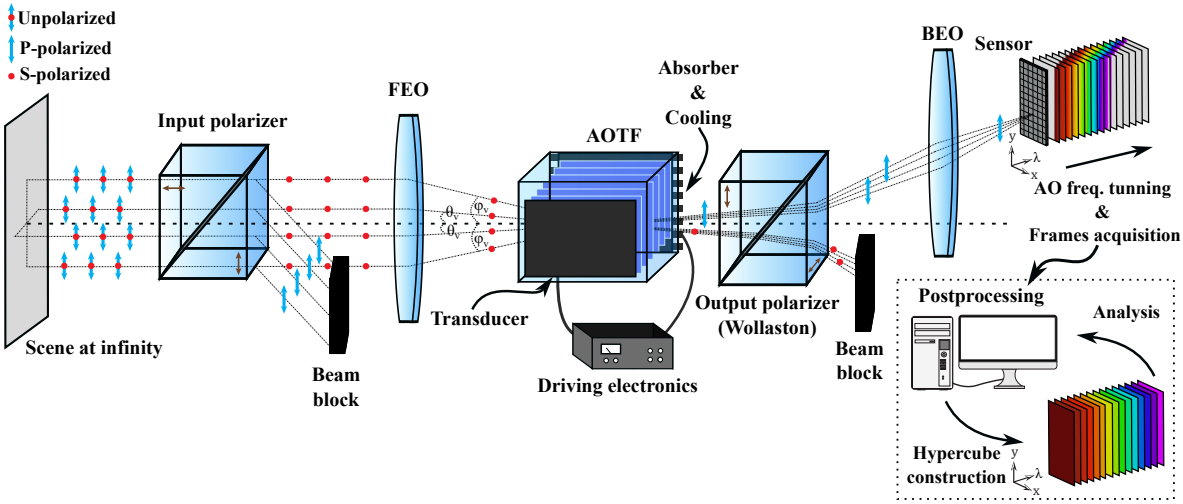

Figure 2.8: An example of the spatio-spectral AOTF-based hyperspectral system and its operation.

of a quasi-collinear AOTF suitable for such a system was investigated and proposed as an alternative to improve the original concept [A.2]. The following paragraphs focus on the general description of potential parameters and operation of the spatio-spectral hyperspectral system specifically based on the quasi-collinear AOTF (exploiting mercurous halide crystals). Furthermore, this quasi-collinear spatial-spectral concept is one of the applicable options for the ESA THETIS project.

As mentioned above, the overall concept of the AOTF spatio-spectral hyperspectral system is shown in Figure 2.8. The whole system is designed to be relatively robust and compact without the need for moving parts. Moreover, the concept could be relatively lightweight with a further appropriate design of driving electronics. Nevertheless, due to the usage of an AOTF, the whole concept is polarization sensitive. Therefore, the polarizer, which operates in the same spectral band as the AOTF (the same applies to all optical devices), must be integrated into the FEO. Polarizer integration also applies to the output BEO, which is located after the AOTF (in terms of the optical path).

The uniqueness of this system lies in the spatial-spectral concept of hyperspectral imaging. The main focus is on the AOTF and the specific acoustic wave induced into the anisotropic single crystal of the AOTF. As the incoming wavefront from the object space passes through the FEO and then enters the AOTF through the front window, the interaction between the incoming radiation and the acoustic wave occurs. Now, assume a thick diffraction grating created by the acoustic wave inside the AOTF single crystal that allows a sufficient interaction length L between the incident radiation and the acoustic wave. This should ensure that the AOTF operates in the Bragg regime instead of the Raman–Nath regime [215]. The interaction can then be described by a well-known Bragg diffraction expression (condition) [165]

$$\sin\theta_B = \frac{\lambda}{2\lambda}, \tag{2.8}$$

where λ denotes the wavelength within the crystal medium, θ_B is the Bragg angle, and λ is the wavelength of the acoustic wave. For simplicity, only the Bragg angle specific to the relevant crystal environment is considered (without considering Snell's law) [216]. Thus, at the

output of the AOTF, the transmitted and diffracted radiation (according to the equation 2.8)) can be obtained. It should be noted that the expression (2.8) is only valid for the isotropic case. For anisotropic AOTF operation, the more complex Dixon equations [217] must be used, taking into account the momentum matching (further described below) between the incident radiation, the diffracted radiation, and the acoustic wave. However, at this stage, the AO interaction may be simplified for the basic description of the spatio-spectral operation.

Assume that the broadband radiation incident on the crystal medium is in the form of rays with different angles of incidence and that the wavelength of the acoustic wave propagating in the crystal is fixed. Then at the output of the crystal medium, multiple diffracted beams (depending on the incident radiation angle θ_B and λ) appear. Unlike conventional AOTF-based systems, this system does not use collimated input radiation, but instead encodes spectral information through the angles of the incident radiation, enabling spatial-spectral mode. Moreover, by tuning the acoustic wave frequency, the Bragg condition changes, and the spectral output will also be changed. In this way, a series of spatio-spectral images can be acquired, which can then be postprocessed into a final hyperspectral cube I_{HS}.

The spatio-spectral imaging can also be described as a mapping from the viewing angles θ_v and ϕ_v into a plane of the sensor XY as $\theta_v \rightarrow x$ and $\phi_v \rightarrow y$. Due to the AO interaction, the mapping depends on the Bragg condition and therefore on the angle of incidence, the acoustic wave frequency, and the wavelength of the radiation. It is also necessary to take into account that the Bragg condition is satisfied for a narrow range of $\Delta\theta_v$ that deviates from the angle θ_v, known as the angular acceptance or chromatic field of view that emerges from the phase-matching condition (further described below). The acceptance angle then affects the mapping into the x coordinate, and the diffracted radiation will cover some spatial range Δx. In the y coordinate, the mapping should remain unchanged. Given a specific acoustic frequency of the acoustic wave f_a within the AOTF, from diverse viewing angles $\Delta\theta_v$, the different wavelengths satisfying the Bragg condition should be mapped into diverse x spatial coordinates in range Δx. This can be described as an AO transformation of the view-angle function through the functions of AO diffraction into a spatio-spectral image I_S (matrix slice) acquired by a 2D image sensor as

$$F(\Delta\theta_v, \phi_v, \lambda_v) \underset{f_a}{\longrightarrow} \begin{matrix} F\left(\Delta x_1, y, \lambda_1\right) \\ F\left(\Delta x_2, y, \lambda_2\right) \\ \vdots \\ F\left(\Delta x_{\eta_x}, y, \lambda_{\eta_x}\right) \end{matrix} \xrightarrow[\text{2D sensor}]{} I_S\left(\Delta x_{c_x}, y\right). \tag{2.9}$$

In the expression (2.9), λ_v represents wavelengths within a broadband incident radiation, $c_x = 1, \ldots, \eta_x$ and denotes the number of cases (spectral channels) when the radiation is successfully diffracted to the sensor plane. By tuning the acoustic wave frequency, M spatio-spectral images can be obtained (due to the changes in the AO interaction). The hyperspectral image can then be reconstructed as a matrix of slices from multiple spatio-spectral images as

$$I_S\left(\Delta x_{c_x}, y, m_{f_a}\right) \xrightarrow[\text{reconstruction}]{} I_{HS}\left(x_w, y_h, \lambda_{c_x}\right), \tag{2.10}$$

in a postprocessing scheme proposed by [37], with indices $m_{f_a} = 1, \ldots, M$, $w = 1, \ldots, \eta_w$ and $h = 1, \ldots, \eta_h$, where η_w, η_h correspond to the width and height of the image, respectively. The whole procedure is also illustrated in Figure 2.8.

This spatio-spectral concept can be used in the VIS spectral region as well as in the UV or IR band, depending on the optimized AOTF and the optical material. Therefore, it is

apparent that the type of AOTF device used within such a system is crucial for the operation of the spatio-spectral system. The design and demonstration of spatio-spectral operation using a quasi-collinear AOTF based on mercurous halides, along with a demonstration of its advantages, was the subject of [A.2].

The quasi-collinear interaction, sometimes called close-to-collinear interaction, was introduced by Voloshinov in [168]. In recent years, several publications have focused on the study and design of the quasi-collinear AOTF [218–224]. The main advantage of the quasi-collinear approach is the extension of the interaction length, which leads to an improvement of the diffraction efficiency, the spectral resolution, and the possibility of a wide aperture. The following lines focus on the quasi-collinear description and diffraction efficiency in a little more detail.

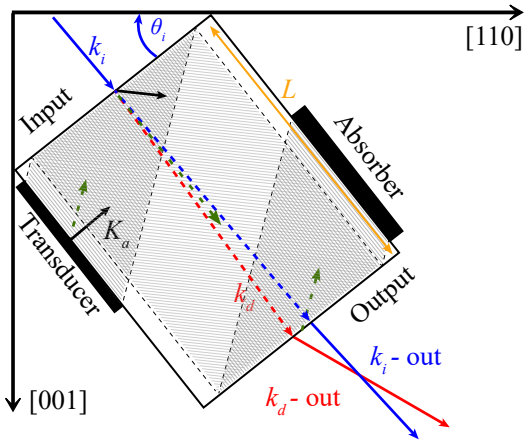

Figure 2.9: An example of a quasi-collinear AOTF scheme drawn in convenient crystallographic orientation for mercurous halides. The blue arrows (solid and dashed) correspond to the incident and transmitted radiation described by the wave vector k_i. The red arrows (solid and dashed) correspond to the AO-generated diffracted radiation denoted by the wave vector k_d. The green dashed arrows correspond to the energy propagation of the acoustic wave within the AO crystal. The black solid arrow represents the orientation of the acoustic wave group velocity vector. The symbol θ_i is the incident angle, denoted as the angle between the AOTF input facet and the crystallographic axis [110]. L is the AO interaction length. This figure has been modified and redrawn from [A.2].

In general, an example of a quasi-collinear AOTF scheme in a suitable crystallographic orientation for mercurous halides ([001], [110]) is shown in Figure 2.9. In this example, the acoustic wave emitted by the transducer propagates within the optical material (anisotropic crystal). The acoustic wave is then totally reflected at the input facet of the crystal and propagates collinearly with the input incident radiation. The acoustic wave is then reflected at the output facet of the crystal and then absorbed by an absorber device. The interaction length L is thus determined by the physical size of the crystal. This configuration exploits S-polarized ordinary input radiation and diffracts the radiation beam with extraordinary P-polarization. The quasi-collinear principle lies in the fact that the acoustic phase velocity vector (orientation of the acoustic wavefronts) and the acoustic group velocity vector (energy propagation of the acoustic wave) have diverse orientations.

The quasi-collinear AO interaction (shown in Figure 2.9) can be expressed by the wave-vector equation [215]

$$\vec{k_d} = \vec{k_i} + \vec{K_a}. \tag{2.11}$$

This equation (2.11) describes the phase matching between the incident radiation wave vector k_i, acoustic phase velocity wave vector $\vec{K}$, and the diffracted radiation wave vector $\vec{k_d}$. A detailed description, explanation, and modeling of AO phase matching can be found in the core publication [A.2] within Chapter 3.

It is apparent that by changing the parameters of the acoustic wave or incident radiation (e.g., wavelength, direction), the phase matching could be violated. The phase matching deviation could be expressed as

$$\vec{\Delta k} = \vec{k_d} - \vec{k_i} - \vec{K_a}, \tag{2.12}$$

where $\vec{\Delta k}$ is the phase mismatch. The phase mismatch is one of the key parameters affecting the diffraction efficiency of the interaction and thus of the entire AOTF operation. The diffraction efficiency of the AO interaction ζ_{diff} can be expressed as the ratio I_d/I_i between the diffracted and incident radiation intensities, or more precisely as [215]

$$\zeta_{\text{diff}} = \Gamma^2 \cdot \frac{\sin^2 \sqrt{\Gamma^2 + \left(\frac{\Delta k \cdot L}{2}\right)^2}}{\Gamma^2 + \left(\frac{\Delta k \cdot L}{2}\right)^2}. \tag{2.13}$$

The symbol Γ can then be derived in more detail as

$$\Gamma = \frac{\pi}{\lambda} \cdot \sqrt{\frac{M_2 \cdot P_a \cdot L}{2 \cdot H}}. \tag{2.14}$$

Here the AO figure of merit M_2 appears again. The next symbol P_a represents the acoustic power, and H is the height of the acoustic beam (standardly limited by the transducer size).

To obtain the spectral resolution from the diffraction efficiency, one can look at the fact that the diffraction efficiency is represented by a $sinc^2$ function. The best achievable spectral resolution $\Delta\lambda$ at full width half maximum (FWHM) of $sinc^2$ ($\Delta kL \approx 0.9\pi$) can then be derived as

$$\Delta\lambda = \frac{1.8\pi\lambda^2}{bL\sin^2\theta_i}, \tag{2.15}$$

where θ_i is for the example presented Figure 2.9 an angle from the [110] axis and b is a dispersion constant related to the birefringence of the crystal material that is equal to [225]

$$b = 2\pi\lambda^2 \cdot \frac{\partial}{\partial\lambda}\left(\frac{|\, n_o - n_e \,|}{\lambda}\right). \tag{2.16}$$

The next important characteristic of the AOTF is also the already mentioned chromatic field of view. This characteristic refers to the angular acceptance in conventional AOTFs and is represented by the maximum angular deviation from normal incidence at a given wavelength and acoustic wavelength for which the phase-matching condition is satisfied. Due to the spatio-spectral nature of the AOTF operation, the angle is used to encode spectral information,

and therefore the angular resolution of the AOTF is limited by the constraints imposed by the chromatic field of view. The chromatic field of view $\Delta\theta$ can also be derived from the diffraction efficiency equation (2.13). For a given wavelength, $\Delta kL \approx \pi$ and $\Delta\lambda \approx 0$, and the chromatic field of view then can be expressed [167, 225] as

$$\Delta\theta = \sqrt{\frac{2\pi \cdot \lambda}{L \cdot b \cdot \mid 3\cos^2\theta_i - 1 \mid}}. \tag{2.17}$$

It is evident that increasing the interaction length L of the AO interaction greatly improves the performance of the AOTF, which promotes the quasi-collinear interaction. In addition, it has been shown that the operation of the AOTF is strongly dependent on the properties of the crystal substrate material chosen for its construction (e.g., transmission, birefringence, and acoustic wave velocity). Accurate design and modeling of the expected AOTF performance is therefore critical [A.2].

This section has focused on the introduction, basic description, and state of the art regarding the quasi-collinear AOTF and the operation of the spatio-spectral AOTF-based hyperspectral system. It has already been mentioned that the entire AOTF operation is sensitive to polarization. Therefore, it is necessary that the implemented spatio-spectral system includes linear polarizers (with excellent polarization parameters, ideally crystal-based) to ensure a high degree of input polarization and sufficiently block the unwanted output polarization. For the operation in the LWIR spectral band, there is currently no commercially available anisotropic crystal material that could be exploitable for such a purpose. Thus, mercurous halides can fill this gap, and it is important to study their polarization properties along with the design and optimization of such crystalline polarizers based on them.

2.2.2 Crystalline polarizers

Crystalline or crystal polarizers offer important properties in terms of a degree of polarization and broadband spectral operation compared to standard foil or wire grid polarizers. These properties are required in a wide range of polarimetric applications such as astronomy [226, 227], biomedical imaging [228], HSI [229–231], [A.2], and others [232, 233]. However, the construction and operation of crystal polarizers are limited by the material properties (even material purity) of the growth and polished crystals. The currently used polarizer materials do not offer a high birefringence and are limited by their spectral transparency. One can mention the transparency ranges and birefringence values for some selected materials such as quartz (SiO_2; 0.12 µm – 3.5 µm; 0.009 at 633 nm) [234], magnesium fluoride (MgF_2; 0.2 µm – 6 µm; 0.0118 at 633 nm) [235], yttrium orthovanadate (YVO_4; 0.9 µm – 3.4 µm, 0.2229 at 633 nm) [236], calcite ($CaCO_3$; 0.35 µm – 2.3 µm, 0.1808 at 633 nm) [234] or barium borate (BaB_2O_4; 0.19 µm – 3.5 µm; 0.1174 at 633 nm) [237]. From the band 6 µm up to the LWIR or even up to the FIR spectral band, there are currently no usable crystalline polarizers. The exploitation of mercurous halides as crystalline polarizers is then directly promoted.

In recent years, various strategies and ideas have been introduced for utilizing mercurous halides as polarizers [187]. These efforts have primarily concentrated on Glan-type polarizers, with a particular emphasis on mercurous bromide (Hg_2Br_2) [188]. However, comprehensive optimization, design, and ray-tracing analyses have not yet been presented.

In general, there are some very typical crystal polarizer schemes that are used in practice, such as the already mentioned Glan-type polarizers (e.g., Glan-Taylor, Glan- Foucault, Glan-Thompson) [238]. Example schemes of these polarizers can be seen in Figure 2.10. The

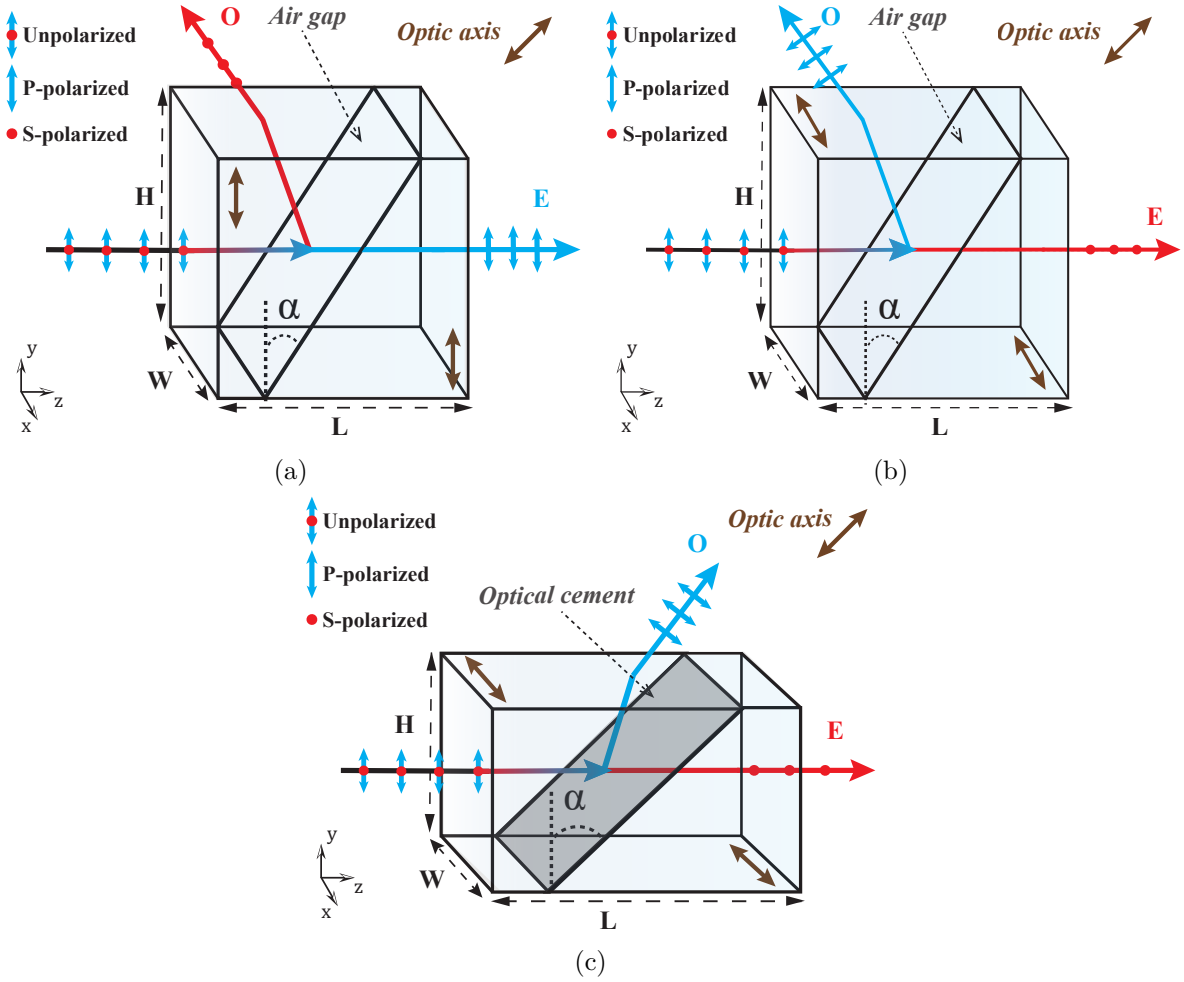

Figure 2.10: Example of Glan-Taylor polarizer (Figure 2.10a), Glan-Foucault polarizer (Figure 2.10b), and Glan-Thompson polarizer (Figure 2.10c) schemes. The *O* symbol represents the ordinary beam. The *E* symbol corresponds to the extraordinary beam. The dimensions of each polarizer are indicated as W (width), L (length), and H (height).

next group of polarizers are the beam-splitting types (e.g., Rochon, Senarmont, Wollaston). Example schemes of the beam-splitting polarizers can be seen in Figure 2.11. Both groups of these standard polarizers are constructed from two combined wedge-shaped prisms. The crystallographic orientation of these polished wedges is critical, especially the orientation of the optic axis. This orientation determines the behavior of the polarizer for incident unpolarized radiation composed of S- and P-polarized beams. Thus, the orientation of the optic axis determines which polarization will propagate through the birefringent wedge as an ordinary or extraordinary wave (with an ordinary or extraordinary index of refraction). The radiation beam polarized parallel to the optic axis behaves as an extraordinary wave. The beam polarized orthogonally to the optic axis behaves as an ordinary wave.

The polarizer behavior is also determined by the type of birefringent substrate material. Uniaxial anisotropic materials are typically used in the construction of crystalline polarizers. However, it depends on whether it is a uniaxial crystal with positive or negative birefringence, and therefore on the difference between its extraordinary and ordinary refractive indices.

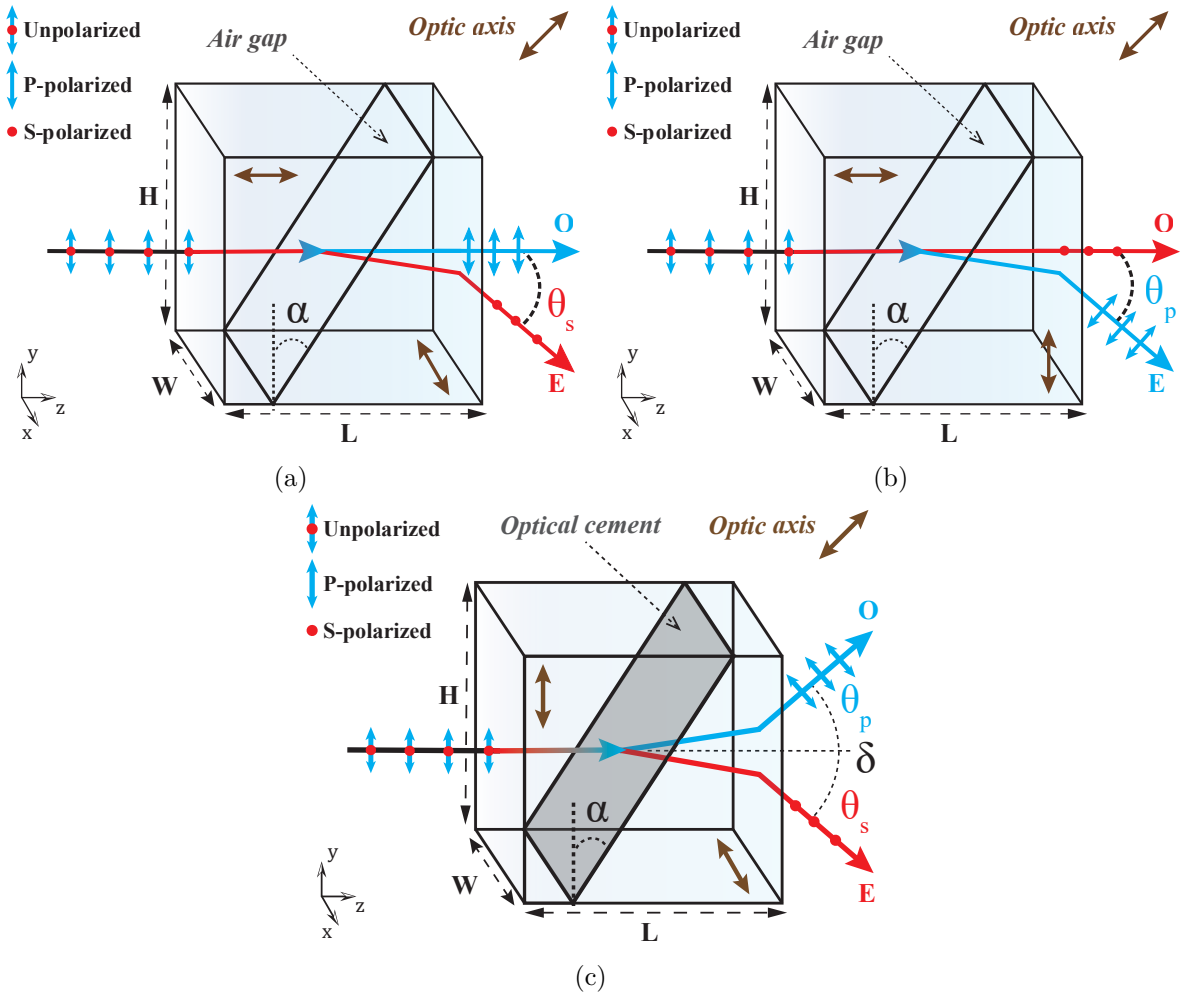

Figure 2.11: An example of Rochon polarizer (Figure 2.11a), Senarmont polarizer (Figure 2.11b), and Wollaston polarizer (Figure 2.11c) schemes. The O symbol represents the ordinary beam. The E symbol corresponds to the extraordinary beam. The dimensions of each polarizer are indicated as W (width), L (length), H (height). Figure 2.11c) has been adopted from [A.4].

Given the above characteristics and the propagation of unpolarized radiation through the polarizer, the total transmission and losses can be calculated using the well-known Fresnel coefficients [193] as

$$t_{\mathrm{s}} = \frac{2n_{\mathrm{in}} \cos\theta_{\mathrm{in}}}{n_{\mathrm{in}} \cos\theta_{\mathrm{in}} + n_{\mathrm{out}} \cos\theta_{\mathrm{out}}}, \tag{2.18}$$

$$t_{\mathrm{p}} = \frac{2n_{\mathrm{out}} \cos\theta_{\mathrm{out}}}{n_{\mathrm{out}} \cos\theta_{\mathrm{out}} + n_{\mathrm{in}} \cos\theta_{\mathrm{in}}}, \tag{2.19}$$

$$r_{\mathrm{s}} = \frac{n_{\mathrm{in}} \cos\theta_{\mathrm{in}} - n_{\mathrm{out}} \cos\theta_{\mathrm{out}}}{n_{\mathrm{in}} \cos\theta_{\mathrm{in}} + n_{\mathrm{out}} \cos\theta_{\mathrm{out}}}, \tag{2.20}$$

$$r_{\mathrm{p}} = \frac{n_{\mathrm{out}} \cos\theta_{\mathrm{out}} - n_{\mathrm{in}} \cos\theta_{\mathrm{in}}}{n_{\mathrm{out}} \cos\theta_{\mathrm{out}} + n_{\mathrm{in}} \cos\theta_{\mathrm{in}}}. \tag{2.21}$$

The coefficients t_s, t_p, r_s, and r_p represent the transmission and refraction coefficients for S- and P-polarized radiation at a specific surface interface, respectively. The variables n_{in} and n_{out} correspond to the refractive indices at the input and output sides of the specific dielectric interface. Similarly, θ_{in} and θ_{out} denote the angles of incidence and refraction of the radiation at the particular dielectric interface, respectively. The values of the refractive indices θ_{in} and θ_{out} depend on the above-mentioned orientation of the optic axis of the prism and thus on whether the S- or P-polarized radiation is transmitted as an ordinary or extraordinary wave. Suppose that the radiation propagates through several dielectric interfaces, denoted by the index i (similar to standard radiation propagating through a polarizer).

The total transmittance for each polarization T_s and T_p can then be calculated as

$$T_s = \prod_i T_s(i), \quad T_p = \prod_i T_p(i), \tag{2.22}$$

where

$$T_s(i) = t_s^2(i)\frac{n_{out}(i)\cos\theta_{out}(i)}{n_{in}(i)\cos\theta_{in}(i)}, \quad T_p(i) = t_p^2(i)\frac{n_{out}(i)\cos\theta_{out}(i)}{n_{in}(i)\cos\theta_{in}(i)}. \tag{2.23}$$

The total reflected radiation for each orthogonal polarization R_s and R_p can be calculated from

$$R_s = \prod_i R_s(i), \quad R_p = \prod_i R_p(i), \tag{2.24}$$

where

$$R_s(i) = r_s^2(i), \quad R_p(i) = r_p^2(i). \tag{2.25}$$

For a standard type of polarizer, the number of dielectric interfaces is in the range $i = 1, \ldots, 4$. It is apparent that the total transmittance significantly affects the prism cut angle α (shown in both polarizer examples in Figures 2.10 and 2.11). Finding the optimal value of α, taking into account the characteristics of the crystal material, is one of the most critical tasks for polarizer designers. For example, the entire operation of Glan-type polarizers depends on α, so that one of the incident polarizations is totally reflected at the output interface of the first wedge prism of the polarizer and brought out through the side of the polarizer. Typically, α is optimized to maximize the transmission for the desired output polarization. The other parameters, such as clear aperture or field of view, are in turn influenced by the size of the manufactured polarizer (physical dimensions of the input window of the polarizer). For the beam-splitting type of polarizer, an additional parameter δ is introduced. This parameter corresponds to the separation angle of the output orthogonally (S and P) polarized beams. This angle can be written as

$$\delta = |\theta_s - \theta_p|, \tag{2.26}$$

where θ_s is the refracted output angle of the S-polarized radiation and θ_p is the refracted output angle of the P-polarized radiation. For some types of beam-splitting polarizers, the refracted output angles may be close to or equal to zero. It is worth mentioning that due to the dispersion of the refractive index in the transparency range of the used optical material used for the prism, the transmittances T_s, T_p and the polarization separation output angle δ vary with the wavelength of the input radiation.

There are also types of prisms that require optical cement (adhesive immersion) for their proper functionality. This optical cement is used to bond two wedge prisms together in polarizers. Finding a suitable refractive index of this optical cement, together with optimizing the α, makes the analysis and design of the polarizers more difficult. The case of finding the optimal optical cement particularly concerns the Glan-Thompson and Wollaston polarizers (see [A.4]). In practice, it is the Wollaston polarizer that is the most commonly used. Wollaston prisms find their use in a variety of optical applications, such as microscopy [239, 240], spectroscopy [241, 242], polarimetry [243–246], and also HSI [231].

However, the problem arises in the design of a Wollaston polarizer based on mercurous halides. In the first place, a suitable optical cement needs to be found. Ideally, due to high birefringence, the refractive index of such an optical cement for mercurous halides should be very high and should match the refractive index between the ordinary and extraordinary indices. The investigation of the optimal design and refractive index of the optical cement for the Wollaston polarizer was the focus of the core publication [A.4].

In general, the study of the characteristics of polarizers (not only the Wollaston type) based on mercurous halides holds great promise for the design and eventual construction of such a polarizer. Due to its inherent capabilities, this polarizer has great potential for use not only in HSI but also in other applications, especially in the LWIR spectral region.

2.3 Spectral feature exploration in hyperspectral/multispectral image data

In general, besides the development of hyperspectral techniques and instruments, the subsequent challenge is to find a suitable application where HSI can be useful, and then how to process the acquired hyperspectral image data appropriately. This task becomes more complex due to the fact that hyperspectral data contain full spectral information from the operational spectral band of the instrument. In many common cases, this spectral information comes from the reflection of radiation from an object or area of interest [247].

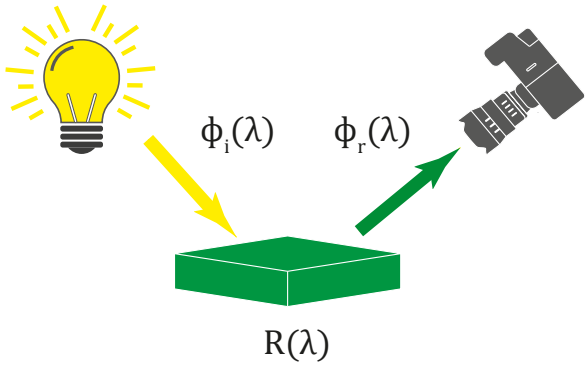

Figure 2.12: An illustration example expressing the spectral reflectance of objects. Adopted from [A.3].

Having radiation with defined spectral characteristics $\Phi_{\mathrm{i}}(\lambda)$ incident on the object, taking into account the reflected flux $\Phi_r(\lambda)$, the reflectance $R(\lambda)$ can then be expressed as

$$\mathrm{R}(\lambda) = \frac{\Phi_r(\lambda)}{\Phi_i(\lambda)}. \tag{2.27}$$

In this case, only a specular reflection with a general angle Θ is assumed. An illustration of the reflectance can be seen in Figure 2.12. Transferring this idea to the problem of HSI and incorporating hyperspectral or multispectral instruments, the spatial distribution of the reflected radiation from the object along the coordinates x and y can be considered. Given the sensitivity of the hyperspectral system $\Psi(x, y, \lambda)$, the transformed hyperspectral image I_{HS} can then be obtained as

$$\phi_r(x, y, \lambda) \longrightarrow I_{HS}(x, y, \lambda), \tag{2.28}$$

where

$$I_{HS}(x, y, \lambda) = \phi_i(x, y, \lambda) R(x, y, \lambda) \Psi(x, y, \lambda). \tag{2.29}$$

This hyperspectral image therefore contains the spatial information of the scene x, y and also the reflected spectral information λ for each pixel of the image. To some extent, this image is reconstructed in a similar way to the images from the above AOTF-based spatial-spectral system (equation (2.10)) or the standard push-broom system (Figure 2.2). In many cases, of course, it is not only the reflectance spectrum that is recorded, but also the emission (thermal or fluorescence) at certain wavelengths.

The spectral information contained in hyperspectral images can then be used to analyze and evaluate the spectral properties of individual objects in the scene and investigate their similarities or differences. The ability to determine spectral properties is problematic in the case of RGB multispectral data, although the color information can still be successfully used to evaluate the properties of different objects [A.1]. In order to evaluate the spectral differences of the captured objects, a number of spectral measures [248] can be used, or the evaluation within a data-dependent transformed spectral space can be used [A.3]. These topics are covered in the following sections.

2.3.1 Spectral Similarity Measures

Metrics or measures of spectral similarity and evaluation of spectral properties of objects have their place in almost every application of hyperspectral imaging, e.g., medicine [249], remote sensing [250], cultural heritage [251], food [252], forensics [253], and soil analysis [254].

Currently, there are many spectral similarity measures that are used on a daily basis for hyperspectral tasks. In some cases, there are even hybrid spectral metrics that are a combination of two or more standard metrics. For the purpose of this thesis, only some classical spectral measures are introduced to quantify the spectral differences of various objects.

Suppose one or more spectral pixels in the rectangular region that are extracted from the original hyperspectral image I_{HS}. The hyperspectral image is labeled as $I_e(x_{w'}, y_{h'} \lambda_c)$. The indices can be represented as $w' = 1, \ldots, \eta'_w$, $h' = 1, \ldots, \eta'_h$ and $c = 1, \ldots, \eta_c$, where η'_w, η'_h are the width and height of the rectangular pixel area, and η_c denotes the number of spectral channels of the hyperspectral image. The average spectra (spectral signature) from the pixel area can then be recovered as

$$\overline{R}(\lambda_c) = \frac{1}{\eta'_w \eta'_h} \sum_{w'=1}^{\eta'_w} \sum_{h'=1}^{\eta'_h} I_e(x_{w'}, y_{h'}, \lambda_c). \tag{2.30}$$

Two recovered average spectra $\overline{R}_1(\lambda_c)$ and $\overline{R}_2(\lambda_c)$ can then be compared using various similarity measures. One of the most basic measures is the spectral angle mapper (SAM) [255],

which can be calculated as

$$\mathrm{SAM}_{\overline{\mathrm{R}_1},\overline{\mathrm{R}_2}} = \cos^{-1}\left(\frac{\sum_{c=1}^{\eta_c}\overline{R_1}\left(\lambda_c\right)\overline{R_2}\left(\lambda_c\right)}{\sqrt{\sum_{c=1}^{\eta_c}\overline{R_1}\left(\lambda_c\right)^2}\sqrt{\sum_{c=1}^{\eta_c}\overline{R_2}\left(\lambda_c\right)^2}}\right). \tag{2.31}$$

The obtained SAM value is a spectral angle in the range 0 rad – 3.142 rad. A lower SAM value implies a strong match between the two compared spectral signatures.

The other very frequently used spectral similarity measure is the spectral information divergence (SID) [256]. The SID method calculates spectral similarity by measuring the difference between the probability distributions of two spectra. These probability distributions can be obtained as

$$D_1(\lambda_c) = \overline{R_1}(\lambda_c)/\sum_{c=1}^{\eta_c}\overline{R_1}(\lambda_c), \tag{2.32}$$

$$D_2(\lambda_c) = \overline{R_2}(\lambda_c)/\sum_{c=1}^{\eta_c}\overline{R_2}(\lambda_c). \tag{2.33}$$

Then the SID measure is calculated as

$$\mathrm{SID}_{\overline{\mathrm{R}_1},\overline{\mathrm{R}_2}} = \sum_{c=1}^{\eta_c} D_2\left(\lambda_c\right)\log\left(\frac{D_2\left(\lambda_c\right)}{D_1\left(\lambda_c\right)}\right) + \sum_{c=1}^{\eta_c} D_1\left(\lambda_c\right)\log\left(\frac{D_1\left(\lambda_c\right)}{D_2\left(\lambda_c\right)}\right). \tag{2.34}$$

A lower SID value implies a strong match between the two compared spectral signatures.

Building on the two metrics presented, a third hybrid metric that combines the two can be introduced. This hybrid measure is called the spectral information divergence spectral angle mapper (SIDSAM) [257] and can be calculated as

$$\mathrm{SIDSAM}_{\overline{\mathrm{R}_1},\overline{\mathrm{R}_2}} = \mathrm{SID}_{\overline{\mathrm{R}_1},\overline{\mathrm{R}_2}} \times \tan\left(\mathrm{SAM}_{\overline{\mathrm{R}_1},\overline{\mathrm{R}_2}}\right). \tag{2.35}$$

Again, a lower SIDSAM value implies a strong match between the two compared spectral signatures.

The last of the fundamental spectral metrics is the spectral correlation mapper (SCM) [258, 259]. The SCM measure is based on the Pearson correlation coefficient and can be calculated as

$$\mathrm{SCM}_{\overline{\mathrm{R}_1},\overline{\mathrm{R}_2}} = \frac{\eta_c\sum_{c=1}^{\eta_c}\overline{R_1}\left(\lambda_c\right)\overline{R_2}\left(\lambda_c\right) - \sum_{c=1}^{\eta_c}\overline{R_1}\left(\lambda_c\right)\sum_{c=1}^{\eta_c}\overline{R_2}\left(\lambda_c\right)}{\sqrt{\eta_c\sum_{c=1}^{\eta_c}\overline{R_1}\left(\lambda_c\right)^2 - \left(\sum_{c=1}^{\eta_c}\overline{R_1}\left(\lambda_c\right)\right)^2}\sqrt{\eta_c\sum_{c=1}^{\eta_c}\overline{R_2}\left(\lambda_c\right)^2 - \left(\sum_{c=1}^{\eta_c}\overline{R_2}\left(\lambda_c\right)\right)^2}}. \tag{2.36}$$

The SCM score ranges from 1 to -1, where a value of 1 indicates that the two spectral signatures are identical, 0 implies a complete lack of correlation, and -1 suggests perfect opposition between the two spectra. Sometimes the SCM measure is associated with the spectral correlation angle (SCA) [260], which defines the spectral similarity converted to an angle based on the SCM.

A more advanced spectral similarity measure that compares two spectral features is the Jeffries-Matusita spectral angle mapper (JMSAM) [261]. The measure also belongs to the

hybrid metrics and consists of the fusion of the Jeffries–Matusita distance (JMD) and the SAM. The JMD can be obtained as

$$\mathrm{JMD}_{\overline{\mathrm{R}_1},\overline{\mathrm{R}_2}} = 2\left(1 - \exp\left(-BD_{\overline{R_1},\overline{R_2}}\right)\right). \tag{2.37}$$

An important distance metric appears in the above expression, namely the Bhattacharyya distance (BD) [262, 263]. The Bhattacharyya distance $BD_{\overline{R_1},\overline{R_2}}$ can be calculated as

$$BD_{\overline{R_1},\overline{R_2}} = \frac{1}{8}\left(\mu_1 - \mu_2\right)^{\intercal}\left(\frac{\sigma_1 + \sigma_2}{2}\right)^{-1}\left(\mu_1 - \mu_2\right)\frac{1}{2}\ln\left(\frac{\det\left(\frac{\sigma_1+\sigma_2}{2}\right)}{\sqrt{\det\sigma_1 \det\sigma_2}}\right), \tag{2.38}$$

where μ_1, μ_2 are the mean values of the compared spectral features σ_1, σ_2 and their variances. The JMD is very similar to the Bhattacharyya coefficient (BC), which, like the JMD, is used to assess the separability of properties of different objects or groups of objects (classes), whether spectral or otherwise. Nevertheless, to compute the full spectral measure JMSAM, the JMD is combined with the SAM measure as follows:

$$\mathrm{JMSAM}_{\overline{\mathrm{R}_1},\overline{\mathrm{R}_2}} = \mathrm{JMD}_{\overline{\mathrm{R}_1},\overline{\mathrm{R}_2}} \times \tan\left(\mathrm{SAM}_{\overline{\mathrm{R}_1},\overline{\mathrm{R}_2}}\right). \tag{2.39}$$

In this section, relevant spectral metrics have been presented in the context of preselected applications where the evaluation of spectral characteristics could be applied. These applications include assessing the color variation among different cloud types in ground-based all-sky images [A.1], as well as distinguishing among different types of printing inks to determine the authenticity of prints and to evaluate the suitability of inks for long-term preservation of printed artwork [A.3].

As mentioned earlier, an alternative approach to comparing the spectral properties of objects via spectral measures is to transform them into an appropriate data-dependent space, where the spectral channels of different objects can be more efficiently described and more easily compared. This concept is further discussed in the following section.

2.3.2 Principle Component Analysis

It is well known that the hyperspectral image very often exhibits redundancy between adjacent spectral bands, resulting in a high correlation between them. Techniques such as Principal Component Analysis (PCA) can be employed to decorrelate the entire hyperspectral image, resulting in a set of new orthogonal bases known as principal components (PCs). The first few PCs typically capture the majority of the variance in the original hyperspectral image, allowing for a concise representation of the image using only a small number of PCs. In general, PCA-based techniques are often used for various applications in hyperspectral imaging, such as dimensionality reduction [264], denoising [265], spectral similarity assessment [A.3], or general classification tasks [266–268].

Suppose there is a hyperspectral image described as $I_{HS}\left(x_w, y_h, \lambda_c\right)$. By stacking the spectral information of the pixels in rows (denoted by r), the hyperspectral image can be straightforwardly transformed into a 2D matrix slice representation, described as $X\left(r_\iota, \lambda_c\right)$, where the indices are $\iota = 1, \ldots, \eta_r$, $c = 1, \ldots, \eta_c$, and $\eta_r = \eta_w \times \eta_h$. The subsequent step involves mean-centering of the transformed matrix as

$$X'\left(r_\iota, \lambda_c\right) = X\left(r_\iota, \lambda_c\right) - \frac{1}{\eta_r}\sum_{\iota=1}^{\eta_r} X\left(r_\iota, \lambda_c\right). \tag{2.40}$$

On this prepared matrix slice, a decomposition by the singular value decomposition (SVD) method [269] based on the dimensions of X' can be performed as

$$X'\left(r_\iota, \lambda_c\right) = \mathbf{U}_{\eta_r \times \eta_r}\, \mathbf{S}_{\eta_r \times \eta_c}\, \mathbf{V}^{\intercal}_{\eta_c \times \eta_c}, \tag{2.41}$$

where $\mathbf{U}_{\eta_r \times \eta_r}$ and $\mathbf{V}^{\intercal}_{\eta_c \times \eta_c}$ are unitary matrices carrying the principal components and eigenvectors, respectively. The diagonal matrix $\mathbf{S}_{\eta_r \times \eta_c}$ contains the singular values. Then the matrix $\mathbf{U}_{\eta_r \times \eta_r}$ can be reduced to the matrix $\mathbf{U}_{\eta_r \times \eta_c}$. By extracting the diagonal values from the matrix $\mathbf{S}_{\eta_r \times \eta_c}$ and forming a vector $\mathbf{s}_{\eta_c \times 1}$, the eigenvalues can be recovered from the expression

$$\mathbf{eig}_{\eta_c \times 1} = \frac{\mathbf{s}^2_{\eta_c \times 1}}{\eta_r - 1}, \tag{2.42}$$

where $\mathbf{eig}_{\eta_c}$ corresponds to a vector of all eigenvalues. The transformation of the original matrix slice $X'\left(r_\iota, \lambda_c\right)$ into the new orthogonal coordinate system based on the $I(x_w, y_h, \lambda_c)$ values.

The transformation of the original matrix slice $X'\left(r_\iota, \lambda_c\right)$ into the new orthogonal coordinate system based on the $I_{HS}\left(x_w, y_h, \lambda_c\right)$ values can be done as

$$X_t\left(r_\iota, P_c\right) = \mathbf{U}_{\eta_r \times \eta_c} \mathbf{s}^{\intercal}_{\eta_c \times 1}, \tag{2.43}$$

where $X_t\left(r_\iota, P_c\right)$ is the transformed matrix slice, and where the original wavelength domain λ_c has been transformed into the new principal component domain P with the same index c.

The variance vector containing the explained variance for each generated principal component can be calculated using the following expression

$$\boldsymbol{\sigma}^2_{\eta_c \times 1} = \frac{100 \cdot \mathbf{eig}_{\eta_c \times 1}}{\sum \mathbf{eig}_{\eta_c \times 1}}, \tag{2.44}$$

where each element of the vector $\boldsymbol{\sigma}^2_{\eta_c \times 1}$ represents the explained variance of the particular PC. As a result of PCA, the transformed image can typically be represented in a lower dimensionality, utilizing only a subset of the PCs that account for more than 95 % or 99 % of the cumulative variance of the original image. The index c, ranging from 1 to η_c, refers to the maximum number of PCs – η_c. This number can then be reduced to the specified value (η'_c).

As was already mentioned, PCA is data-dependent, as its outcomes are influenced by the specific characteristics of the data. Nevertheless, it is possible to express a different hyperspectral image by utilizing a set of PC components, represented by eigenvectors, obtained by applying the PCA method to another hyperspectral image.

Assume a diverse hyperspectral image denoted as $I_{HS_2}\left(x_{w''}, y_{h''}, \lambda_c\right)$ that is reshaped into a matrix slice $N\left(r_{\iota''}, \lambda_c\right)$ for indices $\iota'' = 1, \ldots, \eta''_w \times \eta''_h$ and $c = 1, \ldots, \eta_c$, where η''_w and η''_h represent the width and height of the new hyperspectral image. Then, as in the previous case, assume a matrix of eigenvectors $\mathbf{V}_{\eta_c \times \eta_c}$ generated from the original hyperspectral image $I_{HS}\left(x_w, y_h, \lambda_c\right)$ by equation (2.41). The matrix $N\left(r_{\iota''}, c\right)$ can then be transformed into the coordinate system dependent on the data values of the original hyperspectral image $I_{HS}\left(x_w, y_h, \lambda_c\right)$ as follows

$$N'\left(r_{\iota''}, \lambda_c\right) = N\left(r_{\iota''}, \lambda_c\right) - \frac{1}{\eta_r} \sum_{\iota=1}^{\eta_r} X\left(r_\iota, \lambda_c\right), \tag{2.45}$$

and

$$N_t\left(r_{\iota''}, P_c\right) = N'\left(r_{\iota''}, \lambda_c\right) \mathbf{V}_{\eta_c \times \eta_c}. \tag{2.46}$$

Consequently, the reshaped pixel values of the original hyperspectral image $X_t\left(r_\iota, P_c\right)$ and the new test hyperspectral image $N_t\left(r_{\iota''}, P_c\right)$ can be compared within a unified coordinate system established from the original hyperspectral image. To quantify the differences between the pixel values in this coordinate system, the standard Euclidean distance can be utilized. Suppose that a subset of pixel values extracted from $X_t\left(r_\iota, P_c\right)$ is denoted as $X'_t\left(r_{\iota_s}, P_c\right)$, where $\iota_s = 1, \ldots, \eta'_r$ represents the index of the pixel subset. Similarly, suppose a subset of pixels from the transformed image $N_t\left(r_{\iota''}, P_c\right)$, denoted as $N'_t\left(r_{\iota''_s}, P_c\right)$ with pixel indexing $\iota''_s = 1, \ldots, \eta''_r$. The mean value vector across the selected PC dimensions for both defined subsets is expressed as

$$\overline{\chi_1}\left(P_c\right) = \frac{1}{\eta'_r} \sum_{\iota_s=1}^{\eta'_r} X'_t\left(r_{\iota_s}, P_c\right), \tag{2.47}$$

$$\overline{\chi_2}\left(P_c\right) = \frac{1}{\eta''_r} \sum_{\iota''_s=1}^{\eta''_r} N'_t\left(r_{\iota''_s}, P_c\right). \tag{2.48}$$

The standard deviations of the pixel subsets can be obtained in a similar manner as follows

$$\sigma_{\chi_1}\left(P_c\right) = \sqrt{\frac{1}{\eta'_r} \sum_{\iota_s=1}^{\eta'_r} \left(X'_t\left(r_{\iota_s}, P_c\right) - \overline{\chi_1}\left(P_c\right)\right)^2}, \tag{2.49}$$

$$\sigma_{\chi_2}\left(P_c\right) = \sqrt{\frac{1}{\eta''_r} \sum_{\iota''_s=1}^{\eta''_r} \left(N'_t\left(r_{\iota''_s}, P_c\right) - \overline{\chi_2}\left(P_c\right)\right)^2}. \tag{2.50}$$

Then the Euclidean distance d_e in the PCA-based space between the mean vectors $\overline{\chi_1}\left(P_c\right)$ and $\overline{\chi_2}\left(P_c\right)$, considering a selected number of principal components η'_c, can be defined as

$$d_e = \sqrt{\sum_{c=1}^{\eta'_c} \left(\overline{\chi_1}\left(P_c\right) - \overline{\chi_2}\left(P_c\right)\right)^2}. \tag{2.51}$$

Considering subsequent error propagation, the standard deviation σ_{d_e} of the above described distance d_e can be expressed as

$$\sigma_{d_e} = \frac{1}{d_e} \sqrt{\sum_{c=1}^{\eta'_c} \left(\overline{\chi_1}\left(P_c\right) - \overline{\chi_2}\left(P_c\right)\right)^2 \left(\sigma_{\chi_1}\left(P_c\right)^2 + \sigma_{\chi_2}\left(P_c\right)^2\right)}. \tag{2.52}$$

By utilizing this methodology, it becomes possible to compare the distances within the established space, thus allowing the evaluation of spectral properties for multiple objects, as in [A.3]. The following section is dedicated to specific identified promising applications where PCA and spectral similarity measures can be used to assess the properties of different objects of interest in multispectral or hyperspectral images.

2.4 Selected applications for spectral feature assessment

This section presents two compelling applications that demonstrate the use of multispectral and hyperspectral imaging. These applications involve the analysis of spectral properties of objects of interest and the investigation of their differences. The selection of these applications is based primarily on their high potential for practical application. Each of these applications is the subject of the publications [A.1, A.3] presented in Chapter 4.

The first of these publications aims to contribute to the topic of ground-based all-sky imaging of clouds and possible cloud detection and classification based on their color feature similarities. This topic is of practical interest because accurate and fast cloud detection can have an impact on meteorology and provide a good way to predict meteorological phenomena such as torrential rain. However, in order to correctly detect clouds based on their color similarities, it is useful to find out in which color spaces these clouds are suitably distributed. This is the subject of the publication [A.1].

The second publication focuses on inkjet printing research. Many contemporary works of art are printed, and artists or ordinary consumers aspire to have a work of art that will look the same for decades. Today, there is also a high demand for certification of printed artworks by selected laboratories to provide a mark of authenticity. Both of these tasks are expensive. Therefore, various types of forgeries are produced to reduce costs. HSI could therefore be used for authentication. Since different types of inks are used to print artwork and photographs, it is important to investigate their properties. The publication [A.3] contributes to this field.

2.4.1 Ground-based all-sky cloud color feature investigation

The ground-based all-sky astronomical systems for imaging the night sky have been around for some time. In the not-so-distant past, there has been a growing trend in the construction of ground-based all-sky systems specifically designed to evaluate meteorological conditions during the day. These systems play an important role in several applications, including predicting solar power generation for photovoltaic systems. They use cloud cover assessment data obtained from ground-based systems and contribute to the accurate estimation of incident solar power [270–273]. So the whole topic is closely related to weather forecasting. However, the key is always the correct analysis of the image data generated by these systems. Since current systems are mostly based on RGB (multispectral) imaging, there is a possibility to use the color information obtained from the image data for this purpose. This is especially relevant for the topic of cloud detection and classification based on color information [274, 275]. Various image processing methods can be used for this purpose [276–282], but the original color representation of the input images is also very important. Moreover, existing approaches do not thoroughly investigate the representation of different cloud types in different color spaces and thus the color properties of each cloud type.

A simple concept of k-means++ [283] segmentation in different color spaces described in [284] can serve as input for color cloud detection. Testing the color k-means++ segmentation on multispectral (color) data from all-sky cameras with appropriate representation of atmospheric phenomena (clouds) was only part of the publication [A.1]. Transformations to the CIE XYZ [285] and CIE L*, a*, b* [286] color spaces were used to evaluate the quality and accuracy of the segmentation. The WILLIAM system (introduced in [287]) was chosen as a suitable type of all-sky system for the analysis of the quality of atmospheric phenomena segmentation.

Figure 2.13: The WILLIAM all-sky ground-based imaging and monitoring system. Adopted from [A.1].

Initially, the concept of the WILLIAM system involved a fully autonomous ground-based all-sky imaging system with the aim of continuously monitoring the night sky and identifying visible stellar objects as well as variable stars [288]. The example of the WILLIAM system can be seen in Figure 2.13. Later, however, the focus shifted to real-time weather monitoring based on daytime sky imaging. Currently, the system captures RAW image data with an adjustable 10-minute period throughout the day. There are several generations of the WILLIAM system, but the one located in Jarošov nad Nežárkou (South Bohemia, Czech Republic, GPS 49.185° N, 15.072° E) can be considered one of the most important. In terms of parameters, the system is equipped with a NIKON D5100 camera using a CMOS sensor with a size of 23.5 × 15.6 mm. This camera is capable of a maximum resolution of 3264 × 4928 pixels and has a color depth of 24 bits. A Sigma 10 mm diagonal fisheye lens is used to capture the all-sky scenery, providing a field of view of 154° (180° when used with a Nikon full-frame camera).

Due to the significant amount of data collected by WILLIAM during each year, a subset of the data was selected and manually annotated with respect to cloud type phenomena and made available through the WILLIAM Meteo Database[2] (WMD). This database contains 2044 daytime images that have been carefully selected to cover diverse conditions across different times of the day and seasons. The images in the WMD are labeled with cloud phenomena and classified into ten fundamental cloud classes based on the World Meteorological Organization (WMO) classification system (introduced in 1975 in [289]). However, further divisions into cloud species and varieties have not been specified in this dataset.

The WMD also incorporates cloud cover data from the Aire Limitée, Adaptation Dynamique, Development International numerical (ALADIN) weather model [290], which provides information on different cloud levels. The identified cloud types have been further grouped into three cloud categories of clouds with similar characteristics customized for the data captured by the WILLIAM system. These three groups were divided into high-level clouds, low-level cumuli-type clouds, and rainy clouds. The fourth category was clear sky (either without clouds or with parts of clear sky). Within the WMD, there are 492 images featuring high-level clouds, 833 images showing low-level cumuli-type clouds, 793 images displaying rainy clouds, and 1411 images representing clear sky. These cloud groups serve as the primary classification categories, aligning with the WMO cloud level classification system and helping to mitigate

[2] `http://william.multimediatech.cz/meteorology-camera/william-meteo-database/`

potential classification bias. Additional information about the WMD and processed data is in [A.1].

For such a database, the segmentation quality of the k-means++ clustering method could have been investigated. As mentioned above, the WMD image data were transformed into selected color spaces CIE XYZ and CIE L*, a*, b*. The cloud and clear sky parts of the images were then segmented according to their color similarity with a predefined number of segments, but only within the color channels, excluding the luminance channels of the color spaces. The quality of the segmented parts of the images could then be compared to the ground truth labeled segments. An example of color-based segmentation for the WMD data is shown in Figure 2.14. The whole process of investigating segmentation quality for the WILLIAM data is further described in the publication [A.1].

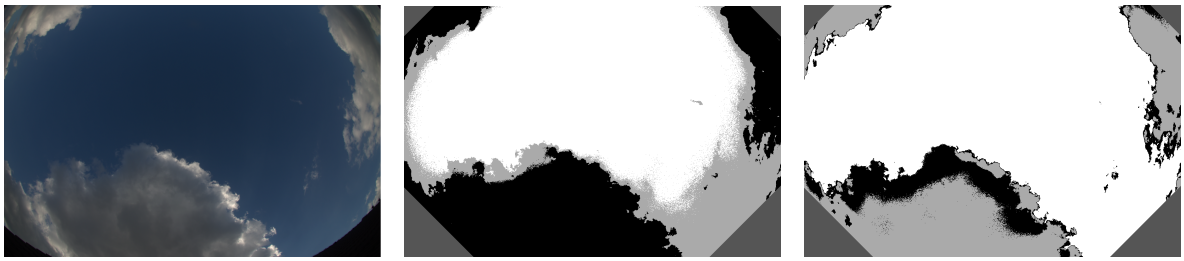

(a) (b) (c)

Figure 2.14: An example of an all-sky image (Figure 2.14a) from the WILLIAM system showing cumulus-type clouds. Figure 2.14b represents the segmentation results within the channels of the CIE XYZ color space. Figure 2.14c shows the segmentation within the channels of the CIE L*, a*, b* color space. Adopted from [A.1].

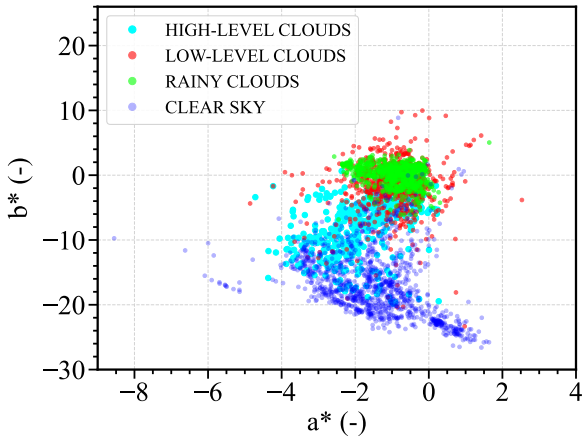

Figure 2.15: Diagram of a*, b* with cloud segments obtained from the the WMD. Each point represents the segmented cluster average value that has been classified as one of the four cloud groups. Reproduced from [A.1].

Since the cloud and sky segments had been created and a suitable color space for their creation had been evaluated, the resulting segments (regions in individual WMD images) could be further processed. The generated image segments were assigned to one of the four cloud or clear sky groups introduced above for WMD. The WMD images could then be transformed

again into different color spaces, and first-order statistics (mean and variance/standard deviation) could then be calculated for segments belonging to the same group in a given image. These statistics could then be treated as color features in the given color spaces and plotted for each group over all image WMD data in the coordinate systems of the given color spaces. This made it possible to examine how the individual color (spectral) features of the cloud groups are distributed in these coordinate systems. In order to assess whether these groups form separate clusters in these coordinate systems, it was possible to use the BC mentioned above. This metric, with the BD at its core, measured the degree of separability (similarity) of different cloud groups and determined whether these groups could be used as input for classification algorithms. An example of the distribution of different spectral features of cloud groups generated from the WMD within the a*, b* domain can be seen in Figure 2.15. In general, the results specifically for the CIE L*, a*, b* space proved very promising and showed potential for using k-means++ segmentation and subsequent segment color feature extraction as a preprocessing step for possible cloud type classification. More details on the research results are presented in Chapter 4.

2.4.2 Spectral characteristics investigation of inkjet prints

As already mentioned, hyperspectral imaging has been active for many years in the field of cultural heritage, especially in the field of artworks [110, 111]. The same is true for the authenticity assessment of various art objects [112–114]. Despite today's digital capabilities, many things are still printed, but with a greater emphasis on value retention and durability. There are many printing applications where it is desirable that prints retain their value and can be archived, such as printing artwork, but also fine art photography, printing paper documents, or printing securities and banknotes.

The demand for fine art photography and document printing has led to the development of various photo printers that meet the requirements of perfect color representation and archiving parameters. In the field of fine art printing and archiving, inkjet printing holds significant importance [291]. The two most commonly used inkjet printing techniques are dye-based and pigment-based. Each type has its own set of applications, catering to specific needs and requirements. Dye-based printers are more affordable and popular among hobbyists, while pigment-based printers provide professional printing solutions (used in professional labs) suitable for photography and fine art printing with a focus on archiving [292, 293]. However, due to cost reduction, pigment-based printing is often replaced or forged by dye-based printing, which is less suitable for long-term archiving.

Despite advances in dye-based printing technology, dye-based prints still have significantly lower lightfastness and fade resistance compared to pigment-based prints. Moreover, the wide color gamut of dye-based prints and their similarity in appearance to pigment-based prints make it easy for dye-based forgeries to go unnoticed. This interchangeability and difficulty in identification are challenging, even for experts.

Dye-based and pigment-based inks, although both water-based, differ in the technology of color creation. However, although the prints may appear similar, their spectral behavior can be different. Therefore, HSI can serve as a valuable and straightforward technique to assess the spectral characteristics of dye- and pigment-based inks across the entire print and even identify the printer of origin. While some approaches have focused on color measurement [294], spectral analysis of dyes [295], pigments [110, 296], and ink-printed documents [297], direct

spectral comparisons to differentiate between dye- and pigment-based inkjet prints have not been extensively explored (until [A.3]).

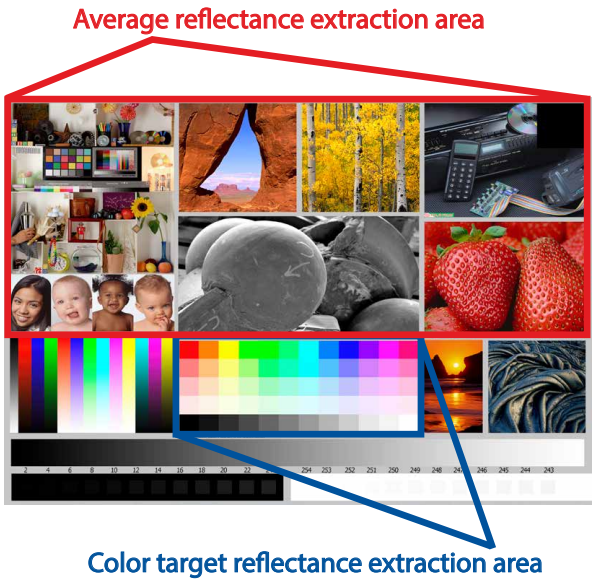

Figure 2.16: The selected test image with targets for evaluating the spectral characteristics of dye- and pigment-based prints. The test pattern was designed by ©Bill Atkinson, Jack Flesher, and Uwe Steinmueller [2], and is widely used for print quality assessment. The highlighted parts express the image areas specifically assessed for the hyperspectral analysis.

Various techniques, such as microscopy, mass spectrometry, colorimetry, standard reflectance spectroscopy, chemical analysis, and X-ray methods, are used for art analysis and forgery identification [298]. However, not all these techniques are suitable for evaluating inkjet prints. In comparison, HSI provides a fast, simple, and non-invasive method for comprehensive spectral analysis across the entire print [253], making it particularly advantageous for inkjet print evaluation. The evaluation of VNIR evaluation of HSI prints based on dyes and pigments, their spectral comparison, and quantification of their spectral differences was the subject of the [A.3].

Two different printers were used for the comparison: the EPSON L1800 (a hobby dye-based printer) and the EPSON SC-P9500 (a professional pigment-based printer). The used standardized test print image from [2] with some highlighted areas and targets used for the subsequent spectral analysis can be seen in Figure 2.16.

Test photographs were printed on three different types of photo paper and then hyperspectrally captured and analyzed. The first photo paper chosen was the semi-gloss FOMEI Archival Velvet with a weight of $265\,\mathrm{g\,m^{-2}}$. It is designed for hobby and professional archiving purposes and contains a small amount of optical brighteners. The second photo paper, also semi-glossy, was the FOMEI PRO Pearl, with the same weight of $265\,\mathrm{g\,m^{-2}}$. This photo paper is widely used by amateur and professional photographers and contains a significant amount of optical brighteners. The final photo paper selected was the matte-textured FOMEI Cotton Textured, which weighs $240\,\mathrm{g\,m^{-2}}$ and is made from 100% cotton. This special art inkjet photo paper is free of optical brighteners, acid-free, and primarily intended for fine art applications.

The scanning principle used for the print image capturing has already been shown in Figure 2.2. For the purpose of this study, the VNIR hyperspectral system SPECIM PFD4K-65-V10E was used. Its parameters can be found in [A.3]. The image data of the captured dye- and pigment-based prints (printed on diverse photo papers) were then studied in terms of spectral reflectances. From the specific areas of the captured images, the average reflectance spectra were extracted and compared via spectral reflectance measures, which were introduced above in Section 2.3.1. Regarding the applied JMSAM similarity measure, the same BD was used as for the color feature distributions of the cloud groups above. In addition, the PCA method was used to compare the spectral characteristics of dye-based and pigment-based inks. The specific reflectances of dye-based and pigment-based prints were then compared in the same PCA-based space, and their differences were evaluated by a Euclidean distance derived in the above equation (2.51).

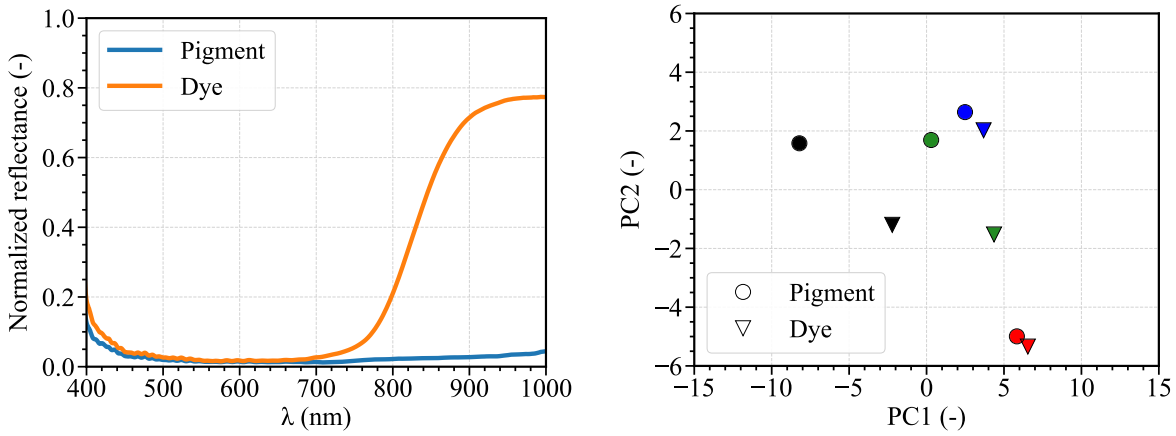

(a) (b)

Figure 2.17: The extracted average reflectance curves in the VNIR spectral band for dye- and pigment-based prints corresponding to the pure black target (Figure 2.17a) printed on a Pro Pearl photo paper. The λ symbol represents the wavelength. Figure 2.17b shows the example results of transforming (via PCA) the averaged pixel spectral values of the color print targets into a pigment-based coordinate system. In the figure, the data points corresponding to dye-based prints are denoted by triangles, while the data points representing pigment-based prints are represented by circles. The example results specifically focus on the first two principal components, PC1 and PC2, which capture the most significant variations in the data. Each color point in the figure corresponds to a specific color target, providing insight into the distribution and clustering of colors in the pigment-based coordinate system. Reproduced from [A.3].

In general, the spectral similarity analysis indicated significant differences between the dye- and pigment-based inks, especially in the NIR spectral band. These differences were also confirmed by the yielded scores of the spectral similarity measures (see above Section 2.3.1) and the subsequent PCA analysis. The most noticeable spectral differences were observed between the print targets corresponding to pure black. An example of the average pure black reflectance comparing the dye- and pigment-based photo prints can be seen in Figure 2.17a. In addition, Figure 2.17b expresses an example of the spectral differences between the averaged pixel values of the print color targets transformed into the PC space (pigment print spectral value-based)

by the mentioned PCA method. The examples are shown only for the printed images on the PRO Pearl type of photo paper. Thus, the analysis showed a significant potential for the use of VNIR HSI for fast analysis and evaluation of ink type and possible automation for the identification of counterfeits or the type of original printer. More detailed information about the settings and results of the study is again presented in Chapter 4.

3

Design and optimization of optical devices based on mercurous halides for infrared hyperspectral imaging

This chapter presents two of the author's core publications dealing with the optical modeling, optimization, and design of mercurous halide-based devices with a focus on their applicability for IR HSI, e.g., within a TIR spectral region. The first article:

> [A.2] L. Krauz, P. Páta, J. Bednář, and M. Klíma, "Quasi-collinear IR AOTF based on mercurous halide single crystals for spatio-spectral hyperspectral imaging," *Optics Express*, vol. 29, no. 9, pp. 12813–12832, 2021

published in the journal Optics Express in 2021, focuses on the optimization of the quasi-collinear AOTF for the IR spectral region. The optimization was carried out with the aim of using the AOTF as a mercurous halide-based dispersive element for a spatio-spectral hyperspectral imaging system.

The performed analysis dealt with the general description of the quasi-collinear AOTF and compared the suitable optical materials for IR operation. For this purpose, the anisotropic material properties, focusing mainly on the acousto-optic properties, of tellurium dioxide (TeO_2) and mercurous halides (Hg_2Cl_2, Hg_2Br_2, Hg_2I_2) were considered. The general assessment was in favor of the mercurous halides, especially in terms of optical transparency up to the FIR spectral band, where TeO_2 cannot compete. Moreover, the acousto-optic figure of merit (M_2) is much higher for the mercurous halides.

Based on the performed analysis, Hg_2Cl_2 was selected as a suitable representative of the mercurous halide family for the detailed quasi-collinear AOTF modeling. With the main objective of AOTF operation in the TIR band, the model was analyzed and optimized for maximal spectral resolution. Other parameters were also evaluated, such as the acoustic power required for adequate diffraction efficiency of the AOTF in the TIR band, the diffraction

efficiency for different angles of incidence of the broadband radiation, and the chromatic field of view. Thus, the spatio-spectral operation of such a quasi-collinear AOTF was demonstrated.

As shown in the above-mentioned manuscript [A.2], the operation of the introduced quasi-collinear AOTF is polarization sensitive, and the hyperspectral system based on this device needs to incorporate a polarizer at the input (to select the correct polarization), but also at the output (to block the undiffracted output radiation). These hyperspectral systems can operate over the entire VIS and LWIR spectral range. Therefore, the polarizers should also be able to operate over such a broad spectral range. For this reason, mercurous halides, with their exceptional birefringence and optical properties, are ideal for this type of operation and for constructing crystalline polarizers. Assuming a crystal-based polarizer that promises a high degree of polarization, a Wollaston-type prism might be suitable for such broadband applications and for a spatio-spectral hyperspectral system.

In general, Wollaston prisms find usage among applications such as microscopy, astronomy, and already mentioned hyperspectral imaging. However, the currently used optical materials limit their operational spectral range (up to 6 µm). For the farther IR band, only a non-crystal polarizer is applicable, which limits the degree of polarization and broadband functionality. However, there are a number of drawbacks, and the Wollaston polarizer based on mercurous halides must be properly designed to work reliably over a wide spectral range. This was the subject of the next core publication of this thesis:

[A.4] L. Krauz, P. Páta, J. Bednář, M. Klíma, and P. Janout, "Broadband Wollaston prism with a large output beam separation based on mercurous halides," *Optics Express*, vol. 30, no. 26, pp. 47388–47403, 2022

published in Optics Express in 2022, which provided a parameter optimization for a design of a Wollaston prism based on promising mercurous halide optical materials that offer exceptional output beam separation and operation in an unconventionally broad spectral range from the visible up to the FIR band.

The publication outlines the unique characteristics of mercurous halides and their optical properties suitable for polarizer design. The manuscript also discusses the specific fundamental parameters of the Wollaston polarizer based on mercurous halides. As a main result, the Wollaston polarizer design was optimized and evaluated using Zemax optical software. The manuscript also shows the possibility of an air-gap Wollaston prism construction.

Both presented publications are closely related to the topic of hyperspectral imaging in the VIS and IR spectral bands. The optimization of both optical devices (quasi-collinear AOTF and Wollaston polarizer) is dedicated to a possible VIS and IR operation, given the optical properties of the mercurous halide materials. Moreover, both devices are required for the possible construction of a spatio-spectral hyperspectral system.

Research Article | Vol. 29, No. 9 / 26 April 2021 / Optics Express 12813
Optics EXPRESS

Quasi-collinear IR AOTF based on mercurous halide single crystals for spatio-spectral hyperspectral imaging

LUKÁŠ KRAUZ, PETR PÁTA, JAN BEDNÁŘ, AND MILOŠ KLÍMA

Department of Radioelectronics, Faculty of Electrical Engineering, Czech Technical University in Prague, Technická 2, 166 27 Prague 6, Czech Republic
*krauzluk@fel.cvut.cz

Abstract: The paper aims to show the advantages of the infrared-optimised quasi-collinear AOTF (acousto-optic tunable filter) for the spatio-spectral hyperspectral imaging system. The optimisation process is presented based on the selected tetragonal anisotropic materials with exceptional optical and acousto-optical properties in IR (infrared) spectral region. These materials are further compared in terms of their features and suitability for AOTF design. The spectral resolution is considered as the main optimising parameter. Resulting from the analysis, the mercurous chloride (Hg_2Cl_2) single crystal is selected as a representative of the mercurous halide family for the presentation of the quasi-collinear AOTF model operating in LWIR (long-wave infrared) spectral band. The overall parameters of the AOTF model such as spectral resolution, chromatic field of view, acoustic frequency, and operational power requirements are estimated and discussed in results.

1. Introduction

Hyperspectral imaging has become considerably popular in several areas of interest, such as remote sensing [1], medicine [2], forensics [3], food quality control [4], chemistry [5], and many others [6]. The main part of the hyperspectral systems form diverse dispersive components such as diffraction gratings, prisms, liquid crystals, and AOTFs (Acousto-optic Tunable Filters) [7].

The hyperspectral imaging in IR (infrared) spectral region ($0.75 - 20\mu m$) has recently also increased its popularity in the mentioned applications. Several remote sensing hyperspectral systems [8] operate within this spectral region, but usually in a narrower spectral band, depending on the atmospheric windows. Frequently, two main spectral bands MWIR (Mid-wave-infrared $3 - 5\mu m$) and LWIR ($8 - 10\mu m$) are selected [8–10]. The key parameters of hyperspectral systems are the spectral resolution and the number of resolvable spectral channels. Commonly, the systems offer in the MWIR and LWIR bands spectral resolution about tens of *nm*. Concerning the spectral resolution, the exploitation of the AOTF as a main disperse device for the IR hyperspectral instruments has been more frequently studied in previous years. Compared to standard dispersive devices such as diffraction gratings, the AOTF offers no mechanical parts, fast tuning, better spectral resolution, and a higher number of resolvable spectral channels in the operational spectral band. These features offer faster capturing of the scene and its spectral decomposition compared to standard push-broom systems.

There have been several approaches of AOTF designs suitable for the hyperspectral imaging in a IR spectral region [11–17]. These AOTFs are frequently based on the non-collinear interaction [18] between the RF (radio-frequency) acoustic wave and the input light. In some cases, the standard collinear interaction is exploited [19,20]. The main problem of the non-collinear AOTF design is the interaction length between the input light and the acoustic wave, which is a critical parameter determining the spectral resolution. The collinear design offers a higher spectral resolution but limits the aperture. In addition, some AOTF fabrication materials cannot

#420571 https://doi.org/10.1364/OE.420571
Journal © 2021 Received 22 Jan 2021; revised 16 Mar 2021; accepted 24 Mar 2021; published 12 Apr 2021

Research Article | Vol. 29, No. 9 / 26 April 2021 / Optics Express 12814
Optics EXPRESS

be used for the collinear interaction [21]. To overcome this issue, Voloshinov introduced an interesting approach of close-to-collinear or quasi-collinear interaction [22]. This approach has also been studied and improved in the following years by several other authors [23–26]. The main advantage of the quasi-collinear approach is the extension of the interaction length, therefore, an improvement in the spectral resolution, and a possibility of the wide aperture.

A new concept of a collinear AOTF-based spatio-spectral hyperspectral system was proposed by Maksimenka in [27]. In the paper, the authors presented their promising idea of the mentioned system operation and built two breadboard imager prototypes based on the Hg_2Cl_2 collinear AOTF operating in MWIR and LWIR bands. The operability has been subsequently demonstrated by captured images of the black body source and a propane flame. To obtain a full hypercube image, the authors also outlined the fundamental principle of their post-processing algorithm based on the AO (acousto-optic) phase matching wavelength dependency through AO material refractive indices. The authors have selected the Earth remote sensing as a possible application of the proposed hyperspectral system. The physical properties of the AOTF were concluded as the main limitation of the presented spatio-spectral hyperspectral system. Nevertheless, the replacement of this type of AOTF by the quasi-collinear-based one could keep the hyperspectral system properties and even improve its performance. The design of this AOTF, however, depends on in-depth optimisation due to many degrees of freedom, which must be addressed during the design process. One of the key decisions is an AOTF material selection. Convenient selection of the fabrication material can highly influence and improve the properties (e.g. spectral resolution) of the final instrument and, therefore, worth focusing on.

This paper presents optimisation criteria for designing a quasi-collinear AOTF based on several optical materials suitable for the IR AOTF operation. The presented optimisation is based on the AOTF spatio-spectral hyperspectral system requirements and aims to maximise the AOTF spectral resolution parameter. The selected materials for this optimisation process are well-known tetragonal crystals with high birefringence and exceptional AO properties. The first material is TeO_2, which is commonly used for the AOTF fabrication [28–30]. The other explored materials are Mercurous Halides (Hg_2Cl_2, Hg_2Br_2, Hg_2I_2), which has been also under research for several optical applications [31–36] and for AOTF design and fabrication [37–43]. In this paper, we assess the quasi-collinear AOTF parameters for several IR spectral bands, but mainly at $4\mu m$. This wavelength has been chosen in purpose as a representative of the MWIR spectral band with high atmospheric transmission window, which is exploited for several remote sensing applications [44]. Moreover, the selected materials offer great transparency at this wavelength and can be compared in terms of the AOTF properties. Apart from the comparison of the selected materials, we provide a model of the quasi-collinear AOTF based on one selected tetragonal material with bandwidth operation $8-10\mu m$ for thermal sensing applications. The presented model parameters are then further discussed and assessed their suitability for the spatio-spectral hyperspectral system.

The paper is structured into six main sections. The Introduction is followed by a description of the selected concept of the spatio-spectral hyperspectral system. Then the paper focuses on the theory of the quasi-collinear AOTF, its parameters, and optimisation criteria. The next section aims to compare the selected fabrication materials for the quasi-collinear AOTF. Apart from the Conclusion, the two last sections present the quasi-collinear AOTF model based on Hg_2Cl_2 and assess the results and discuss its suitability for the spatio-spectral hyperspectral system.

2. Spatio-spectral AOTF-based hyperspectral system

Maksimenka has introduced the concept of the spatio-spectral AOTF-based hyperspectral system in [27]. Despite the traditional hyperspectral systems, this concept exploits the AOTF as the main diffractive instrument. Suppose the acoustic wave of specific RF frequency propagating within the AOTF crystal. The incoming light from a captured scene incident on the input AOTF aperture

Optics EXPRESS

(facet or window of the single crystal). The input light of specific wavelength and incident angle then interacts within the crystal with the acoustic wave, which results in diffraction. This is given by a well-known Bragg condition [46]. Therefore, for varying incident angles and wavelengths, there are several diffracted beams of the imaging scene. Despite the commonly used concept of AOTF devices, this system relies on encoding the spectral information by an incident light angle. Thus, the spatio-spectral image can be obtained. By tuning the acoustic wave frequency, the Bragg condition is changed. Therefore, different spectral information (wavelengths) will be diffracted and captured at the same incident angle. The final hyperspectral cube of the captured scene might be retrieved by post-processing of the detected image data. The introduced concept of the described hyperspectral system is outlined in Fig. 1.

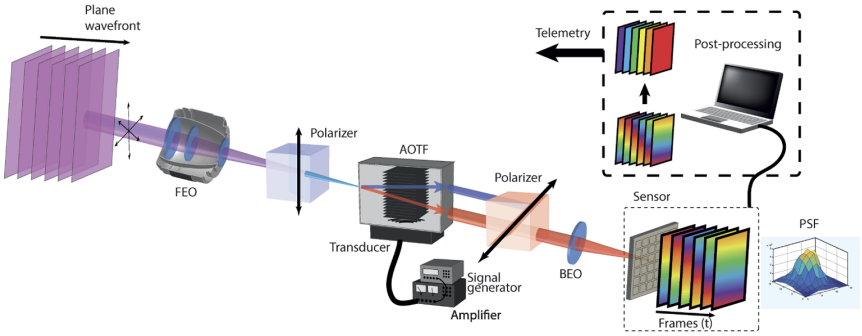

Fig. 1. The concept of the spatio-spectral hyperspectral imagining system, with the AOTF. The input light wavefronts are decomposed and diffracted into several spectral lines according to the incidence input angle, which fulfils the Bragg condition at a specific wavelength and tuning frequency of the AOTF. To obtain the full hyperspectral 3D cube, the RF tuning frequency must be changed. Subsequently, all the spatio-spectral images have to be post-processed. The system is also composed of several other necessary devices such as front and back optics, polarisers detectors, supply electronics and others. For more details see [45].

This concept may be exploited in VIS (visible) spectral region similarly as in UV (ultraviolet) or IR spectral band. Nevertheless, the system operation and even the post-processing of the data would highly depend on the AOTF construction material. Therefore, the detailed and specific design of the AOTF is crucial, and it highly affects the system performance. In this paper, we propose a quasi-collinear AOTF model as a convenient selection for the introduced system. Because of the complexity of the presented system, it is necessary to precisely design and evaluate the properties of such AOTF and identify possible hold-backs that may occur. Therefore, the next sections of the paper focus on the optimisation of the quasi-collinear AOTF and the selection of suitable fabrication materials.

3. Quasi-collinear AOTF

In the paper, the operation of the quasi-collinear AOTF for all selected single crystal materials has been set in a [001], [110] crystallographic plane. This plane offers exceptional AO properties, especially the acoustic slow shear wave phase velocities, which strengths the AO interaction. This means that the transverse acoustic wave propagates perpendicularly to the crystallographic plane along the [110] axis for the selected orientation. This paper deals with the quasi-collinear principle of the AOTF, which exploits S-polarized ordinary input light and diffracts the light beam with the extraordinary P-polarization.

Research Article | Vol. 29, No. 9 / 26 April 2021 / Optics Express 12816
Optics EXPRESS

For all selected tetragonal anisotropic materials, the propagation of the acoustic wave in the [001], [110] plane [21] can be described as a slowness ellipse

$$V(\theta_a) = \sqrt{V_{110}^2 \cos^2\theta_a + V_{001}^2 \sin^2\theta_a}. \tag{1}$$

The V_{110} and V_{001} are the sound velocities in the [110], [001] directions. Nevertheless, in the anisotropic materials, it is necessary to differentiate an acoustic wavefront propagation (phase velocity) and an energy propagation (group velocity), because they do not have to be similarly oriented. The acoustic phase velocity can be represented as a wave vector with a particular direction within the acoustic slowness ellipse and with the acoustic wave velocity according to Eq. (1). However, the direction of the acoustic group velocity vector is represented as a normal vector to the tangent of the slowness ellipse for a given direction of the acoustic phase velocity vector. The angle θ_a^g between the acoustic group velocity vector and the [110] axis can be described as

$$\theta_a^g = \arctan\left(\left(\frac{V_{001}}{V_{110}}\right)^2 \cdot \tan\theta_a\right). \tag{2}$$

The $\tan\theta_a$ stands for the acoustic phase velocity angle measured from the [110] axis. The acoustic group velocity should be oriented in a collinear direction with the input light to obtain an AO quasi-collinear interaction. Contrary to that, the acoustic phase velocity does not have to be collinear. With this collinear approximation, the θ_a^g can be replaced in Eq. (2) by θ_i, where θ_i is the incident light angle measured from the [110] axis.

In addition, a standard vector phase matching equation can be obtained for the AO quasi-collinear interaction. Assume the ordinarily polarised light represented as a wave vector $\vec{k}_i$ and an acoustic phase velocity wave vector $\vec{K}$. The extra-ordinarily polarised wave vector of diffracted light $\vec{k}_d$ then can be expressed as

$$\vec{k}_d = \vec{k}_i + \vec{K}. \tag{3}$$

Scalar representation of Eq. (3) can be re-written as

$$\frac{2\pi n_d(\theta_d)}{\lambda} = \frac{2\pi n_i}{\lambda} + \frac{2\pi f}{V(\theta_a)}, \tag{4}$$

where λ is a wavelength, f is a particular frequency, $n_i = n_o$ and corresponds to the ordinary refraction index of a specific anisotropic material. Diffractive index of refraction n_d is for tetragonal uniaxial crystals equal to

$$n_d(\theta_d) = \frac{n_o n_e}{\sqrt{n_o^2 \cos^2\theta_d + n_e^2 \sin^2\theta_d}}. \tag{5}$$

The angle between the wave vector of diffraction $\vec{k}_d$ and the [110] axis is θ_d, and n_e stands for the extraordinary refractive index of the material.

Since the input light vector $\vec{k}_i$ and the acoustic group velocity vector are collinear for the quasi-collinear interaction, the acoustic phase vector direction $\vec{K}$ is also known. Therefore, from the ideal phase matching [Eq. (4)], it is possible to derive the parameters of diffracted wave vector $\vec{k}_d$ and the necessary frequency of the acoustic wave. The wave vector diagram, which describes the presented situation of the phase matching for the quasi-collinear AO interaction, is provided in Fig. 2.

Assume there is an intersection point of the vector $\vec{k}_i$ and ordinary refractive index of the anisotropic material represented by an optical slowness circle with radius $2\pi n_o/\lambda$. This intersection point has coordinates $[I_x, I_y]$, where x replaces [110] axis and y replaces [001] axis. Suppose, the acoustic phase wave vector $\vec{K}$ is represented by a line expression $y = mx + c$, where

Optics EXPRESS

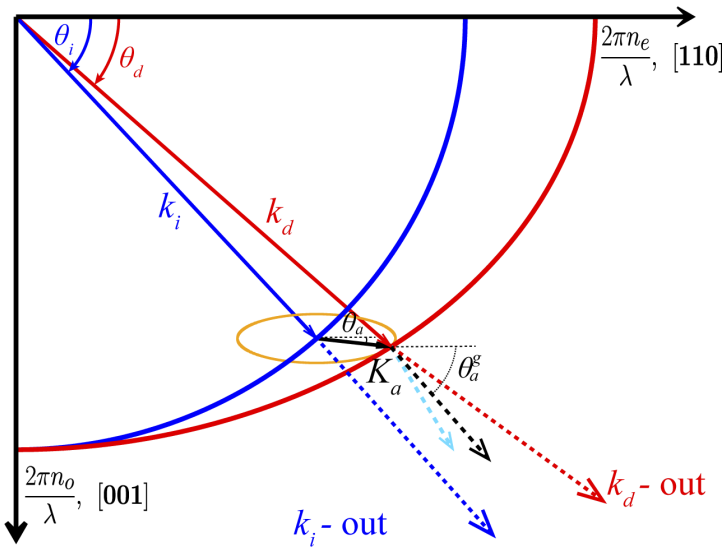

Fig. 2. Phase matching vector diagram of quasi-collinear AO interaction in [001], [110] plane. A blue curve indicates an ordinary slowness circle of the birefringent material with a radius $2\pi n_o/\lambda$. A red curve represent an extra-ordinary slowness ellipse of the birefringent material, with axes $2\pi n_o/\lambda$ and $2\pi n_e/\lambda$. A blue vector k_i represents the ordinary polarised input light beam wave vector. A red vector k_d is the extraordinary polarised diffracted light wave vector, and a black K vector represents the acoustic wave vector. The blue and black dashed lines of the input light and acoustic phase vector indicate the quasi-collinear principle. The input light wave vector has a collinear direction as a black-dashed group velocity vector of the acoustic wave. However, an acoustic phase velocity vector K has different direction with angle θ_a from [110] axis. The angle of the acoustic group velocity θ_a^g to the [110] axis has also been shown. An Azure-dashed vector shows the group-velocity direction of the diffracted beam within the material. The red-dash vector indicates the refraction of the diffracted beam from the birefringent material to air.

$m = \tan\theta_a$ and $c = I_y - m \cdot I_x$. Additionally, the optical slowness ellipse of the extraordinary refractive index for the uniaxial anisotropic material is represented as $x^2/a^2 + y^2/b^2 = 1$, with $a = 2\pi n_o/\lambda$ and $b = 2\pi n_e/\lambda$. Thus, the intersection coordinates $[D_x, D_y]$ of the acoustic wave vector $\vec{K}$ and the extraordinary refractive index ellipse may be obtained as

$$D_x = \frac{-a^2mc + ab\sqrt{a^2m^2 + b^2 - c^2}}{b^2 + a^2m^2}, \tag{6}$$

$$D_y = \frac{b^2c + abm\sqrt{a^2m^2 + b^2 - c^2}}{b^2 + a^2m^2}. \tag{7}$$

The angle of diffraction θ_d can be then derived as

$$\theta_d = \arctan\left(\frac{D_x}{D_y}\right). \tag{8}$$

Moreover, the particular frequency for the ideal phase matching can be retrieved as

$$f = \frac{\sqrt{V_{110}^2K_x^2 + V_{001}^2K_y^2}}{2\pi}, \tag{9}$$

Research Article | Vol. 29, No. 9 / 26 April 2021 / Optics Express 12818
Optics EXPRESS

where K_x, K_y were obtained from the phase matching condition as $K_x = D_x - I_x$ and $K_x = D_y - I_y$. The non-collinear orientation of the acoustic wave phase velocity allows fulfilling the parallel tangent matching condition in the input angle vicinity. This increases the angular aperture of the AOTF [18]. Therefore, for a fixed magnitude and direction of the acoustic wave vector, the phase matching can be considered as satisfied for several values of the incident light directions.

However, by changing the magnitude of the acoustic wave vector, wavelength or input light angle, the phase matching condition may be violated. The deviation from the ideal phase matching can be determined by the phase mismatch factor $\vec{\Delta k}$. The phase mismatch significantly influences one of the main parameters of the AOTF, which is the diffraction efficiency η. From the phase matching condition, the phase mismatch parameter is equal to

$$\vec{\Delta k} = \vec{k_d} - \vec{k_i} - \vec{K_a}. \tag{10}$$

Scalar representation of $\vec{\Delta k}$ may be analytically obtained as a minimal distance to extraordinary slowness ellipse from the acoustic phase vector end-point $[K_x^a,\ K_y^a]$. This can be considered as an optimisation problem and solved, for example, by standard Lagrange multipliers as

$$\Delta k = \min\left\{ \left(\Delta k_x - K_x^a\right)^2 + \left(\Delta k_y - K_y^a\right)^2 \,\middle|\, \frac{x^2}{a^2} + \frac{y^2}{b^2} = 1 \right\}, \tag{11}$$

where $[\Delta k_x,\ \Delta k_y]$ are intersection coordinates between $\vec{\Delta k}$ and extraordinary slowness ellipse with $a = 2\pi n_o/\lambda$ and $b = 2\pi n_e/\lambda$. For the ideal phase matching, $[K_x^a, K_y^a] = [K_x, K_y]$ and $\Delta k = 0$. Thus, the diffraction efficiency can be defined [21] as

$$\eta = \frac{I_d}{I_i} = \Gamma^2 \cdot \frac{\sin^2 \sqrt{\Gamma^2 + \left(\frac{\Delta k \cdot L}{2}\right)^2}}{\Gamma^2 + \left(\frac{\Delta k \cdot L}{2}\right)^2}, \tag{12}$$

where

$$\Gamma = \frac{\pi}{\lambda} \cdot \sqrt{\frac{M_2 \cdot P_a \cdot L}{2 \cdot H}}. \tag{13}$$

The ratio I_d/I_i represents both diffracted and input light intensities. M_2 is an AO figure of merit. P_a is an acoustic power. H represents a height of the acoustic beam (usually limited by the transducer size), and L is an interaction length. The AO figure of merit M_2 represents the strength of the AO interaction and significantly influences the diffraction efficiency and the AOTF performance. The value of M_2 is entirely defined by the material from which the AOTF crystal is fabricated. It depends on the index of refraction of a birefringent material, acoustic slowness, density ρ of the material, and crystallographic orientation, which means the directional dependency. M_2 is given by

$$M_2 = \frac{n_o^3 \left(n_d\left(\theta_d\right)\right)^3 p_{\text{eff}}^2}{\rho \left(V\left(\theta_a\right)\right)^3}. \tag{14}$$

The effective elasto-optic constant p_{eff} comes from the mentioned crystallographic orientation of the material and from a geometry of the AO interaction. For tetragonal crystals in the [001], [110] plane the p_{eff} can be estimated [28] as

$$p_{\text{eff}} = p_{44} \cos\theta_i \sin\theta_a - \frac{(p_{11} - p_{12})}{2} \sin\theta_i \cos\theta_a. \tag{15}$$

The elasto-optic coefficients p_{44}, p_{11}, p_{12} comes from the fourth-rank elasto-optic tensor. These coefficients are material-dependent and must be assessed separately for each material.

Optics EXPRESS

For sufficient diffraction efficiency, the power of the acoustic beam is also essential. Acoustic energy needed for the AO interaction and at least 50% diffraction efficiency during the ideal phase matching can be additionally obtained from Eq. (12) and expressed as

$$P = \frac{H \cdot \lambda^2}{8 \cdot L \cdot M_2}. \tag{16}$$

Therefore, the AO figure of merit M_2 and interaction length L are critical for the design of the AOTF, especially for the transducer requirements and other additional electronics such as electric supply amplifiers and so on.

In general, the diffraction efficiency is according to Eq. (12) represented as $sinc^2$ function. Taken that into consideration, the expression for the best achievable spectral resolution $\Delta\lambda$ can be derived at FWHM (full width half maximum) of the $sinc^2$ ($\Delta kL \approx 0.9\pi$) as

$$\Delta\lambda = \frac{1.8\pi\lambda^2}{bL\sin^2\theta_i}, \tag{17}$$

where b is a dispersion constant equal to

$$b = 2\pi\lambda^2 \cdot \frac{\partial}{\partial\lambda}\left(\frac{|\, n_o - n_e \,|}{\lambda}\right). \tag{18}$$

The expression for the diffraction efficiency also indicates that the phase matching condition fulfilment can be achieved for several wavelengths at different input angles and one particular acoustic beam frequency. It allows the encoding of spectral information into the incident angle. The concept was mentioned in the previous section and outlined in Fig. 1. The acoustic beam energy travels collinearly with the light incident on the AOTF input window because of the quasi-collinear concept. Therefore, the instrument overall field of view will be limited by the width and height of the acoustic beam. These parameters are determined by the transducer size and proportions of the AOTF crystal. Another important parameter of the AOTF for the spatio-spectral hyperspectral system is the chromatic field of view. This term represents the standard angular aperture - maximum full angle deviation from the normal incidence for which the phase matching condition is fulfilled at a given wavelength and acoustic frequency. Therefore, the hyperspectral instrument overall angular resolution is also limited by the chromatic field of view. Similarly, from the diffraction efficiency Eq. (12), for a given wavelength, $\Delta kL \approx \pi$ and $\Delta\lambda \approx 0$ the chromatic field of view $\Delta\theta$ can be approximated [18,47] as

$$\Delta\theta = \sqrt{\frac{2\pi \cdot \lambda}{L \cdot b \cdot \,|\, 3\cos^2\theta_i - 1 \,|}}. \tag{19}$$

From Eqs. (12), (16), and (17) it is apparent, that the improvement of the AO interaction length L significantly increases the performance of the AOTF and favours the quasi-collinear interaction. However, there is also a trade-off between the high spectral resolution and chromatic field of view. Extension of the interaction length L and increase in birefringence by selecting a suitable anisotropic material improves the spectral resolution significantly but decreases the chromatic field of view. Since the design of the AOTF uses the spectral encoding by the angle of incidence and expects diffraction of several wavelengths at one RF frequency, the maximisation of the spectral resolution is then prioritised over the chromatic field of view.

The presented theory shows that the AOTF properties are highly material-dependent. The next parameters, which influence the AOTF, are the single crystal proportions. Therefore, selecting a suitable material is the first prerequisite for the AOTF design that should be made.

Research Article | Vol. 29, No. 9 / 26 April 2021 / Optics Express 12820
Optics EXPRESS

4. Characteristics of selected tetragonal single crystals

Tetragonal anisotropic materials with high birefringence are an excellent choice for the AOTF construction. These uniaxial crystals offer superb optical and elasto-optical properties. From a variety of tetragonal materials suitable for modelling of the quasi-collinear AOTF, we have selected specific types with exceptional optical features, transparency in IR spectral band, high and positive birefringence and extensive AO figure of merit. The materials are TeO_2 (Paratellurite) and Mercurous Halide single crystals such as Hg_2Cl_2 (Calomel), Hg_2Br_2 (Kuzminite), and Hg_2I_2 (Moschelite). This paper compares the fundamental properties of the selected materials and assesses their performance as fabrication optical materials for the quasi-collinear AOTF design.

In general, TeO_2 is the most common material for the AOTF construction. However, compared to Mercurous Halides, TeO_2 is transparent only in a spectral region 0.35 - 5μm. Mercurous Halides are slightly less transparent in VIS spectral band, but they are highly transparent in a wide IR spectral region (up to 20μm and even more). The summarised general properties [34,48] of the selected materials are in Table 1. As was mentioned above, these materials offer high birefringence. The evolution of their refractive indexes in the selected bandwidth is shown in Fig. 3. The ordinary and extraordinary refraction indices have been modelled via Cauchy's dispersion formula [49]

$$n(\lambda) = A + \frac{B}{\lambda^2} + \frac{C}{\lambda^4} + \frac{D}{\lambda^6} + \dots . \tag{20}$$

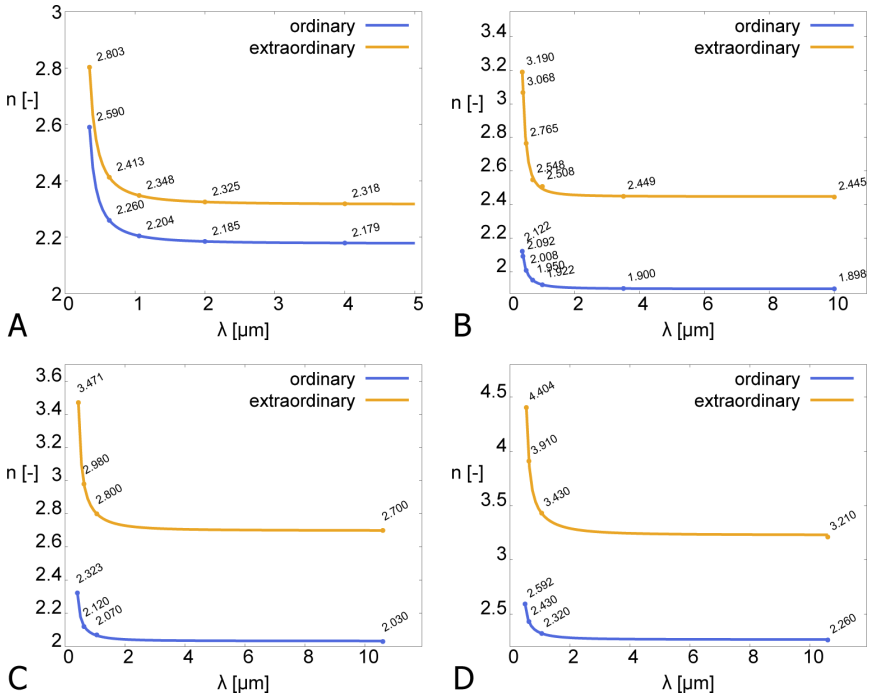

Fig. 3. Ordinary and extraordinary refractive indices for materials of TeO_2 (A), Hg_2Cl_2 (B), Hg_2Br_2 (C), Hg_2I_2 (D), respectively (refractive indexes obtained in [50,51]).

The estimated coefficients A, B, C, D for the selected materials are summarised in Table 2. The significant birefringence of the materials is apparent from the presented diagrams. At the

Optics EXPRESS

Table 1. General material properties.

Materials / properties	TeO_2	Hg_2Cl_2	Hg_2Br_2	Hg_2I_2
Density - $\rho[g/cm^3]$	6.00	7.190	7.307	7.70
Hardness [Mohs]	4.5	1.5	1.5	1 - 2
Transmission [μm]	0.35 - 5	0.35–20	0.40 – 30	0.45 – 40
Birefringence (λ = 632.8nm) [-]	0.35	0.66	0.86	1.48
Band gap [eV]	3	3.9	2.6	2.4

selected wavelength 4μm, Calomel offers approx. birefringence 0.5536, Kuzminite 0.6838, and Moschelite even 0.9831, which is significantly higher than birefringence 0.1392 of Paratellurite. To assess sufficiently all selected materials and compare them in the IR region, the selected wavelength 4μm has been retained.

Table 2. Calculated coefficients of Cauchy's dispersion formula for the selected tetragonal materials (refractive indexes obtained in [50,51]) .

	TeO_2		Hg_2Cl_2		Hg_2Br_2		Hg_2I_2	
	n_o	n_e	n_o	n_e	n_o	n_e	n_o	n_e
A	2.177	2.316	2.033	2.699	2.264	3.228	1.898	2.448
B	0.029	0.034	0.040	0.124	0.069	0.259	0.024	0.035
C	0.001	0.001	−0.004	−0.015	−0.009	−0.063	0.0004	0.0108
D	0.0002	0.0003	0.001	0.004	0.003	0.027	0.0001	−0.0001

A significant parameter for the AO interaction in the [001], [110] plane, that can be compared, is the acoustic shear wave velocity. For the selected crystallographic plane, the overall velocity can be provided by Eq. (1). Specifically important are the velocities V_{001} and V_{110}. The summary of the selected material acoustic velocities are in Table 3. The exceptional low values of V_{110} for Calomel (V_{110}<350m/s), Kuzminite (V_{110}<285m/s) and Moschelite (V_{110}<255m/s) significantly increase the AO figure of merit [Eq. (14)] and, therefore, favour Mercurous Halides over Paratellurite (V_{110}<616m/s).

Table 3. The acoustic wave velocities in the crystallographic plane [001], [110] for the selected materials.

Materials / acoustic velocities	TeO_2	Hg_2Cl_2	Hg_2Br_2	Hg_2I_2
V_{001} [m/s]	2104	1084	1008	871
V_{110} [m/s]	616	347	282	253

The AO figure of merit M_2 represents the AO interaction parameters and is completely based on the material characteristics. Moreover, M_2 is also determined by the effective elasto-optic coefficient, which can be calculated for the plane [001], [110] according to Eq. (15). The known elasto-optic coefficients p_{11}, p_{12}, p_{44} are listed in Table 4. All the elasto-optic coefficients are currently known only for the TeO_2 material. For Calomel material, one remaining elasto-optic coefficient p_{44} is still unknown and usually considered equal to 0 [24,25]. For Kuzminite and Moschelite, the elasto-optic coefficients have not yet been determined. It is mainly caused by their problematic growth and polishing processes. Therefore, for calculating the M_2, we exploited the correct refractive indices of these materials and combined them with the Calomel elasto-optic coefficients, which can be considered as a sufficient approximation [24,25].

Assuming the general quasi-collinear interaction for the incoming light beam at 4μm, the AO figure of merit M_2 of the selected materials can be calculated against the input light angle

Research Article | Vol. 29, No. 9 / 26 April 2021 / Optics Express 12822
Optics EXPRESS

Table 4. The elasto-optic coefficients of the selected materials. For Hg_2Br_2 and Hg_2I_2, the coefficients are currently unknown. The elasto-optic coeficient p_{44} of Calomel is also unknown and is commonly considered as equal to 0.

Materials / elasto-optic coefficients	TeO_2	Hg_2Cl_2	Hg_2Br_2	Hg_2I_2
p_{11} [-]	0.0074	0.551	UNK	UNK
p_{12} [-]	0.187	0.440	UNK	UNK
p_{44} [-]	−0.17	0 (UNK)	UNK	UNK

(measured from the [110] axis). The results can be seen in Fig. 4(A). It is clear that Moschelite outperforms significantly the remaining materials mainly due to the low acoustic velocities and high birefringence. However, all Mercurous Halides outperform the Paratellurite in general. It is also possible to approximate the M_2 for several values of Calomel elasto-optic coefficient p_{44}. Figure 4(B), indicates that for values of $p_{44}>0$, the M_2 rises and reaches higher values than shows the 4(A). The evaluation of Calomel coefficient p_{44} has also been studied in other research [40] and must be addressed in the future.

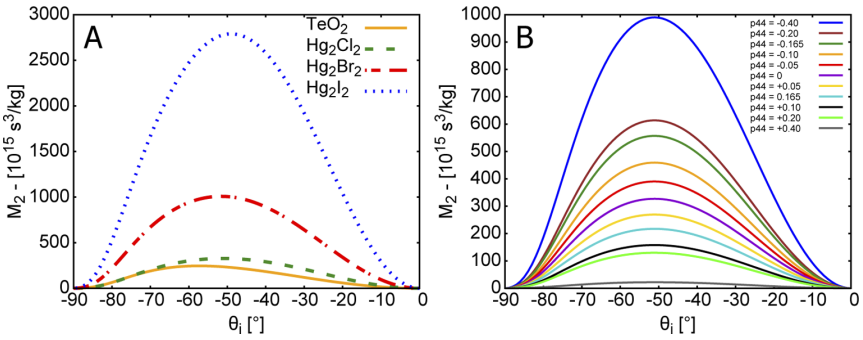

Fig. 4. The AO figure of merit versus input angle calculated for quasi-collinear AO interaction in [001], [110] with assumed the light wavelength 4μm. Sub-figure A shows the M_2 for all selected materials - TeO_2 (orange line), Hg_2Cl_2 (green dashed line), Hg_2Br_2 (red dashed line), Hg_2I_2 (blue dashed line). Sub-figure B express the estimation of Calomel M_2 versus input angle for several values of elasto-optic coefficient p_{44}, which is currently unknown and usually estimated as 0. The exploited values of p_{44} varies in interval from −0.4 to +0.4

In addition, for the varying input angle, other parameters of the general quasi-collinear AOTF can also be estimated based on the material characteristics. The best theoretically achievable values of the quasi-collinear AOTF for the 4μm wavelength are summarised for all materials in Table 5. The properties based on the proportions of the AOTF single crystals such as interaction length L and height of the acoustic wave H has been selected for the sake of simplification as $L = 3cm$, $H = 0.8cm$. Interesting are the values of spectral resolution, which result from the high birefringence. Mercurous Halides are better in spectral resolution over $2.75nm$ than Paratellurite, which makes a notable difference.

Currently, the TeO_2 optical material is the most exploited for the AOTF fabrication. However, as was mentioned above, it has a limited spectral band within the IR spectral region, and above 5μm is not transparent. It is a limitation for devices that want to operate in LWIR (long-wave infrared) spectral band. This bottleneck may be suppressed by Mercurous Halide materials, which offer even better properties and are transparent over 20μm and highly suitable, for example,

Optics EXPRESS

Table 5. Estimated values of quasi-collinear AOTF properties based on the selected materials. For the estimation the interaction length has been set equal to $L = 3cm$ and the width of the acoustic wave was set equal to $H = 0.7cm$. For all parameters, the incident angle of the light has been selected for their maximisation.

Materials / AO properties at $\lambda = 4\mu m$	TeO_2	Hg_2Cl_2	Hg_2Br_2	Hg_2I_2
Dispersive constant - b [-]	0.874	3.479	4.297	6.177
AO figure of merit - M_2 $[10^{-15}\ s^3/kg]$	246	327	1008	2790
Spectral resolution - $\Delta\lambda$ $[nm]$	3.45	0.87	0.70	0.49
Chromatic filed of view - $\Delta\theta$ $[mrad]$	4.73	2.37	2.14	1.78
Acoustic power - $P_a(\eta \approx 50\%)$ $[W]$	2.17	1.63	0.53	0.19

for the LWIR operation. Concerning Mercurous Halides, currently, only Calomel has been grown to a sufficient size for the AOTF fabrication [33,38]. The ongoing research on the growth of Kuzminite and Moschelite, which ensures sizeable and robust crystals, is still in progress [35,52]. In addition, the bonding of the transducer to the Mercurous Halide crystals is currently also under ongoing research [53].

Considering the analysed characteristics of the selected tetragonal crystals, Calomel has been chosen for a design of the quasi-collinear AOTF model. In general, Calomel can be considered as a valid representative of Mercurous Halides and possess several of their properties. Compared to TeO_2, Calomel also offers wider operational bandwidth due to its transparency and higher spectral resolution, which was selected as the main optimising parameter.

5. Calomel-based quasi-collinear AOTF

In general, the properties of Calomel single crystals allow the operation in the thermal LWIR spectral band. Therefore, in this paper, we propose optimisation criteria and model of the quasi-collinear AOTF operating at wavelengths $8 - 10\mu m$. From the previous analysis, it is clear, that the design and performance of such AOTF is highly related to the crystallographic orientation and thus directionally-dependent. Resulting from that, a cut angle of the crystal input window within the selected [001], [110] plane is crucial. In general, the cut angle of the AOTF crystal determines the input angle of the light at normal incidence (measured from the [110] axis) and affects the parameters of the AOTF. For the presented model, assume, the acoustic wave emitting transducer placed on the crystal side. Therefore, the overall cut of the single crystal is also crucial. An example of a convenient crystal shape for the quasi-collinear AOTF and its operation may be seen in Fig. 5(A). For the quasi-collinear AOTF, the transducer may be oriented in a way that the acoustic group velocity vector propagates to the input facet of the crystal. The acoustic group velocity (energy) is then reflected at the crystal input window, and it propagates collinearly with the input light at normal incidence. After the reflection at the input window, the acoustic phase wave velocity vector should be conveniently oriented for the maximisation of AOTF parameters, such as AO figure of merit M_2, diffraction efficiency, and chromatic aperture. As was mentioned above, the different directions (walk-off angle) of the acoustic group (energy flow) and phase velocities (wavefront orientation) vectors are caused by the characteristics of the anisotropic medium. In addition, the shape of the presented crystal is constrained by symmetricity. The output facet of the crystal should be parallel to the input window. The sides of the crystal should also be parallel. Thus, the acoustic wave can be reflected at the output window and absorbed by the crystal lateral side by the additional acoustic absorber.

To maximise the M_2, Fig. 4 may be used. Therefore, for the Calomel-based quasi-collinear AOTF, the input window cut angle should be between $-45°$ and $-60°$ (measured from the [110] axis). The separation of the diffracted and input light beam not only by polarisation may also be a

Research Article | Vol. 29, No. 9 / 26 April 2021 / Optics Express 12824
Optics EXPRESS

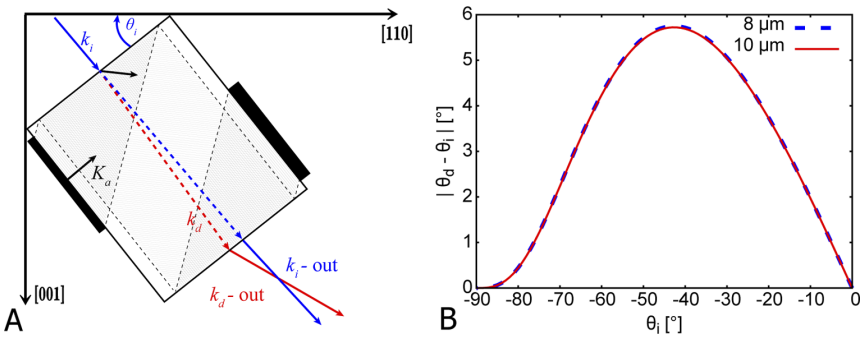

Fig. 5. The example of proposed design of the quasi-collinear AOTF (A) and deviation angle between input and diffracted light beams (B). The transducer bonded to the crystal emits acoustic shear wave in the selected crystallographic plane [001], [110]. The acoustic wave group velocity does not follow the acoustic phase velocity due to the significant walk-off angle. Therefore, the acoustic wave directs to the crystal input window, where the acoustic wave is reflected. Thus, the input light wave and acoustic wave propagates collinearly. The phase velocity vector of the acoustic beam has, however, different orientation. The acoustic wave is then similarly reflected at the crystal output window and can be absorbed in the backside. The polishing of the crystal, therefore, has to be symmetrical.

critical factor. The spatial separation between the input light beam and the diffracted light beam can be represented as $|\theta_d - \theta_i|$. The results of separation between the incident and diffracted light beams for Calomel material at 8μm and 10μm can be seen in Fig. 5(B). Due to the low birefringence changes in the IR region, the separation between the diffracted and incident light almost does not vary. Conveniently, for the maximal spatial separation, the input window cut angle should be from $-40°$ to $-50°$.

Because of the directional dependence of the M_2, the cut angle of the AOTF input window influence required acoustic power for sufficient diffraction efficiency. This power dependency may be expressed by Fig. 6 and via Eq. (16), where 8μm wavelength was selected as dominant. The required power profile corresponds proportionally to the shape of the AO figure of merit M_2 and confirms its high impact on the AOTF performance. The interaction length also lowers the power requirements.

From the provided analysis, we can conclude that the recommended cut angle for the Calomel crystal for the selected type of AOTF should be set between $-45°$ and $-60°$ from the [110] crystal axis.

For the model of the quasi-collinear Calomel-based AOTF, suppose, that the input cut angle has been selected equal to $-48°$ (measured from the [110] axis). It is also possible to analyse the spectral resolution of such AOTF via Eq. (17). The spectral resolution dependence on the wavelength and interaction length can be seen in Fig. 7. The figure shows that the increase of the interaction length favours the quasi-collinear AO interaction. The difference may be up to tens of nm.

Selecting the interaction length equal to 3 cm as a typical length for currently grown Calomel crystals [33,34,54] other parameters of the quasi-collinear AOTF may be modelled. Firstly, the frequency dependence on the wavelengths in $8 - 10\mu m$ spectral band can be analysed for the quasi-collinear AOTF with selected parameters. The results of the required frequency for ideal phase matching during the normally incident light may be seen in Fig. 8(A).

The necessary power requirements for at least 50% diffraction efficiency for the modelled quasi-collinear AOTF may also be analysed. The results are plotted in Fig. 8(B). The spectral

Optics EXPRESS

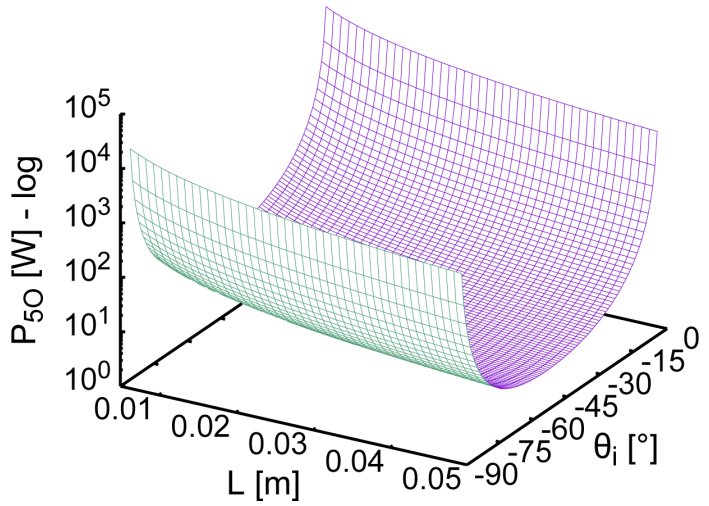

Fig. 6. The required power for the 50% diffraction efficiency of the calomel-based quasi-collinear AOTF depending on the input angle of the light and interaction length. For the simplicity, the interaction length has been set equal to 3cm and width of the acoustic beam to 0.8cm. For this approximation, the wavelength equal to 8μm has been selected.

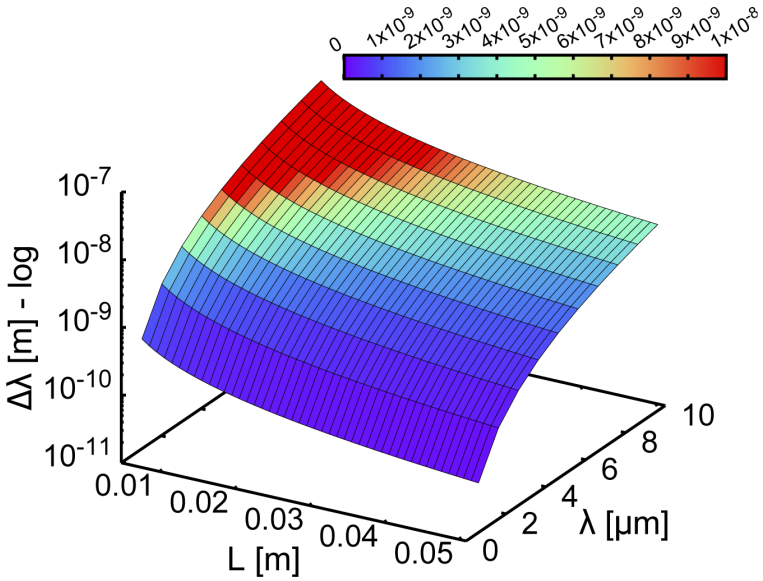

Fig. 7. The spectral resolution versus wavelength and interaction length for the calomel-based quasi-collinear AOTF. For this estimation, the input angle of the light has been selected equal to $-48°$ form the [110] crystallographic axis.

Research Article Vol. 29, No. 9 / 26 April 2021 / Optics Express 12826
Optics EXPRESS

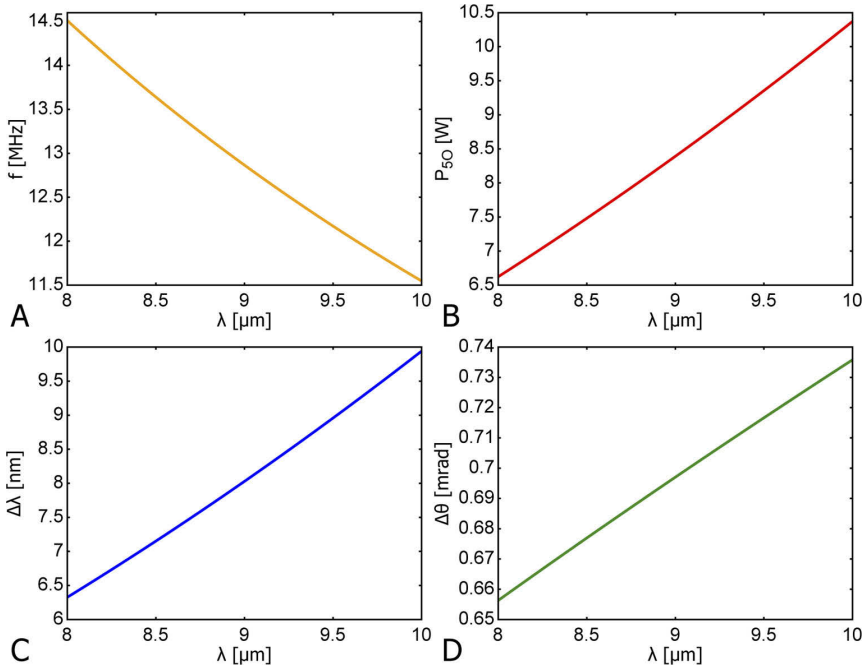

Fig. 8. Estimated properties of the Calomel-based quasi-collinear AOTF operating in $8-10\mu m$ spectral band. The first diagram (A) represents the tuning acoustic frequency dependence on the wavelength. The next diagram (B) shows the required power for at least 50% diffraction efficiency versus the input wavelength. The diagram (C) shows estimated spectral-resolution of modelled AOTF against the input light wavelength. The last diagram (D) represent approximated chromatic aperture versus the input wavelength. For the sake of simplicity, the interaction length has been set equal to $3cm$ and width of the acoustic beam to $0.8cm$. The cut angle of input window of the calomel crystal has been selected equal to $-48°$, measured from the [110] crystallographic axis.

resolution for the selected wavelengths and the chromatic aperture may be seen in Figs. 8(C), 8(D), respectively.

Having a specific cut of the AOTF input window in the [001], [110] crystallographic plane, we can also assess the diffracted light output for different incident light angles and wavelengths in the IR region. Therefore, it is possible to evaluate the spatio-spectral output expected from the introduced hyperspectral concept.

Setting the acoustic beam frequency to $12.87MHz$, the deviation from the phase matching condition may be shown [Eq. (11)]. Only a narrow band of wavelengths and input angles create a small enough mismatch for obtaining the diffracted output beam. For the quasi-collinear AOTF model, the results of the phase mismatch are plotted against the wavelength and incident light angle in Fig. 9.

Based on the obtained phase mismatch and Eq. (12), it is also possible to evaluate the diffraction output. Assume the same acoustic frequency $12.87MHz$ and the acoustic beam power equal to the $8.39W$. Figure 10 shows the diffraction output for incident wavelengths in $8-10\mu m$ spectral band and incident light angle varying from $-40°$ to $-58°$ (measured from the [110] axis). For the sake of simplification, the multispectral light beam is considered to incident at the centre of

Optics EXPRESS

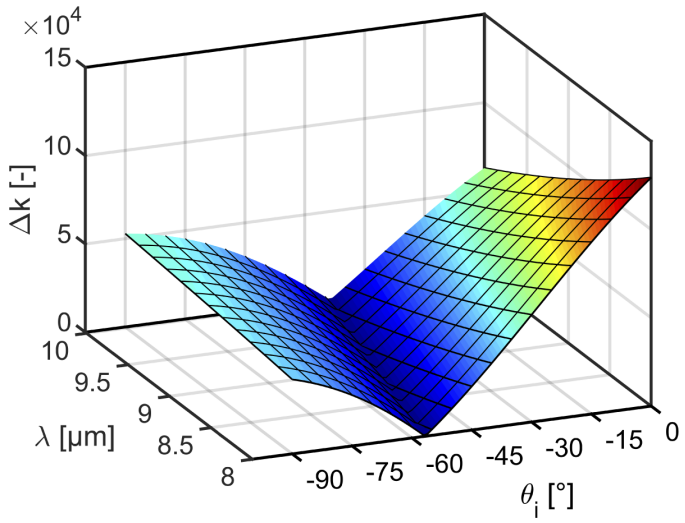

Fig. 9. Estimated phase mismatch Δk for the calomel-based quasi-collinear AOTF with a cut angle of the input window equal to -48° form the [110] axis. The values of the mismatch are plotted against the wavelength and input angle of the incident light. The frequency of the acoustic wave is $12.87MHz$, and the input power of the acoustic beam was set to $8.39.W$.

the input window of the AOTF, similarly as it is shown in Fig. 5. From the observable peaks of the diffraction efficiency, which corresponds to the ideal phase matching condition, it is apparent that the spatio-spectral hyperspectral imaging concept was achieved. It is clear that the diffracted output equal to $9\mu m$ properly corresponds to the diffracted output peak with 50% diffraction efficiency for $8.39W$, as was expected. However, it can be seen that lower and higher wavelengths are, due to one selected frequency and level of power, diffracted with varying efficiency levels. This phenomenon must be addressed in the future by the design of the post-processing of the captured data.

Research Article | Vol. 29, No. 9 / 26 April 2021 / Optics Express 12828
Optics EXPRESS

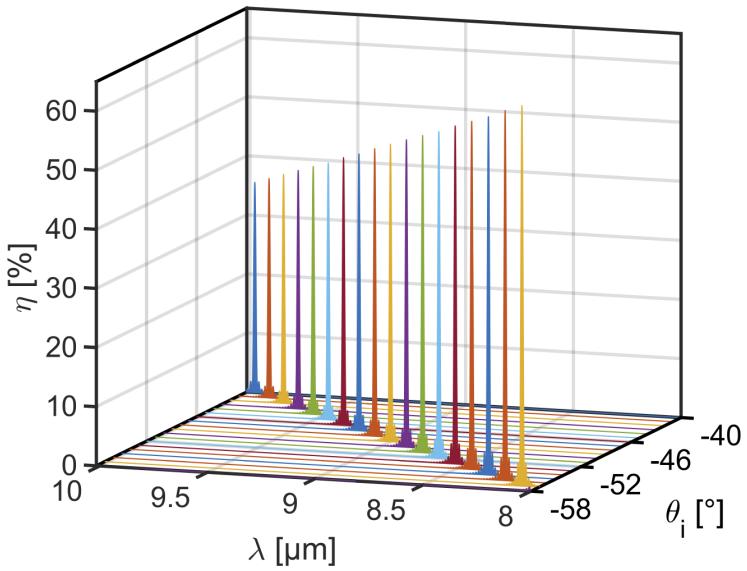

Fig. 10. Diffraction output from the calomel-based quasi-collinear AOTF model. The diffraction output corresponds to the phase mismatch obtained in Fig. 9. The acoustic wave frequency was kept at $12.865MHz$, and the input power of the acoustic beam was set to $8.39W$. These values are set for the 50% diffraction of the $9\mu m$ beam at normal incidence on the crystal input window ($-48°$ from [110] axis). The results properly correspond to the expected phase matching. The diffraction is observable for several input wavelengths and incident angles. Thus, spatio-spectral imaging through the AOTF may be achieved. For diffraction of other wavelengths, the acoustic frequency should be tuned. The whole spectral information may be obtained after several steps of tuning and post-processing.

6. Results and discussion

The principle of the quasi-collinear AOTF for spatio-spectral hyperspectral imaging was demonstrated in the previous section. It has been shown, the characteristics of the selected tetragonal materials may offer significant benefits for the quasi-collinear AOTF in the IR region. The selection of the material highly depends on the chosen operational spectral band. The material crystallographic plane has been selected as [001], [100] due to the slow shear wave speed of the acoustic wave within this plane. The refractive indices evolution in the VIS and IR bands for all selected materials have been shown in Fig. 3. The primary optimised parameter is the spectral resolution. The spectral resolution of the quasi-collinear AOTF depends mainly on the used crystal proportions and material characteristics [Eq. (17)]. The maximally achievable spectral resolution for the AOTF based on the selected materials, at MWIR wavelength $4\mu m$ and for selected crystal proportions, was shown in Table 5. Frequently used Paratellurite single crystal offers spectral resolution $3.45nm$ for the quasi-collinear AOTF at the $4\mu m$ wavelength. Contrary to that, exceptional parameters were exhibited by Mercurous Halide single crystals. The spectral resolution for quasi-collinear AOTF based on Calomel was estimated as $0.87nm$ at the same wavelength. Kuzminite and Moschelite offered even narrower spectral resolution $0.7nm$ and $0.49nm$ respectively. Comparing the other parameters such as AO figure of merit M_2 and related acoustic power requirements, Mercurous Halides provided even better results. The M_2 for Paratellurite-based quasi-collinear AOTF was estimated as $246 \cdot 10^{-15} s^3/kg$. and necessary

Optics EXPRESS

power ($\eta \approx 50\%$) equal to $2.17W$. Estimated M_2 and acoustic power ($\eta \approx 50\%$) for Calomel, Kuzminite and Moschelite was $327 \cdot 10^{-15} s^3/kg$, $1008 \cdot 10^{-15} s^3/kg$, $2790 \cdot 10^{-15} s^3/kg$ and $1.63W$, $0.53W$ and $0.19W$ respectively. However, due to the nature of this type of the AOTF and high birefringence of Mercurous Halides, the trade-off is the lower value of the maximal chromatic field of view $2.37mrad$, $2.14mrad$, $1.78mrad$, compared to Paratellurite maximal chromatic field of view $4.73mrad$. Nevertheless, the biggest advantage of Mercurous Halides is the broadband IR spectral operation over $20\mu m$. Hence, the operation in the LWIR spectral band allow only Mercurous Halides. Concerning the results, Mercurous Halides or more precisely Calomel has been selected as a suitable material for the quasi-collinear AOTF modelling.

The cut angle selection of the Calomel single crystal input window had also been discussed and optimised. The crystal input window cut highly influences the parameters such as M_2, power requirements, the deviation between the input and diffracted light, and others. The highest value for the Calomel M_2 was according to Fig. 4 between $-45°$ and $-60°$ for the cut angle of the crystal window (measured from the [110] axis). This selection was confirmed by Fig. 6. This figure represented the power requirements of the AOTF for at least 50% diffraction efficiency and showed the importance of the AO interaction length. The extension of the AO interaction length from $1cm$ up to $5cm$ lowered the power requirements almost by an order. Another important benefit of the AO interaction length extension has been shown in Fig. 7. A similar extension of the interaction length up to $5cm$ improved the spectral resolution $\Delta\lambda$ also almost by an order.

For the model of the Calomel-based quasi-collinear AOTF, the input cut angle has been selected equal to $-48°$. A shape of the quasi-collinear AOTF, which ensures the collinear interaction between the input light and the acoustic beam, has been proposed in Fig. 5(A). For this model, the energy propagation of the acoustic wave is diverse from the acoustic waterfront orientation. It is caused by the walk-off angle between the phase and group acoustic velocities within the anisotropic medium. Therefore, in the presented model, the acoustic wave is reflected at the crystal input window and propagates collinearly with the light. The obtained parameters of this type of AOTF have been presented in Fig. 8. Introduced AOTF model achieved the spectral resolution and chromatic field of view approximately $\Delta\lambda \approx 6.3nm$, $\Delta\theta \approx 0.65mrad$ at $8\mu m$ and $\Delta\lambda \approx 9.95nm$, $\Delta\theta \approx 0.73mrad$ at $10\mu m$. The tuning acoustic frequency and power ($\eta \approx 50\%$) have been $14.5MHz$ with $6.6W$ at $8\mu m$ and $11.5MHz$ with $10.3W$ at $10\mu m$ respectively.

The presented model also served for the estimation of the phase mismatch and allowed the diffraction output evaluation. The phase mismatch results with the frequency $12.865MHz$ and the power $8.39W$ against the wavelength and the light incident angle have been shown in Fig. 9. The lowest mismatch values were estimated between the incident angles $-35°$ and $-60°$ (measured from the [110] axis) for operational wavelength interval $8 - 10\mu m$. Subsequently, according to the phase mismatch results, the diffracted output has been modelled. We exploited the same acoustic beam frequency and power. The diffracted output for varying wavelength and light input angles is shown in Fig. 10. The presented diffracted output corresponded to several $sinc^2$ function peaks depending on the phase matching and the acoustic beam power. The expected diffraction peak, which corresponds to the 50% diffraction efficiency at $9\mu m$ and normal light incidence at the crystal input window ($-48°$) have been obtained. The spectral resolution at the FWHM of the $sinc^2$ function at $9\mu m$ was approximately $10nm$. This spectral resolution is about $2nm$ worse than the overall estimation in Fig. 8(C). This difference resulted from the limited acoustic power selected for 50% diffraction efficiency. The other diffracted peaks, which fulfilled the Bragg condition, have been obtained with varying efficiency due to the unchanged level of acoustic power. In general, there were obtained 18 diffraction peaks within the operational spectral region. By tuning the frequency and the acoustic power, different mismatch and diffraction peaks may be obtained. Thus, the spatio-spectral concept of the AOTF has been demonstrated.

Considering the presented results, the suitability of the quasi-collinear AOTF for the spatio-spectral hyperspectral system has been shown. The future work should focus on the fabrication

Research Article | Vol. 29, No. 9 / 26 April 2021 / Optics Express 12830
Optics EXPRESS

of the presented quasi-collinear AOTF based on Mercurous Halides and its integration into the introduced hyperspectral system. The fabrication of Mercurous Halides-based AOTF and further test procedures may allow specifying the missing elasto-optic coefficients of the materials precisely. This would also help to describe the AOTF parameters more accurately and improve its design optimisation. In addition, the overall optical modelling of the introduced hyperspectral system should also be a priority. The determination of its other parameters such as PSF, field of view, spatial resolution, and others should be focused on. Apart from the AOTF, these parameters are influenced by the additional system instruments such as fore and back optics, detector, electrical amplifiers, necessary polarisers, and so on. Therefore, the appropriate selection and further optimisation of these instruments would be necessary for the final construction and parameter determination of the presented hyperspectral system.

7. Conclusion

This paper has proposed the analysis of the quasi-collinear AOTF suitable for the spatio-spectral IR hyperspectral imaging system. Apart from the quasi-collinear interaction theory, we have analysed and discussed the properties of suitable anisotropic materials for the AO IR operation and compared them against each other. The materials were selected among the tetragonal single crystals with high positive birefringence and exceptional AO properties. Conveniently, the quasi-collinear AO interaction for the selected materials proceeded in the [001], [110] crystallographic planes. The Calomel single crystal has been chosen as the suitable representative for the quasi-collinear AOTF model from the provided comparison. We have shown and discussed the convenient cut of the input window of the Calomel-based AOTF and showed the undeniable advantages of the quasi-collinear interaction. In addition, the power requirements, the maximal achievable spectral resolution, and the angular aperture of the quasi-collinear AOTF have also been discussed. Finally, the evaluation of the spatio-spectral hyperspectral concept by the AOTF model has been confirmed and presented.

Funding. Grantová Agentura České Republiky (20-10907S); Grant Agency of the Czech Technical University in Prague (SGS20/179/OHK3/3T/13).

Disclosures. The authors declare no conflicts of interest.

References

1. J. M. Bioucas-Dias, A. Plaza, G. Camps-Valls, P. Scheunders, N. Nasrabadi, and J. Chanussot, "Hyperspectral remote sensing data analysis and future challenges," IEEE Geosci. Remote. Sens. Mag. **1**(2), 6–36 (2013).
2. G. Lu and B. Fei, "Medical hyperspectral imaging: a review," J. Biomed. Opt. **19**(1), 010901 (2014).
3. M. Á. F. de la Ossa, J. M. Amigo, and C. García-Ruiz, "Detection of residues from explosive manipulation by near infrared hyperspectral imaging: A promising forensic tool," Forensic Sci. Int. **242**, 228–235 (2014).
4. Y. Liu, H. Pu, and D.-W. Sun, "Hyperspectral imaging technique for evaluating food quality and safety during various processes: A review of recent applications," Trends Food Sci. Technol. **69**, 25–35 (2017).
5. A. A. Gowen, Y. Feng, E. Gaston, and V. Valdramidis, "Recent applications of hyperspectral imaging in microbiology," Talanta **137**, 43–54 (2015).
6. M. J. Khan, H. S. Khan, A. Yousaf, K. Khurshid, and A. Abbas, "Modern trends in hyperspectral image analysis: A review," IEEE Access **6**, 14118–14129 (2018).
7. A. Jullien, R. Pascal, U. Bortolozzo, N. Forget, and S. Residori, "High-resolution hyperspectral imaging with cascaded liquid crystal cells," Optica **4**(4), 400 (2017).
8. J. Transon, R. d'Andrimont, A. Maugnard, and P. Defourny, "Survey of hyperspectral earth observation applications from space in the sentinel-2 context," Remote Sens. **10**(3), 157 (2018).
9. D. Manolakis, M. Pieper, E. Truslow, R. Lockwood, A. Weisner, J. Jacobson, and T. Cooley, "Longwave infrared hyperspectral imaging: Principles, progress, and challenges," IEEE Geosci. Remote. Sens. Mag. **7**(2), 72–100 (2019).
10. R. Scafutto and C. de Souza Filho, "Detection of methane plumes using airborne midwave infrared (3–5 μm) hyperspectral data," Remote Sens. **10**(8), 1237 (2018).
11. V. Batshev, A. Machikhin, G. Martynov, V. Pozhar, S. Boritko, M. Sharikova, V. Lomonov, and A. Vinogradov, "Polarizer-Free AOTF-Based SWIR Hyperspectral Imaging for Biomedical Applications," Sensors **20**(16), 4439 (2020).

Optics EXPRESS

12. N. B. Singh, D. Kahler, D. J. Knuteson, M. Gottlieb, D. Suhre, A. Berghmans, B. Wagner, J. Hedrick, T. Karr, and J. J. Hawkins, "Operational characteristics of a long-wavelength IR multispectral imager based on an acousto-optic tunable filter," Opt. Eng. **47**(1), 013201 (2008).
13. D. R. Suhre, "Long-wave infrared spectral imager with an 8cm1 passband acousto-optic tunable filter," Opt. Eng. **44**(9), 094601 (2005).
14. N. Gupta, "Acousto-optic tunable filter based visible- to near-infrared spectropolarimetric imager," Opt. Eng. **41**(5), 1033 (2002).
15. J. Ward, M. Farries, C. Pannell, and E. Wachman, "An acousto-optic based hyperspectral imaging camera for security and defence applications," (Toulouse, France, 2010), p. 78350U.
16. X. Zhang, W. Liu, H. Tong, Y. Liu, X. Wang, C. Zhang, Y. Wang, H. Wang, Z. Sheng, Z. Tan, W. Qiu, X. Huang, and P. Wang, "High-Resolution Hyperspectral Microscopic Imaging With Single Acousto-Optic Tunable Filter Based on Double Filtering," IEEE Access **8**, 11570–11576 (2020).
17. R. Abdlaty, J. Orepoulos, P. Sinclair, R. Berman, and Q. Fang, "High Throughput AOTF Hyperspectral Imager for Randomly Polarized Light," Photonics **5**(1), 3 (2018).
18. I. C. Chang, "Tunable Acousto-Optic Filters: An Overview," (San Diego, 1976), pp. 12–22.
19. N. Gupta and N. Fell Jr, "A compact collinear aotf raman spectrometer," Talanta **45**(2), 279–284 (1997).
20. V. Pustovoit and N. Gupta, "Collinear acousto-optic spectrometers and their applications," in *Proceedings of the First Army Research Laboratory Acousto-Optic Tunable Filter Workshop*, (1997), pp. 33–44.
21. J. Xu and R. Stroud, *Acousto-optic devices: principles, design, and applications*, Wiley series in pure and applied optics (Wiley, New York, 1992).
22. V. B. Voloshinov, "Close to collinear acousto-optical interaction in TeO2 single crystal," (Gdansk-Jurata, Poland, 1992), pp. 162–176.
23. S. Mantsevich, V. Balakshy, V. Molchanov, and K. Yushkov, "Influence of acoustic anisotropy in paratellurite on quasicollinear acousto-optic interaction," Ultrasonics **63**, 39–46 (2015).
24. P. Tournois, "Design of acousto–optic programmable filters in mercury halides for mid-infrared laser pulse shaping," Opt. Commun. **281**(15-16), 4054–4056 (2008).
25. R. Maksimenka and P. Tournois, "Mid-infrared high-frequency high-resolution reflective acousto-optic filters in mercury halides," Opt. Commun. **285**(5), 715–719 (2012).
26. D. Kaplan and P. Tournois, "Acoustic-optical filtering method and device based on a long acousto-optical interaction," (EU Patent - EP2431791B1 2012).
27. R. Maksimenka, N. Forget, D. Kaplan, R. Hasal, C. Barta, J. Jaeck, and R. Haïdar, "High spectral resolution AOTF-based hyperspectral imaging system for thermal infrared," in *Proceedings of the 4S Symposium*, (ESA, 2014).
28. N. Uchida and Y. Ohmachi, "Elastic and photoelastic properties of teo2 single crystal," J. Appl. Phys. **40**(12), 4692–4695 (1969).
29. N. Gupta, "Materials for imaging acousto-optic tunable filters," (Baltimore, Maryland, USA, 2014), p. 91000C.
30. V. B. Voloshinov, A. Y. Tchernyatin, E. Blomme, and O. J. Leroy, "A dozen Bragg effects in tellurium dioxide single crystal," (Gdansk-Jurata, Poland, 1998), pp. 141–152.
31. N. Singh, M. Gottlieb, G. Brandt, A. Stewart, R. Mazelsky, and M. Glicksman, "Growth and characterization of mercurous halide crystals: mercurous bromide system," J. Cryst. Growth **137**(1-2), 155–160 (1994).
32. P. M. Amarasinghe, J.-S. Kim, S. Trivedi, J. Soos, M. Diestler, F. Jin, S. B. Qadri, N. Gupta, J. L. Jensen, and J. Jensen, "Long wavelength infrared (LWIR) AOTF and AOM modulators using Hg2Br2 crystals," in *Infrared Sensors, Devices, and Applications VII*, vol. 10404 P. D. LeVan, A. K. Sood, P. Wijewarnasuriya, and A. I. D'Souza, eds., International Society for Optics and Photonics (SPIE, 2017), pp. 185–191.
33. P. Pata, M. Klima, J. Bednar, P. Janout, C. Barta, R. Hasal, L. Maresi, and S. Grabarnik, "OFT sectorization approach to analysis of optical scattering in mercurous chloride single crystals," Opt. Express **23**(16), 21509 (2015).
34. C. Bárta and C. Barta Jr., "Physical Properties of Single Crystals of The Calomel Group (Hg_2X_2 : X=Cl, Br)[1]," Mater. Sci. Forum **61**, 93–150 (1991).
35. T. H. Kim, H. T. Lee, Y.-M. Kang, G.-E. Jang, I. H. Kwon, and B. Cho, "In-depth investigation of hg2br2 crystal growth and evolution," Materials **12**(24), 4224 (2019).
36. R. Maksimenka, P. Nuernberger, K. F. Lee, A. Bonvalet, J. Milkiewicz, C. Barta, M. Klima, T. Oksenhendler, P. Tournois, D. Kaplan, and M. Joffre, "Direct mid-infrared femtosecond pulse shaping with a calomel acousto-optic programmable dispersive filter," Opt. Lett. **35**(21), 3565–3567 (2010).
37. J.-S. Kim, S. B. Trivedi, J. Soos, N. Gupta, and W. Palosz, "Development of mercurous halide crystals for acousto-optic devices," (San Diego, CA, 2007), pp. 66610B.
38. S. Valle, J. Ward, C. Pannell, and N. P. Johnson, "Acousto-optic tunable filter for imaging application with high performance in the IR region," (San Francisco, California, United States, 2015), p. 93590E.
39. J. D. Ward and S. Valle, "Acousto-optic devices for operation in the infrared," in *Fiber Lasers and Glass Photonics: Materials through Applications*, S. Taccheo, M. Ferrari, and J. I. Mackenzie, eds. (SPIE, Strasbourg, France, 2018), p. 76.
40. A. Pierson and C. Philippe, "Acousto-optic interaction model with mercury halides (Hg2Cl2 and Hg2Br2) as AOTF cristals," in *International Conference on Space Optics — ICSO 2018*, N. Karafolas, Z. Sodnik, and B. Cugny, eds. (SPIE, Chania, Greece, 2019), p. 219.

Research Article | Vol. 29, No. 9 / 26 April 2021 / Optics Express 12832

Optics EXPRESS

41. D. Porokhovnichenko, J. Ryu, D. Zinkin, and V. Voloshinov, "Analysis of wide-angle acousto-optic interaction geometry in single crystal mercury bromide," in *Fourteenth School on Acousto-Optics and Applications*, I. Grulkowski, B. B. J. Linde, and M. Duocastella, eds. (SPIE, Torun, Poland, 2019), p. 12.
42. D. J. Knuteson, "Crystal growth, fabrication, and design of mercurous bromide acousto-optic tunable filters," Opt. Eng. **46**(6), 064001 (2007).
43. E. Dyakonov, D. Porokhovnichenko, J. Ryu, and V. Balakshy, "Implementation of the wide-angle acousto-optical interaction geometry in a mercury bromide single crystal," Appl. Opt. **60**(8), 2348–2353 (2021).
44. D. S. Boyd and F. Petitcolin, "Remote sensing of the terrestrial environment using middle infrared radiation (3.0–5.0μm)," Int. J. Remote. Sens. **25**(17), 3343–3368 (2004).
45. P. Janout, "Modeling of space variant optical systems," Ph.D. thesis, Czech Technical University in Prague (2018).
46. W. H. Bragg and W. L. Bragg, "The reflection of x-rays by crystals," Proceedings of the Royal Society of London. Series A, Containing Papers of a Mathematical and Physical Character **88**, 428–438 (1913).
47. A. P. Goutzoulis, D. R. Pape, and S. V. Kulakov, eds.. "Design and fabrication of acousto-optic devices," no. v. 41 in Optical engineering (M. Dekker, New York, 1994).
48. M. J. Weber, *Handbook of optical materials* (CRC Press, Boca Raton, 2003). OCLC: 51281488.
49. J. W. Gooch, *Cauchy's Dispersion Formula* (Springer New York, New York, NY, 2011), p. 125.
50. N. Uchida, "Optical properties of single-crystal paratellurite (te o 2)," Phys. Rev. B **4**(10), 3736–3745 (1971).
51. C. Barta and B. C. Jr., "Physical properties of single crystals of the calomel group (hg2x2)," in *Proc. Symposium on mercury(I) halides, Libice*, (1976), p. p.13.
52. O. Kwon, K. Kim, S.-G. Woo, G.-E. Jang, and B. Cho, "Comparative analysis of hg2br2 and hg2brxcl2-x crystals grown via pvt," Crystals **10**(12), 1096 (2020).
53. S. Valle, "Design and application of high performance acousto-optic tunable filters," Ph.D. thesis, University of Glasgow (2017).
54. J.-S. Kim, S. B. Trivedi, J. Soos, N. Gupta, and W. Palosz, "Growth of hg2cl2 and hg2br2 single crystals by physical vapor transport," J. Cryst. Growth **310**(10), 2457–2463 (2008).

Research Article | Vol. 30, No. 26 / 19 Dec 2022 / Optics Express 47388

Optics EXPRESS

Broadband Wollaston prism with a large output beam separation based on mercurous halides

LUKÁŠ KRAUZ,[1,*] PETR PÁTA,[1] JAN BEDNÁŘ,[1] MILOŠ KLÍMA,[1] AND PETR JANOUT[1,2]

[1]*Department of Radioelectronics, Faculty of Electrical Engineering, Czech Technical University in Prague, Technická 2, 166 27 Prague 6, Czech Republic*
[2]*European Southern Observatory, Karl-Schwarzschild-Straße 2, 85748 Garching bei München, Germany*
[*]*krauzluk@fel.cvut.cz*

Abstract: The paper proposes a Wollaston-type crystal polarizer suitable for broadband operation within the visible spectral band up to the far infrared band based on unique optical materials, mercurous halides (Hg_2X_2). This paper introduces the general characteristics and optical properties of these birefringent tetragonal optical materials, as well as the general description of a Wollaston prism and the process of its parameter optimization. In general, the Wollaston polarizer is constructed from two combined wedge-shaped prisms. The key parameters that affect the properties of the Wollaston polarizer are then the cut angle of these two prisms and the refractive index of the exploited optical cement (immersion) that bonds the prisms together. The optimal prism cut angles and immersion refractive index are investigated to maximize the Wollaston parameters, such as the transmittance of the polarized radiation and the separation angle of the output orthogonally polarized beams. This process is significantly dependent on the characteristics of all selected mercurous halides (Hg_2Cl_2, Hg_2Br_2, Hg_2I_2). The optimal values of the prism cut angle for each material are selected based on the outlined results. In addition, the Wollaston prism behaviour regarding real radiation propagation is modelled in detail via the Zemax optical studio. The presented models aim to aid in the real design and fabrication of a broadband Wollaston polarizer based on mercurous halides.

1. Introduction

Today, many applications in optics and photonics exploit the polarization phenomenon of electromagnetic radiation [1–5]. The simplest way to obtain and operate with polarized radiation is using a standard linear or circular type of polarizer [6]. There are several types of these devices, such as wire-grid, thin-film, or birefringent crystal polarizers, each with its specific usage [7,8]. The thin-film and wire-grid polarizers are not commonly optimized for broadband operation and focus on specific spectral bands. Aiming mainly at the infrared spectral bands, the menu of usable polarizing devices thickens. Although wire grid polarizers are applicable in the TIR (thermal infrared) spectral band from 7 μm to 15 μm, they usually do not offer a superior degree of polarization and are mainly specialized on narrower bands. Therefore, crystal polarizers are most commonly used to achieve a superior degree of polarization for radiation propagation through the polarizer across as wide spectral range as possible. Nevertheless, the usage of such a polarizer is limited by selecting a suitable optical material that can be used for a polarizer fabrication. Among the materials that are used most frequently for polarizer fabrication is standard calcite ($CaCO_3$), with transparency ranging between 0.3 μm and 2.3 μm [9], which covers the VIS (visible), NIR (near-infrared), and SWIR (short-wave infrared) spectral bands. The other frequently commercially used material magnesium fluoride (MgF_2) is transparent in an even wider spectral range of 0.2 μm - 6 μm and additionally covers a MWIR (mid-wave infrared) band [10]. However, there are no commercially used crystal polarizers that would cover VIS-TIR spectral bands and even parts of the FIR (far-infrared) band. Highly promising optical materials

#477544 https://doi.org/10.1364/OE.477544
Journal © 2022 Received 14 Oct 2022; revised 18 Nov 2022; accepted 20 Nov 2022; published 13 Dec 2022

Research Article | Vol. 30, No. 26 / 19 Dec 2022 / Optics Express 47389
Optics EXPRESS

capable of filling this void are mercurous halides (Hg_2X_2), such as calomel (Hg_2Cl_2), kuzminite (Hg_2Br_2), and moschelite (Hg_2I_2) [11]. These materials offer exceptional transparency from 0.35 μm to 40 μm and birefringence up to 1.48.

Several proposals have been made for the use of mercurous halides as polarizers in the past [12,13], but most research focuses on their extraordinary acousto-optical properties and applications [14–22]. For example, [23] analyzed in detail the characteristic of mercurous halides regarding their acousto-optical properties, such as the acousto-optic figure of merit, but their polarizing behaviour important for the polarizer construction has been omitted. Nevertheless, the current problem of mercurous halides is with their complicated growth, polishing treatment, and quality evaluation [24–30]. Moreover, for the successful fabrication of a polarizer based on mercurous halides, a suitable design scheme for precise cutting and polishing of the growth mercurous halide crystal has to be introduced.

In the past years, there has been a short introduction regarding the exploitation of mercurous halide crystalline materials as polarizers [12]. However, detailed analysis and optimization schemes on how the polarizers should be designed have been omitted. Recently, a study on Glan-type polarizer based on mercurous halides was proposed. [13]. The authors investigated their own design of a Glan-type polarizer, but mainly for kuzminite and primarily with a focus on the acceptance angles. Reviewing these studies up to the present, a detailed design and construction study focusing on a standard Wollaston polarizer based on mercurous halides has been almost completely omitted.

Contrary to the Glan-type polarizers, the Wollaston polarizer usually needs for its operation a specified optical cement (adhesive immersion) that bonds together the two fundamental Wollaston crystal wedge prisms. Finding a suitable refractive index of immersion, together with a correct cut angle of the wedge prisms, makes analyzing and designing the Wollaston prism more difficult.

In general, Wollaston polarizers find applications in various optical fields, such as polarimetry [31–35], microscopy [36,37], and spectroscopy [38,39]. Taking advantage of a mercurous halide-based Wollaston prism and using it for the mentioned applications may enrich them and extend these fields to a broader spectral range. Specifically, this type of polarizer could be used efficiently for thermal hyperspectral imaging systems [23]. Nevertheless, for all these applications, a precise design of this type of Wollaston polarizer is necessary to optimize its performance in specified spectral bands.

Considering the current state of the mercurous halide-based polarizers described above, this paper presents an analysis and proposes design parameters for the mercurous halide-based Wollaston prism with the aim of maximizing the transmittance and the output beam separation angle over as wide spectral range as possible. For this analysis, a high focus is given to the maximal exploitation of the unique material properties of mercurous halides. Suitable cut angles of the Wollaston wedge prisms and a convenient refractive index of the necessary optical cement are proposed and selected. The analysis is performed separately for all mercurous halides, calomel, kuzminite, and moschelite. Following the cut angle and immersion selection, a ray-tracing of the mercurous halide Wollaston prism based on the Zemax optic studio is performed.

The paper is structured into five main sections. The introduction is followed by the general characterization of mercurous halides in Section 2. A detailed description of the optimized Wollaston parameters is presented in Section 3. Section 4 presents the analysis and ray-tracing results and provides a subsequent discussion on this topic. The paper is then summarized in conclusion Section 5.

2. Mercurous halide characteristics

Fundamentally, mercurous halides are ranked among tetragonal uniaxial anisotropic crystals. To evaluate the optical polarization behaviour of these materials, it is convenient to describe how they affect the electric field of electromagnetic radiation. In general, the electric field in any

Optics EXPRESS

linear dielectric anisotropic material can be expressed [6] as

$$\mathbf{E} = \boldsymbol{\epsilon}^{-1}\mathbf{D}, \tag{1}$$

where $\mathbf{D}$ is a vector of electrical induction, $\mathbf{E}$ represents a vector of electrical intensity, and $\boldsymbol{\epsilon}^{-1}$ is a tensor of electrical impermeability. Thus, the dielectric properties of the material are fully described by the impermeability tensor. For an anisotropic material with a certain symmetry in a principal coordinate system xyz, Eq. (1) can be rewritten as

$$\begin{pmatrix} E_x \\ E_y \\ E_z \end{pmatrix} = \begin{pmatrix} 1/n_1^2 & 0 & 0 \\ 0 & 1/n_2^2 & 0 \\ 0 & 0 & 1/n_3^2 \end{pmatrix} \begin{pmatrix} D_x \\ D_y \\ D_z \end{pmatrix}. \tag{2}$$

where $1/n_1^2$, $1/n_2^2$, $1/n_3^2$ denote the main values of the impermeability tensor. This tensor can then be represented in the xyz-coordinate system as an index ellipsoid by equation

$$\frac{x^2}{n_1^2} + \frac{y^2}{n_2^2} + \frac{z^2}{n_3^2} = 1, \tag{3}$$

where n_1, n_2, n_3 are the refractive indices of a particular anisotropic crystal. Since mercurous halides are uniaxial optical crystals, the refractive indices follow the conditions $n_1 = n_2 = n_\mathrm{o}$ and $n_3 = n_\mathrm{e}$, where n_o and n_e are ordinary and extraordinary refractive indices. The example of an index ellipsoid for the calomel crystal as a representative member of the mercurous halide family can be illustrated by Fig. 1.

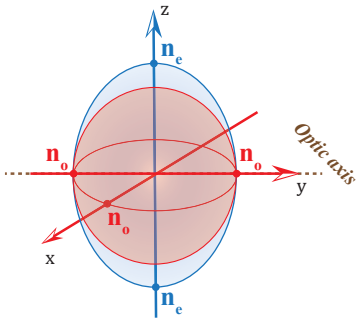

Fig. 1. Index ellipsoid of uniaxial mercurous halide (calomel).

The undeniable advantage of mercurous halides is their high positive birefringence. At a wavelength 0.633 μm the ordinary and extraordinary refractive indices of calomel reach values equal to $n_\mathrm{o} = 1.96$, $n_\mathrm{e} = 2.61$. Furthermore, the refractive indices of kuzminite and moschelite reach values $n_\mathrm{o} = 2.12$, $n_\mathrm{e} = 2.98$ and $n_\mathrm{o} = 2.43$ $n_\mathrm{e} = 3.88$ at the same wavelength, respectively. Assuming the mentioned values of the refractive indices, the birefringence Δn dependent on the wavelength (λ) can be expressed as

$$\Delta n(\lambda) = |n_\mathrm{e}(\lambda) - n_\mathrm{o}(\lambda)|. \tag{4}$$

The values of the ordinary and extraordinary refractive indices are estimated from Cauchy's dispersion formula [40] written as

$$n(\lambda) = A + \frac{B}{\lambda^2} + \frac{C}{\lambda^4} + \frac{D}{\lambda^6} + \dots, \tag{5}$$

Research Article | Vol. 30, No. 26 / 19 Dec 2022 / Optics Express 47391
Optics EXPRESS

where the coefficients A, B, C, D (adopted from [23]) are unified in Table 1. Thus, the birefringence spectra of mercurous halides in the range 0.4 – 12 μm can be seen in Fig. 2.

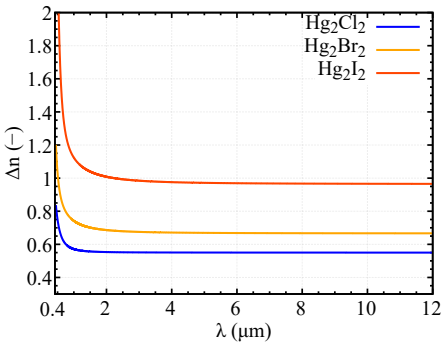

Fig. 2. Birefringence Δn of mercurous halides versus wavelength λ.

Table 1. The coefficients used in Cauchy's dispersion formula for the estimation of the refractive indices of mercurous halides. The measured refractive indices exploited for coefficient estimation were obtained from [11].

	Hg_2Cl_2		Hg_2Br_2		Hg_2I_2	
	n_o	n_e	n_o	n_e	n_o	n_e
A	2.033	2.699	2.264	3.228	1.898	2.448
B	0.040	0.124	0.069	0.259	0.024	0.035
C	−0.004	−0.015	−0.009	−0.063	0.0004	0.0108
D	0.001	0.004	0.003	0.027	0.0001	−0.0001

For the polarizer construction, another key parameter is the transparency range. The transparency range for calomel covers a spectral band from 0.35 μm up to 20 μm. The range for kuzminite and moschelite is even wider, from 0.4 μm up to 30 μm and from 0.45 μm to 40 μm, respectively [9]. This allows to exploit these materials in a highly broadband spectral region. However, design optimization of this wide-band polarizer would be significantly more complicated than for some specified narrow spectral bands. There are other parameters that are crucial for the exploitation of mercurous halides as materials for optical devices. These materials are very soft (hardness 1.5-2 according to the Mohs scale) and therefore problematic for polishing. Some other selected properties of mercurous halides, such as density or band gap, are summarized in Table 2.

Table 2. General properties of mercurous halides [9,41].

Materials / properties	Hg_2Cl_2	Hg_2Br_2	Hg_2I_2
Density (g/cm^3)	7.190	7.307	7.70
Hardness (Mohs)	1.5	1.5	1 - 2
Transparency range (μm)	0.35–20	0.40 – 30	0.45 – 40
Birefringence (-), λ = 0.633 μm	0.66	0.86	1.48
Band gap (eV)	3.9	2.6	2.4

Optics EXPRESS

Furthermore, due to the mentioned high birefringence (0.66, 0.86, 1.48 at 0.633 μm), the transmission losses of radiation incident on a mercurous halide material are significant. The explanation is illustrated by Fig. 3. Let us assume radiation with wavelength 10.6 μm and the optic axis orientation of the mercurous halide crystal as in Fig. 3(a). The refractive index of the material, as well as the refractive angle and the transmittance, can be calculated based on the incidence angle θ_i on the surface of the air / mercurous halide (see Figs. 3(b)–(d). This simulated behaviour is based on standard Fresnel equations [6] and Snell's law, incorporating the optical parameters of mercurous halides. All presented simulations of the mercurous halide characteristics may then be further exploited for the Wollaston modelling. Knowing the behaviour of the extraordinary refractive index in dependence on the incident angle (Fig. 3(b)), the parameters of both ordinary and extraordinary rays can be obtained. The refractive deviation of the beams can also be obtained 3(c)). The symmetrical shape of the curves in Fig. 3(c) also suggested all possible incident angle exploitation in the whole field of view. The symmetrical shape of the curves is also related to the symmetry of the crystalline materials. Moreover, focusing on transmittance maximization, Brewster's angle for the ordinary beam around the incident angles ±60° for all materials at the

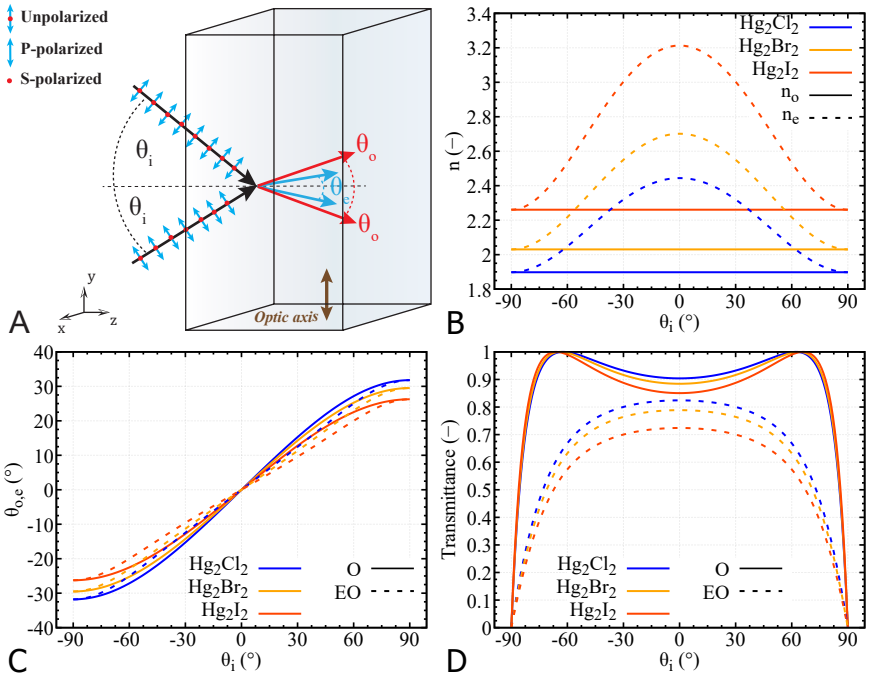

Fig. 3. Optical behaviour at the interface of air/mercurous halides (Fig. A). At this interface, the unpolarized incident radiation refracts as ordinary (S-polarized) and extraordinary (P-polarized) rays with different refractive indices and refraction angles. Fig. B shows the change in the refractive index n against the incident angle of the radiation θ_i. Figure C describes the angle of refraction $\theta_{o,e}$ versus the θ_i. Fig. D shows the transmittance against the θ_i. In all graphs, the straight lines correspond to the behaviour of the ordinary ray. Complementarily, the dashed lines correspond to the behaviour of the extraordinary ray. The symbols n_o and n_e represent the ordinary and extraordinary refractive index of mercurous halides.

Research Article | Vol. 30, No. 26 / 19 Dec 2022 / Optics Express 47393
Optics EXPRESS

presented wavelength can also be obtained, as well as the minimal transmittance difference at the normal incidence (Fig. 3(d)).

In order to obtain the characterization of the Wollaston prism based on mercurous halides, the equations used for the above modelling are described and derived in more detail in the following section concerning the Wollaston prism characterization.

3. Wollaston prism parameters

In general, a Wollaston polarizer is constructed from two combined prisms. These two prisms are usually bonded together by suitable optical cement (immersion). Therefore, the transmitted radiation incident at the input facet of the polarizer undergoes several refractions and splits into two orthogonal highly polarized beams at the output of the polarizer separated by a particular angle. The standard scheme of the Wollaston polarizer with highlighted optical axes and cut angle of the wedge prisms is shown in Fig. 4.

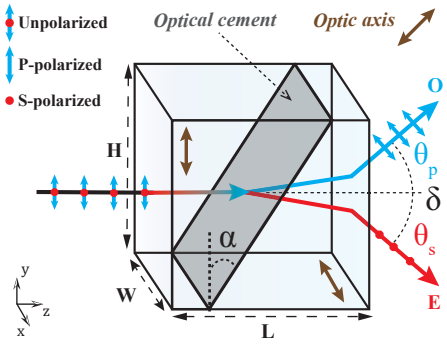

Fig. 4. Wollaston scheme and illustration of unpolarized radiation propagation through it. The symbols L (length), W (width), and H (height) are the sizes of the Wollaston cube. α represents the cut angle of the wedge prisms, and δ corresponds to the output beam separation angle. θ_p is the refracted output angle of the P-polarized radiation and θ_s is the refracted output angle of the S-polarized radiation. The brown double arrow symbol indicates the orientation of the optic axis of each of the prisms.

The Wollaston polarizer can be evaluated according to several parameters. Many of these parameters, such as wavelength range or extinction ratio, depend on the properties and purity of the used optical crystalline material (substrate). Other parameters, such as clear aperture or field of view, are highly dependent on the size of the manufactured polarizer. Apart from the size and mentioned material properties, there are other key optimization parameters of the Wollaston polarizer that affect its polarizing behaviour, beam propagation, beam separation, and power transmission. Suppose ideally polished crystals with properly selected optical axes of each wedge prism. The two crucial parameters are the cut angle α of the wedge and the refractive index of the selected optical immersion n_{oc} that bonds the wedges together. The optimization of the mentioned parameters for the Wollaston scheme based on mercurous halides is described in the following paragraphs.

Let us assume transmitted unpolarized radiation through the Wollaston polarizer. This radiation consists of two orthogonally polarized rays, annotated as the S-polarized beam and the P-polarized beam. The S-polarized beam corresponds to the beam perpendicular to the incident surface of the Wollaston prism facet. The P-polarized beam is a beam parallel to the incident surface of the Wollaston prism facet. The orientation of the optic axis of each wedge prism is crucial. For the first wedge of the Wollaston polarizer, the optic axis is standardly oriented in parallel with the

Optics EXPRESS

plane of incidence and the input facet. The optic axis of the latter wedge is then perpendicular to the optic axis of the first one. This orientation decides which of the input polarizations corresponds to the ordinary or extraordinary ray transmitted through each wedge.

Since mercurous halides are optical materials with positive birefringence, the S-polarized ray transmits through the first wedge as an ordinary ray with an ordinary refractive index. Complementarily, the P-polarized ray behaves as an extraordinary ray with an extraordinary index of refraction. During transmission through the second wedge of the Wollaston polarizer, the roles of orthogonal polarizations exchange. Therefore, the S-polarized beam behaves as the extraordinary ray with the extraordinary refractive index, and the P-polarized beam is the ordinary ray with the ordinary index of refraction. The expected propagation of polarized radiation through the Wollaston polarizer is also indicated in Fig. 4. In general, the ordinary index of refraction is the same in all directions of propagation of the ordinary beam. However, the extraordinary refractive index depends on the crystal orientation and the angle of incidence of the extraordinary beam. Thus, the extraordinary index of refraction can be recovered from the expression

$$n_{\mathrm{e}}(\theta) = \sqrt{(n_{\mathrm{e}} \cos\theta)^2 + (n_{\mathrm{o}} \sin\theta)^2}, \tag{6}$$

where θ is the angle from the optic axis and the traveling extraordinary beam. The beam-directional determination of the extraordinary refractive index is important for ray-tracing and transmission or loss evaluation. Suppose still the unpolarized input radiation propagating through the Wollaston polarizer. Then, at each interface of the Wollaston prism, the well-known Fresnel coefficients [6], used for the determination of transmission and reflection, can be calculated as follows:

$$t_{\mathrm{s}} = \frac{2n_{\mathrm{in}} \cos\theta_{\mathrm{in}}}{n_{\mathrm{in}} \cos\theta_{\mathrm{in}} + n_{\mathrm{out}} \cos\theta_{\mathrm{out}}}, \tag{7}$$

$$t_{\mathrm{p}} = \frac{2n_{\mathrm{out}} \cos\theta_{\mathrm{out}}}{n_{\mathrm{out}} \cos\theta_{\mathrm{out}} + n_{\mathrm{in}} \cos\theta_{\mathrm{in}}}, \tag{8}$$

$$r_{\mathrm{s}} = \frac{n_{\mathrm{in}} \cos\theta_{\mathrm{in}} - n_{\mathrm{out}} \cos\theta_{\mathrm{out}}}{n_{\mathrm{in}} \cos\theta_{\mathrm{in}} + n_{\mathrm{out}} \cos\theta_{\mathrm{out}}}, \tag{9}$$

$$r_{\mathrm{p}} = \frac{n_{\mathrm{out}} \cos\theta_{\mathrm{out}} - n_{\mathrm{in}} \cos\theta_{\mathrm{in}}}{n_{\mathrm{out}} \cos\theta_{\mathrm{out}} + n_{\mathrm{in}} \cos\theta_{\mathrm{in}}}, \tag{10}$$

where t_{s}, t_{p}, r_{s}, and r_{p} are transmission and refraction coefficients for S- and P-polarized radiation at a particular surface interface, respectively. The symbols n_{in} and n_{out} correspond to the input and output refractive indices at the particular dielectric interface. Similarly, θ_{in} and θ_{out} are the angles of incident and output radiation at the particular dielectric interface, respectively.

The values of the input and output refractive indices n_{in} and n_{out} in the above equations depend on whether the S- or P-polarized light propagates through the birefringent material as an ordinary or extraordinary wave. They also depend on the refractive index of the initial dielectric (usually air) and on the refractive index of a particular optical cement that bonds the polarizer wedges together. Moreover, the refraction and propagation of the S- and P-polarized radiation also depend on the selected crystal wedge cut angle α. This angle significantly affects the refraction angles between the output and input interfaces of the first and second Wollaston wedge prisms. Suppose that i is the index of the dielectric interfaces through which unpolarized radiation is transmitted. The overall transmittance [42] for each orthogonal polarization T_{s} and T_{p} can then

Research Article | Vol. 30, No. 26 / 19 Dec 2022 / Optics Express 47395
Optics EXPRESS

be determined as

$$T_s = \prod_i T_s(i), \quad T_p = \prod_i T_p(i), \tag{11}$$

where

$$T_s(i) = t_s^2(i)\frac{n_{out}(i)\cos\theta_{out}(i)}{n_{in}(i)\cos\theta_{in}(i)}, \quad T_p(i) = t_p^2(i)\frac{n_{out}(i)\cos\theta_{out}(i)}{n_{in}(i)\cos\theta_{in}(i)}. \tag{12}$$

The total reflected radiation for each orthogonal polarization R_s and R_p can be calculated from

$$R_s = \prod_i R_s(i), \quad R_p = \prod_i R_p(i), \tag{13}$$

where

$$R_s(i) = r_s^2(i), \quad R_p(i) = r_p^2(i). \tag{14}$$

For the standard Wollaston polarizer, the number of dielectric interfaces that should be evaluated corresponds to $i = 1, \ldots, 4$. At the last interface $i = 4$ the important parameter for evaluating the Wollaston design is the separation angle δ, which describes the output separation between the S- and P-polarized beams. This angle can be denoted as

$$\delta = |\theta_s - \theta_p|, \tag{15}$$

where θ_s corresponds to the refracted output angle of the S-polarized radiation at the output surface of the Wollaston prism and θ_p is the refracted output angle of the P-polarized radiation at the output surface of the Wollaston prism. However, due to the dispersion of the refractive index in the transparency range of mercurous halides, key parameters such as transmittances T_s, T_p, and polarization separation output angle δ also change with the wavelength of input radiation.

4. Parameter analysis and discussion

The previous section introduced the main maximization parameters of the Wollaston prism, such as the total energy transmission and the output beam separation angle. These parameters highly depend on the main optimization attributes, such as the prism wedge cut angle α and the optical cement refractive index n_{oc} that have also been mentioned above. As mentioned, the overall construction sizes (length, width, height) of the Wollaston wedge prisms are also important but do not affect the total transmission and the output beam separation. In general, the process of growth and polishing of the mercurous halide crystals is complex and problematic. Currently, for the calomel prisms, the size of the crystal bowls is limited [24]. To optimize the Wollaston polarizer based on mercurous halides while taking into account the crystal size limits, a standard cube shape with sizes 10 mm, 10 mm, and 10 mm for length, width, and height, respectively, has been selected. Because the transmittance and the output beam separation change with the input radiation wavelength, the optimization is performed for several selected wavelengths from the VIS to the TIR spectral band. These wavelengths are 0.633 μm, 0.946 μm, 1.152 μm, 0.208 μm, 3.391 μm, 5 μm, 7 μm, and 10.6 μm, and they are selected according to important laser wavelength lines in these bands. In addition, for most optimization processes, the normal incidence of the radiation at the input facet of the polarizer is considered.

In the first place, an optimal selection of the optical cement is necessary for the Wollaston construction. Due to the high birefringence, it is clear that for mercurous halides, the refractive index of the optical cement n_{oc} should also be very high and, ideally, match the refractive index between the ordinary and extraordinary indices of the optical material. Subsequently, it should be compatible with the optical material in terms of its physical and chemical properties. However, there is no exact definition of how exactly the immersion should be selected.

In order to investigate the amount of unpolarized radiation transmission through the Wollaston polarizer at a particular wavelength (e.g. 10.6 μm - CO_2 laser), the transmission may be plotted

Optics EXPRESS

against the refractive index of the optical cement and against the cut angle of the prism wedge (see Fig. 5). Currently, no crystal polarizers are available for this specific wavelength of (10.6 μm) or, more precisely, for the TIR spectral band. Moreover, many applications could benefit from the possible utilization of polarizers operating in the TIR band [23,43–45]. Therefore, the transmission depending on the specific α and n_{oc} is analyzed at the TIR wavelength in the following graphs.

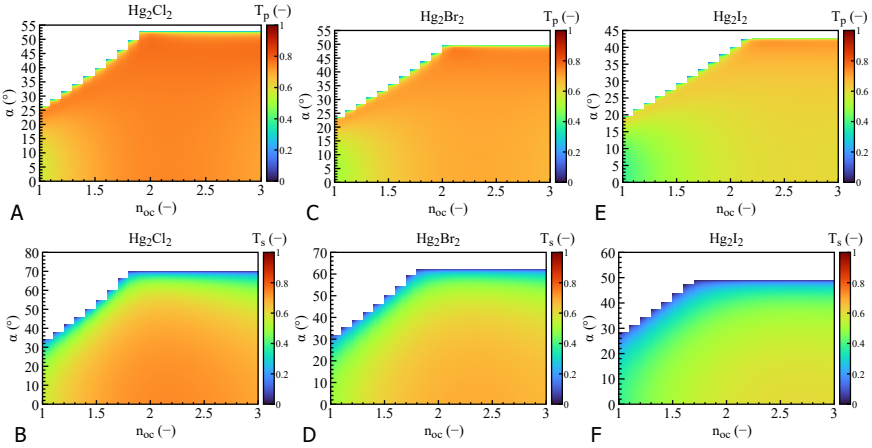

Fig. 5. Transmittance of the Wollaston prism based on mercurous halides for the P-polarized beam T_p and the S-polarized beam T_p against the refractive index of the optical cement n_{oc} and the cut angle α of the Wollaston prism. The wavelength 10.6 μm has been selected for the presented analysis. Figures A, C, and E show the T_p for calomel, kuzminite, and moschelite types of the Wollaston prism, respectively. Similarly, Figures B, D, and F show the T_s for calomel, kuzminite and moschelite types of the Wollaston prism, respectively.

The results in Fig. 5 correspond to the calculated transmittance at the output of the polarizer for S- and P-polarized beams. These results show that only some cut angles of the wedged prism are acceptable, depending on the optical cement refractive index selection. Considering only an air gap between the Wollaston prism wedges, proper functionality of the polarizer is possible for prism cut angles up to 23° for the calomel optical material and up to 22°, 19° for kuzminite and moschelite, respectively. With an increase of the n_{oc} between the Wollaston wedges, the possible prism cut angle increases. The increase of the possible α of the Wollaston prism also maximizes the possible transmittance of the P-polarized beam. Moreover, for a low α, the increase of the n_{oc} could mean an increase of the T_p up to tens of percent. However, as shows Fig. 5, the increase of the T_p is limited up to the specific α. Calomel-based Wollaston prism with a refractive index of optical cement greater than 1.9 can be designed only up to a prism cut angle of 53°. Similarly, the kuzminite-based Wollaston prism with a refractive index of optical cement greater than 2 can be designed up to the α 49° and the moschelite-based Wollaston polarizer with the n_{oc} 2.2 can be designed up to the α equal to 43°. Thus, for cut angles greater than those mentioned, the P-polarized beam experiences a total internal refraction at the output facet of the polarizer and the Wollaston polarizer does not operate properly at the exploited wavelength 10.6 μm.

The transmittance of the S-polarized beam through the Wollaston prism shows a different effect. With an increase in the cut angle α, the S-polarized transmittance decreases. This can also be improved by increasing the refractive index of the optical cement n_{oc}. Similarly, as for the T_p above, assuming a low rigid cut angle of the Wollaston prism, the T_s can then be increased in the order of tens of percent by the increase of the n_{oc}. However, seeing the presented results, a

Research Article | Vol. 30, No. 26 / 19 Dec 2022 / Optics Express 47397
Optics EXPRESS

trade-off must be considered between maximizing the transmission of S- or P- polarized beams for optimizing the Wollaston polarizer based on mercurous halides.

Focusing primarily on the P-polarized output ray and maximization of its transmittance, pairs of the α and the n_{oc} for which the T_p is at maximum can be selected. Complementarily, the maximal possible cut angle with the non-zero T_p can also be selected. The results of combined α and n_{oc} with max. T_p and min. non-zero T_p are shown in Fig. 6. Due to the change of the refractive index of mercurous halides, the optimal cut angle, which maximizes the P-polarized transmission, moves from lower angles to higher ones. Assuming the lowest and the highest wavelength equal to 0.633 μm or 10.6 μm, the overall difference between the prism cut angle for a maximal transmission at these wavelengths is about 3° for calomel, 3° for kuzminite and 5° for moschelite. Simultaneously, aiming for as broadband usage as possible, ideally from the VIS to the TIR spectral band, the ideal refractive index of optical material n_{oc} should be approximately greater or equal to 2, depending on the mercurous halide material. As mentioned, for the n_{oc} higher than 2, the increase of the α does not cause the expected increase of the T_p, due to the physical properties of mercurous halides and their refractive index. As both Fig. 5 and Fig. 6 illustrate, from the n_{oc} around 2 a substantial increase of the α is not possible because the P-polarized beam is then totally reflected at the output facet of the Wollaston polarizer, and the polarizer does not work properly. Moreover, although the cut angles selected according to the IR wavelengths offer higher maximal values of the T_p (see Fig. 5), the possible operational band is narrowing (see Fig. 6). Therefore, to ensure as broadband operation of the polarizer as possible, the Wollaston prism cut angle should be selected according to the lower VIS wavelengths rather than the IR ones.

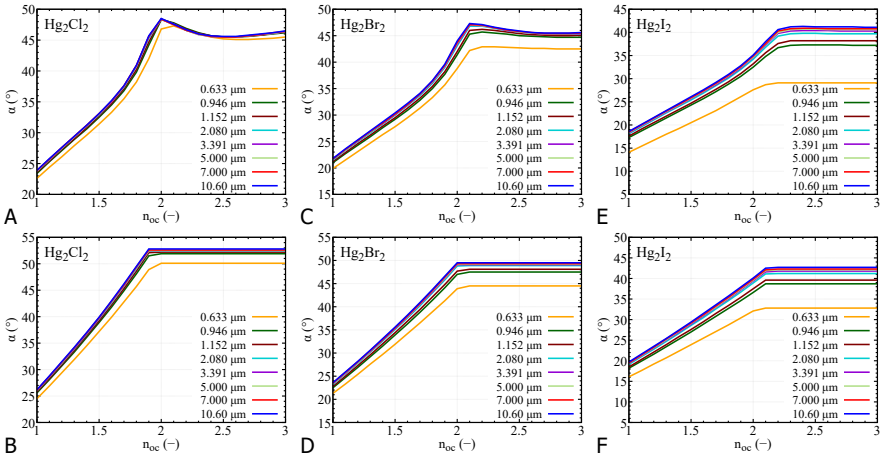

Fig. 6. Figures A, C, and E illustrate the connected maximum transmittance peaks from Fig. 5 for each pair n_{oc} (refractive index of optical cement) and α (cut angle of the Wollaston prism) at selected wavelengths. Figures B, D, and F show the connected maximal possible Wollaston prism cut angle α with the non-zero T_p for mercurous halides.

Variations between the prism cut angle α and the refractive index of optical cement n_{oc} can also be used to calculate the output beam separation angle δ of the Wollaston prism. The results of the output separation angle for the Wollaston prism based on mercurous halides are shown in Figs. 7(a), 7(c), and 7(e). These results are also calculated for an operational wavelength equal to 10.6 μm.

Optics EXPRESS

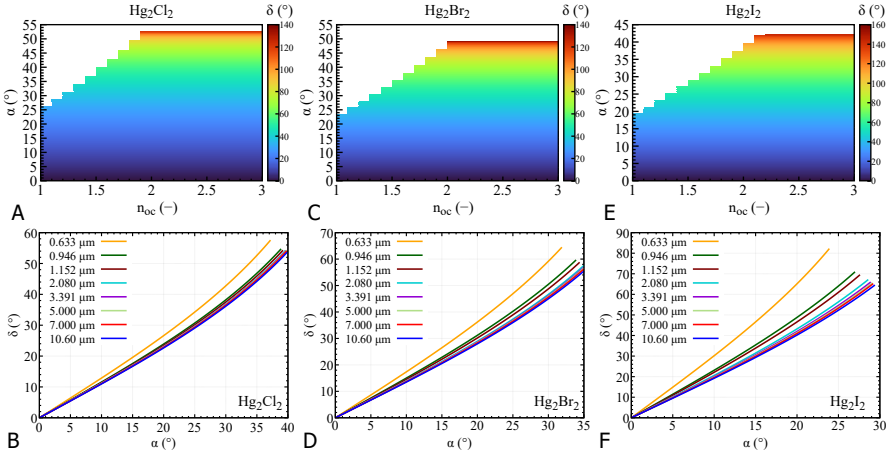

Fig. 7. The value of the output beam separation angle δ for the Wollaston prism based on mercurous halides against the refractive index of the optical cement n_{oc} and the cut angle α of the Wollaston prism for the input radiation wavelength 10.6 μm. Figures A, C, and E show the δ for calomel, kuzminite, and moschelite types of the Wollaston prism, respectively. Figures B, D, and F show only δ versus α at selected wavelengths for calomel, kuzminite and moschelite types of the Wollaston prism, respectively (n_{oc} = 1.5).

Apart from the same non-functional combinations of the α and the n_{oc}, as was shown above in the transmittance results (Fig. 5), it is apparent that the δ increases with the increasing α. Nevertheless, the δ is almost independent on the increase of the n_{oc}. According to the presented results, the Wollaston design based on mercurous halides offers exceptional output beam separation angles because of their high refractive index. Assuming only an air-gap Wollaston design without any optical cement, the separation angle values between orthogonally polarized output beams can reach values up to 35°, 45°, and even 55° for calomel, kuzminite, and moschelite, respectively. Suppose the n_{oc} greater than 2 together with the α greater than 40°. The output separation angle δ can then reach values close to 70°, 80°, and even 110° for calomel, kuzminite, and moschelite, respectively. For an operation in parts of the VIS spectral band, where mercurous halides are still transparent, the values of the beam separation angle may achieve even greater values than 90° for calomel, 120° for kuzminite, and 140° for moschelite. Due to the independence of the n_{oc} increase on the results of the δ, the values of δ can be plotted only against the varying prism cut angle α. This is shown for several wavelengths in Figs. 7(d) – 7(f). The dispersion of mercurous halides mainly causes the changes of the separation angle between the tested wavelengths. The higher the cut angle α of the prism wedge, the more significant the separation angle difference. For VIS and TIR wavelengths and prism cut angle about 30°, the difference may reach values greater than 10°, 15°, and 25° for calomel, kuzminite, and moschelite, respectively.

In general, the problem of current adhesive-based optical cement is that its refractive index usually does not exceed the value of 1.6. According to the results presented above, this refractive index value is not optimal for the mercurous halide-based Wollaston polarizer. Moreover, the next issue may be a possible chemical reaction of mercurous halides with various substances. Assuming a currently available cyanoacrylate-based bonding [46] (compatible with mercurous halides) with a refractive index of approximately 1.5 across the VIS-TIR band, the graphs presented above (especially with respect to transmittance) can be simplified for optimal selection

Research Article | Vol. 30, No. 26 / 19 Dec 2022 / Optics Express 47399
Optics EXPRESS

of the Wollaston prism wedge cut angle α. The results of the Wollaston output transmittance depending on the prism cut angle α are shown in Fig. 8.

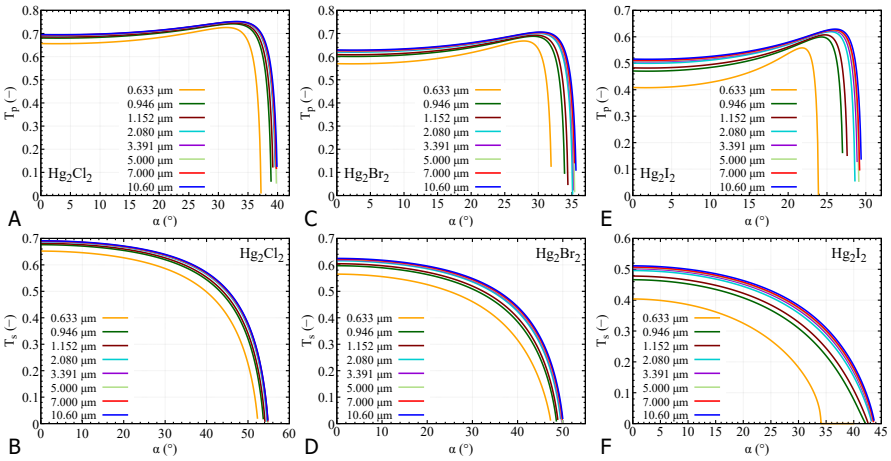

Fig. 8. Transmittance of the Wollaston prism based on mercurous halides for the P-polarized beam T_p and the S-polarized beam T_p against the cut angle α of the Wollaston prism at selected wavelengths. The refractive index of the optical cement n_{oc} has been set equal to 1.5. Figures A, C, and E show the T_p for calomel, kuzminite, and moschelite types of the Wollaston prism, respectively. Similarly, Figures B, D, and F show the T_s for the calomel, kuzminite and moschelite types of the Wollaston prism, respectively.

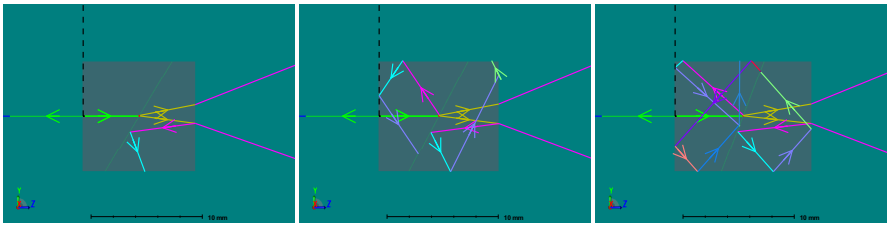

Fig. 9. Zemax ray-racing of the Wollaston prism based on mercurous halides. The ray-racing is performed for reflections and refractions up to 5% of input energy. The ray colour is changed with every reflection or refraction. Input radiation is unpolarized with wavelength 0.633 μm. The normal incidence of the input radiation is used for the models. The dashed-black line represents the orientation of optic axis of the first prism. The left subfigure corresponds to the Wollaston prism based on the calomel optical material with the prism cut angle α_{select} equal to 31°. The middle subfigure corresponds to the Wollaston prism based on the kuzminite optical material with the prism cut angle α_{select} equal to 28°. The right subfigure corresponds to the Wollaston prism based on the moschelite optical material with the prism cut angle α_{select} equal to 21°.

The selection of a suitable cut angle for the Wollaston prism depends on the planned band of operation. As was mentioned, for as broadband operation as possible, the curve for a HeNe laser (0.633 μm) from Fig. 8 can be used. Presented graphs show that the overall P-polarized transmittance does not exceed 0.8 for calomel and is even lower for other mercurous halides.

Optics EXPRESS

Therefore, exploiting an anti-reflex coating would be necessary to minimize losses at the interfaces. Regarding S-polarized transmittance, with an increase in the prism cut angle α, the transmittance decreases, and thus it is necessary to determine how much energy loss is still acceptable. Using the results of Figs. 8(a), 8(c), 8(e), the suitable prism cut angle α_{select} has been selected by the following equations:

$$\alpha_{\max} = \arg\max_{\alpha,\lambda} f(\alpha), \tag{16}$$

$$\alpha_{\text{select}} = \text{sgn}\,(\alpha_{\max})\,\lceil |\alpha_{\max}| - 0.5 \rceil, \tag{17}$$

where λ corresponds to 0.633 μm. Maximization of $f(\alpha)$ and selection of the cut angle is performed according to the maximal transmittance T_{p} of the P-polarized beam. This cut angle is then rounded half toward zero to obtain an integer number. The selected prism cut angles α_{select} then corresponded to 31°, 28° and 21° for calomel, kuzminite, and moschelite, respectively.

After determining the most critical fabrication parameters of a Wollaston prism from the above-presented analysis, the overall ray-tracing and precise modelling can be performed via a Zemax environment (see Fig. 9). The analysis proceeded in both SC (sequential) and NSC (non-sequential) modes of the Zemax environment. For the material description, data from Table 1 and Table 2 have been used. The sizes and parameters selected for the modelled polarizers based on mercurous halides are summarized in Table 3 together with calculated features such as transmittance T_{p}, T_{s}, and output beam separation angle δ. For more illustrative clarity, only one unpolarized direct beam with wavelength 0.633 μm approaching the center of the input polarizer interface has been selected. The ray-tracing process has been monitored for an input power level of the radiation beam equal to 1 W. The rays within the crystal have been tracked up to a power level equal to 0.05 W, up to 100 intersections, or up to 500 segments per ray. According to the presented models, the ideally polished Wollaston prism based on mercurous halides with defined cut angles α should split the unpolarized input beam exactly into two orthogonal polarizations, as expected from the above calculations. The results calculated above are also confirmed by the polarization output pupil graphs shown in Fig. 10. The overall transmittance of P-polarized radiation through the Wollaston prism is close to (considering the interpolations effects of Zemax) the expected 0.73 for calomel and 0.66 or 0.52 for kuzminite and moschelite, respectively. The S-polarized output pupil modelling confirms the same results, where the transmission is close to the expected values of 0.58, 0.5 and 0.33 for calomel, kuzminite, and moschelite, respectively. Significant output beam separation angles are also shown for several wavelengths from 0.633 μm up to 10.6 μm in the footprint diagrams in Fig. 10. Separation angles are for the center of the footprints close to the expected values 44° for calomel, 50° for kuzminite, and 70° for moschelite.

Table 3. Parameters of Zemax-modeled Wollaston polarizers based on mercurous halides

Materials / parameters	Hg_2Cl_2	Hg_2Br_2	Hg_2I_2
Size L × W × H (mm)	10 × 10 × 10	10 × 10 × 10	10 × 10 × 10
α_{select} (°)	31	28	21
n_{oc} (-)	1.5	1.5	1.5
δ (°), λ = 0.633 μm	44	50	70
T_{p} (-), λ = 0.633 μm	0.72	0.66	0.52
T_{s} (-), λ = 0.633 μm	0.58	0.50	0.33

The results of the presented analysis of mercurous halide-based Wollaston polarizer can be compared to the parameters of conventional commercial Wollaston polarizers. The commercial Wollaston polarizes based on the quartz (SiO_2) substrate offer a limited wavelength range from 0.2 μm to 2.3 μm with the output separation angle in order of degrees ($2° - 3°$). Other commercial

Research Article | Vol. 30, No. 26 / 19 Dec 2022 / Optics Express 47401
Optics EXPRESS

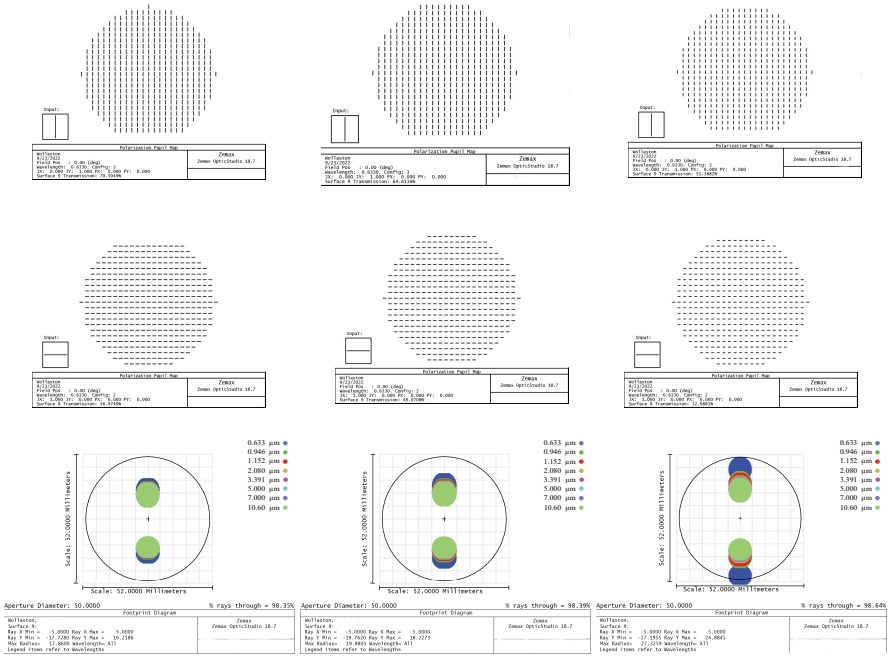

Fig. 10. Polarization pupil maps and footprint diagrams of output polarized beams obtained from the Zemax-modeled Wollaston prisms based on mercurous halides. The first row corresponds to the results of the output polarization pupil of the P-polarized beam. The second row corresponds to the output polarization pupil of the S-polarized beam. The last row corresponds to the output footprint diagram of both polarizations coming out from the Wollaston polarizer. The results of the calomel-based, kuzminite-based, and moschelite-based Wollaston prisms are in the first, second, and third columns, respectively.

polarizers based on calcite ($CaCO_3$), magnesium fluoride (MgF_2), yttrium orthovanadate (YVO_4), and alpha-barium borate (αBaB_2O_4) offer the wavelength range 0.35 µm−2.3 µm, 0.2 µm−6 µm, 0.4 µm − 4 µm, and 0.19 µm − 3.5 µm, respectively. The output separation angles of the Wollaston polarizers based on these materials are (16.7° − 22.5°), (1.7° − 3.1°), (19.6° − 22.3°), and (15° − 27°), respectively. Thus, in terms of wavelength range and output separation angle, the mercurous halide-based Wollaston polarizer offers superior parameters compared to the remaining commercial Wollaston polarizers.

Assessing the presented Zemax models of mercurous halide-based Wollaston, it is clear that the fabricated Wollaston prism with the correct orientation of the optic axes and polishing should be functional as expected for all VIS-TIR wavelengths. Currently, the limiting factor of the polarizer construction is the complicated growth and fabrication of mercurous halide crystals. Some of the recent advances in this field appear to be promising. Currently, calomel crystals are grown to a large enough size and some tests are carried out with them [18,24]. Similarly, there are some advances in kuzminite growth [25,27–30]. Still, the mentioned research appears only as the first stage of real calomel and kuzminite exploitation as photonic devices. Moreover, the growth of moschelite crystals appears to be the most complicated because there is not any recently published research on this topic. Nevertheless, the presented study mainly aimed to show the exceptional properties of mercurous halides and their possible exploitation as polarizing

Optics EXPRESS

devices. After the point of sufficient size and quality of the mercurous halide crystals is reached, the construction of a Wollaston polarizer based on these materials will extend several photonic applications in an infrared spectral band, such as microscopy or hyperspectral imaging.

5. Conclusion

This paper provided analysis and proposed construction parameters of a Wollaston prism based on the mercurous halide (Hg_2X_2) crystals. Due to the exceptional properties of mercurous halides such as calomel (Hg_2Cl_2), kuzminite (Hg_2Br_2), and moschelite (Hg_2I_2), the Wollaston prism based on these materials can operate within a wide spectral range, from VIS to TIR spectral bands. In addition, due to the high birefringence, the Wollaston prism based on mercurous halides offers a high separation angle of the output orthogonally polarized beams. The main Wollaston parameters, such as the transmittance of the polarized beams and their output separation angle, affect two main factors, the cut angle of the Wollaston wedge prism and the refractive index of the used optical cement that bonds them together. This paper provided an analysis on the determination of these factors and the subsequent selection of their optimal values. While assuming a standard refractive index of adhesive bonding used as an optical cement equal to 1.5, the optimal selection of a prism cut angle of a Wollaston polarizer has been determined equal to 31° for calomel, 28° kuzminite, and 21° for moschelite. On the basis of these optimized factors, precise modelling of a Wollaston prism based on mercurous halides has been performed using a Zemax optic studio. The functional operation of such polarizer devices has been confirmed. Thus, the Wollaston polarizer based on mercurous halides may find many applications in photonics setups and devices and additionally also extend the fields of microscopy and hyperspectral imaging in several infrared spectral bands.

Funding. Grant Agency of the Czech Technical University in Prague (SGS20/179/OHK3/3T/13).

Disclosures. "The authors declare no conflicts of interest."

Data availability. Data underlying the results presented in this paper are not publicly available at this time but may be obtained from the authors upon reasonable request.

References

1. J. Hough, "Polarimetry: a powerful diagnostic tool in astronomy," Astron. & Geophys. **47**(3), 3.31–3.35 (2006).
2. C. A. Marques, L. B. Bilro, N. J. Alberto, D. J. Webb, and R. N. Nogueira, "Narrow bandwidth bragg gratings imprinted in polymer optical fibers for different spectral windows," Opt. Commun. **307**, 57–61 (2013).
3. C. A. Marques, L. Bilro, L. Kahn, R. A. Oliveira, D. J. Webb, and R. N. Nogueira, "Acousto-optic effect in microstructured polymer fiber bragg gratings: simulation and experimental overview," J. Lightwave Technol. **31**(10), 1551–1558 (2013).
4. J. C. Ramella-Roman, I. Saytashev, and M. Piccini, "A review of polarization-based imaging technologies for clinical and preclinical applications," J. Opt. **22**(12), 123001 (2020).
5. C. He, H. He, J. Chang, B. Chen, H. Ma, and M. J. Booth, "Polarisation optics for biomedical and clinical applications: a review," Light: Sci. Appl. **10**(1), 194 (2021).
6. B. E. Saleh and M. C. Teich, *Fundamentals of photonics* (john Wiley & sons, 2019).
7. D. H. Goldstein, *Polarized light* (CRC press, 2017).
8. E. Collett, *Field guide to polarization* (Spie Bellingham, WA, 2005).
9. M. J. Weber, *Handbook of optical materials* (CRC Press, Boca Raton, 2003). OCLC: 51281488.
10. R. A. Chipman, W.-S. T. Lam, and G. Young, *Polarized light and optical systems* (CRC press, 2018).
11. B. C. Barta Jr., "Physical properties of single crystals of the calomel group (Hg_2X_2)," in *Proc. Symposium on mercury(I) halides, Libice* (1976), p. 13.
12. Č. Barta and J. Trnka, "New types of polarizers made from crystals of the calomel group," Cryst. Res. Technol. **17**(4), 431–438 (1982).
13. D. L. Porokhovnichenko, E. A. Dyakonov, J. Ryu, and V. I. Balakshy, "Broadband glan-type polarization scheme based on mercury halide crystal," Opt. Eng. **60**(02), 020501 (2021).
14. J.-S. Kim, S. B. Trivedi, J. Soos, N. Gupta, and W. Palosz, "Development of mercurous halide crystals for acousto-optic devices," in *Imaging Spectrometry XII*, vol. 6661 (SPIE, 2007), pp. 94–105.
15. P. Tournois, "Design of acousto–optic programmable filters in mercury halides for mid-infrared laser pulse shaping," Opt. Commun. **281**(15-16), 4054–4056 (2008).

Research Article | Vol. 30, No. 26 / 19 Dec 2022 / Optics Express 47403

Optics EXPRESS

16. R. Maksimenka and P. Tournois, "Mid-infrared high-frequency high-resolution reflective acousto-optic filters in mercury halides," Opt. Commun. **285**(5), 715–719 (2012).
17. N. Gupta, "Materials for imaging acousto-optic tunable filters," in *Image Sensing Technologies: Materials, Devices, Systems, and Applications*, vol. 9100 (SPIE, 2014), pp. 41–50.
18. S. Valle, J. Ward, C. Pannell, and N. Johnson, "Acousto-optic tunable filter for imaging application with high performance in the ir region," in *Optical Components and Materials XII*, vol. 9359 (SPIE, 2015), pp. 65–73.
19. A. Pierson and C. Philippe, "Acousto-optic interaction model with mercury halides (Hg_2Cl_2 and Hg_2Br_2) as aotf cristals," in *International Conference on Space Optics—ICSO 2018*, vol. 11180 (SPIE, 2019), pp. 2196–2206.
20. E. Dyakonov, D. Porokhovnichenko, J. Ryu, and V. Balakshy, "Implementation of the wide-angle acousto-optical interaction geometry in a mercury bromide single crystal," Appl. Opt. **60**(8), 2348–2353 (2021).
21. P. M. Amarasinghe, J.-S. Kim, and S. Trivedi, *et al.*, "Mercurous bromide (Hg_2Br_2) acousto-optic tunable filters (AOTFs) for the long wavelength infrared (LWIR) region," J. Electron. Mater. **50**(10), 5774–5779 (2021).
22. E. Dyakonov and D. Porokhovnichenko, "Spectral-polarization acousto-optical filtering of infrared radiation in a mercury bromide crystal," Bull. Russ. Acad. Sci.: Phys. **86**(1), 66–69 (2022).
23. L. Krauz, P. Páta, J. Bednář, and M. Klíma, "Quasi-collinear ir aotf based on mercurous halide single crystals for spatio-spectral hyperspectral imaging," Opt. Express **29**(9), 12813–12832 (2021).
24. P. Pata, M. Klima, J. Bednar, P. Janout, C. Barta, R. Hasal, L. Maresi, and S. Grabarnik, "Oft sectorization approach to analysis of optical scattering in mercurous chloride single crystals," Opt. Express **23**(16), 21509–21526 (2015).
25. P. M. Amarasinghe, J.-S. Kim, and H. Chen, *et al.*, "Growth of high quality mercurous halide single crystals by physical vapor transport method for aom and radiation detection applications," J. Cryst. Growth **450**, 96–102 (2016).
26. P. M. Amarasinghe, J.-S. Kim, S. Trivedi, S. B. Qadri, E. P. Gorzkowski, G. Imler, J. Soos, N. Gupta, and J. Jensen, "Negative thermal expansion of mercurous halides," J. Electron. Mater. **48**(11), 7063–7067 (2019).
27. T. H. Kim, H. T. Lee, Y.-M. Kang, G.-E. Jang, I. H. Kwon, and B. Cho, "In-depth investigation of Hg_2Br_2 crystal growth and evolution," Materials **12**(24), 4224 (2019).
28. O. Kwon, K. Kim, S.-G. Woo, G.-E. Jang, and B. Cho, "Comparative analysis of Hg_2Br_2 and $Hg_2BrXCl_2 - x$ crystals grown via pvt," Crystals **10**(12), 1096 (2020).
29. L. Liu, R. Li, L. Zhang, P. Zhang, G. Zhang, S. Xia, and X. Tao, "Long wavelength infrared acousto-optic crystal Hg_2Br_2: Growth optimization and photosensitivity investigation," J. Alloys Compd. **874**, 159943 (2021).
30. O. Kwon, Y. Song, S.-G. Woo, W. Park, and B. Cho, "Physical vapor transport process for highly purified Hg_2Br_2 crystal: from powder purification to crystal growth," Korean J. Met. Mater. **60**(7), 551–556 (2022).
31. T. Mu, C. Zhang, C. Jia, and W. Ren, "Static hyperspectral imaging polarimeter for full linear stokes parameters," Opt. Express **20**(16), 18194–18201 (2012).
32. J. D. Perreault, "Triple wollaston-prism complete-stokes imaging polarimeter," Opt. Lett. **38**(19), 3874–3877 (2013).
33. Q. Liu, C. Bai, J. Liu, J. He, and J. Li, "Fourier transform imaging spectropolarimeter using ferroelectric liquid crystals and wollaston interferometer," Opt. Express **25**(17), 19904–19922 (2017).
34. C. A. Díaz, C. A. Marques, M. F. F. Domingues, M. R. Ribeiro, A. Frizera-Neto, M. J. Pontes, P. S. André, and P. F. Antunes, "A cost-effective edge-filter based fbg interrogator using catastrophic fuse effect micro-cavity interferometers," Measurement **124**, 486–493 (2018).
35. W. Ren, J. Ning, Z. Xu, Y. Xie, R. Zhang, and D. Wu, "Coded apertured snapshot spectrapolarimetric imager with a wollaston prism," in *Computational Optical Sensing and Imaging*, (Optical Society of America, 2020), pp. JTh2A–37.
36. A. Doblas, S. Bedoya, and C. Preza, "Wollaston prism-based structured illumination microscope with tunable frequency," Appl. Opt. **58**(7), B1–B8 (2019).
37. Y. Wang, Q. Yang, S. He, R. Wang, and H. Luo, "Computing metasurfaces enabled broad-band vectorial differential interference contrast microscopy," ACS Photonics (2022).
38. A. R. Harvey and D. W. Fletcher-Holmes, "Birefringent fourier-transform imaging spectrometer," Opt. Express **12**(22), 5368–5374 (2004).
39. J. Chamoun and S. Farhadi, "Hyperspectral imaging using a wollaston prism," in *Optics and Photonics for Sensing the Environment*, (Optical Society of America, 2020), pp. EM2C–5.
40. J. W. Gooch, *Cauchy's Dispersion Formula* (Springer New York New York, NY, 2011), pp. 125.
41. C. Bárta and C. Barta Jr., "Physical Properties of Single Crystals of The Calomel Group (Hg_2X_2 : X=Cl, Br)[1]," Mater. Sci. Forum **61**, 93–150 (1991).
42. K. Xu, "Silicon electro-optic micro-modulator fabricated in standard cmos technology as components for all silicon monolithic integrated optoelectronic systems," J. Micromech. Microeng. **31**(5), 054001 (2021).
43. N. Li, Y. Zhao, Q. Pan, and S. G. Kong, "Removal of reflections in lwir image with polarization characteristics," Opt. Express **26**(13), 16488–16504 (2018).
44. N. Li, Y. Zhao, R. Wu, and Q. Pan, "Polarization-guided road detection network for lwir division-of-focal-plane camera," Opt. Lett. **46**(22), 5679–5682 (2021).
45. H. Shi, Y. Liu, C. He, C. Wang, Y. Li, and Y. Zhang, "Analysis of infrared polarization properties of targets with rough surfaces," Opt. Laser Technol. **151**, 108069 (2022).
46. H. Mikuni, "Instant adhesives (cyanoacrylate adhesives)," Three Bond Techn News **2**, 1–10 (1991).

4

SPECTRAL FEATURE EXPLORATION BASED ON IMAGE DATA FROM MULTISPECTRAL AND HYPERSPECTRAL SYSTEMS

This chapter is dedicated to two remaining core publications of the author related to this thesis. Both publications focus on the investigation of the spectral characteristics of various objects of interest from multispectral and later hyperspectral imaging systems. The first publication on this topic:

[A.1] L. Krauz, P. Janout, M. Blažek, and P. Páta, "Assessing Cloud Segmentation in the Chromacity Diagram of All-Sky Images," *Remote Sensing*, vol. 12, no. 11, p. 1902, 2020

published in 2020 in the journal Remote Sensing was focused on the color characteristics behavior of various clouds captured by the ground-based all-sky remote sensing imaging system WILLIAM. Since the system was designed as a standard RGB-based imaging system, the processing of the acquired data was considered multispectral, a precursor to hyperspectral data.

The article presents long-term research on cloud color-based k-means++ segmentation applied to all-sky images. The WMD database containing 2044 daytime images with labeled cloud phenomena has been exploited for such a purpose. The segmentation quality of particular cloud types within two diverse color spaces (CIE L*, a*, b* and CIE XYZ) was assessed. Based on the preselected color spaces and segmented clouds, the color space features of diverse cloud types have been extracted and investigated. The distributions of the color-space cloud features have been plotted into particular 2D coordinate spaces and explored. The diverse cloud types showed promising distribution and cluster forming within these 2D color dimensions. The diversity of different color-space cloud feature distributions has also been objectively assessed via the BC, which utilizes the BD. The obtained results then lead to the possible exploitation

of the whole color-based k-means++ segmentation method as a preprocessing step towards a subsequent cloud classification in all-sky images based on generated cloud color-space features.

Selected approaches of spectral (or color) feature similarity assessment were then used for more complex and different applications: VNIR hyperspectral assessment of dye- and pigment-based ink characteristics and thus possible printed fine art forgeries identification. This topic was the subject of the next article:

[A.3] L. Krauz, P. Páta, and J. Kaiser, "Assessing the Spectral Characteristics of Dye-and Pigment-Based Inkjet Prints by VNIR Hyperspectral Imaging," *Sensors*, vol. 22, no. 2, p. 603, 2022

published in 2022 in the Sensors journal. Since professional long-lasting and fade-resistant pigment prints used for document printing and artwork archiving are very often replaced or counterfeited by cheaper hobby dye-based prints with lower fade resistance and lightfastness, identification of pigment-based originals is critical. However, this task is complicated by the fact that dye-based prints are usually indistinguishable from pigment-based inkjet prints at first glance. Advanced hyperspectral imaging was chosen to solve this problem. The aim of this publication was to show and prove that VNIR HSI is a suitable and simple tool for the identification of dye-based and pigment-based inkjet prints and is able to distinguish between them.

For the purpose of dye- and pigment-based print identification, diverse ink spectral features were extracted from the captured hyperspectral images of test charts printed on the three diverse professional photo papers. These spectral features were then visually and objectively compared via several similarity measures, where some of them were based on the already mentioned Bhattacharyya distance. Subsequently, the projection into a diverse pigment PCA-based coordinate space was exploited to illustrate more thoroughly the differences between the dye- and pigment-based spectral features. The obtained results indicated significant differences between these inks and thus a potential for automatic dye-based inkjet print forgery identification via VNIR HSI. The manuscript also suggests a potential for optical brightener identification and a different perspective for printed fine art inspection.

The manuscripts presented in this chapter relate to the topic of hyperspectral imaging in terms of practical exploration and extraction of spectral or color features extracted from multispectral or hyperspectral image data. It has been shown that these spectral features can then be used for various applications, such as the automatic detection of cloud types or the identification of counterfeit (e.g., dye-based) printed art. Thus, in both articles, appropriate methods for spectral feature exploration were evaluated, and then the real application based on the explored spectral features was proposed.

remote sensing

MDPI

Letter

Assessing Cloud Segmentation in the Chromacity Diagram of All-Sky Images

Lukáš Krauz [1,*], Petr Janout [1], Martin Blažek [2] and Petr Páta [1]

[1] Department of Radioelectronics, Faculty of Electrical Engineering, Czech Technical University in Prague, Technická 2, 166 27 Prague 6, Czech Republic; janoupe3@fel.cvut.cz (P.J.); pata@fel.cvut.cz (P.P.)
[2] Instituto de Astrofísica de Andalucía, CSIC, Glorieta de la Astronomía s/n, 18008 Granada, Spain; alf@iaa.es
* Correspondence: krauzluk@fel.cvut.cz; Tel.: +420-22435-2113

Received: 24 April 2020; Accepted: 9 June 2020; Published: 11 June 2020

Abstract: All-sky imaging systems are currently very popular. They are used in ground-based meteorological stations and as a crucial part of the weather monitors for autonomous robotic telescopes. Data from all-sky imaging cameras provide important information for controlling meteorological stations and telescopes, and they have specific characteristics different from widely-used imaging systems. A particularly promising and useful application of all-sky cameras is for remote sensing of cloud cover. Post-processing of the image data obtained from all-sky imaging cameras for automatic cloud detection and for cloud classification is a very demanding task. Accurate and rapid cloud detection can provide a good way to forecast weather events such as torrential rainfalls. However, the algorithms that are used must be specifically calibrated on data from the all-sky camera in order to set up an automatic cloud detection system. This paper presents an assessment of a modified k-means++ color-based segmentation algorithm specifically adjusted to the WILLIAM (WIde-field aLL-sky Image Analyzing Monitoring system) ground-based remote all-sky imaging system for cloud detection. The segmentation method is assessed in two different color-spaces (L*a*b and XYZ). Moreover, the proposed algorithm is tested on our public WMD database (WILLIAM Meteo Database) of annotated all-sky image data, which was created specifically for testing purposes. The WMD database is available for public use. In this paper, we present a comparison of selected color-spaces and assess their suitability for the cloud color segmentation based on all-sky images. In addition, we investigate the distribution of the segmented cloud phenomena present on the all-sky images based on the color-spaces channels. In the last part of this work, we propose and discuss the possible exploitation of the color-based k-means++ segmentation method as a preprocessing step towards cloud classification in all-sky images.

Keywords: WILLIAM; all-sky images; ground-based; WILLIAM Meteo Database; k-means++; cloud segmentation; cloud detection; cloud classification

1. Introduction

Every day, ground-based all-sky imaging systems generate a great amount of all-sky image data that are suitable for advanced image processing. Using these data, a range of weather phenomena can be detected, analyzed, and classified. In recent years, all-sky image data from ground-based systems have been exploited for various astronomical and weather evaluation purposes. During the daytime, all-sky image data are exploited for cloud observation, for cloud detection, and also for cloud classification. Several approaches have been implemented for cloud detection and cloud classification [1,2], segmentation [3–5] (often color-based segmentation [6]), neural networks [7], and other approaches [8–11]. Cloud color-based segmentation also involves selecting a suitable color-space into which the image data are transformed, followed by evaluations of the accuracy of

the segmentation. Usually, the color-based segmentation approaches select only one of the color channels [12] or color channels affected by the luminance [13–15]. In addition, the mentioned approaches do not study the color representation of different cloud types in different color-spaces.

A promising approach was selected in [16], where the authors investigated simple k-means segmentation applied to narrow field image data transformed into different color-spaces. The results in the referenced paper implied that cloud segments that comprise several cloud types form cluster areas within those color-spaces. Verifying these claims for all-sky image data and evaluating the performance of the proposed color-based k-means++ algorithm could lead to the development of a powerful image processing tool. This tool could be exploited for cloud detection or for cloud classification and could then be used for weather forecasting and even for predicting torrential rainfalls. We, therefore, aim to investigate the classification criteria based on the color features of different cloud types within the selected color-spaces. However, the first fundamental question is: What are the results of the color-based k-means++ segmentation approach applied to all-sky images from the ground-based imaging system? It is therefore important to test the suitability of the algorithm for broad application in all-sky imaging systems. Our study was also aimed at exploiting opportunities provided by the raw all-sky image data generated by our own ground-based all-sky imaging system.

This paper provides an evaluation of the modified daylight k-means++ color-based segmentation method adjusted for all-sky image data from the WILLIAM (WIde-field aLL-sky Image Analyzing Monitoring) system (introduced in [17], see Figure 1) and presents an analysis of the cloud type formations within selected color-spaces. The segmentation accuracy of the evaluated method within selected color-spaces has also been assessed and quantified by several objective metrics. In addition, we discuss the potential of cloud color representation within selected color-spaces for automatic cloud color-based detection and classification. The paper is structured into five main sections. The next section presents the WILLIAM imaging system and the WMD (WILLIAM Meteo database). The section on Methods and Algorithms presents the color segmentation algorithm and its customization for application to our all-sky image data. The last two sections present and discuss the results and draw conclusions.

Figure 1. The WILLIAM all-sky ground-based imaging and monitoring system.

2. The WILLIAM Imaging System

The original idea of the WILLIAM system was to create a completely autonomous ground-based all-sky detecting system, which would monitor the night sky and would detect visible stellar objects and variable stars [18]. We then aimed to evaluate weather conditions in real-time as a support experiment for autonomous robotic telescopes. The WILLIAM system automatically captures image data at 10 min intervals throughout the day by default, but until now, there has been no exploitation of the image data.

Currently, the WILLIAM system operates in Jarošov nad Nežárkou (South Bohemia, Czechia, GPS 49.185°N, 15.072°E). This station is equipped with a NIKON D5100 camera with a CMOS 23.5 × 15.6 mm sensor, which provides a maximal resolution of 3264 × 4928 pixels and 24 bit color depth. An all-sky scenery display with a field-of-view equal to 154° (180° with a Nikon full-frame camera) is provided by a Sigma 10 mm diagonal fish-eye lens. The standard setting for daytime image acquisition is f/2.8, exposure value 1/2000 s, and ISO 100. Images are automatically saved on the remote server in the RAW data format.

The camera with supporting electronics is enclosed in a weather-proof housing box, allowing observation throughout the year, irrespective of the weather conditions. The housing was also tested in the climate chamber.

The WILLIAM system captures a huge amount of image data each year. One set of data has been manually labeled and made available in the WILLIAM Meteo Database (WMD (http://william.multimediatech.cz/meteorology-camera/william-meteo-database/)). WMD contains 2044 daytime images with labeled cloud phenomena. The images have been preselected to cover a variety of conditions during a different daytime and during the year. The clouds in the images have been classified into ten fundamental cloud classes, according to the WMO (World Meteorological Organization [19]) classification. No division into cloud species and varieties has been specified. The cloud cover data for various cloud levels from the ALADIN (Aire Limitée, Adaptation Dynamique, Development International [20]) numerical weather model has also been exploited for the classification. The cloud types have been split into four cloud groups, also according to the WMO cloud level classification system. These cloud groups have been customized for the data from the WILLIAM system. Each cloud group incorporates the clouds with similar characteristics and appearance on all-sky images. The cloud groups, their color labels used in the diagrams, and their qualitative descriptors are listed in Table 1. The WMD contains 492 images with high-level clouds, 833 images with low-level cumuli-type clouds, 793 images with rain clouds, and 1411 images with clear sky. The cloud groups serve as the primary classification categories and are based on the WMO system. The division into the cloud groups also offers minimization of the systematic classification bias. For further consistent color processing results, all RAW all-sky images have been preserved in TIFF format and have been white-balanced to noon-day light of 6000 Kelvin.

Table 1. Used WMO (World Meteorological Organization) cloud classes.

Group No.	Cloud Types	Qualitative Descriptors	Color Labels
1	Cirrus (CIR), Cirrocumulus (CIR-CUM), Cirrostratus (CIR-STR), Altocumulus (ALT-CUM) *	high-level clouds	cyan
2	Cumulus (CUM), Stratocumulus (STR-CUM), Altocumulus (ALT-CUM) Cumulonimbus (CUM-NIMB) **	low-level cumulus type clouds	red
3	Stratus (STR), Altostratus (ALT-STR), Nimbostratus (NIMB-STR), Cumulonimbus (CUM-NIMB)	rain clouds	green
4	Clear Sky	-	blue

* Sparse altocumulus clouds located at a such altitude that are indistinguishable on the image from the high-level clouds; ** Possible cumulonimbus cloud, which is far from the center of the image and is indistinguishable from other cumulus-type clouds.

3. Methods and Algorithms

Let the input all-sky color RGB (Red, Green, Blue) image be represented as a set of slices $I_{RGB}(i, j, c)$, where the indices are used for spatial and color dimensions. Indices $i = 1, \ldots, W$, $j = 1, \ldots, H$, and $c = 1, \ldots, N_c$. Symbols W, H are used for the width and the height of the image. N_c is the number of color channels that are used. Based on the results presented in Blažek [16], we selected the two most suitable color-spaces for cloud segmentation, CIE La*b* [21] and CIE XYZ [22]. These two color-spaces offer the greatest sensitivity in the chromaticity diagram for separating the cloud types

from the blue sky tone. Applying the equations from [23] to the input, I_{RGB} can be transformed into a new color basis as:

$$I_{RGB} \rightarrow I_{XYZ} \tag{1}$$

$$I_{RGB} \rightarrow I_{La^*b^*} \tag{2}$$

The RGB to CIE XYZ transformation can be described as:

$$[X\ Y\ Z] = [R\ G\ B]\, M \tag{3}$$

Assuming the CIE standard illuminant D65, the conversion matrix M [24] may be represented as:

$$M = \begin{bmatrix} 0.4124 & 0.3576 & 0.1805 \\ 0.2126 & 0.7152 & 0.7220 \\ 0.1933 & 0.1192 & 0.9505 \end{bmatrix} \tag{4}$$

To obtain the chromaticity x, y, z values from the CIE XYZ space, the tristimulus X, Y, Z values have to be normalized as:

$$x = \frac{X}{X+Y+Z},\ y = \frac{Y}{X+Y+Z},\ z = \frac{Z}{X+Y+Z} \tag{5}$$

However, $x + y + z = 1$, and therefore, only two chromaticity components are necessary for defining the chrominance. Subsequently, the RGB to CIE La*b* transformation builds on the previous RGB to CIE XYZ transformation and is defined as:

$$L = 116 f\left(\frac{Y}{Y_n} - 16\right), \tag{6}$$

$$a^* = 500\left[f\left(\frac{X}{X_n}\right) - f\left(\frac{Y}{Y_n}\right)\right], \tag{7}$$

$$b^* = 500\left[f\left(\frac{Y}{Y_n}\right) - f\left(\frac{Z}{Z_n}\right)\right], \tag{8}$$

for:

$$f(x) = \begin{cases} x^{\frac{1}{3}} & x \geq 0.008856 \\ 7.787x + \frac{16}{116}, & x \leq 0.008856 \end{cases}, \tag{9}$$

and for $X_n = 95.04$, $Y_n = 100.00$, and $Z_n = 108.88$. For the purpose of this work, a^*, b^*, and x, z are chromaticity channels and L, Y are luminosity channels. The luminosity channels are used only for equalizing the sensor illumination, and they can be omitted for the segmentation method. Reducing the color-space dimension to a set of two independent chromaticity components leads to more effective convergence.

The proposed segmentation method was based on a heuristic approach derived from the modified k-means++ algorithm [25]. The maximum number of different cloud classes in the analyzed image is K_{max}. Typically, the maximum number can be set to $K_{max} \leq 4$ (see Table 1), plus other classes in reserve to cover other disturbing details in the image, e.g., parts of buildings, planes, and other artificial objects. The cost function for the analysis is set to:

$$\Delta_s^{\varrho} = \frac{1}{WHN_c}\sqrt{\sum_{c=2}^{N_c}\sum_{i=1}^{W}\sum_{j=1}^{H} ||\mathrm{I(i,j,c)} - \mu_{s-1}^{\varrho}(c)||^2}, \tag{10}$$

where s is the index of the current iteration and $\varrho = 1, \ldots, K_{max}$ is used for the index of the cloud group. $I(i,j,c)$ are pixels of the image in the CIE L*a*b* (I_{Lab}) and CIE XYZ (I_{XYZ}) representation, and two chromaticity channels were used. The luminosity channel $I(i,j,1)$ was omitted for the cloud groups separation. The aim was to minimize the Euclidean distance of the image pixel color values to the initial centroids $\mu_{s-1}(c)$. The centroids were derived each time in the previous iteration $s-1$. The initial approximation of the centroid position can be set as:

$$\mu_0^{\varrho}(c) = \text{rand}\{\min(I(i,j,c)), \max(I(i,j,c))\} \qquad c = 1,2, \forall i,j. \tag{11}$$

The value of criterion function Δ_s^{ϱ} was calculated in each step. The distance between pixel $I(i,j,c)$ and the center of the cloud centroid is expressed as:

$$D^{\varrho}(i,j) = \frac{1}{N_c}\sqrt{\sum_{c=1}^{N_c}(I(i,j,c) - \mu_{s-1}^{\varrho})^2}. \tag{12}$$

Pixels with the distance-satisfying condition:

$$D^{\varrho}(i,j) \leq \varepsilon\Delta_s^{\varrho} \tag{13}$$

are marked as potentially classified as a single cloud class ϱ. $\varepsilon > 0$ is a sensitivity parameter of the convergence of the method. The segmentation process is completed when each pixel can be distinguished as a single cloud group (see Table 1) in the chromaticity color-space, or when the maximum number of iterations has been taken. The input image can also contain unwanted artificial objects. To remove these areas of the image, a special pixel color mask is applied to the images. These objects can be simply masked out as an additional color cluster.

4. Results and Discussion

Since all of the images have been classified and evaluated, the next step was an investigation of the segmentation accuracy of the proposed method. Two different color-spaces were chosen for the comparison: CIE L*a*b* and the CIE XYZ space.

Figure 2 presents the segmentation of the phenomena in the a^*, b^* color channels. Figure 3 presents a similar segmentation in the x, z channels. Firstly, a visual inspection of the segmentation accuracy was done for all images in the WMD database. In general, the separation of the clouds and the clear sky segments was more precise in the a^*, b^* channels than in the x, z channels. In particular, parts of low-level clouds were frequently separated into one of the produced segments together with a clear sky in the x, z channels (see the light-gray segment in Figure 3). By contrast, the clear sky and the clouds were very precisely separated into stand-alone segments in the a^*, b^* channels. We supported these observations by several segmentation accuracy metrics such as pixel accuracy, the F-score, also known as the Dice coefficient, and IoU (Intersection over Union), also known as the Jaccard coefficient.

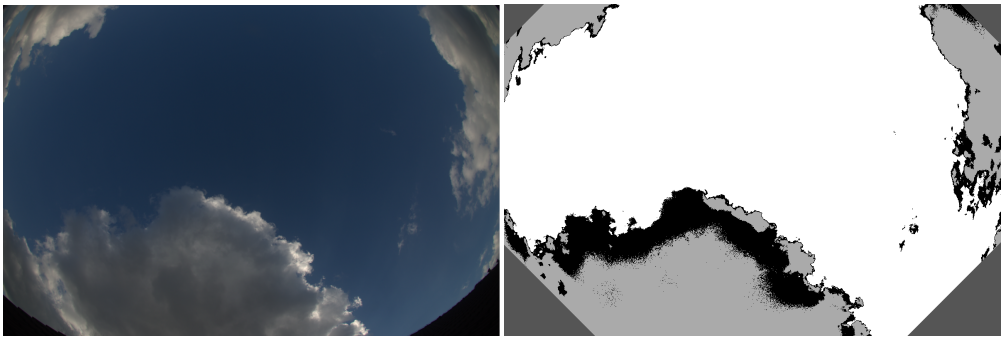

Figure 2. An example of an all-sky image from the WILLIAM system (**left**), showing cumulus-type clouds and the results of k-means++ color-based segmentation (**right**). The image was transformed into a^*, b^* channels and was segmented into four clusters. One cluster represents the masked static objects at the edges of the image. The next white cluster was classified as Clear Sky (Group 4 in Table 1). The remaining black and grey cluster was classified as Cumulus Group 2. The solar zenith angle of the image is 65.31°.

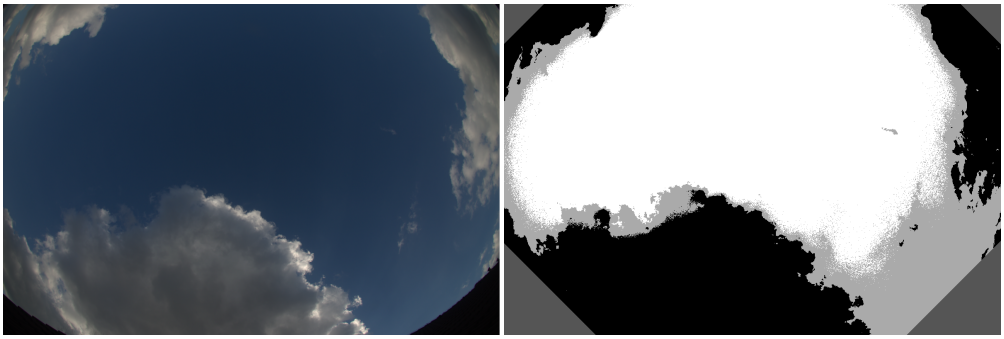

Figure 3. The same example of an all-sky image from the WILLIAM system (**left**) as was presented in Figure 2 and the results of k-means++ color-based segmentation (**right**). The image was transformed into x, z channels and was also segmented into four clusters. In this case, the white and grey clusters were classified as Clear Sky (Group 4), and the one black cluster was classified as Cumulus Group 2. The solar zenith angle of the image is 65.31°.

From the WMD database, there were annotated (classified) cloud groups for each image. In addition, each cloud group had its own, manually labeled, ground truth segments. Ground truth represents pixel areas that contained a particular cloud group or artificial objects and edges in an image. If an image contained several cloud groups, each group in the image had its own ground truth. The artificial objects also had their own ground truth pixel area. The k-means++ method produced several segments. They had to be manually assigned to one of the cloud groups or artificial objects. One cloud group could comprise several generated segments, which were joined together. Subsequently, the pixels within the generated and classified segment could be compared with the pixels of the equally classified ground truth. The number of different ground truth segments in the image was equal to K_{max}. The number of generated and classified segments (pixel areas, which belonged to the cloud groups or artificial objects) had to be also equal to K_{max}. Therefore, the score of each metric for one image had to be calculated separately for K_{max} cases and then averaged over K_{max}. Assume a binary representation, where pixels are either zero if they do not belong to the selected area (segment) or one if they belong to the selected area (segment). Let there be a pixel-wise task, where pixels within a generated segment are evaluated against pixels of a ground truth segment as TP (True Positive),

TN (True Negative), FP (False Positive), and FN (False Negative). For one image, assume K_{max} such pixel-wise tasks. Then, the pixel accuracy metric, F-score, and IoU, respectively, are defined as:

$$\text{Accuracy} = \frac{1}{K_{max}} \sum_{i=1}^{K_{max}} \frac{TP_i + TN_i}{TP_i + TN_i + FP_i + FN_i}\,, \tag{14}$$

$$\text{F-score} = \frac{1}{K_{max}} \sum_{i=1}^{K_{max}} \frac{2 \times TP_i}{2 \times TP_i + FP_i + FN_i}\,, \tag{15}$$

$$\text{IoU} = \frac{1}{K_{max}} \sum_{i=1}^{K_{max}} \frac{TP_i}{TP_i + FP_i + FN_i}\,. \tag{16}$$

Figure 4 presents the results of the metrics for our segmented all-sky images. All three metrics showed higher values and lower variation for the cloud group segmentation in the a^*, b^* color channels than in the x, z color channels. This, therefore, indicated higher segmentation accuracy of the cloud groups within the a^*, b^* channels.

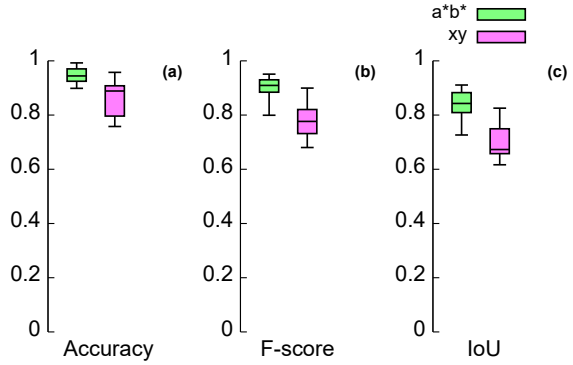

Figure 4. The box-plot diagrams of selected objective metrics. The metrics represent the segmentation accuracy of the segmented cloud groups within the a^*, b^* and x, z color channels against the ground truth. The first diagram (**a**) represents the pixel accuracy metric; the second diagram (**b**) expresses the F-score; the third diagram (**c**) represents the IoU. The whiskers represent extreme values; the top and bottom edges of the boxes indicate the 25th and 75th percentiles; the central line within the boxes corresponds to the median. Values of the metrics are normalized between zero and one.

After the visual inspection combined with the results of the introduced objective metrics, we could conclude that the a^*, b^* color channels were more suitable than the x, z color channels for color-based segmentation of all-sky images. Due to the inaccurate separation in the x, z channels, an additional bias in the color values of the cloud segments was anticipated.

For the investigation of cloud groups color features, it was convenient to extract the color values (features) from the generated segments. Subsequently, the investigation of the distribution of these cloud-segment color features was carried out within the color-spaces that were introduced. The original images were again transformed into the CIE XYZ and CIE La*b* color-spaces. During the previous process of segmentation accuracy evaluation, k-means++ generated segments could be merged and classified as one of the cloud groups. The pixel areas in the again transformed images, which belonged to the classified segments, were extracted. For such segments, the mean values of each color-space channel were calculated. Due to the repeated color transformations, we were also able to extract the luminosity channels Y and L of the cloud group segments. It was possible to compare the features of the cloud-group segments in the chrominance and luminosity channels, even though the luminosity channels were previously omitted from the segmentation process. For the investigation of cloud-segment color features, we exploited the diagrams of the selected color-space channels plotted

against each other (Figures 5–7). To clarify, each data point in the following diagrams represents a segment classified into one of four main cloud groups. For example, Figure 2 represents two segments joined and classified as low-level clouds and one segment of the clear sky. However, due to the inaccurate segmentation, Figure 3 represents one classified segment of low-level clouds and two joined and classified segments of clear sky. The segments of masked out artificial objects were generally omitted from the color evaluation.

In this paper, we present and discuss only those color diagrams with the most promising and most significant results. The most exploited color diagrams that we introduce here mainly show the color components of the CIE L*a*b* color-space. Only to support the exclusion of the CIE XYZ color-space from the cloud-segment color analysis, we also present a color diagram of the x, z components in which the segmentation proceeded. As expected, the previous segmentation inaccuracy significantly influenced the distribution of our segments within the x, z diagram (Figure 5). There was massive overlapping of the cloud segment data points by the clear sky data points (blue). Due to this overlapping distribution, it was not possible to perform any further statistical analysis or to make any other use of the data. In general, we considered that the CIE XYZ color-space was unsuitable for cloud color segmentation of all-sky images.

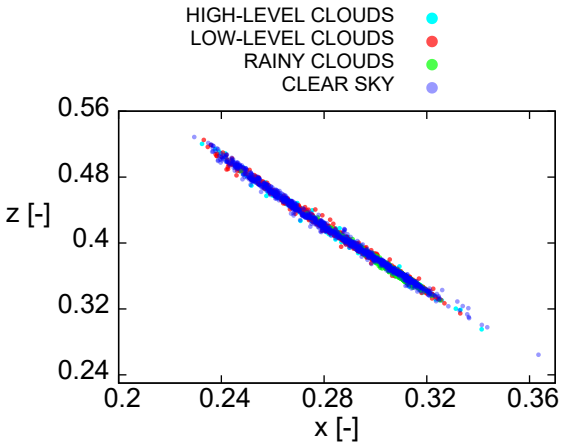

Figure 5. Cloud group color diagram for components x, z obtained from the data in the database. Each point represents the segmented cluster average value classified into four cloud groups.

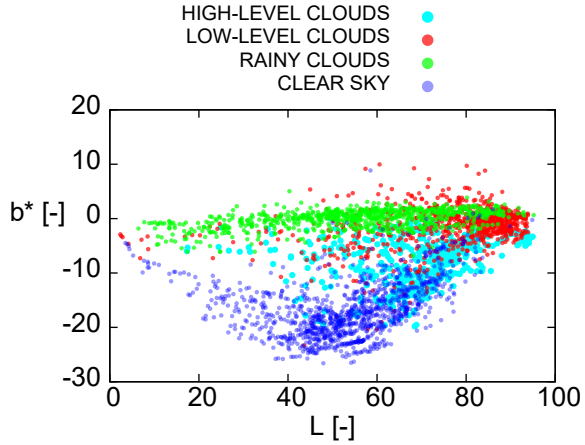

Figure 6. Cloud group color diagram for components L, b^* obtained from the data in the database. Each point represents the segmented cluster average value classified into four cloud groups.

Diagrams L, b^* (Figure 6) and a^*, b^* (Figure 7) offered much more promising data distributions. The inaccurate segmentation and cloud separation in the image data taken close to sunrise or sundown were already observed during the classification process. This inaccuracy was imprinted in the diagrams. Although we segmented the data only in the chrominance channels, the low-light conditions affected the segmentation results. The F-score lower extreme was close to 0.79. This conclusion was confirmed by the L, b^* diagram (Figure 6). The points representing clear sky (blue) with low L values were closer to the points representing rain clouds (green). However, with average light L values, the clear sky points were completely separated from the rainy points. The highly solar irradiated scene also significantly affected the color values of the segments. This could be observed in the L, b^* diagram, in which the points of all groups with L values greater than 80 significantly overlapped each other.

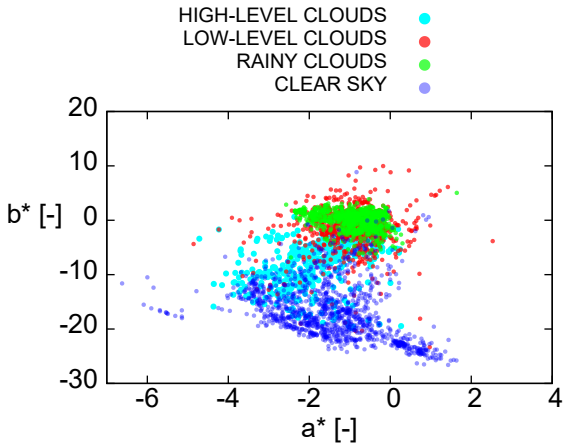

Figure 7. Cloud group color diagram for components a^*, b^* obtained from the data in the database. Each point represents the segmented cluster average value classified into four cloud groups.

Despite the frequent overlapping caused by the significant number of segments and the segmentation bias, however, it was apparent that each of the cloud groups formed a cluster within the diagram. If we evaluated each cloud group separately and computed the mean value with the standard deviation for each group, we obtained the diagram in Figure 8, in which these centroids were clearly separated. The separation between the cloud group data distribution was measured by the Bhattacharyya coefficient [26,27], which approximates the relative closeness between the distributions. BC values are equal to one when two data distribution are identical and equal to zero when two data distributions have no intersection. The Bhattacharyya coefficient (BC) is defined as:

$$BC = 1/\exp\left(BD_{1,2}\right), \tag{17}$$

where $BD_{1,2}$ represents the Bhattacharyya distance between two multivariate distributions with their mean values $\boldsymbol{\mu}_1$, $\boldsymbol{\mu}_2$ and covariance matrices $\boldsymbol{\Sigma}_1$, $\boldsymbol{\Sigma}_2$. The Bhattacharyya distance is expressed as:

$$BD_{1,2} = \frac{1}{8}\left(\boldsymbol{\mu}_1 - \boldsymbol{\mu}_2\right)^{\mathrm{T}}\left(\frac{\boldsymbol{\Sigma}_1 + \boldsymbol{\Sigma}_2}{2}\right)^{-1}\left(\boldsymbol{\mu}_1 - \boldsymbol{\mu}_2\right)\frac{1}{2}\ln\left(\frac{\det\left(\frac{\boldsymbol{\Sigma}_1+\boldsymbol{\Sigma}_2}{2}\right)}{\sqrt{\det\boldsymbol{\Sigma}_1\det\boldsymbol{\Sigma}_2}}\right). \tag{18}$$

Especially, rain cloud (green) and clear sky (blue) segments or low-level cumulus-type clouds (red) and clear sky (blue) segments reported low values of the BC, 0.05 and 0.13, respectively, and therefore, a high separation between them within the L, b^* channels. All values of the BC for the cloud groups within the L, b^* channels are listed in Table 2. The values of BC in the table indicated that the cloud groups' data distributions were non-identical in the L, b^* space. It was, therefore, possible to exploit the

cloud groups in this space as classification classes for a classification task. However, due to the frequent overlapping of some data points, the classification task only in the L, b^* space may be problematic. It was apparent that even if the luminosity was omitted from the segmentation process, the illumination conditions of a taken scene affected the color values of the cloud segments. The color of the cloud groups varied during the day. For future work, it is substantial to incorporate some machine learning techniques into the process of cloud classification development. Additional parameters, which would take into consideration the illumination of the scene and the variation of the cloud color during the day, have to be introduced.

Table 2. The Bhattacharyya coefficient (BC) for the possibility of the cloud groups' separation in L, b* channels. The coefficient is normalized between values of zero and one, supposing the high and low possibility of separation, respectively.

Cloud Group No. and Color Label	1 (Cyan)	2 (Red)	3 (Green)	4 (Blue)
1 (cyan)	1	0.66	0.28	0.56
2 (red)	0.66	1	0.63	0.13
3 (green)	0.28	0.63	1	0.05
4 (blue)	0.56	0.13	0.05	1

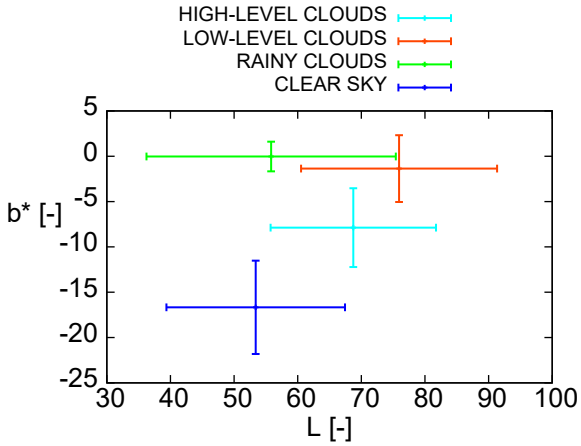

Figure 8. Centroids calculated from data in Figure 6, representing the mean values and the standard deviation for each cloud group.

The next color diagram (Figure 7) of component a^* versus b^* also provided interesting results. In this diagram, the rain cloud segment points (green) had similar color features to those of the low-level cumulus-type clouds (red). This supported similar claims in [16]. Similarly, the high-level clouds (magenta) were also located close to the points of clear sky (blue).

Despite the overlapping of some points, it was apparent that the low-level clouds (red) and the rain clouds (green) formed their own clusters within these channels. These clusters were clearly separated from the high-level clouds and the clear sky points, which formed clusters of their own. We therefore decided to calculate the mean value of these clusters with the standard deviation and to plot these centroids in the new color diagram (Figure 9). The separation of the centroids of the cloud groups confirmed the formation of the cloud-group clusters within the a^*, b^* space. For the inspection of the separation between the cloud groups within the a^*, b^* channels, the Bhattacharyya coefficient was again calculated. The values of the coefficient are listed in Table 3. In the a^*, b^* space, BC also indicated that the cloud group distributions were non-identical. However, rain clouds and low-level

clouds were more closely related in this space (higher BC). It was more problematic to differentiate between them. The differentiation of the cloud groups in this space was still possible, and this space was valuable for the possible classification task. In the future, it would be necessary to incorporate all the cloud color features from the La*b* color-spaces and also an investigation of cloud color variations during the day. In addition, for the cloud types' classification, exploitation of some machine learning techniques, especially the soft-classification methods, would be beneficial.

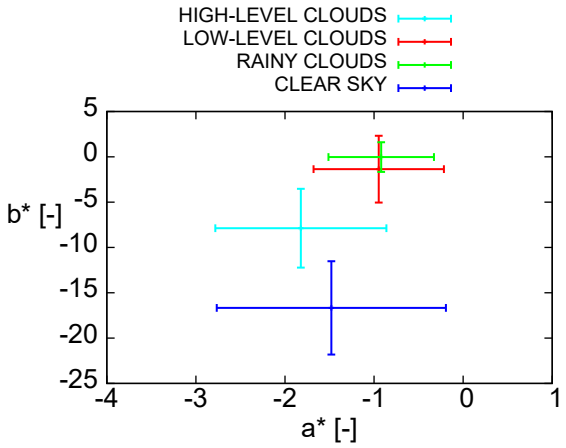

Figure 9. Centroids calculated from the data in Figure 7, representing the mean values and the standard deviation for each cloud group.

Table 3. The Bhattacharyya coefficient (*BC*) for the possibility of cloud groups' separation in a, b* channels. The coefficient is normalized between values of zero and one, supposing the high and low possibility of separation, respectively.

Cloud Group No. and Color Label	1 (Cyan)	2 (Red)	3 (Green)	4 (Blue)
1 (cyan)	1	0.67	0.35	0.58
2 (red)	0.67	1	0.78	0.11
3 (green)	0.35	0.78	1	0.03
4 (blue)	0.58	0.11	0.03	1

In general, the results confirmed that cloud detection on all-sky images could be performed by color segmentation within the CIE L*, a*, b* color-space. In addition, the color diagrams explored the diverse color features of the clouds merged into the defined groups. It was therefore possible to distinguish a variety of clouds on all-sky images according to their color features. Due to the sufficient quantity of the classified data from the WMD database, the cloud color features could be exploited as training data for developing a new automatic cloud classification algorithm. The separation of the cloud groups within the color diagrams implied that a properly designed algorithm, based for example on machine learning techniques or on neural networks, would automatically classify the clouds on all-sky images, after k-means++ preprocessing and after extracting the color-features. This cloud classification algorithm could then be extended for detecting rain clouds or for predicting the probability of rain. The proposed method based on k-means++ and other required image processing techniques could easily be optimized, and the algorithm could even operate in real-time on all-sky imaging systems. Color-based classification of clouds in all-sky images could therefore be a promising field of investigation for research groups with their own ground-based all-sky imaging system.

5. Conclusions

This paper presented an evaluation of the k-means++ cloud color-based segmentation algorithm based on all-sky image data from the WILLIAM ground-based whole sky imaging system. The algorithm was tested on 2044 cloud-classified all-sky images, which had been consolidated into the WMD database.

The evaluation proceeded in two color-spaces, CIE L^*, a^*, b^* and CIE XYZ, the segmentation accuracy of which was compared. For further cloud color analysis, the clouds within the segments were classified into four distinct cloud groups. The color features of these classified segments were also investigated. The overall results indicated that the CIE XYZ color-space was unsuitable for segmentation of all-sky images. However, segmentation in CIE L^*, a^*, b^* offered better accuracy. Suitable objective metrics were used for assessing the segmentation accuracy. In addition, the color values of the cloud-group segments were promisingly distributed and formed their own separate clusters within this color-space. The cluster separation of the rain cloud types was especially important. All-sky image color segmentation and cloud-type color-feature clustering therefore have tremendous potential for the development of color-based cloud detection and classification algorithms. The proposed method based on k-means++ color segmentation of all-sky image data could therefore be exploited in the future for color-based weather and rainfall prediction based on automatic all-sky systems and could be used for further cloud color-based research.

Author Contributions: Conceptualization, L.K. and M.B.; methodology, L.K. and M.B.; software, L.K.; validation, L.K., M.B., and P.P.; formal analysis, L.K.; investigation, L.K. and M.B.; resources, P.J.; data curation, L.K. and P.J.; writing, original draft preparation, L.K. and P.J.; writing, review and editing, L.K., P.J., and P.P.; visualization, L.K. and P.J.; supervision, P.P. and M.B.; project administration, P.J. and M.B.; funding acquisition, P.P. and P.J. All authors have read and agreed to the published version of the manuscript.

Funding: This work was supported by the Grant Agency of the Czech Technical University in Prague, Grant No. SGS20/179/OHK3/3T/13, "Modern Optical Imaging Systems with Non-linear Point Spread Function and Advanced Algorithms for Image Data Processing", and by the Grant Agency of the Czech Republic, Grant No. 20-10907S, "Meteor clusters: An evidence for fragmentation of meteoroids in interplanetary space". Martin Blažek acknowledges funding under Fellowship Number PTA2016-13192-I and financial support from the State Agency for Research of the Spanish MCIUthrough the "Center of Excellence Severo Ochoa" award to the Instituto de Astrofísica de Andalucía (SEV-2017-0709).

Conflicts of Interest: The authors declare no conflict of interest.

References

1. Neshat, M.; Ahmadi, M. Recognising the kind of cloud using a new fuzzy knowledge-based system. *Int. J. Reason. Based Intell. Syst.* **2016**, *8*, 168–180. [CrossRef]
2. Sun, R.; Yu, S.; Zhao, C.; Zhang, W. Algorithms for surveying and cataloguing space debris utilizing a wide field of view telescope. *Publ. Astron. Soc. Jpn.* **2019**, *71*, 67. [CrossRef]
3. Dev, S.; Nautiyal, A.; Lee, Y.H.; Winkler, S. CloudSegNet: A Deep Network for Nychthemeron Cloud Image Segmentation. *IEEE Geosci. Remote Sens. Lett.* **2019**, *16*, 1814–1818. [CrossRef]
4. Liu, S.; Zhang, L.; Zhang, Z.; Wang, C.; Xiao, B. Automatic Cloud Detection for All-Sky Images Using Superpixel Segmentation. *IEEE Geosci. Remote Sens. Lett.* **2015**, *12*, 354–358. [CrossRef]
5. Dev, S.; Savoy, F.M.; Lee, Y.H.; Winkler, S. High-dynamic-range imaging for cloud segmentation. *Atmos. Meas. Tech.* **2018**, *11*, 2041–2049. [CrossRef]
6. Dev, S.; Lee, Y.H.; Winkler, S. Color-Based Segmentation of Sky/Cloud Images From Ground-Based Cameras. *IEEE J. Sel. Top. Appl. Earth Obs. Remote Sens.* **2017**, *10*, 231–242. [CrossRef]
7. Taravat, A.; Del Frate, F.; Cornaro, C.; Vergari, S. Neural Networks and Support Vector Machine Algorithms for Automatic Cloud Classification of Whole-Sky Ground-Based Images. *IEEE Geosci. Remote Sens. Lett.* **2015**, *12*, 666–670. [CrossRef]
8. Ye, L.; Cao, Z.; Xiao, Y.; Yang, Z. Supervised Fine-Grained Cloud Detection and Recognition in Whole-Sky Images. *IEEE Trans. Geosci. Remote Sens.* **2019**, *57*, 7972–7985. [CrossRef]
9. Cheng, H.Y.; Lin, C.L. Cloud detection in all-sky images via multi-scale neighborhood features and multiple supervised learning techniques. *Atmos. Meas. Tech.* **2017**, *10*, 199–208. [CrossRef]

10. Zhuo, W.; Cao, Z.; Xiao, Y. Cloud Classification of Ground-Based Images Using Texture–Structure Features. *J. Atmos. Ocean. Technol.* **2014**, *31*, 79–92. [CrossRef]
11. Oikonomou, S.; Kazantzidis, A.; Economou, G.; Fotopoulos, S. A local binary pattern classification approach for cloud types derived from all-sky imagers. *Int. J. Remote Sens.* **2019**, *40*, 2667–2682. [CrossRef]
12. Dev, S.; Savoy, F.M.; Lee, Y.H.; Winkler, S. Rough-Set-Based Color Channel Selection. *IEEE Geosci. Remote Sens. Lett.* **2017**, *14*, 52–56. [CrossRef]
13. Heinle, A.; Macke, A.; Srivastav, A. Automatic cloud classification of whole sky images. *Atmos. Meas. Tech.* **2010**, *3*, 557–567. [CrossRef]
14. Kazantzidis, A.; Tzoumanikas, P.; Bais, A.F.; Fotopoulos, S.; Economou, G. Cloud detection and classification with the use of whole-sky ground-based images. *Atmos. Res.* **2012**, *113*, 80–88. [CrossRef]
15. Long, C.N.; Sabburg, J.M.; Calbó, J.; Pagès, D. Retrieving Cloud Characteristics from Ground-Based Daytime Color All-Sky Images. *J. Atmos. Ocean. Technol.* **2006**, *23*, 633–652. [CrossRef]
16. Blazek, M.; Pata, P. Colour transformations and K-means segmentation for automatic cloud detection. *Meteorol. Z.* **2015**, *24*, 503–509. [CrossRef]
17. Janout, P.; Blažek, M.; Páta, P. New generation of meteorology cameras. In *Photonics, Devices, and Systems VII*; Fliegel, K., Páta, P., Eds.; International Society for Optics and Photonics, SPIE: Bellingham, WA, USA, 2017; Volume 10603, pp. 312–318. [CrossRef]
18. Janout, P.; Páta, P.; Bednář, J.; Anisimova, E.; Blažek, M.; Skala, P. Stellar objects identification using wide-field camera. In *Photonics, Devices, and Systems VI*; Tománek, P., Senderáková, D., Páta, P., Eds.; SPIE: Bellingham, WA, USA, 2015; Volume 9450, pp. 380–388. [CrossRef]
19. World Meteorological Organization. *International Cloud Atlas*; WMO [publications]; no. 407; Secretariat of the World Meteorological Organization: Geneva, Switzerland, 1975.
20. Wang, Y.; Bellus, M.; Wittmann, C.; Steinheimer, M.; Weidle, F.; Kann, A.; Ivatek-Šahdan, S.; Tian, W.; Ma, X.; Tascu, S.; et al. The Central European limited-area ensemble forecasting system: ALADIN-LAEF. *Q. J. R. Meteorol. Soc.* **2011**, *137*, 483–502. [CrossRef]
21. McLaren, K. XIII-The Development of the CIE 1976 (L* a* b*) Uniform Colour Space and Colour-difference Formula. *J. Soc. Dye. Colour.* **2008**, *92*, 338–341. [CrossRef]
22. Smith, T.; Guild, J. The C.I.E. colorimetric standards and their use. *Trans. Opt. Soc.* **1931**, *33*, 73–134. [CrossRef]
23. Meshta, L.K. *Control of Colour Imaging Systems: Analysis and Design*; CRC Press: Boca Raton, FL, USA, 2009; pp. 628–641.
24. Giorgianni, E.J.; Madden, T.E. *Digital Color Management: Encoding Solutions*; Addison-Wesley Longman Publishing Co., Inc.: Boston, MA, USA, 1998.
25. Arthur, D.; Vassilvitskii, S. K-means++: the advantages of careful seeding. In Proceedings of the 18th Annual ACM-SIAM Symposium on Discrete Algorithms, New Orleans, LA, USA, 7–9 January 2007.
26. Bhattacharyya, A. On a measure of divergence between two statistical populations defined by their probability distributions. *Bull. Calcutta Math. Soc.* **1943**, *35*, 99–109.
27. Koutroumbas, K.; Theodoridis, S. *Pattern Recognition*; Elsevier: Amsterdam, The Netherlands, 2008.

sensors

MDPI

Article

Assessing the Spectral Characteristics of Dye- and Pigment-Based Inkjet Prints by VNIR Hyperspectral Imaging

Lukáš Krauz [1,*], Petr Páta [1] and Jan Kaiser [1,2]

[1] Department of Radioelectronics, Faculty of Electrical Engineering, Czech Technical University in Prague, Technická 2, 166 27 Prague, Czech Republic; pata@fel.cvut.cz (P.P.); kaiser@fomei.com (J.K.)
[2] FOMEI s.r.o., U Libeňského pivovaru 2015, 180 00 Prague, Czech Republic
* Correspondence: krauzluk@fel.cvut.cz; Tel.: +420-22435-2113

Abstract: Fine art photography, paper documents, and other parts of printing that aim to keep value are searching for credible techniques and mediums suitable for long-term archiving purposes. In general, long-lasting pigment-based inks are used for archival print creation. However, they are very often replaced or forged by dye-based inks, with lower fade resistance and, therefore, lower archiving potential. Frequently, the difference between the dye- and pigment-based prints is hard to uncover. Finding a simple tool for countrified identification is, therefore, necessary. This paper assesses the spectral characteristics of dye- and pigment-based ink prints using visible near-infrared (VNIR) hyperspectral imaging. The main aim is to show the spectral differences between these ink prints using a hyperspectral camera and subsequent hyperspectral image processing. Two diverse printers were exploited for comparison, a hobby dye-based EPSON L1800 and a professional pigment-based EPSON SC-P9500. The identical prints created via these printers on three different types of photo paper were recaptured by the hyperspectral camera. The acquired pixel values were studied in terms of spectral characteristics and principal component analysis (PCA). In addition, the obtained spectral differences were quantified by the selected spectral metrics. The possible usage for print forgery detection via VNIR hyperspectral imaging is discussed in the results.

Keywords: hyperspectral imaging; VNIR; inkjet printing; dyes; pigments; photo paper; archiving

Citation: Krauz, L.; Páta, P.; Kaiser, J. Assessing the Spectral Characteristics of Dye- and Pigment-Based Inkjet Prints by VNIR Hyperspectral Imaging . *Sensors* **2022**, *22*, 603. https://doi.org/10.3390/s22020603

Academic Editor: Arturo Sanchez-Azofeifa

Received: 3 December 2021
Accepted: 10 January 2022
Published: 13 January 2022

Publisher's Note: MDPI stays neutral with regard to jurisdictional claims in published maps and institutional affiliations.

1. Introduction

Currently, there is a vast range of scientific and industrial fields where hyperspectral imaging (HSI) finds its usage. Among those fields, plant [1] and soil [2] monitoring, agriculture [3], medicine [4,5], food analysis [6], remote sensing [7], forensics [8–10], or cultural heritage [11] can be counted. In general, HSI can be applied in a variety of spectral bands. There are HSI applications in the short-wave infrared (SWIR) 1–3 μm [12], mid-wave infrared (MWIR) 3–5 μm [13], and long-wave infrared (LWIR) 8–14 μm [14] bands. Nevertheless, the applications of HSI in visible near-infrared (VNIR) 0.3–1 μm spectral band are most frequent [15,16]. Concerning specifically cultural heritage, HSI has found its utilization in historical painting analysis [17–19], art forgery detection [20], and painting restoration [21].

Recently, there has also been a high demand for fine art photography, but also for document printing, which requires a perfect color representation and archiving parameters. This segment of art and document printing is filled by a variety of photo printers fitting the mentioned requirements. Two dominant types of printing techniques are dye and inkjet printing [22]. In general, for art printing and archiving, inkjet printing plays a major role. There are inkjet printers based on two dominant ink approaches, dye-based and pigment-based. However, each type is suitable for different applications. Less expensive dye-based printers find their place among the common customers for hobby printing purposes. On the contrary, pigment-based printers provide a professional printing solution included

in specialized printing labs, and they are suitable particularly for documents, photographs, and fine art printing purposes with the emphasis on archiving [23,24]. Frequently, due to a reduction in costs, pigment-based prints are replaced or forged by dye-based prints that are less suitable for archiving. Despite the significant improvements in the dye-based printing technology, current dye-based prints still reach only a quarter lightfastness and fade resistance compared to pigment-based prints. Moreover, due to the cutting-edge dye-based printing technology and its broader color gamut, a dye-based forged print can be easily mistaken for pigment-based prints and remain unrecognized.

Although both types of ink are used for highly dissimilar purposes, they may be easily interchanged and unidentified by the naked eye, even by professionals. Nevertheless, it is well known that dye- and pigment-based inks are water-based inks, but consist of different technologies of color creation. Therefore, the spectral characteristics may also behave differently, even if the dye- and pigment-based prints appear similar. To assess the spectral characteristics of the dye- and pigment-based inks across the whole print and to identify the origin printer, HSI may become a useful and straightforward tool. There have also been some approaches focused on the color measurement [25] and spectral analysis of dyes [26], pigments [27,28], and ink-printed documents [29]. However, direct spectral comparisons that aim at dye- and pigment-based inkjet print differences have not been performed. There are also other techniques for art analysis and forgery identification such as simple microscopy, mass spectrometry, colorimetry, standard reflectance spectroscopy, chemical analysis, and X-ray methods [30]. However, some of these techniques may not be suitable for inkjet print evaluation. Compared to the mentioned approaches, HSI provides a fast, simple, and non-invasive method for thorough spectral analysis across the whole print, which favors its usage.

This paper focuses on the VNIR HSI assessment of dye- and pigment-based prints, their spectral comparison, and the quantification of their spectral differences. To eliminate the spectral effects of the photo paper, the prints were assessed on three different types of paper. For the assessment, various spectral similarity metrics were used, as well as principal component analysis (PCA) of the hyperspectral (HS) image data. Therefore, the main goal was the verification that VNIR HSI may be used for validation and identification of whether the print is made by a professional and long-lasting pigment-based printer with archive potential or by a hobby dye-based printer.

The paper is structured into five main sections. The Introduction is followed by the section on the color dye- and pigment-based printing and hyperspectral reflectance representation. The following section describes the exploited methods, algorithms, and the HS data acquisition process. The fourth section is focused on the obtained results' presentation and subsequent discussion. The last section provides the overall conclusion.

2. Print Color Management and Hyperspectral Representation

As was mentioned in the Introduction, among the inkjet printers, dye- and pigment-based inks are the two main types of inks used for photograph printing purposes. In general, both ink types fall under the set of water-based or aqueous inks. Dye-based inks are homogeneous color fluids with fully dissoluble dyes. They are usually used in hobby inkjet printers due to their lower manufacturing costs. Dye-based inks also do not provide such lightfastness and fade resistance as pigment-based inks. On the contrary, dye-based inks usually offer a broader color gamut than pigment-based ones, especially on glossy papers. Usually, the dye-based inkjet printers contain six separate inks. Except for the standard cyan, magenta, yellow, black (CMYK) configuration, these printers have two additional colors, light cyan and light magenta.

On the contrary, pigment-based inks consist of microscopic color grains inserted in the sheer liquid. These inks are exploited in professional inkjet printers and labs due to their superb lightfastness. Therefore, pigment-based inks are often used for fine art printing purposes, photo archiving, and large format photography. Typically, the pigment-based printers include nine different inks, but very often, there are several more inks included.

High-level pigment-based printers standardly contain a 12-ink set. Two types of black inks (selected according to the print purpose) are appended by cyan, light cyan, yellow, vivid magenta, vivid light magenta, violet, orange, green, grey, and light grey.

Not only the different characteristics of the presented inks and printers, but also the type of photo paper may play a significant role in the printed photograph's lightfastness and appearance. There are several types of photo paper suitable for various applications with matte, semiglossy, or glossy surfaces. They may also be created from a variety of materials, such as standard resin-coated (RC) paper, cotton paper, baryte paper, and others.

All the influences mentioned above affect the final parameters of photograph prints. Although the dye- and pigment-based colors in the printed photograph may appear similar, their spectral characteristics may significantly vary. Measuring the simple spectral signature of a single spatial point of the print, standard spectroscopy techniques can be used. However, aiming for a more complex ink spectral analysis across the whole printed image, the hyperspectral imaging tool can be exploited. Assume a printed photograph, either dye- or pigment-based, subjected to a source of radiation. Such radiation then may be absorbed, transmitted, or reflected from the photograph. For the spectral measurement, the amount of reflected light captured by the HS camera is the most critical parameter. Let an illumination with defined spectral characteristics $\phi_i(\lambda)$ be described as incident flux on the object, where λ represents the spectral wavelength. Similarly, assume a flux reflected from the object defined as $\phi_r(\lambda)$. The reflectance then may be expressed as:

$$R(\lambda) = \frac{\phi_r(\lambda)}{\phi_i(\lambda)}. \tag{1}$$

This process is represented by Figure 1. For simplicity, the specular reflection with particular angle θ is assumed. In the case of the the HS measurement of the photo-printed inks, the overall photo reflectance $R(\lambda)$ consists of the characteristics of the underlay paper $R_{paper}(\lambda)$, as well as single or mixed printer color inks $R_{ink}(\lambda, c)$, where c represents the color mixture index. In a simplified way, the reflected light flux $\phi_r(\lambda)$ consists of two parts. The first one:

$$\phi'_r(\lambda) = \phi_i(\lambda) \cdot R_{ink}(\lambda, c) \tag{2}$$

is the directly reflected light flux from the ink layer. The second one:

$$\phi''_r(\lambda) = \phi_i(\lambda) \cdot R_{paper}(\lambda) \cdot T^2_{ink}(\lambda, c) \tag{3}$$

is the part of the flux reflected from the surface of the photo paper after propagation through the ink layer, where $T^2_{ink}(\lambda, c)$ is the transmission of the ink mixture layer. The overall reflected flux is:

$$\phi_r(\lambda) = \phi_i(\lambda) \cdot \Big[R_{paper}(\lambda) \cdot T^2_{ink}(\lambda, c) + R_{ink}(\lambda, c)\Big]. \tag{4}$$

Therefore, the reflectance of the printed image should be represented as:

$$R(\lambda) = R_{paper}(\lambda) \cdot T^2_{ink}(\lambda, c) + R_{ink}(\lambda, c). \tag{5}$$

With the exploitation of the HS camera, the additional two spatial x_s, y_s dimensions may be also added to the above-described spectral measurement. The reflected light from the object $\phi_r(\lambda)$ with the spatial coordinates x_s, y_s may be acquired and transformed into the HS 3D image (hypercube) $I_{HS}(x_s, y_s, \lambda)$ considering the HS camera sensitivity $\psi(x_s, y_s, \lambda)$ as:

$$\phi_r(x_s, y_s, \lambda) \longrightarrow I_{HS}(x_s, y_s, \lambda), \tag{6}$$

where:

$$I_{HS}(x_s, y_s, \lambda) = \phi_i(x_s, y_s, \lambda) R(x_s, y_s, \lambda) \psi(x_s, y_s, \lambda). \tag{7}$$

Thus, the obtained hypercube can be processed and analyzed in terms of the particular spectral reflectance for each obtained pixel of the captured photograph print.

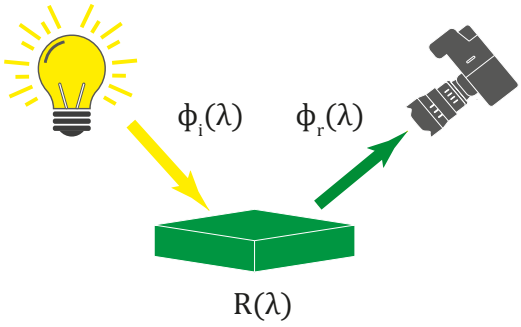

Figure 1. Illustration of spectral reflectance depending on the illumination.

3. Methods and Algorithms

The key decision for the dye- and pigment-based ink print comparison was the selection of the inkjet printer representatives. In the first place, the hobby inkjet printer EPSON L1800 with 6 color inks was selected as a dye-based representative. Complementarily, the professional inkjet printer EPSON SC-P9500 equipped with 12 diverse pigment inks was chosen. To cover the different possibilities of ink and paper chemical interactions, and therefore variations in measured reflectance, 3 types of distinct photo papers with size A4 were selected. Each photo paper was selected on purpose as the most common representative from a different application photo paper class. The most commonly exploited photo papers from diverse application classes were selected as representatives. The first photo paper was semigloss FOMEI Archival Velvet with a weight of 265 g/m^2, which contains a small amount of optical brighteners and is designed for hobby and professional archiving purposes. The second selected photo paper was also semigloss FOMEI PRO Pearl with the same weight of 265 g/m^2. This paper contains a significant amount of optical brighteners and is most frequently used among amateur, but also professional photographers. The last selected paper was a matte-textured paper FOMEI Cotton Textured that weighs 240 g/m^2 and is made from 100% cotton. This art inkjet photo paper does not contain any optical brighteners, is acid free, and is primarily used for fine art applications.

Furthermore, as an example image, the standardized test image from [31] was selected. This test image allows a comprehensive evaluation of diverse colors and scenes with changing patterns. Therefore, the prints of this image are suitable for ink reflectance analysis. The test image with highlighted areas used for a detailed reflectance analysis can be seen in Figure 2.

Thus, all dye- and pigment-based images printed on all the above-mentioned photo papers were recaptured by the hyperspectral camera and further analyzed. The acquisition and overall hyperspectral image data processing are described in the following sections.

3.1. Acquisition

The dye- and pigment-based prints were scanned by the hyperspectral camera SPECIM PFD4K-65-V10E. This camera type is based on the pushbroom line scanning principle. The scanned object was placed on the movable table under the fore camera optics. The table was then illuminated by the halogen lamp connected to the whole table setup. After adjusting the suitable movement speed of the table, the moving object was scanned line by line until the full scan was finished. During the scanning process, each scanned line or, more precisely, each pixel was decomposed into the whole spectral range of the camera. For this purpose, some dispersion components such as prisms, diffraction grating, or their combination were used among the camera internal parts. The full hyperspectral scan

was then digitally processed, and the hypercube with all merged hyperspectral lines was constructed. The whole scanning principle is outlined in Figure 3.

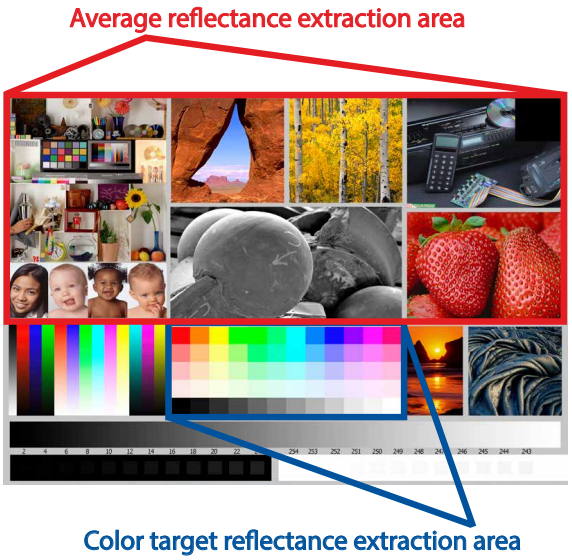

Figure 2. The selected test image (created by Bill Atkinson, Jack Flesher, and Uwe Steinmueller) for dye- and pigment-based prints [31]. This image contains a series of varying scenes, as well as printed color targets that may be easily used for the reflectance analysis. The red rectangle highlights the image area that was used for the overall average reflectance analysis. The blue rectangle highlights the image area used for the reflectance extraction of specific color samples.

The overall spectral range of the SPECIM hyperspectral camera covers the VNIR spectral band 400–1000 nm. The camera provides decomposition into 768 separate spectral channels. The FWHM spectral resolution corresponds to 3 nm. The camera is equipped with a fore optics OLE 23, with focal length 23 mm, f-number f/2.4, and transparency in the whole VNIR spectral band. The remaining parameters of the camera are outlined in Table 1. All captured HS images of the prints were taken with the following settings: a frame rate equal to 25 Hz and exposition equal to 39 ms.

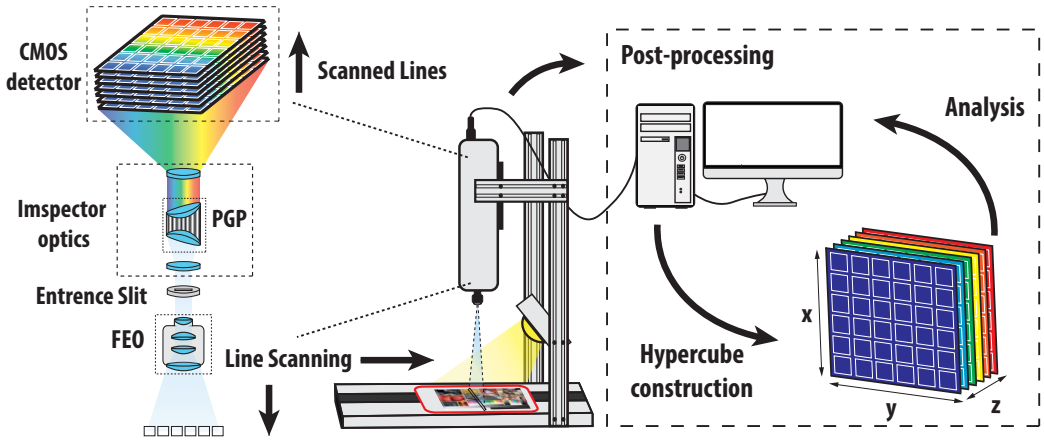

Figure 3. Hyperspectral image capturing and hypercube construction.

Table 1. Parameters of the SPECIM PFD4K-65-V10E hyperspectral camera.

Spectral range	400–1000 nm
Spectral resolution FWHM	3.0 nm
Spectral sampling	0.78–6.27 nm/pixel
Spatial resolution RMS spot size	<9 µm
Focal length	23 mm
F-number	F/2.4
Slit width	30 µm
Effective slit length	14.2 mm
Total efficiency (typical)	>50 % (polar. ind.)
Detector	CMOS
Spatial pixels	1775
Spectral bands	768
Pixel size	8.0 × 8.0 µm

3.2. Image Data Pre-Processing

Let a hyperspectral image captured directly from the above-described HS system be represented as a hypercube. To minimize the noise influence of the camera components and illumination effects, radiometric calibration is necessary. According to Equation (7), assume the hypercube consisting of matrix slices $I_{HS}(x, y, z)$, where indices $x = 1, \ldots, H$ and $y = 1, \ldots, W$ represent the spatial dimension of the image (see Figure 3). The last symbol $z = 1, \ldots, S$ is the wavelength index of each matrix slice depending on the operational spectral range of the HS system. During the hypercube capturing process, several dark and white reference images were recorded. The dark image was usually taken with a closed camera shutter as a sequence of images. The dark frame is represented by the pushbroom system as $I_{DARK}(i, y, z)$, where $i = 1, \ldots, N$, and N is the number of dark frames taken. The white reference spectrum image was taken by capturing an image sequence of the calibration target with known reflectance (typically 99 %). Usually, for pushbroom systems, several spectral images of one spatial line are acquired. The white reference image is then represented as $I_{WHITE}(i, y, z)$, where $i = 1, \ldots, M$ and M also corresponds to the number of frames taken, similar as for the dark image. Due to the matrix mismatch between the captured hypercube, dark image, and white image, the resulting calibrated hypercube with normalized reflectance must be evaluated for each row of the hypercube $I_r(y, z)$ separately as:

$$I_D(y, z) = \frac{1}{N} \sum_{i=1}^{N} I_{DARK}(i, y, z), \tag{8}$$

$$I_W(y, z) = \frac{1}{M} \sum_{i=1}^{M} I_{WHITE}(i, y, z), \tag{9}$$

$$I_r(y, z) = \frac{I_{HS}(y, z) - I_D(y, z)}{I_W(y, z) - I_D(y, z)}. \tag{10}$$

The whole normalized hypercube $I_{norm}(x, y, z)$ was obtained by stacking the calibrated rows $I_r(y, z)$ in the original hypercube shape. Even though radiometric calibration was performed, the calibrated hyperspectral image usually still contained spectral noise. Therefore, a standard Savitzky–Golay [32] filtering was performed. For this purpose, the third-order polynomial with a 15-point window was selected [33]. The Savitzky–Golay method was

separately applied to each hyperspectral pixel, filtering only the spectral dimension. The filtering process [34] can be expressed as:

$$I^*(z) = \frac{\sum_{k=-m}^{k=m} c_k I(z+k)}{2m+1}, \tag{11}$$

where $I^*(z)$ corresponds to one spectral data point of the selected pixel, m is half of the filter window, and c_k is the filter convolution coefficient for the k-th filtering. Then, the key step of the filtering is fitting the original spectral data points by the n-th order polynomial in a defined sliding window via the least-squares estimation.

3.3. Spectral Similarity Measures

With a spectral response (reflectance) for all pixels from the captured dye- and pigment-based prints, it is possible to quantify the spectral differences by various spectral similarity measures. Assume a pre-processed HS image of either a dye- or pigment-based test image print. Furthermore, suppose that the average reflectance $\overline{R}(z)$ of the selected HS image pixel area $I_{sub}(x', y', z)$ is expressed as:

$$\overline{R}(z) = \frac{1}{H'W'} \sum_{x'=1}^{H'} \sum_{y'=1}^{W'} I_{sub}(x', y', z), \tag{12}$$

where indices $x' = 1, \ldots, H'$ and $y' = 1, \ldots, W'$ correspond to the height and width of the selected subimage pixel area.

One of the fundamental metrics for the comparison of two reflectance $\overline{R_1}, \overline{R_2}$ is the spectral angle mapper (SAM) [35]. It can be written as:

$$\mathrm{SAM}_{\overline{R_1},\overline{R_2}} = \cos^{-1}\left(\frac{\sum_{z=1}^{S} \overline{R_1}(z)\overline{R_2}(z)}{\sqrt{\sum_{z=1}^{S} \overline{R_1}(z)^2}\sqrt{\sum_{z=1}^{S} \overline{R_2}(z)^2}} \right). \tag{13}$$

The other metric that may be used for reflectance comparison is the spectral information divergence (SID) [36]. This metric returns the divergence between two probability distributions extracted from two spectral signatures defined as:

$$D_1(z) = \overline{R_1}(z) / \sum_{z=1}^{S} \overline{R_1}(z), \tag{14}$$

$$D_2(z) = \overline{R_2}(z) / \sum_{z=1}^{S} \overline{R_2}(z). \tag{15}$$

The SID is then represented as:

$$\mathrm{SID}_{\overline{R_1},\overline{R_2}} = \sum_{z=1}^{S} D_2(z) \log\left(\frac{D_2(z)}{D_1(z)}\right) + \sum_{z=1}^{S} D_1(z) \log\left(\frac{D_1(z)}{D_2(z)}\right). \tag{16}$$

Having defined the fundamental spectral similarity metrics, the combined hybrid methods may be introduced. From the definition above, the hybrid method the spectral information divergence spectral angle mapper (SIDSAM) [37] can be expressed as:

$$\mathrm{SIDSAM}_{\overline{R_1},\overline{R_2}} = \mathrm{SID}_{\overline{R_1},\overline{R_2}} \times \tan\left(\mathrm{SAM}_{\overline{R_1},\overline{R_2}}\right). \tag{17}$$

Another and more advanced hybrid spectral similarity metric for reflectance comparison is Jeffries–Matusita spectral angle mapper (JMSAM) [38]. Similar to the SIDSAM, the JMSAM involves the fusion of two metrics, the JM distance and the SAM. The JM distance:

$$\mathrm{JM}_{\mathrm{dist}} = 2(1 - \exp(-BD_{1,2})) \tag{18}$$

involves a computation of the Bhattacharyya distance $BD_{\overline{R_1},\overline{R_2}}$ of two compared spectral reflectances as:

$$BD_{\overline{R_1},\overline{R_2}} = \frac{1}{8}(\mu_1 - \mu_2)^{\intercal}\left(\frac{\sigma_1 + \sigma_2}{2}\right)^{-1}(\mu_1 - \mu_2)\frac{1}{2}\ln\left(\frac{\det\left(\frac{\sigma_1+\sigma_2}{2}\right)}{\sqrt{\det\sigma_1 \det\sigma_2}}\right), \tag{19}$$

where μ_1, μ_2 are the mean values of the compared reflected spectra σ_1, σ_2 and their variance. The JMSAM then can be computed as:

$$\mathrm{JMSAM}_{\overline{R_1},\overline{R_2}} = \mathrm{JM}_{\mathrm{dist}} \times \tan\left(\mathrm{SAM}_{\overline{R_1},\overline{R_2}}\right). \tag{20}$$

Each of the presented measures gives a particular score assessing the similarity between the reflectance spectra. In general, a lower score of these metrics indicates a strong match between the compared spectral signatures. For the purpose of this work, the hybrid JMSAM and SIDSAM metrics were selected as representatives of the comparison of the dye- and pigment-based ink prints.

3.4. Principle Component Analysis

In general, the captured HS image often includes redundancy in the neighbor spectral bands and, therefore, a high correlation between them. Techniques such as PCA allow decorrelating the whole HS image into a set of new orthogonal bases, also known as principal components (PCs). The first few principal components usually contain the most captured variance of the original HS image, and therefore, this HS image can be described by only a few PCs.

Assume the original HS image $I(x, y, z)$ reshaped into a 2D matrix $X(i, z)$, where indices $i = 1, \ldots, HW$ and $z = 1, \ldots, S$. This matrix is then mean-centered as:

$$X'(i, z) = X(i, z) - \frac{1}{HW}\sum_{i=1}^{HW} X(i, z). \tag{21}$$

Subsequently, the matrix $X'(i, z)$ may be decomposed by the singular-value decomposition (SVD) method [39] as:

$$X'(i, z) = U(i, i)S(i, z)V^{\intercal}(z, z), \tag{22}$$

where $U(i, i)$ and $V^{\intercal}(z, z)$ are unitary matrices carrying the principal components and eigenvectors, respectively. Diagonal matrix $S(i, z)$ holds the singular values. For the following operations, the reduction of the matrix $U(i, i)$ to $U(i, z)$ is eligible. After the extraction of diagonal values from $S(i, z)$ into a vector $s(z)$, the eigenvalues can be obtained from the expression:

$$\Lambda(z) = \frac{s^2(z)}{HW - 1}, \tag{23}$$

where $\Lambda(z)$ is a vector of all eigenvalues. The transformation of the original matrix $X'(i, z)$ into the new orthogonal coordinate system based on the $I(x, y, z)$ values may be calculated according to the following expression:

$$X_t(i, z) = U(i, z)s^{\intercal}(z). \tag{24}$$

Nevertheless, the index z does not now correspond to the wavelength index, but to the PC index in the new coordinate system.

The explained variance for each generated PC can be computed by the expression:

$$\sigma^2(z) = \frac{100 \cdot \Lambda(z)}{\sum_{z=1}^{S} \Lambda(z)}, \tag{25}$$

where every element of vector $\sigma^2(z)$ corresponds to the explained variance of the particular PC. Due to the nature of the PCA, the transformed image may be usually expressed with a reduced dimension of only some PCs that cover more than 95% or 99% of the cumulative variance of the original image. The index $z = 1, \ldots, S$ may be from the maximal number of PCs S reduced to the specified number S'.

It is apparent that the the PCA method is data dependent. However, it is possible to express a different hyperspectral image using a set of PC components, or more precisely eigenvectors, derived from the PCA method applied to another HS image. Let a new HS image $I_{new}(x'', y'', z)$ be reshaped into matrix $N(i'', z)$ for indices $i'' = 1, \ldots, H''W''$ and $z = 1, \ldots, S$ depending on the spatial dimension of the new HS image. Then, suppose the previously generated diagonal eigenvector matrix $V(z, z)$ of the original HS image $I(x, y, z)$ from Expression (22). The matrix $N(i'', z)$ then can be transferred to the coordinate system dependent on the original HS image $I(x, y, z)$ data values as:

$$N'(i'', z) = N(i'', z) - \frac{1}{HW} \sum_{i=1}^{HW} X(i, z), \tag{26}$$

$$N_t(i'', z) = N'(i'', z) V(z, z). \tag{27}$$

Thus, the pixel values of the original $X_t(i, z)$ and new test HS image $N_t(i'', z)$ may be compared in one coordinate system created from the original HS image. To quantify the differences between the pixel values in this coordinate system, the standard Euclidean distance can be exploited. Suppose a subset of pixel values extracted from $X_t(i, z)$ labeled as $P(i_s, z)$, where $i_s = 1, \ldots, K$ is the pixel subset index. Similarly, assume a subset of pixels of the transformed image $N_t(i'', z)$ represented as $Q(i_s, z)$ with pixel indexation $i_s = 1, \ldots, L$. Then, the mean value vector across the selected PC dimensions for both defined subsets is given as:

$$\overline{p}(z) = \frac{1}{K} \sum_{i_s=1}^{K} P(i_s, z), \tag{28}$$

$$\overline{q}(z) = \frac{1}{L} \sum_{i_s=1}^{L} Q(i_s, z). \tag{29}$$

Analogically, the standard deviation vectors of these pixel subsets are:

$$\sigma_{\boldsymbol{p}}(z) = \sqrt{\frac{1}{K} \sum_{i_s=1}^{K} (P(i_s, z) - \overline{p}(z))^2}, \tag{30}$$

$$\sigma_{\boldsymbol{q}}(z) = \sqrt{\frac{1}{K} \sum_{i_s=1}^{L} (Q(i_s, z) - \overline{q}(z))^2}. \tag{31}$$

The Euclidean distance d in the PCA space between $\overline{p}(z)$ and $\overline{q}(z)$ with selected number of PCs S' then can be described as:

$$d = \sqrt{\sum_{z=1}^{S'} (\overline{p}(z) - \overline{q}(z))^2}. \tag{32}$$

Considering also the obtained standard deviations and subsequent error propagation, the standard deviation σ_d of d can be expressed as:

$$\sigma_d = \frac{1}{d}\sqrt{\sum_{z=1}^{S'}(\overline{p}(z)-\overline{q}(z))^2\left(\sigma_p(z)^2+\sigma_q(z)^2\right)}. \quad (33)$$

4. Results and Discussion

As was previously mentioned, the reflectance analysis of the dye- and pigment-based ink photographs was performed on three different types of photo paper. However, only the blank photo papers were captured by the VNIR HS camera as a first step. Then, the average reflectance was extracted and analyzed across the whole HS image directly according to Equation (12). The results for all papers are shown in the whole VNIR spectral range in Figure 4. One can observe that the reflected spectra from the PRO Pearl and Archival Velvet paper are considerably similar. This can be due to their semigloss character and the content of optical brighteners in the paper layer. The presence of optical brighteners within the selected papers creates a notable spectral reflectance peak around 440 nm. This is inflicted by the illumination of the paper, which initiates a fluorescence process. The overall photograph then seems whiter and brighter. Due to the fluorescence, the reflectance values may even exceed the level of one near the wavelength of 440 nm. However, the spectral response of the optical brighteners is affected by the spectral distribution of the light source, especially in the ultraviolet (UV) spectral band. The higher amount of UV light incident on the photo paper with optical brighteners, a richer spectral response can be observed.

The influence of the optical brighteners is mainly seen by the reflectance curve of the PRO Pearl paper, which contains significantly more optical brighteners than the Archival Velvet photo paper. On the contrary, the Cotton Textured paper is perfectly matte and does not contain any optical brighteners. Thus, the reflected spectra of the cotton paper moves around the value 0.8 for the whole VNIR spectral range. The presented results also confirmed and quantified the spectral similarity metrics SIDSAM and JMSAM, which are summarized in Tables 2 and 3.

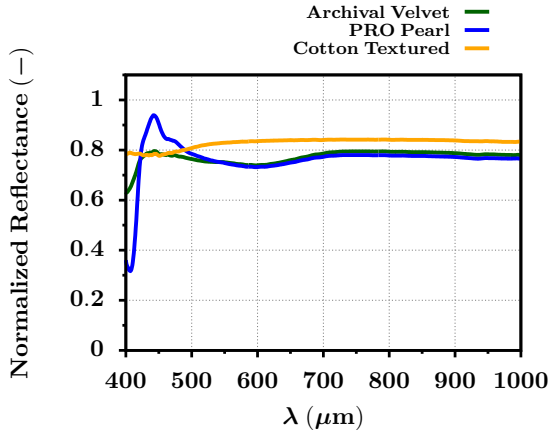

Figure 4. The reflected spectral signature in the VNIR spectral range for the three different blank photo papers extracted from their HS image (FOMEI Archival Velvet, FOMEI PRO Pearl, and FOMEI Cotton Textured).

Table 2. The SIDSAM score of the spectral comparison between the VNIR reflectance of blank photo papers FOMEI Archival Velvet, FOMEI PRO Pearl, and FOMEI Cotton Textured.

	Archival Velvet	PRO Pearl	Cotton Textured
Archival Velvet	0.0	2.9	7.9
PRO Pearl	2.9	0.0	26.9
Cotton Textured	7.9	26.9	0.0

Table 3. The JMSAM score of the spectral comparison between the VNIR reflectance of blank photo papers FOMEI Archival Velvet, FOMEI PRO Pearl, and FOMEI Cotton Textured.

	Archival Velvet	PRO Pearl	Cotton Textured
Archival Velvet	0.0	6.6×10^{-4}	6.3×10^{-4}
PRO Pearl	6.6×10^{-4}	0.0	16×10^{-4}
Cotton Textured	6.3×10^{-4}	16×10^{-4}	0.0

Regarding the SIDSAM metric, the reflectance comparison of the Archival Velvet photo paper against the PRO Pearl and Cotton Textured photo papers gave scores of 2.9 and 7.9, respectively. The SIDSAM score for the reflectance comparison between the blank Cotton Textured paper and PRO Pearl paper equaled 26.9. On the contrary, the JMSAM metric gave almost similar results for the reflectance comparison between Archival Velvet and the remaining papers PRO Pearl and Cotton Textured with scores of 6.6×10^{-4} and 6.3×10^{-4}, respectively. However, the JMSAM metric still evaluated with a higher score (16×10^{-4}) the difference between the Cotton Texture and PRO Pearl paper. It was apparent that the most significant difference between the blank paper reflectance was between wavelengths of 400 nm and 550 nm due to the mentioned fluorescence process of the embedded optical brighteners within the layers of the photo paper. With further analysis and more HS image data, it may be even possible to evaluate the amount of brighteners within the paper or photograph and automatically assess the photographic quality.

The next phase proceeded with fully printed dye- or pigment-based test images on all selected photo papers. These photograph prints were recaptured by the HS camera, with the earlier-mentioned settings. Having all printed testing images, the overall average reflectance (Equation (12)) was extracted from the defined sections of the HS images (see Figure 2). The extracted average reflectance is shown for all photo papers in Figure 5. There was an apparent difference between the dye- and pigment-based ink reflectance values, similar for all selected photo papers. Concerning the dye-based prints, the reflectance increased almost up to a value of 0.8, especially in the spectral band from 800–1000 nm. However, the reflectance of pigment-based inks in the same spectral band did not exceed the level of 0.6. The rise of the dye-based print reflectance started around red colors (around 650 nm). In the band from 400–650 nm, the reflectance of dye- and pigment-based prints was more similar for all papers. The dissimilarity of the average reflectance for dye- and pigment-based prints also supported the spectral metrics. The results of these metrics between the average dye- and pigment-based print reflectance for all photo papers can be seen in Table 4. The SIDSAM metric implied that the difference between the average dye- and pigment-based print reflectance was significant, especially on the PRO Pearl photo paper, with a score of 8.2. For the case of the Archival Velvet photo paper and Cotton Textured photo paper, the scores were 3.2 and 3.1, respectively. According to the SIDSAM metric, the dye- and pigment-based print reflectances were most similar for the prints on the Cotton Textured photo paper, but the spectral difference was still significant. Some influences may also have optical brighteners omitted in the Cotton Textured paper, and therefore, the subsequent fluorescence did not affect the measured reflectance of the inkjet prints. On the contrary, the JMSAM score gave approximately similar results for dye- and pigment-based print reflectance on all selected photo papers. The JMSAM scores were equal to 9.5×10^{-4}, 11.0×10^{-4}, and

10.0×10^{-4} for the Archival Velvet, PRO Pearl, and Cotton Textured paper, respectively. Therefore, the differences between the dye- and pigment-based prints were also confirmed by the spectral metrics.

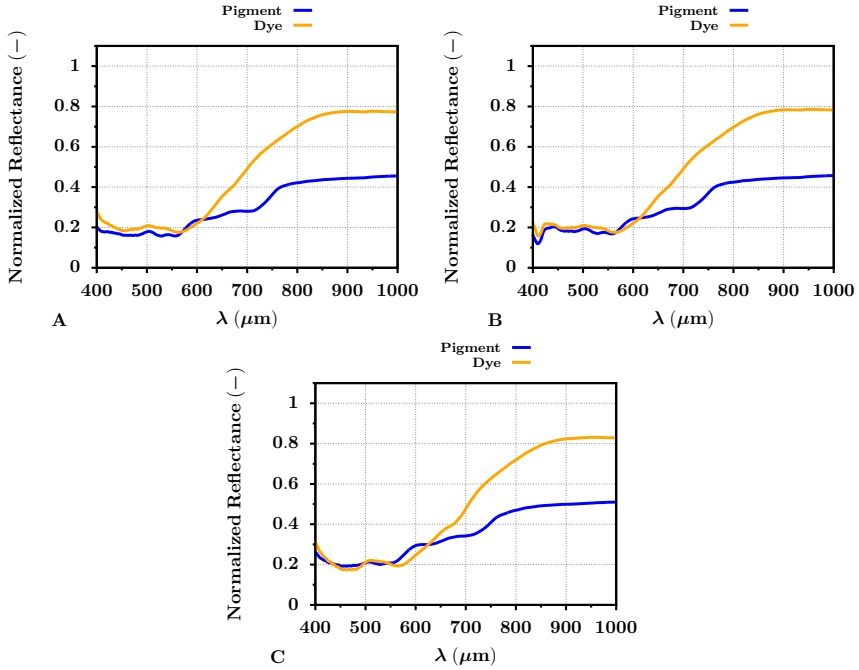

Figure 5. Average VNIR band reflectance of dye- (orange) and pigment-based (blue) test image prints regarding the Archival Velvet (**A**), PRO Pearl (**B**), and Cotton Textured (**C**) photo papers.

Table 4. The spectral metrics values of the extracted average reflectance of dye- vs. pigment-based prints.

	SIDSAM	**JMSAM**
Archival Velvet	3.1	9.5×10^{-4}
PRO Pearl	8.2	11.0×10^{-4}
Cotton Textured	3.2	10.0×10^{-4}

Subsequently, the selected color targets or samples (red, green, blue, and black) from the test image (Figure (2)) were marked for a similar reflectance assessment and comparison between dye- and pigment-based inks. From each color target area of the HS images, the average reflectance pertaining to the selected colors was extracted and plotted. For simplification, only two distinct photo papers, FOMEI PRO Pearl and FOMEI Cotton Textured, were selected.

The extracted reflectances of specific colors (red, green, blue, and black) for the PRO Pearl photo paper are shown in Figure 6. The significant differences between dye- and pigment-based printed targets were apparent for all selected colors, but mainly for green and black. The red color target reflected the radiation almost similarly for both types of inks across the VNIR spectrum. The same may be observed for the blue ink color target, where the difference between the dye- and pigment-based targets was apparent in the band from 600–800 nm. The reflectance difference in this spectral band was even more visible for the green color ink targets, where the dye-based green target reflected significantly more radiation than the pigment-based one. The NIR spectral band appeared to be the most

important for the black printed color target. The reflectance of the pigment-based black target was low (near the zero level) across the whole VNIR spectrum. Contrary to that, the reflectance of the dye-based black target increased almost up to the level of 0.8 in the NIR spectral band. This increase was apparent approximately from 800 nm. Therefore, the pigment-based black ink almost ideally reflected the radiation in the VNIR spectrum compared to the dye-based ink.

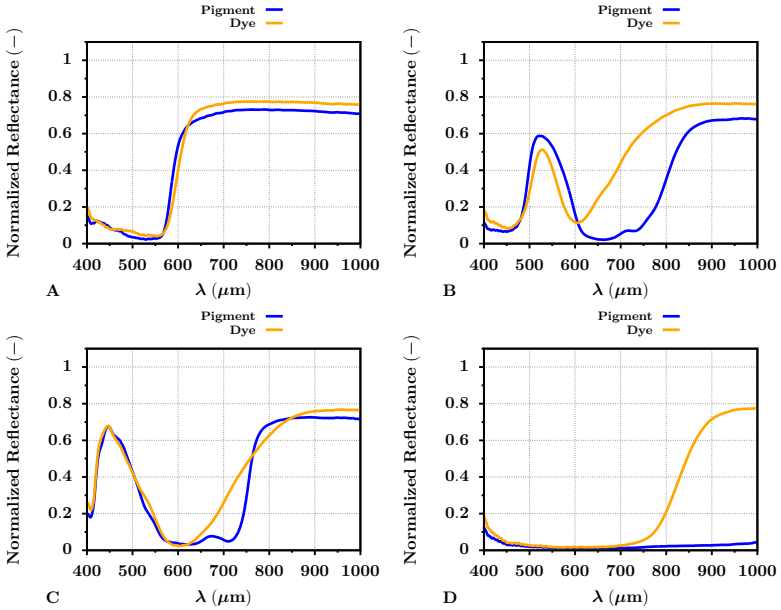

Figure 6. Average color VNIR band reflectance of dye- (orange) and pigment-based (blue) prints on the PRO Pearl inkjet photo paper. The letters (**A**–**D**) represent colors red, green, blue, and black, respectively.

Almost similar results were given by the reflectance analysis of the dye- and pigment-based print color targets for the Cotton Textured inkjet art paper. The results can be seen in Figure 7. The reflectance results differed between the selected photo papers, especially for the blue color target, where the blue reflectance peak was at 450 nm, broader than the blue target reflectance peak for the PRO Pearl paper. Again, this can be caused by the optical brighteners in the PRO Pearl photo paper and subsequent fluorescence. However, the difference between the reflectances of the dye- and pigment-based print color targets did not appear to differ from the results for the PRO Pearl paper significantly. The notable spectral difference among the green, black, and blue color targets remained.

The presented graph results of the dye- and pigment-based color targets also supported the selected spectral metrics, the SIDSAM and JMSAM (see Table 5). The VNIR spectral similarity between the red color targets, either dye- or pigment-based, was evaluated by the SIDSAM metric with scores of 0.4 and 1.6 for the PRO Pearl and Cotton Textured photo papers, respectively. The JMSAM gave for the red color target scores of 3.6×10^{-6} and 6.2×10^{-7} for these types of photo papers. These results suggested the mentioned similarity between the dye- and pigment-based red color print targets. The results of the SIDSAM spectral metric for green and blue target prints corresponded to 134 and 10.9 for the PRO Pearl photo paper and 85 and 6.1 for the Cotton Textured photo paper. Similarly, the results of the JMSAM metric for green dye or pigment-based VNIR reflectance comparison were 4.7×10^{-4} and 2.7×10^{-4} for the photo papers, in the same order. The obtained JMSAM score for the dye- and pigment-based print blue target comparison was 2.7×10^{-5} and 1.9×10^{-5} for targets printed on the PRO Pearl and Cotton Textured

paper. The spectral metrics also supported the significant difference between the black print targets. The SIDSAM and JMSAM difference score for the targets printed on PRO Pearl photo paper was 547 and 2.2×10^{-2}. For the targets printed on the Cotton Textured photo paper, the SIDSAM and JMSAM score was 870 and 2.2×10^{-2}, respectively. Especially the score values between the black dye- and pigment-based inks were essential and at least for the JMSAM score, two orders greater than for the remaining color targets. This result indicated a significant dissimilarity between the dye- and pigment-based black ink. This dissimilarity then may serve, for example, a task such as hyperspectral-based automatic ink classification and specific printer identification.

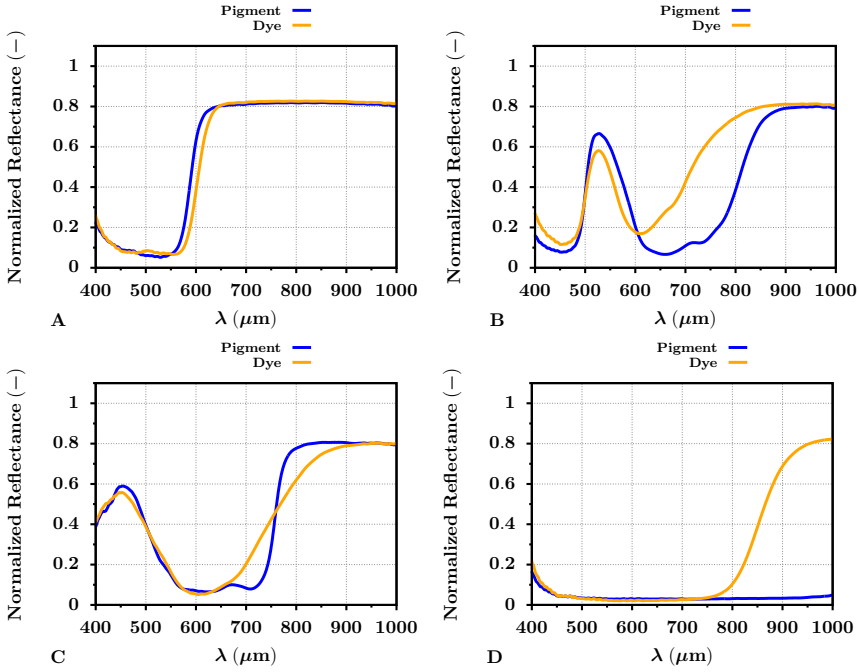

Figure 7. Average color VNIR band reflectance of dye- (orange) and pigment-based (blue) prints on the Cotton Textured inkjet art paper. The letters (**A**–**D**) represent colors red, green, blue, and black, respectively.

Table 5. Dye- vs. pigment-based reflectance comparison for the specific color selection.

	Red		**Green**		**Blue**		**Black**	
	SIDSAM	**JMSAM**	**SIDSAM**	**JMSAM**	**SIDSAM**	**JMSAM**	**SIDSAM**	**JMSAM**
Archival Velvet	0.4	2.9×10^{-6}	119	5.0×10^{-4}	11.1	2.3×10^{-5}	612	2.1×10^{-2}
PRO Pearl	0.5	3.6×10^{-6}	134	4.7×10^{-4}	10.9	2.7×10^{-5}	547	2.2×10^{-2}
Cotton Textured	1.6	6.2×10^{-7}	85	2.9×10^{-4}	6.1	1.9×10^{-5}	870	2.2×10^{-2}

PCA Analysis

In addition, the PCA method was selected for advanced dye- and pigment-based print color target difference analysis. Similarly, as in the previous reflectance analysis, the test image, dye- and pigment-based, was printed on all mentioned photo papers and subsequently captured via the HS camera. The pixel area within the HS image that served for the average dye- and pigment-based reflectance analysis (see Figure 2) was selected as an input for the hyperspectral PCA. The input data were decorrelated and transformed

into a set of new orthogonal bases. The HS image then may be expressed by fewer PCs (channels) than the original HS image. Moreover, the variance of the data concerning such PCs can also be easily described. The result of the explained variance from 0–100 % that was covered by the first 10 PCs is introduced in Figures 8 and 9, for the images printed on the PRO Pearl and Cotton Textured paper, respectively. For both of these figures, Subfigure A represents the explained variance pertaining to the specific principal component of the HS image data taken from the pigment-based prints. Complementarily, the subfigures with label B present the explained variance for the PCs obtained from the HS image data of the dye-based prints. From both figures, it is apparent that the first PC generated from the image data of the pigment-based prints covered about 5 % more variance than the first PC of the dye-based print image data. Thus, the variance of the dye-based print images was scattered into more PCs, especially in the second PC. As also shown by the cumulative variance curve within the figures, the images printed by the professional pigment-based printer may be described with fewer PCs, covering 99 % of the total data variance, than the images printed by the hobby dye-based printer. This result seemed to be independent of the photo paper.

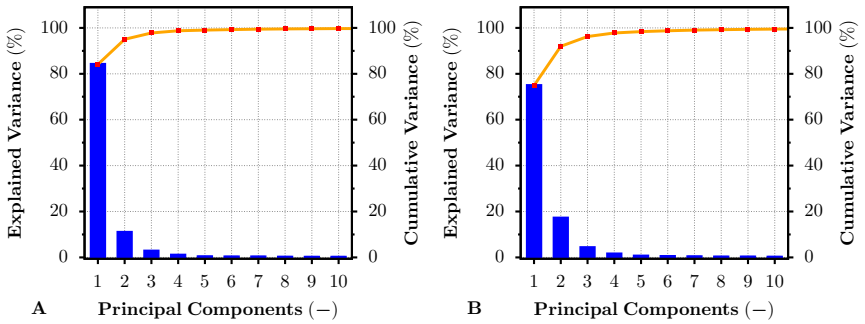

Figure 8. Explained and cumulative variance for the first 10 principal components of PCA-transformed pigment-based (**A**) and dye-based (**B**) inkjet-printed HS image. The result correspond to the dye- and pigment-based test prints on the PRO Pearl inkjet photo paper.

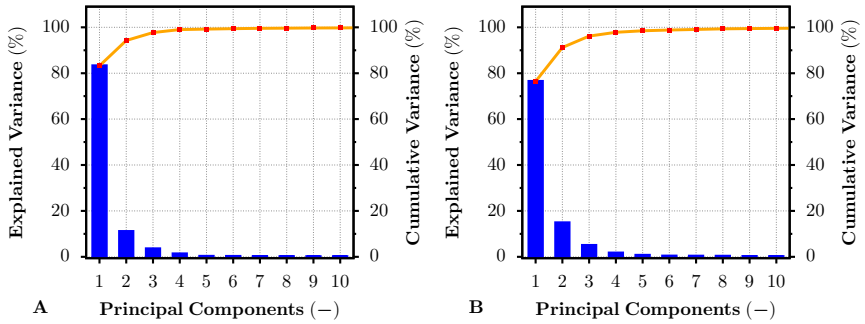

Figure 9. Explained and cumulative variance for the first 10 principal components of PCA-transformed pigment-based (**A**) and dye-based (**B**) inkjet-printed HS image. The result correspond to the dye- and pigment-based test prints on the Cotton Textured inkjet art paper.

During the PCA analysis process, unique eigenvectors were generated from the input image data. These generated eigenvectors may be subsequently used for the new input image data transformation process. This process then transforms the new image input data into a coordinate system based on the previously generated eigenvectors. The transformation may be described according to Equations (26) and (27). Thus, the dye- and

pigment-based print images, or more precisely the pixels with spectral values, can be compared within one coordinate system.

Assume a pigment-based test photo print taken by the HS camera. Then, suppose the PCA procedure that exploits the spectral pixels from the created HS image as an input. The eigenvectors generated by this PCA procedure then can be used for the projection of the new input image data of a dye-based photo print into the original pigment-based PCA space. Selecting a specific set of pixels from a specific image location for both transformed images, for example from a particular color target pixel area (see Figure 2), the values of these pixels can be easily compared within this space. For the comparison of the color targets within the pigment-based transformed space, Figure 10 was selected. For this purpose, the same color targets as in the previous analysis, red, green, blue, and black, were selected. The transformed pixel values of these color targets were averaged (see Equation (28)) and plotted. The standard deviations of each averaged point were also computed, but due to the low values and for visual clearness, they were omitted from the presented graphs. The figures were generated separately for the PRO Pearl and Cotton Textured photo papers. For simplicity, only the first two principal components (PC1, PC2) that covered most of the variance were selected. One can see that the color target values for dye- (triangle points) and pigment-based (circle points) inks confirmed the previous reflectance analysis for both types of photo papers. The most significant distances were observable for the pair of black color targets, followed by the green color targets. The red and blue color target pair points, as their reflectances, were positioned considerably closer together, which indicated a high similarity. These results were similar for all photo papers used.

The presented results were also supported by the calculated Euclidean distance d (see Equation (32)) between the color target pairs (dye and pigment) across the first 20 PC pigment-based PCA-transformed space. The results can be seen in Table 6. The distances between the red, green, blue, and black targets for the PRO Pearl photo paper were 1.2, 6.25, 2.42, and 9.88, respectively. The distances between the red, green, blue, and black targets for the Cotton Textured paper were equal to 1.45, 5.7, 2.03, and 9.55, respectively. The significant difference between the dye- and pigment-based print color targets was also supported by the standard deviation σ_d of the obtained distances. For all distances, $d >> 3 \cdot \sigma_d$ applied. The results for the Archival Velvet paper confirmed the presented conclusions. Therefore, the calculated distance confirmed the significant differences between the dye- and pigment-based print color targets in one common coordinate system.

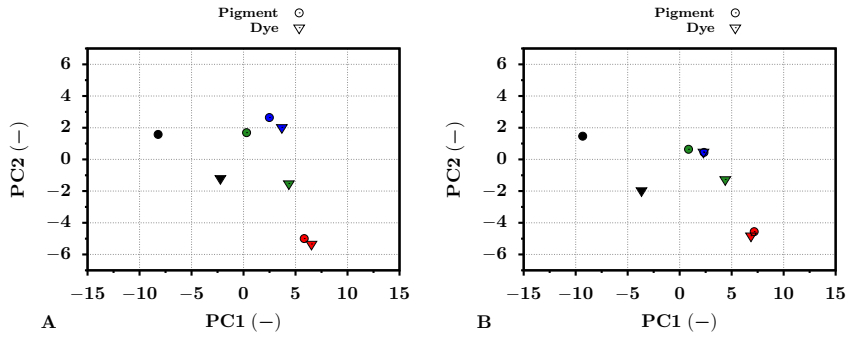

Figure 10. The results of averaged pixel values of the print color targets transformed by the PCA method into the pigment-based coordinate system for dye (triangles) and pigment-based (circles) prints. The results are shown for the first two principal components PC1 and PC2. The point color represents the particular color target. Subfigure (**A**) represents the results for the test images printed on the PRO Pearl photo paper. Subfigure (**B**) presents the results for the test images printed on the Cotton Textured art paper.

Table 6. Euclidean distance d and its standard deviation σ_d between the averaged pixel values of the dye- and pigment-based print color targets. The pixel values of both type print targets were transformed into the pigment-based PCA coordinate system. The distances were calculated across the first 20 PCs.

	Red		**Green**		**Blue**		**Black**	
	d	σ_d	d	σ_d	d	σ_d	d	σ_d
Archival Velvet	1.13	0.11	6.19	0.08	2.42	0.08	10.71	0.08
PRO Pearl	1.2	0.12	6.25	0.08	2.42	0.12	9.88	0.12
Cotton Textured	1.45	0.18	5.7	0.19	2.03	0.1397	9.55	0.11

In general, both the reflectance and PCA analysis confirmed that dye- and pigment-based prints might be recognized using the hyperspectral camera in the VNIR spectral band. Thus, identifying original pigment-based and forged dye-based documents, art works, or unprofessionally made photographs printed for archiving purposes is possible. In addition, according to the presented results, having a broader database of ink reflectance pertaining to a particular printer, the automatic classification down to the specific printer seems promising. In the future, a broader spectral band, such as UV or SWIR, should be tested for hyperspectral imaging and ink identification and analysis. Especially, the differences between the dye- and pigment-based inks in the SWIR band may become even more eminent. The future focus should also be on the ink and printer spectral database creation and the design of an automatic ink identification algorithm based on spectral signatures. This classification task then may be exploited for counterfeit and forgery exposure. However, in summary, the most significant result is the confirmation that VNIR HSI can be exploited for dye- and pigment-based ink identification with high fidelity and can validate a similar spectral signature of unknown art works and documents.

5. Conclusions

This paper presented the assessment of the spectral characteristics of dye- and pigment-based inkjet prints via VNIR HSI. For the evaluation, the specific test images were printed by the hobby dye-based printer EPSON L1800 and the professional pigment-based printer EPSON SC-P9500. For both selected printers, the test images were printed on three different types of photo paper to cover the variation in the spectral response of the prints. The spectral differences between the dye- and pigment-based prints were assessed via the plotted reflectance and quantified via the selected spectral similarity metrics SIDSAM and JMSAM. The spectral difference measurement was performed separately for the whole printed image and the specific printed color targets. The spectral differences between the printed color targets were also assessed via PCA. It was shown that the overall average reflectance of the pigment-based print in the NIR spectral band was significantly lower than the dye-based one, regardless of the exploited photo paper. The most significant spectral difference was observed for the black printed color target. This was also confirmed by the subsequent PCA procedure applied to the acquired HS image data. With a broader HS database of either dye- or pigment-based prints, an advanced classification algorithm based on the captured spectral data may be developed. Therefore, the presented analysis could be an important step toward the automatic hyperspectral-based classification of inks, whole prints, and even specific printers, and it may lead to a reliable print forgery identification.

Author Contributions: Conceptualization, L.K., P.P. and J.K.; methodology, L.K. and P.P.; software, L.K.; validation, P.P. and J.K.; formal analysis, L.K.; investigation, L.K.; resources, P.P. and J.K.; data curation, L.K.; writing, original draft preparation, L.K.; writing, review and editing, L.K., P.P. and J.K.; visualization, L.K.; supervision, P.P. and J.K.; project administration, P.P.; funding acquisition, L.K. and P.P. All authors have read and agreed to the published version of the manuscript.

Funding: This work was supported bythe Grant Agency of the Czech Technical University in Prague, Grant No. SGS20/179/OHK3/3T/13, "Modern Optical Imaging Systems with Non-linear Point

Spread Function and Advanced Algorithms for Image Data Processing", and by the Grant Agency of the Czech Republic, Grant No. 20-10907S, "Meteor clusters: An evidence for fragmentation of meteoroids in interplanetary space".

Institutional Review Board Statement: Not applicable.

Informed Consent Statement: Not applicable.

Data Availability Statement: The data presented in this study are available from the corresponding author on request.

Acknowledgments: The authors would like to thank Miroslav Růžička for consulting and overall support with the setting adjustment of the hyperspectral imaging system.

Conflicts of Interest: The authors declare no conflict of interest.

References

1. Zhao, R.; An, L.; Song, D.; Li, M.; Qiao, L.; Liu, N.; Sun, H. Detection of chlorophyll fluorescence parameters of potato leaves based on continuous wavelet transform and spectral analysis. *Spectrochim. Acta Part A Mol. Biomol. Spectrosc.* **2021**, *259*, 119768.
2. Shen, Q.; Xia, K.; Zhang, S.; Kong, C.; Hu, Q.; Yang, S. Hyperspectral indirect inversion of heavy-metal copper in reclaimed soil of iron ore area. *Spectrochim. Acta Part A Mol. Biomol. Spectrosc.* **2019**, *222*, 117191.
3. Lu, B.; Dao, P.D.; Liu, J.; He, Y.; Shang, J. Recent advances of hyperspectral imaging technology and applications in agriculture. *Remote Sens.* **2020**, *12*, 2659.
4. Musto, P.; Calarco, A.; Pannico, M.; La Manna, P.; Margarucci, S.; Tafuri, A.; Peluso, G. Hyperspectral Raman imaging of human prostatic cells: An attempt to differentiate normal and malignant cell lines by univariate and multivariate data analysis. *Spectrochim. Acta Part A Mol. Biomol. Spectrosc.* **2017**, *173*, 476–488.
5. Lu, G.; Fei, B. Medical hyperspectral imaging: A review. *J. Biomed. Opt.* **2014**, *19*, 010901.
6. Ren, G.; Wang, Y.; Ning, J.; Zhang, Z. Using near-infrared hyperspectral imaging with multiple decision tree methods to delineate black tea quality. *Spectrochim. Acta Part A Mol. Biomol. Spectrosc.* **2020**, *237*, 118407.
7. Calin, M.A.; Calin, A.C.; Nicolae, D.N. Application of airborne and spaceborne hyperspectral imaging techniques for atmospheric research: Past, present, and future. *Appl. Spectrosc. Rev.* **2021**, *56*, 289–323.
8. e Brito, L.R.; Chaves, A.B.; Braz, A.; Pimentel, M.F. Raman hyperspectral imaging and a novel approach for objective determination of the order of crossing ink lines. *Spectrochim. Acta Part A Mol. Biomol. Spectrosc.* **2019**, *223*, 117287.
9. Ferreira, K.; Oliveira, A.; Gonçalves, A.; Gomes, J. Evaluation of hyperspectral imaging visible/near infrared spectroscopy as a forensic tool for automotive paint distinction. *Forensic Chem.* **2017**, *5*, 46–52.
10. Devassy, B.M.; George, S. Dimensionality reduction and visualisation of hyperspectral ink data using t-SNE. *Forensic Sci. Int.* **2020**, *311*, 110194.
11. Picollo, M.; Cucci, C.; Casini, A.; Stefani, L. Hyper-spectral imaging technique in the cultural heritage field: New possible scenarios. *Sensors* **2020**, *20*, 2843.
12. Biron, C.; Mounier, A.; Le Bourdon, G.; Servant, L.; Chapoulie, R.; Daniel, F. Revealing the colours of ukiyo-e prints by short wave infrared range hyperspectral imaging (SWIR). *Microchem. J.* **2020**, *155*, 104782.
13. Daveri, A.; Paziani, S.; Marmion, M.; Harju, H.; Vidman, A.; Azzarelli, M.; Vagnini, M. New perspectives in the non-invasive, in situ identification of painting materials: The advanced MWIR hyperspectral imaging. *TrAC Trends Anal. Chem.* **2018**, *98*, 143–148.
14. Wang, Z.; Fan, S.; Wu, J.; Zhang, C.; Xu, F.; Yang, X.; Li, J. Application of long-wave near infrared hyperspectral imaging for determination of moisture content of single maize seed. *Spectrochim. Acta Part A Mol. Biomol. Spectrosc.* **2021**, *254*, 119666.
15. Catelli, E.; Randeberg, L.L.; Alsberg, B.K.; Gebremariam, K.F.; Bracci, S. An explorative chemometric approach applied to hyperspectral images for the study of illuminated manuscripts. *Spectrochim. Acta Part A Mol. Biomol. Spectrosc.* **2017**, *177*, 69–78.
16. Khan, M.J.; Khan, H.S.; Yousaf, A.; Khurshid, K.; Abbas, A. Modern trends in hyperspectral image analysis: A review. *IEEE Access* **2018**, *6*, 14118–14129.
17. Bonifazi, G.; Capobianco, G.; Pelosi, C.; Serranti, S. Hyperspectral imaging as powerful technique for investigating the stability of painting samples. *J. Imaging* **2019**, *5*, 8.
18. Pérez, M.; Arroyo-Lemus, E.; Ruvalcaba-Sil, J.; Mitrani, A.; Maynez-Rojas, M.; de Lucio, O. Technical non-invasive study of the novo-hispanic painting the Pentecost by Baltasar de Echave Orio by spectroscopic techniques and hyperspectral imaging: In quest for the painter's hand. *Spectrochim. Acta Part A Mol. Biomol. Spectrosc.* **2021**, *250*, 119225.
19. Daniel, F.; Mounier, A.; Pérez-Arantegui, J.; Pardos, C.; Prieto-Taboada, N.; de Vallejuelo, S.F.O.; Castro, K. Hyperspectral imaging applied to the analysis of Goya paintings in the Museum of Zaragoza (Spain). *Microchem. J.* **2016**, *126*, 113–120.
20. Polak, A.; Kelman, T.; Murray, P.; Marshall, S.; Stothard, D.J.; Eastaugh, N.; Eastaugh, F. Hyperspectral imaging combined with data classification techniques as an aid for artwork authentication. *J. Cult. Herit.* **2017**, *26*, 1–11.
21. Agresti, G.; Bonifazi, G.; Capobianco, G.; Lanteri, L.; Pelosi, C.; Serranti, S.; Veneri, A. Hyperspectral imaging as powerful technique for evaluating the stability of Tattoo Wall®. *Microchem. J.* **2020**, *157*, 104866.
22. Zapka, W. *Handbook of Industrial Inkjet Printing: A Full System Approach*; John Wiley & Sons: Hoboken, NJ, USA, 2017.

23. Nickelson, J. *Fine Art Inkjet Printing: The Craft and Art of the Fine Digital Print*; Rocky Nook, Inc.: San Rafael, CA, USA, 2018.
24. Hoath, S.D. *Fundamentals of Inkjet Printing: The Science of Inkjet and Droplets*; John Wiley & Sons: Hoboken, NJ, USA, 2016.
25. Chlebda, D.K.; Rogulska, A.; Łojewski, T. Assessment of hyperspectral imaging system for colour measurement. *Spectrochim. Acta Part A Mol. Biomol. Spectrosc.* **2017**, *185*, 55–62.
26. Maynez-Rojas, M.; Casanova-González, E.; Ruvalcaba-Sil, J. Identification of natural red and purple dyes on textiles by Fiber-optics Reflectance Spectroscopy. *Spectrochim. Acta Part A Mol. Biomol. Spectrosc.* **2017**, *178*, 239–250.
27. Grabowski, B.; Masarczyk, W.; Głomb, P.; Mendys, A. Automatic pigment identification from hyperspectral data. *J. Cult. Herit.* **2018**, *31*, 1–12.
28. Pouyet, E.; Miteva, T.; Rohani, N.; de Viguerie, L. Artificial Intelligence for Pigment Classification Task in the Short-Wave Infrared Range. *Sensors* **2021**, *21*, 6150.
29. Cardin, V.; Dion-Bertrand, L.I.; Poirier, F.; Marcet, S.; Yvon-Leroux, J. Hyperspectral VIS/SWIR wide-field imaging for ink analysis. In *Hyperspectral Imaging and Applications*; International Society for Optics and Photonics: Bellingham, WA, USA, 2020; Volume 11576, p. 1157609.
30. Ragai, J. *Scientist And The Forger, The: Insights Into The Scientific Detection of Forgery in Paintings*; World Scientific: Singapore, 2015.
31. Steinmueller, U.; Gulbins, J. *Fine Art Printing for Photographers: Exhibition Quality Prints with Inkjet Printers*; Rocky Nook, Inc.: San Rafael, CA, USA, 2013.
32. Savitzky, A.; Golay, M.J. Smoothing and differentiation of data by simplified least squares procedures. *Anal. Chem.* **1964**, *36*, 1627–1639.
33. Bohnenkamp, D.; Kuska, M.; Mahlein, A.K.; Behmann, J. Hyperspectral signal decomposition and symptom detection of wheat rust disease at the leaf scale using pure fungal spore spectra as reference. *Plant Pathol.* **2019**, *68*, 1188–1195.
34. Liu, Y.; Dang, B.; Li, Y.; Lin, H.; Ma, H. Applications of Savitzky–Golay filter for seismic random noise reduction. *Acta Geophys.* **2016**, *64*, 101–124.
35. Van der Meer, F. The effectiveness of spectral similarity measures for the analysis of hyperspectral imagery. *Int. J. Appl. Earth Obs. Geoinf.* **2006**, *8*, 3–17.
36. Chang, C.I. An information-theoretic approach to spectral variability, similarity, and discrimination for hyperspectral image analysis. *IEEE Trans. Inf. Theory* **2000**, *46*, 1927–1932.
37. Du, Y.; Chang, C.I.; Ren, H.; Chang, C.C.; Jensen, J.O.; D'Amico, F.M. New hyperspectral discrimination measure for spectral characterization. *Opt. Eng.* **2004**, *43*, 1777–1786.
38. Padma, S.; Sanjeevi, S. Jeffries Matusita based mixed-measure for improved spectral matching in hyperspectral image analysis. *Int. J. Appl. Earth Obs. Geoinf.* **2014**, *32*, 138–151.
39. Wall, M.E.; Rechtsteiner, A.; Rocha, L.M. Singular value decomposition and principal component analysis. In *A Practical Approach to Microarray Data Analysis*; Springer: Berlin/Heidelberg, Germany, 2003; pp. 91–109.

5

SUMMARY OF RESULTS & DISCUSSION

This chapter summarizes the main results of the thesis based upon the core author's publications presented in the previous Chapter 3 and Chapter 4. The presented results are commented in the context of the research challenges (objectives) related to the identified and presented topics (Chapter 1 and Chapter2) of HSI operation in the VIS and IR spectral band. Furthermore, based on the results, possible future steps and research tasks are proposed and discussed. The results and discussion are divided into separate enumerated sections for each publication included in the previous chapters.

The first part of this chapter is devoted to the two core publications [A.2, A.4], which focus on the investigation of optical devices applicable to an AOTF-based hyperspectral system operating in the IR spectral band. For such a purpose, the mercurous halide materials have been selected as highly promising with excellent optical properties, since there is a lack of competition among the currently used birefringent crystal materials that are transparent from the VIS to the LWIR spectral range.

(1) At first, the suitability of a quasi-collinear AOTF for highly promising spatio-spectral HSI had to be evaluated. For this purpose, the **modeling and analysis of the quasi-collinear AOTF based on mercurous halides operable in the IR spectral band have been performed.** Thus, the quasi-collinear theory was introduced within the article [A.2] with an outline of possible spatio-spectral HSI based on such a device. Furthermore, the acousto-optic properties of mercurous halides based on the current state of knowledge were presented and their suitability for AOTF operation in the IR band was discussed. The comparison with another currently commercially available crystal material TeO_2 suitable for IR operation was also presented. Then as a suitable representative of the mercurous halide family, the Hg_2Cl_2 has been selected for more detailed analysis of a quasi-collinear AOTF model operable in 8 µm–10 µm spectral band. For the investigated Hg_2Cl_2 model, the power requirements, maximal achievable spectral resolution, and chromatic field of view of the quasi-collinear AOTF have also been evaluated. Furthemore, a convenient Hg_2Cl_2 crystal input cut angle in a particular crystallographic plane ([001], [110]) was proposed. In addition, throughout the mismatch and diffraction efficiency evaluation, the possible spatio-spectral operation of

such a quasi-collinear AOTF model in the selected spectral range was also confirmed. The advantages (especially the spectral resolution) of the presented model were then discussed.

Based on the performed analysis, the article proposed several following steps and research challenges that are crucial for a possible spatio-spectral HSI system construction. The first challenge is to focus on the fabrication of the presented quasi-collinear AOTF based on mercurous halides and, subsequently, its integration into the introduced spatio-spectral hyperspectral system. This will allow for the precise determination of missing elasto-optic coefficients of mercurous halides and experimental evaluation of modeled AOTF parameters. Another challenge is the subsequent necessary optical modeling of the introduced hyperspectral system, including the determination of other parameters such as point spread function (PSF), FOV, and spatial resolution. For such a challenge, it is important to take into account the parameters and characteristics of necessary additional instruments of the hyperspectral system, such as fore and back optics, polarizers, sensor, and driving electronics. Critical would be a precise selection of suitable devices for the spatio-spectral hyperspectral system operation and possible commissioning of the final device. These demanding challenges provide excellent opportunities for further research and development in the HSI field. This may lead to unconventional solutions for complete hyperspectral systems usable in a wide range of applications (e.g., day-night thermal remote Earth observation) and more precise HSI techniques in the future.

(2) Emerging from the results of the above-presented publication, the introduced promising spatio-spectral hyperspectral system operable in various bands (e.g., TIR band) based on the AOTF device required for its operation a high-quality polarizer (crystal-based allowing a high degree of polarization) with broadband optical transmittance. Thus, the mercurous halide optical materials, with their promising optical characteristics, appear to be a very suitable candidate for the design of such devices. One of the very frequent constructions of a polarizer, applicable in a variety of applications (astronomy, microscopy, HSI), is the Wollaston-based one (consisting of two wedge prisms with diverse crystallographic orientations). However, usually for its proper operation, an optical cement, or immersion, bonding the two prisms together, needs to be used. Therefore, the second core publication [A.4] was focused on **the analysis and design parameters for a Wollaston prism based on mercurous halide (Hg_2X_2) crystals, specifically Hg_2Cl_2, Hg_2Br_2, and Hg_2I_2**.

The article outlined the optical characteristic of mercurous halides and introduced the procedure for optimization. The cut angle of the wedge prisms of the Wollaston polarizer was identified as a key optimization parameter influencing the overall transmission of radiation energy through the polarizer. The refractive index of the optical cement was then identified as the second optimization parameter. With the goal of maximizing the transmission for as broadband spectral range as possible and also maximizing the separation angle of the output orthogonally polarized beams, the two parameters (prims cut angle and refractive index of the optical cement) were selected as a merit function, and their optimal values were sought. Further optimization and analysis of the ideal cut angle of the Wollaston prism were performed with respect to the current standard adhesives (available on the market) used as the optical cement with an average refractive index equal to 1.5. Subsequently, it was found that the optimal cut angles for Hg_2Cl_2, Hg_2Br_2, and Hg_2I_2 should be around 31°, 28°, and 21°, respectively, assuming a refractive index of 1.5 for the bonding cement. The optimized cut angles were then used to model a Wollaston prism (with a width 10 mm, length 10 mm, and height 10 mm) in Zemax Optic Studio, and the functional operation of the device was

confirmed. In addition, the possibility of constructing an air-gap Wollaston polarizer based on mercurous halides was outlined and analyzed from a functional point of view, which is one of the most interesting results.

Based on the presented Zemax models, it is clear that the mercurous halide-based Wollaston prism can be functional for all VIS-TIR wavelengths, provided that the crystals are correctly oriented and polished. The comparison within the publication [A.4] showed that the mercurous halide-based polarizer may offer superior parameters in terms of both broadband operation and output separation angle. While commercial polarizers based on materials such as SiO_2, $CaCO_3$, MgF_2, YVO_4, and BaB_2O_4 offer a limited spectral range and narrower output separation angles, the mercurous halide-based Wollaston polarizer can operate over a wider spectral range and offer wider separation angles for output orthogonally polarized beams. However, the current limiting factor of the mercurous halide-based polarizer construction is the complicated growth and fabrication of mercurous halide crystals. While recent advances in Hg_2Cl_2, Hg_2Br_2 growth appear to be promising [189, 200–202, 204–207, 210], Hg_2I_2 growth remains a significant challenge.

Despite the current limitations, the exceptional properties of mercurous halides and their possible exploitation as polarizing devices have been demonstrated. Once the crystals are of sufficient size and quality, the construction of a Wollaston polarizer based on these materials will extend several photonic applications in the infrared spectral band, including microscopy and HSI or infrared polarimetry. Experimental evaluation and confirmation of its parameters is therefore the next step in follow-up research, as well as the possible design and construction of other advanced devices, such as lossless polarizers, Glan-type polarizers, or depolarizers.

The second part of this chapter summarizes the results of the next two core publications of this thesis [A.1, A.3], which focused on the topics and disciplines of spectral feature exploration within the multispectral and hyperspectral image data. Two different multispectral and hyperspectral applications were identified as very promising, where spectral characteristic exploration methods were selected as desirable to use. The former, using the WILLIAM multispectral imaging system, focused on ground-based remote sensing of clouds, and the latter on fine art prints and evaluating dye- and pigment-based inks to identify their differences and possible forgeries using VNIR HSI.

(3) The results described in the publication [A.1] were focused on a **spectral (color) assessment of diverse clouds (low-level, high-level, and rainy) based on k-means++ segmentation within diverse color spaces**. Initially, data generated from the WILLIAM ground-based imaging system were pre-selected and merged into a WMD database containing 2044 cloud-classified all-sky images. Subsequently, the k-means++ segmentation method was applied to these pre-selected images transformed into a CIE XYZ and CIE L^*, a^*, b^* color spaces. The accuracy of segmentation within these spaces was then compared and evaluated via suitable objective measures, such as pixel accuracy, F-score, or Intersection over Union (IoU). According to them, the segmentation in CIE L^*, a^*, b^* provided better accuracy of separate clouds than the segmentation within the CIE XYZ color space.

In addition, for each image segment from all the analyzed images belonging to the particular cloud group, the mean and standard deviation have been extracted and considered as a cloud color feature. Their distribution within the color space CIE L^*, a^*, b^* was then investigated. For certain cloud groups, the distributions of their features within the color space appeared very promising with possible cluster characteristics. Thus, the cluster separation (similarity

or closeness assessment) within the CIE L*, a*, b* between each cloud group was measured by the BC, which exploits the BD. The results indicated that the cloud group color features created non-identical clusters within the CIE L*, a*, b* color space. Especially important was the possible cluster separation of the rainy clouds from the different cloud types.

Thus, the explored cloud color features showed a potential that they could be exploited for some automatic machine learning-based approaches that use the previous CIE L*, a*, b* transformation of the captured image data and subsequent k-means++ color-based segmentation as a pre-processing step towards feature extraction and automatic cloud classification. The proposed approach that utilizes k-means++ color segmentation on all-sky image data presents potential for future applications in weather and rainfall forecasting based on automatic all-sky systems. This method may also serve as a valuable tool for advancing research on cloud color-based analysis and classification. Nevertheless, future research should investigate the variation of cloud color characteristics during the day, as well as the consideration of parameters that would account for the changes in illumination of the scene during a variety of weather scenarios.

(4) Following the results of the study of spectral features in multispectral data, the study of the spectral properties of different inks for printing artwork proceeded. The differentiation between professionally certified prints with archival potential and prints made on a hobby printer is a matter of concern for many artists and certification laboratories. The possibility of identifying forgeries is therefore very timely. One of the key findings of the thesis is the study carried out within the publication [A.3] **investigating the potential use of HSI in the VNIR spectral band to differentiate between dye- and pigment-based inkjet prints**. The publication investigated various hyperspectrally captured dye- and pigment-based test prints (taken with the SPECIM PFD4K-65-V10E camera) printed on various photo papers. Two diverse printers were used for this purpose: the hobby dye-based printer EPSON L1800 and the professional pigment-based printer EPSON SC-P9500.

The extracted reflectances and spectral similarity measures (SIDSAM and JMSAM) were used to quantify the spectral differences between the dye- and pigment-based prints. For this purpose, the specific color target from the test images was exploited, but also the entire printed images were used. The applied JMSAM measure exploited the above-tested BD. In addition, PCA was used to assess the spectral differences between the printed color targets. The differences between the dye- and pigment-based inks within the pigment-based PCA space were measured via a standard Euclidean distance metric. Throughout the performed analysis, it was confirmed that the hyperspectral camera and subsequent similarity measurement on the extracted ink spectral features can be effectively used to differentiate between the dye- and pigment-based ink prints. This capability could have a significant impact on the identification of forgeries, particularly in the case of artworks, documents, and photographs printed for archival purposes.

In addition to the hyperspectral-based identification of ink type, the study also indicated the ability to automatically classify down to the specific printer using a broader database of printer-specific ink reflectance data. This finding holds promise for the development of an automatic ink identification algorithm based on spectral signatures that could be used to detect counterfeiting and forgery attempts or for authenticity validation. However, compacted ink and printer spectral databases need to be created for such a purpose. In addition, advanced hyperspectral unmixing techniques should be tested to investigate inks to distinguish between different printers.

The results of this study also suggested that a broader spectral band, such as UV or SWIR,

should be tested for HSI and ink identification and analysis. This is especially true for the SWIR spectral band, as the differences between dye- and pigment-based inks in this band may be even more apparent than in the NIR spectral band. The potential for experimental evaluation of the amount of optical brighteners used in the production of specific photographic papers has also been discovered.

Overall, the findings presented in this publication have significant practical implications for the detection of printed forgeries and authentication in the fields of art, documents, and photograph printing. In addition, the presented results opened further possibilities for future fine art print research.

6

Conclusion

This thesis was devoted to the topic of HSI in the VIS and various IR spectral bands. Given the wide range of topics in HSI applications, two main objectives related to HSI were selected based on a review of the state of the art.

The first main objective of the thesis was directed to the area of new HSI systems, techniques, and instruments applicable in multiple spectral regions from the VIS to the TIR. Following this technical area, a significant part of the thesis was devoted to the promising concept of spatial-spectral HSI based on the AOTF. For the possible functionality of such a system in the thermal domain, it was necessary to select a suitable optical material that would enable such functionality. Among such promising optical materials with high anisotropy are mercurous halides, which were selected as a suitable candidate AOTF substrate for such a hyperspectral system. Therefore, a significant part of this thesis was devoted to the study of the properties, design, and optimization of a mercurous halide-based AOTF that would enable spatial-spectral imaging. Related to this objective was also the design and optimization of a suitable crystal polarizer, which is a necessary component for the functionality of the optimized AOTF, or more precisely, for the whole spatial-spectral AOTF-based imaging. Therefore, a part of this thesis was also dedicated to the design and optimization of mercurous halide-based crystal polarizers, in particular, a standard Wollaston-type polarizer.

The second main objective of this thesis was devoted to the hyperspectral image processing part, or more precisely, to the methods of assessing the spectral characteristics of various objects of interest from data obtained from multispectral and hyperspectral systems. This objective was divided into two main applications that were identified as highly promising and for which spectral feature exploration was highly appropriate. The first application aimed at cloud color similarity evaluation from data generated by the WILLIAM multispectral system. The second application was focused on the evaluation of the spectral properties of different types of inks used for professional and hobby printing of photographs and artwork.

This thesis was divided into six chapters, with the core part devoted to the author's four main publications that addressed the presented objectives. Chapter 1 introduced the general topic of HSI with the different areas and applications involved. It also presented the objectives, milestones, and outline of the thesis. Chapter 2 was dedicated to the related state of the art, the author's contributions, and the outline of the topics or methods related to the

proposed objectives of the thesis. Chapter 3 was devoted to the presentation of the main results of the thesis concerning the design and optimization of optical devices for hyperspectral (spatio-spectral) sensing in the IR (mainly TIR) band based on mercurous halides. Based on these materials, the optimization scheme of quasi-collinear AOTF and Wollaston polarizer was presented. Chapter 4 was devoted to the evaluation of spectral characteristics of objects of interest on data from different multispectral and hyperspectral systems. In the context of multispectral systems, the chosen application was the evaluation of color similarities of different cloud types using data obtained from the ground-based WILLIAM system. The results obtained indicated significant color differences for individual clouds and the ability to automatically distinguish between them. With the knowledge from the results of the methods used for color discrimination of cloud types, a promising HSI application using spectral identification of diverse inks for art printing was selected and investigated. The obtained results suggested significant spectral differences between these ink types, thus offering the application of HSI as a rapid tool for the task of identifying counterfeit prints. Apart from the overall evaluation of the thesis in this Chapter 6, all the results presented in this thesis in relation to the author's publications have been summarized and discussed in Chapter 5.

The results presented in this thesis also provide a basis for further research and open up new avenues of investigation. In Chapter 5, several directions for future research have been outlined and discussed in relation to the results obtained. These avenues mainly revolve around the design and construction of new mercurous halide optical devices suitable for modern, not only hyperspectral, applications. In addition, the results suggest the potential for further research in the field of hyperspectral identification of printed counterfeits as well as automatic cloud type classification based on spectral or color similarity.

BIBLIOGRAPHY

[1] A. F. Goetz, G. Vane, J. E. Solomon, and B. N. Rock, "Imaging spectrometry for earth remote sensing," *science*, vol. 228, no. 4704, pp. 1147–1153, 1985.

[2] U. Steinmueller and J. Gulbins, *Fine art printing for photographers: Exhibition quality prints with inkjet printers*. Rocky Nook, Inc., 2013.

[3] J. Amigo, *Hyperspectral Imaging*. Data Handling in Science and Technology, Elsevier Science, 2019.

[4] D. Manolakis, R. Lockwood, and T. Cooley, *Hyperspectral Imaging Remote Sensing: Physics, Sensors, and Algorithms*. Cambridge University Press, 2016.

[5] A. Ojaghi, M. E. Fay, W. A. Lam, and F. E. Robles, "Ultraviolet hyperspectral interferometric microscopy," *Scientific reports*, vol. 8, no. 1, pp. 1–6, 2018.

[6] N. Kaza, A. Ojaghi, and F. E. Robles, "Ultraviolet hyperspectral microscopy using chromatic-aberration-based iterative phase recovery," *Optics letters*, vol. 45, no. 10, pp. 2708–2711, 2020.

[7] M. Al Ktash, M. Stefanakis, B. Boldrini, E. Ostertag, and M. Brecht, "Characterization of pharmaceutical tablets using UV hyperspectral imaging as a rapid in-line analysis tool," *Sensors*, vol. 21, no. 13, p. 4436, 2021.

[8] J. P. Kerekes and J. R. Schott, "Hyperspectral imaging systems," *Hyperspectral data exploitation: Theory and applications*, pp. 19–45, 2007.

[9] G. ElMasry and D.-W. Sun, "Principles of hyperspectral imaging technology," in *Hyperspectral imaging for food quality analysis and control*, pp. 3–43, Elsevier, 2010.

[10] G. Lu and B. Fei, "Medical hyperspectral imaging: a review," *Journal of biomedical optics*, vol. 19, no. 1, p. 010901, 2014.

[11] A. A. Gowen, Y. Feng, E. Gaston, and V. Valdramidis, "Recent applications of hyperspectral imaging in microbiology," *Talanta*, vol. 137, pp. 43–54, 2015.

[12] G. K. Naganathan, L. M. Grimes, J. Subbiah, C. R. Calkins, A. Samal, and G. E. Meyer, "Visible/near-infrared hyperspectral imaging for beef tenderness prediction," *Computers and electronics in agriculture*, vol. 64, no. 2, pp. 225–233, 2008.

[13] B. Jia, S.-C. Yoon, H. Zhuang, W. Wang, and C. Li, "Prediction of pH of fresh chicken breast fillets by VNIR hyperspectral imaging," *Journal of Food Engineering*, vol. 208, pp. 57–65, 2017.

[14] S. O. Crichton, S. M. Kirchner, V. Porley, S. Retz, G. von Gersdorff, O. Hensel, M. Weygandt, and B. Sturm, "Classification of organic beef freshness using VNIR hyperspectral imaging," *Meat science*, vol. 129, pp. 20–27, 2017.

[15] Y. Zhang and W. Guo, "Moisture content detection of maize seed based on visible/near-infrared and near-infrared hyperspectral imaging technology," *International Journal of Food Science & Technology*, vol. 55, no. 2, pp. 631–640, 2020.

[16] D. Barbin, G. Elmasry, D.-W. Sun, and P. Allen, "Near-infrared hyperspectral imaging for grading and classification of pork," *Meat Science*, vol. 90, no. 1, pp. 259–268, 2012.

[17] K. Sendin, P. J. Williams, and M. Manley, "Near infrared hyperspectral imaging in quality and safety evaluation of cereals," *Critical reviews in food science and nutrition*, vol. 58, no. 4, pp. 575–590, 2018.

[18] P. Reddy, K. M. Guthridge, J. Panozzo, E. J. Ludlow, G. C. Spangenberg, and S. J. Rochfort, "Near-infrared hyperspectral imaging pipelines for pasture seed quality evaluation: An overview," *Sensors*, vol. 22, no. 5, p. 1981, 2022.

[19] A. Siedliska, P. Baranowski, M. Zubik, W. Mazurek, and B. Sosnowska, "Detection of fungal infections in strawberry fruit by VNIR/SWIR hyperspectral imaging," *Postharvest Biology and Technology*, vol. 139, pp. 115–126, 2018.

[20] D. M. Kim, H. Zhang, H. Zhou, T. Du, Q. Wu, T. C. Mockler, and M. Y. Berezin, "Highly sensitive image-derived indices of water-stressed plants using hyperspectral imaging in SWIR and histogram analysis," *Scientific reports*, vol. 5, no. 1, p. 15919, 2015.

[21] A. Jenal, U. Lussem, A. Bolten, M. L. Gnyp, J. Schellberg, J. Jasper, J. Bongartz, and G. Bareth, "Investigating the potential of a newly developed UAV-based VNIR/SWIR imaging system for forage mass monitoring," *PFG–Journal of Photogrammetry, Remote Sensing and Geoinformation Science*, vol. 88, no. 6, pp. 493–507, 2020.

[22] J. Cocking, B. E. Narayanaswamy, C. M. Waluda, and B. J. Williamson, "Aerial detection of beached marine plastic using a novel, hyperspectral short-wave infrared (SWIR) camera," *ICES Journal of Marine Science*, vol. 79, no. 3, pp. 648–660, 2022.

[23] C. I. Honniball, R. Wright, and P. G. Lucey, "MWIR hyperspectral imaging with the MIDAS instrument," in *Infrared Technology and Applications XLIII*, vol. 10177, pp. 118–125, SPIE, 2017.

[24] A. Daveri, S. Paziani, M. Marmion, H. Harju, A. Vidman, M. Azzarelli, and M. Vagnini, "New perspectives in the non-invasive, in situ identification of painting materials: The advanced MWIR hyperspectral imaging," *TrAC Trends in Analytical Chemistry*, vol. 98, pp. 143–148, 2018.

[25] X. Li, M. Gao, J. Liu, Y. Li, and Y. Feng, "Design of MWIR hyperspectral imagers based on acousto-optic tunable filters," *Optik*, p. 170636, 2023.

[26] R. G. Vaughan, W. M. Calvin, and J. V. Taranik, "SEBASS hyperspectral thermal infrared data: surface emissivity measurement and mineral mapping," *Remote Sensing of Environment*, vol. 85, no. 1, pp. 48–63, 2003.

[27] T. A. Russell, L. McMackin, B. Bridge, and R. Baraniuk, "Compressive hyperspectral sensor for LWIR gas detection," in *Compressive Sensing*, vol. 8365, pp. 55–67, SPIE, 2012.

[28] S. Michel, P. Gamet, and M.-J. Lefevre-Fonollosa, "HYPXIM—A hyperspectral satellite defined for science, security and defence users," in *2011 3rd Workshop on Hyperspectral Image and Signal Processing: Evolution in Remote Sensing (WHISPERS)*, pp. 1–4, IEEE, 2011.

[29] V. Kopačková and L. Koucká, "Integration of absorption feature information from visible to longwave infrared spectral ranges for mineral mapping," *Remote Sensing*, vol. 9, no. 10, p. 1006, 2017.

[30] D. Green and M. Schodlok, "Characterisation of carbonate minerals from hyperspectral TIR scanning using features at 14 000 and 11 300 nm," *Australian Journal of Earth Sciences*, vol. 63, no. 8, pp. 951–957, 2016.

[31] C. Liu, R. Xu, F. Xie, J. Jin, L. Yuan, G. Lv, Y. Wang, C. Li, and J. Wang, "New airborne thermal-infrared hyperspectral imager system: Initial validation," *IEEE Journal of Selected Topics in Applied Earth Observations and Remote Sensing*, vol. 13, pp. 4149–4165, 2020.

[32] B. Yousefi, C. I. Castanedo, X. P. Maldague, and G. Beaudoin, "Assessing the reliability of an automated system for mineral identification using LWIR Hyperspectral Infrared imagery," *Minerals Engineering*, vol. 155, p. 106409, 2020.

[33] A. G. Villafranca, J. Corbera, F. Martín, and J. F. Marchán, "Limitations of hyperspectral earth observation on small satellites," *Journal of Small Satellites*, vol. 1, no. 1, pp. 19–29, 2012.

[34] J. Roberts, A. Power, J. Chapman, S. Chandra, and D. Cozzolino, "A short update on the advantages, applications and limitations of hyperspectral and chemical imaging in food authentication," *Applied Sciences*, vol. 8, no. 4, p. 505, 2018.

[35] B. Lu, P. D. Dao, J. Liu, Y. He, and J. Shang, "Recent advances of hyperspectral imaging technology and applications in agriculture," *Remote Sensing*, vol. 12, no. 16, p. 2659, 2020.

[36] M. B. Stuart, M. Davies, M. J. Hobbs, T. D. Pering, A. J. McGonigle, and J. R. Willmott, "High-resolution hyperspectral imaging using low-cost components: Application within environmental monitoring scenarios," *Sensors*, vol. 22, no. 12, p. 4652, 2022.

[37] R. Maksimenka, N. Forget, D. Kaplan, R. Hasal, C. Barta, J. Jaeck, and R. Haïdar, "High spectral resolution AOTF-based hyperspectral imaging system for thermal infrared," in *Proceedings of the 4S Symposium*, ESA, 2014.

[38] P. Janout, *Modeling of Space Variant Optical Systems*. PhD thesis, Czech Technical University in Prague, 2018.

[39] C. Barta and C. Barta Jr, "Physical properties of single crystals of the calomel gorup (hg2x2: X= cl, br) 1," in *Materials Science Forum*, vol. 61, pp. 93–150, Trans Tech Publ, 1990.

[40] N. Singh, M. Gottlieb, G. Brandt, A. Stewart, R. Mazelsky, and M. Glicksman, "Growth and characterization of mercurous halide crystals: mercurous bromide system," *Journal of crystal growth*, vol. 137, no. 1-2, pp. 155–160, 1994.

[41] Č. Barta, I. Silvestrova, J. V. Pisarevskij, N. Moiseeva, and L. Beljaew, "Acoustical properties of single crystals of mercurous halides," *Kristall und Technik*, vol. 12, no. 9, pp. 987–996, 1977.

[42] D.-W. Sun, *Hyperspectral imaging for food quality analysis and control*. Elsevier, 2010.

[43] Y.-Z. Feng and D.-W. Sun, "Application of hyperspectral imaging in food safety inspection and control: a review," *Critical reviews in food science and nutrition*, vol. 52, no. 11, pp. 1039–1058, 2012.

[44] H. Huang, L. Liu, and M. O. Ngadi, "Recent developments in hyperspectral imaging for assessment of food quality and safety," *Sensors*, vol. 14, no. 4, pp. 7248–7276, 2014.

[45] M. Zhu, D. Huang, X.-J. Hu, W.-H. Tong, B.-L. Han, J.-P. Tian, and H.-B. Luo, "Application of hyperspectral technology in detection of agricultural products and food: A Review," *Food Science & Nutrition*, vol. 8, no. 10, pp. 5206–5214, 2020.

[46] J. Qin, M. S. Kim, K. Chao, D. E. Chan, S. R. Delwiche, and B.-K. Cho, "Line-scan hyperspectral imaging techniques for food safety and quality applications," *Applied Sciences*, vol. 7, no. 2, p. 125, 2017.

[47] R. Siche, R. Vejarano, V. Aredo, L. Velasquez, E. Saldana, and R. Quevedo, "Evaluation of food quality and safety with hyperspectral imaging (HSI)," *Food Engineering Reviews*, vol. 8, no. 3, pp. 306–322, 2016.

[48] N. Basantia, L. M. Nollet, and M. Kamruzzaman, *Hyperspectral Imaging Analysis and Applications for Food Quality*. CRC Press, 2018.

[49] D. F. Barbin, G. Elmasry, D.-W. Sun, P. Allen, and N. Morsy, "Non-destructive assessment of microbial contamination in porcine meat using NIR hyperspectral imaging," *Innovative Food Science & Emerging Technologies*, vol. 17, pp. 180–191, 2013.

[50] G. ElMasry, D. F. Barbin, D.-W. Sun, and P. Allen, "Meat quality evaluation by hyperspectral imaging technique: an overview," *Critical reviews in food science and nutrition*, vol. 52, no. 8, pp. 689–711, 2012.

[51] X. Fu and J. Chen, "A Review of Hyperspectral Imaging for Chicken Meat Safety and Quality Evaluation: Application, Hardware, and Software," *Comprehensive Reviews in Food Science and Food Safety*, vol. 18, no. 2, pp. 535–547, 2019.

[52] M. Al-Sarayreh, M. M. Reis, W. Q. Yan, and R. Klette, "Potential of deep learning and snapshot hyperspectral imaging for classification of species in meat," *Food Control*, vol. 117, p. 107332, 2020.

[53] M. Kamruzzaman, G. ElMasry, D.-W. Sun, and P. Allen, "Prediction of some quality attributes of lamb meat using near-infrared hyperspectral imaging and multivariate analysis," *Analytica Chimica Acta*, vol. 714, pp. 57–67, 2012.

[54] F. Tao and Y. Peng, "A method for nondestructive prediction of pork meat quality and safety attributes by hyperspectral imaging technique," *Journal of Food Engineering*, vol. 126, pp. 98–106, 2014.

[55] T. Antequera, D. Caballero, S. Grassi, B. Uttaro, and T. Perez-Palacios, "Evaluation of fresh meat quality by hyperspectral imaging (HSI), nuclear magnetic resonance (NMR) and magnetic resonance imaging (MRI): a review," *Meat Science*, vol. 172, p. 108340, 2021.

[56] D. Lorente, N. Aleixos, J. Gómez-Sanchis, S. Cubero, O. L. García-Navarrete, and J. Blasco, "Recent advances and applications of hyperspectral imaging for fruit and vegetable quality assessment," *Food and Bioprocess Technology*, vol. 5, pp. 1121–1142, 2012.

[57] N.-N. Wang, D.-W. Sun, Y.-C. Yang, H. Pu, and Z. Zhu, "Recent advances in the application of hyperspectral imaging for evaluating fruit quality," *Food analytical methods*, vol. 9, pp. 178–191, 2016.

[58] J. Steinbrener, K. Posch, and R. Leitner, "Hyperspectral fruit and vegetable classification using convolutional neural networks," *Computers and Electronics in Agriculture*, vol. 162, pp. 364–372, 2019.

[59] Y. Lu, Y. Huang, and R. Lu, "Innovative hyperspectral imaging-based techniques for quality evaluation of fruits and vegetables: A review," *Applied Sciences*, vol. 7, no. 2, p. 189, 2017.

[60] R. Ennis, F. Schiller, M. Toscani, and K. R. Gegenfurtner, "Hyperspectral database of fruits and vegetables," *JOSA A*, vol. 35, no. 4, pp. B256–B266, 2018.

[61] J. Qin and R. Lu, "Measurement of the optical properties of fruits and vegetables using spatially resolved hyperspectral diffuse reflectance imaging technique," *Postharvest Biology and Technology*, vol. 49, no. 3, pp. 355–365, 2008.

[62] B. Park and R. Lu, *Hyperspectral imaging technology in food and agriculture*, vol. 1. Springer, 2015.

[63] R. N. Sahoo, S. Ray, and K. Manjunath, "Hyperspectral remote sensing of agriculture," *Current science*, pp. 848–859, 2015.

[64] C. Wang, B. Liu, L. Liu, Y. Zhu, J. Hou, P. Liu, and X. Li, "A review of deep learning used in the hyperspectral image analysis for agriculture," *Artificial Intelligence Review*, vol. 54, no. 7, pp. 5205–5253, 2021.

[65] L. M. Dale, A. Thewis, C. Boudry, I. Rotar, P. Dardenne, V. Baeten, and J. A. F. Pierna, "Hyperspectral imaging applications in agriculture and agro-food product quality and safety control: A review," *Applied Spectroscopy Reviews*, vol. 48, no. 2, pp. 142–159, 2013.

[66] A. Khan, A. D. Vibhute, S. Mali, and C. Patil, "A systematic review on hyperspectral imaging technology with a machine and deep learning methodology for agricultural applications," *Ecological Informatics*, p. 101678, 2022.

[67] N. R. Rao, P. K. Garg, and S. K. Ghosh, "Development of an agricultural crops spectral library and classification of crops at cultivar level using hyperspectral data," *Precision Agriculture*, vol. 8, pp. 173–185, 2007.

[68] P. S. Thenkabail, R. B. Smith, and E. De Pauw, "Hyperspectral vegetation indices and their relationships with agricultural crop characteristics," *Remote sensing of Environment*, vol. 71, no. 2, pp. 158–182, 2000.

[69] Y. Fu, G. Yang, R. Pu, Z. Li, H. Li, X. Xu, X. Song, X. Yang, and C. Zhao, "An overview of crop nitrogen status assessment using hyperspectral remote sensing: Current status and perspectives," *European Journal of Agronomy*, vol. 124, p. 126241, 2021.

[70] M. Gerhards, M. Schlerf, K. Mallick, and T. Udelhoven, "Challenges and future perspectives of multi-/Hyperspectral thermal infrared remote sensing for crop water-stress detection: A review," *Remote Sensing*, vol. 11, no. 10, p. 1240, 2019.

[71] X. Ge, J. Ding, X. Jin, J. Wang, X. Chen, X. Li, J. Liu, and B. Xie, "Estimating agricultural soil moisture content through UAV-based hyperspectral images in the arid region," *Remote Sensing*, vol. 13, no. 8, p. 1562, 2021.

[72] V. Döpper, A. D. Rocha, K. Berger, T. Gränzig, J. Verrelst, B. Kleinschmit, and M. Förster, "Estimating soil moisture content under grassland with hyperspectral data using radiative transfer modelling and machine learning," *International Journal of Applied Earth Observation and Geoinformation*, vol. 110, p. 102817, 2022.

[73] X. Jiang, S. Luo, Q. Ye, X. Li, and W. Jiao, "Hyperspectral Estimates of Soil Moisture Content Incorporating Harmonic Indicators and Machine Learning," *Agriculture*, vol. 12, no. 8, p. 1188, 2022.

[74] W. D. Hively, G. W. McCarty, J. B. Reeves, M. W. Lang, R. A. Oesterling, and S. R. Delwiche, "Use of airborne hyperspectral imagery to map soil properties in tilled agricultural fields," *Applied and Environmental Soil Science*, vol. 2011, 2011.

[75] S. Migdall, P. Klug, A. Denis, and H. Bach, "The additional value of hyperspectral data for smart farming," in *2012 IEEE International Geoscience and Remote Sensing Symposium*, pp. 7329–7332, IEEE, 2012.

[76] P. K. Sethy, C. Pandey, Y. K. Sahu, and S. K. Behera, "Hyperspectral imagery applications for precision agriculture-a systemic survey," *Multimedia Tools and Applications*, pp. 1–34, 2022.

[77] Y. Sun, S. Chen, X. Dai, D. Li, H. Jiang, and K. Jia, "Coupled retrieval of heavy metal nickel concentration in agricultural soil from spaceborne hyperspectral imagery," *Journal of Hazardous Materials*, vol. 446, p. 130722, 2023.

[78] F. Antonucci, P. Menesatti, N. Holden, E. Canali, S. Giorgi, A. Maienza, and S. R. Stazi, "Hyperspectral visible and near-infrared determination of copper concentration in agricultural polluted soils," *Communications in soil science and plant analysis*, vol. 43, no. 10, pp. 1401–1411, 2012.

[79] P. Mishra, M. S. M. Asaari, A. Herrero-Langreo, S. Lohumi, B. Diezma, and P. Scheunders, "Close range hyperspectral imaging of plants: A review," *Biosystems Engineering*, vol. 164, pp. 49–67, 2017.

[80] A. Hennessy, K. Clarke, and M. Lewis, "Hyperspectral classification of plants: A review of waveband selection generalisability," *Remote Sensing*, vol. 12, no. 1, p. 113, 2020.

[81] S. Paulus and A.-K. Mahlein, "Technical workflows for hyperspectral plant image assessment and processing on the greenhouse and laboratory scale," *GigaScience*, vol. 9, no. 8, p. giaa090, 2020.

[82] A.-K. Mahlein, M. T. Kuska, J. Behmann, G. Polder, and A. Walter, "Hyperspectral sensors and imaging technologies in phytopathology: state of the art," *Annual review of phytopathology*, vol. 56, pp. 535–558, 2018.

[83] C. Wu, Z. Niu, Q. Tang, and W. Huang, "Estimating chlorophyll content from hyperspectral vegetation indices: Modeling and validation," *Agricultural and forest meteorology*, vol. 148, no. 8-9, pp. 1230–1241, 2008.

[84] T. Adão, J. Hruška, L. Pádua, J. Bessa, E. Peres, R. Morais, and J. J. Sousa, "Hyperspectral imaging: A review on UAV-based sensors, data processing and applications for agriculture and forestry," *Remote sensing*, vol. 9, no. 11, p. 1110, 2017.

[85] P. S. Thenkabail and J. G. Lyon, *Hyperspectral remote sensing of vegetation*. CRC press, 2016.

[86] F. D. Van der Meer, H. M. Van der Werff, F. J. Van Ruitenbeek, C. A. Hecker, W. H. Bakker, M. F. Noomen, M. Van Der Meijde, E. J. M. Carranza, J. B. De Smeth, and T. Woldai, "Multi-and hyperspectral geologic remote sensing: A review," *International Journal of Applied Earth Observation and Geoinformation*, vol. 14, no. 1, pp. 112–128, 2012.

[87] S. Peyghambari and Y. Zhang, "Hyperspectral remote sensing in lithological mapping, mineral exploration, and environmental geology: an updated review," *Journal of Applied Remote Sensing*, vol. 15, no. 3, pp. 031501–031501, 2021.

[88] T. H. Kurz, S. J. Buckley, and J. A. Howell, "Close-range hyperspectral imaging for geological field studies: Workflow and methods," *International Journal of Remote Sensing*, vol. 34, no. 5, pp. 1798–1822, 2013.

[89] D. Krupnik and S. Khan, "Close-range, ground-based hyperspectral imaging for mining applications at various scales: Review and case studies," *Earth-science reviews*, vol. 198, p. 102952, 2019.

[90] A. F. Goetz, "Three decades of hyperspectral remote sensing of the Earth: A personal view," *Remote sensing of environment*, vol. 113, pp. S5–S16, 2009.

[91] R. Pu, *Hyperspectral remote sensing: fundamentals and practices*. CRC Press, 2017.

[92] J. M. Bioucas-Dias, A. Plaza, G. Camps-Valls, P. Scheunders, N. Nasrabadi, and J. Chanussot, "Hyperspectral remote sensing data analysis and future challenges," *IEEE Geoscience and remote sensing magazine*, vol. 1, no. 2, pp. 6–36, 2013.

[93] S. Veraverbeke, P. Dennison, I. Gitas, G. Hulley, O. Kalashnikova, T. Katagis, L. Kuai, R. Meng, D. Roberts, and N. Stavros, "Hyperspectral remote sensing of fire: State-of-the-art and future perspectives," *Remote Sensing of Environment*, vol. 216, pp. 105–121, 2018.

[94] J. Transon, R. d'Andrimont, A. Maugnard, and P. Defourny, "Survey of hyperspectral earth observation applications from space in the sentinel-2 context," *Remote Sensing*, vol. 10, no. 2, p. 157, 2018.

[95] E. Vangi, G. D'Amico, S. Francini, F. Giannetti, B. Lasserre, M. Marchetti, and G. Chirici, "The new hyperspectral satellite PRISMA: Imagery for forest types discrimination," *Sensors*, vol. 21, no. 4, p. 1182, 2021.

[96] S.-E. Qian, *Hyperspectral satellites and system design*. CRC Press, 2020.

[97] S.-E. Qian, "Hyperspectral satellites, evolution, and development history," *IEEE Journal of Selected Topics in Applied Earth Observations and Remote Sensing*, vol. 14, pp. 7032–7056, 2021.

[98] F. A. Kruse, J. W. Boardman, and J. F. Huntington, "Comparison of airborne hyperspectral data and EO-1 Hyperion for mineral mapping," *IEEE transactions on Geoscience and Remote Sensing*, vol. 41, no. 6, pp. 1388–1400, 2003.

[99] J. Jia, Y. Wang, J. Chen, R. Guo, R. Shu, and J. Wang, "Status and application of advanced airborne hyperspectral imaging technology: A review," *Infrared Physics & Technology*, vol. 104, p. 103115, 2020.

[100] T. Ishida, J. Kurihara, F. A. Viray, S. B. Namuco, E. C. Paringit, G. J. Perez, Y. Takahashi, and J. J. Marciano Jr, "A novel approach for vegetation classification using UAV-based hyperspectral imaging," *Computers and electronics in agriculture*, vol. 144, pp. 80–85, 2018.

[101] Y. Zhong, X. Wang, Y. Xu, T. Jia, S. Cui, L. Wei, A. Ma, and L. Zhang, "MINI-UAV borne hyperspectral remote sensing: A review," in *2017 IEEE International Geoscience and Remote Sensing Symposium (IGARSS)*, pp. 5908–5911, IEEE, 2017.

[102] A. Lucieer, Z. Malenovskỳ, T. Veness, and L. Wallace, "HyperUAS—Imaging spectroscopy from a multirotor unmanned aircraft system," *Journal of Field Robotics*, vol. 31, no. 4, pp. 571–590, 2014.

[103] J. P. Arroyo-Mora, M. Kalacska, D. Inamdar, R. Soffer, O. Lucanus, J. Gorman, T. Naprstek, E. S. Schaaf, G. Ifimov, K. Elmer, *et al.*, "Implementation of a UAV–hyperspectral pushbroom imager for ecological monitoring," *Drones*, vol. 3, no. 1, p. 12, 2019.

[104] I. Makki, R. Younes, C. Francis, T. Bianchi, and M. Zucchetti, "A survey of landmine detection using hyperspectral imaging," *ISPRS Journal of Photogrammetry and Remote Sensing*, vol. 124, pp. 40–53, 2017.

[105] G. J. Edelman, E. Gaston, T. G. Van Leeuwen, P. Cullen, and M. C. Aalders, "Hyperspectral imaging for non-contact analysis of forensic traces," *Forensic science international*, vol. 223, no. 1-3, pp. 28–39, 2012.

[106] M. Á. F. de la Ossa, J. M. Amigo, and C. García-Ruiz, "Detection of residues from explosive manipulation by near infrared hyperspectral imaging: A promising forensic tool," *Forensic science international*, vol. 242, pp. 228–235, 2014.

[107] B. Melit Devassy and S. George, "Forensic analysis of beverage stains using hyperspectral imaging," *Scientific reports*, vol. 11, no. 1, p. 6512, 2021.

[108] R. Qureshi, M. Uzair, K. Khurshid, and H. Yan, "Hyperspectral document image processing: Applications, challenges and future prospects," *Pattern Recognition*, vol. 90, pp. 12–22, 2019.

[109] C. Cucci, J. K. Delaney, and M. Picollo, "Reflectance hyperspectral imaging for investigation of works of art: old master paintings and illuminated manuscripts," *Accounts of chemical research*, vol. 49, no. 10, pp. 2070–2079, 2016.

[110] B. Grabowski, W. Masarczyk, P. Głomb, and A. Mendys, "Automatic pigment identification from hyperspectral data," *Journal of Cultural Heritage*, vol. 31, pp. 1–12, 2018.

[111] M. Picollo, C. Cucci, A. Casini, and L. Stefani, "Hyper-spectral imaging technique in the cultural heritage field: New possible scenarios," *Sensors*, vol. 20, no. 10, p. 2843, 2020.

[112] H. Liang, "Advances in multispectral and hyperspectral imaging for archaeology and art conservation," *Applied Physics A*, vol. 106, pp. 309–323, 2012.

[113] A. Polak, T. Kelman, P. Murray, S. Marshall, D. J. Stothard, N. Eastaugh, and F. Eastaugh, "Hyperspectral imaging combined with data classification techniques as an aid for artwork authentication," *Journal of Cultural Heritage*, vol. 26, pp. 1–11, 2017.

[114] S.-Y. Huang, A. Mukundan, Y.-M. Tsao, Y. Kim, F.-C. Lin, and H.-C. Wang, "Recent Advances in Counterfeit Art, Document, Photo, Hologram, and Currency Detection Using Hyperspectral Imaging," *Sensors*, vol. 22, no. 19, p. 7308, 2022.

[115] M. Manley, "Near-infrared spectroscopy and hyperspectral imaging: non-destructive analysis of biological materials," *Chemical Society Reviews*, vol. 43, no. 24, pp. 8200–8214, 2014.

[116] L. Gao and R. T. Smith, "Optical hyperspectral imaging in microscopy and spectroscopy–a review of data acquisition," *Journal of biophotonics*, vol. 8, no. 6, pp. 441–456, 2015.

[117] X. Dong, M. Jakobi, S. Wang, M. H. Köhler, X. Zhang, and A. W. Koch, "A review of hyperspectral imaging for nanoscale materials research," *Applied Spectroscopy Reviews*, vol. 54, no. 4, pp. 285–305, 2019.

[118] H. L. Offerhaus, S. E. Bohndiek, and A. R. Harvey, "Hyperspectral imaging in biomedical applications," *Journal of Optics*, vol. 21, p. 010202, dec 2018.

[119] J. A. Gutiérrez-Gutiérrez, A. Pardo, E. Real, J. M. López-Higuera, and O. M. Conde, "Custom scanning hyperspectral imaging system for biomedical applications: Modeling, benchmarking, and specifications," *Sensors*, vol. 19, no. 7, p. 1692, 2019.

[120] V. Batshev, A. Machikhin, G. Martynov, V. Pozhar, S. Boritko, M. Sharikova, V. Lomonov, and A. Vinogradov, "Polarizer-free AOTF-based SWIR hyperspectral imaging for biomedical applications," *Sensors*, vol. 20, no. 16, p. 4439, 2020.

[121] J. Stergar, R. Hren, and M. Milanič, "Design and Validation of a Custom-Made Laboratory Hyperspectral Imaging System for Biomedical Applications Using a Broadband LED Light Source," *Sensors*, vol. 22, no. 16, p. 6274, 2022.

[122] M. A. Calin, S. V. Parasca, D. Savastru, and D. Manea, "Hyperspectral imaging in the medical field: Present and future," *Applied Spectroscopy Reviews*, vol. 49, no. 6, pp. 435–447, 2014.

[123] A. ul Rehman and S. A. Qureshi, "A review of the medical hyperspectral imaging systems and unmixing algorithms' in biological tissues," *Photodiagnosis and Photodynamic Therapy*, vol. 33, p. 102165, 2021.

[124] S. Karim, A. Qadir, U. Farooq, M. Shakir, and A. A. Laghari, "Hyperspectral Imaging: A Review and Trends towards Medical Imaging," *Current medical imaging*, vol. 19, no. 5, p. 417—427, 2022.

[125] R. Cui, H. Yu, T. Xu, X. Xing, X. Cao, K. Yan, and J. Chen, "Deep Learning in Medical Hyperspectral Images: A Review," *Sensors*, vol. 22, no. 24, p. 9790, 2022.

[126] T. Vo-Dinh, "A hyperspectral imaging system for in vivo optical diagnostics," *IEEE Engineering in Medicine and Biology Magazine*, vol. 23, no. 5, pp. 40–49, 2004.

[127] M. Barberio, S. Benedicenti, M. Pizzicannella, E. Felli, T. Collins, B. Jansen-Winkeln, J. Marescaux, M. G. Viola, and M. Diana, "Intraoperative guidance using hyperspectral imaging: a review for surgeons," *Diagnostics*, vol. 11, no. 11, p. 2066, 2021.

[128] J. Yoon, "Hyperspectral imaging for clinical applications," *BioChip Journal*, vol. 16, no. 1, pp. 1–12, 2022.

[129] R. Leon, H. Fabelo, S. Ortega, J. F. Piñeiro, A. Szolna, M. Hernandez, C. Espino, A. J. O'Shanahan, D. Carrera, S. Bisshopp, *et al.*, "VNIR–NIR hyperspectral imaging fusion targeting intraoperative brain cancer detection," *Scientific reports*, vol. 11, no. 1, p. 19696, 2021.

[130] I. A. Cruz-Guerrero, R. Leon, D. U. Campos-Delgado, S. Ortega, H. Fabelo, and G. M. Callico, "Classification of hyperspectral in vivo brain tissue based on linear unmixing," *Applied Sciences*, vol. 10, no. 16, p. 5686, 2020.

[131] M. J. Khan, H. S. Khan, A. Yousaf, K. Khurshid, and A. Abbas, "Modern trends in hyperspectral image analysis: A review," *IEEE Access*, vol. 6, pp. 14118–14129, 2018.

[132] H. Yao and D. Lewis, "Spectral preprocessing and calibration techniques," in *Hyperspectral imaging for food quality analysis and control*, pp. 45–78, Elsevier, 2010.

[133] M. Vidal and J. M. Amigo, "Pre-processing of hyperspectral images. Essential steps before image analysis," *Chemometrics and Intelligent Laboratory Systems*, vol. 117, pp. 138–148, 2012.

[134] Y.-h. Li, X. Tan, W. Zhang, Q.-b. Jiao, Y.-x. Xu, H. Li, Y.-b. Zou, L. Yang, and Y.-p. Fang, "Research and application of several key techniques in hyperspectral image preprocessing," *Frontiers in Plant Science*, vol. 12, p. 627865, 2021.

[135] L. Loncan, L. B. De Almeida, J. M. Bioucas-Dias, X. Briottet, J. Chanussot, N. Dobigeon, S. Fabre, W. Liao, G. A. Licciardi, M. Simoes, *et al.*, "Hyperspectral pansharpening: A review," *IEEE Geoscience and remote sensing magazine*, vol. 3, no. 3, pp. 27–46, 2015.

[136] J. M. Bioucas-Dias, A. Plaza, N. Dobigeon, M. Parente, Q. Du, P. Gader, and J. Chanussot, "Hyperspectral unmixing overview: Geometrical, statistical, and sparse regression-based approaches," *IEEE journal of selected topics in applied earth observations and remote sensing*, vol. 5, no. 2, pp. 354–379, 2012.

[137] D. Landgrebe, "Hyperspectral image data analysis," *IEEE Signal processing magazine*, vol. 19, no. 1, pp. 17–28, 2002.

[138] A. Plaza, J. A. Benediktsson, J. W. Boardman, J. Brazile, L. Bruzzone, G. Camps-Valls, J. Chanussot, M. Fauvel, P. Gamba, A. Gualtieri, *et al.*, "Recent advances in techniques for hyperspectral image processing," *Remote sensing of environment*, vol. 113, pp. S110–S122, 2009.

[139] C.-I. Chang, *Hyperspectral data exploitation: theory and applications*. John Wiley & Sons, 2007.

[140] Y. Chen, Z. Lin, X. Zhao, G. Wang, and Y. Gu, "Deep learning-based classification of hyperspectral data," *IEEE Journal of Selected topics in applied earth observations and remote sensing*, vol. 7, no. 6, pp. 2094–2107, 2014.

[141] N. Audebert, B. Le Saux, and S. Lefèvre, "Deep learning for classification of hyperspectral data: A comparative review," *IEEE geoscience and remote sensing magazine*, vol. 7, no. 2, pp. 159–173, 2019.

[142] L. Huang, R. Luo, X. Liu, and X. Hao, "Spectral imaging with deep learning," *Light: Science & Applications*, vol. 11, no. 1, p. 61, 2022.

[143] S. Grusche, "Basic slit spectroscope reveals three-dimensional scenes through diagonal slices of hyperspectral cubes," *Applied optics*, vol. 53, no. 20, pp. 4594–4603, 2014.

[144] J. Eckhard, T. Eckhard, E. M. Valero, J. L. Nieves, and E. G. Contreras, "Outdoor scene reflectance measurements using a Bragg-grating-based hyperspectral imager," *Applied Optics*, vol. 54, no. 13, pp. D15–D24, 2015.

[145] N. Yokoya, N. Miyamura, and A. Iwasaki, "Preprocessing of hyperspectral imagery with consideration of smile and keystone properties," in *Multispectral, Hyperspectral, and Ultraspectral Remote Sensing Technology, Techniques, and Applications III*, vol. 7857, pp. 73–81, SPIE, 2010.

[146] W. Bakker, H. van der Werff, and F. van der Meer, "Determining smile and keystone of lab hyperspectral line cameras," in *2019 10th Workshop on Hyperspectral Imaging and Signal Processing: Evolution in Remote Sensing (WHISPERS)*, pp. 1–5, IEEE, 2019.

[147] R. O. Green, M. L. Eastwood, C. M. Sarture, T. G. Chrien, M. Aronsson, B. J. Chippendale, J. A. Faust, B. E. Pavri, C. J. Chovit, M. Solis, *et al.*, "Imaging spectroscopy and the airborne visible/infrared imaging spectrometer (AVIRIS)," *Remote sensing of environment*, vol. 65, no. 3, pp. 227–248, 1998.

[148] P. Wang, C. G. Ebeling, J. Gerton, and R. Menon, "Hyper-spectral imaging in scanning-confocal-fluorescence microscopy using a novel broadband diffractive optic," *Optics Communications*, vol. 324, pp. 73–80, 2014.

[149] T. Funatomi, T. Ogawa, K. Tanaka, H. Kubo, G. Caron, E. M. Mouaddib, Y. Matsushita, and Y. Mukaigawa, "Eliminating temporal illumination variations in whisk-broom hyperspectral imaging," *International Journal of Computer Vision*, vol. 130, no. 5, pp. 1310–1324, 2022.

[150] B. Arad and O. Ben-Shahar, "Sparse recovery of hyperspectral signal from natural RGB images," in *Computer Vision–ECCV 2016: 14th European Conference, Amsterdam, The Netherlands, October 11–14, 2016, Proceedings, Part VII 14*, pp. 19–34, Springer, 2016.

[151] N. Hagen and M. W. Kudenov, "Review of snapshot spectral imaging technologies," *Optical Engineering*, vol. 52, no. 9, pp. 090901–090901, 2013.

[152] K. Monakhova, K. Yanny, N. Aggarwal, and L. Waller, "Spectral DiffuserCam: lensless snapshot hyperspectral imaging with a spectral filter array," *Optica*, vol. 7, no. 10, pp. 1298–1307, 2020.

[153] H. Li, W. Liu, B. Dong, J. V. Kaluzny, A. A. Fawzi, and H. F. Zhang, "Snapshot hyperspectral retinal imaging using compact spectral resolving detector array," *Journal of biophotonics*, vol. 10, no. 6-7, pp. 830–839, 2017.

[154] W. R. Johnson, D. W. Wilson, W. Fink, M. Humayun, and G. Bearman, "Snapshot hyperspectral imaging in ophthalmology," *Journal of biomedical optics*, vol. 12, no. 1, pp. 014036–014036, 2007.

[155] J. Wu, B. Xiong, X. Lin, J. He, J. Suo, and Q. Dai, "Snapshot hyperspectral volumetric microscopy," *Scientific reports*, vol. 6, no. 1, pp. 1–10, 2016.

[156] X. Yuan, D. J. Brady, and A. K. Katsaggelos, "Snapshot compressive imaging: Theory, algorithms, and applications," *IEEE Signal Processing Magazine*, vol. 38, no. 2, pp. 65–88, 2021.

[157] N. Gat, "Imaging spectroscopy using tunable filters: a review," *Wavelet Applications VII*, vol. 4056, pp. 50–64, 2000.

[158] N. Gupta, "Development of staring hyperspectral imagers," in *2011 IEEE Applied Imagery Pattern Recognition Workshop (AIPR)*, pp. 1–8, IEEE, 2011.

[159] R. Abdlaty, S. Sahli, J. Hayward, and Q. Fang, "Hyperspectral imaging: comparison of acousto-optic and liquid crystal tunable filters," in *Medical Imaging 2018: Physics of Medical Imaging*, vol. 10573, pp. 700–708, SPIE, 2018.

[160] J. Zhang, Y. Liu, X. Zhang, and X. Hu, "Evaluation and consistency calibration of hyperspectral imaging system based on liquid crystal tunable filter for fabric color measurement," *Color Research & Application*, vol. 47, no. 2, pp. 401–415, 2022.

[161] K. B. Yushkov, J. Champagne, J.-C. Kastelik, O. Y. Makarov, and V. Y. Molchanov, "AOTF-based hyperspectral imaging phase microscopy," *Biomedical optics express*, vol. 11, no. 12, pp. 7053–7061, 2020.

[162] Y. Öhman, "A new monochromator," *Nature*, vol. 141, no. 3563, pp. 291–291, 1938.

[163] J. Beeckman, K. Neyts, and P. J. Vanbrabant, "Liquid-crystal photonic applications," *Optical Engineering*, vol. 50, no. 8, pp. 081202–081202, 2011.

[164] C. Li and W. Wang, "LCTF Hyperspectral Imaging for Vegetable Quality Evaluation," *Hyperspectral Imaging Technology in Food and Agriculture*, pp. 331–357, 2015.

[165] W. H. Bragg and W. L. Bragg, "The reflection of X-rays by crystals," *Proceedings of the Royal Society of London. Series A, Containing Papers of a Mathematical and Physical Character*, vol. 88, no. 605, pp. 428–438, 1913.

[166] S. Harris and R. Wallace, "Acousto-optic tunable filter," *Josa*, vol. 59, no. 6, pp. 744–747, 1969.

[167] I. C. Chang, "Tunable Acousto-Optic Filters: An Overview," in *Acousto-Optics: Device Development/Instrumentation/Applications* (J. B. H. Jr., ed.), vol. 0090, pp. 12 – 22, International Society for Optics and Photonics, SPIE, 1976.

[168] V. B. Voloshinov, "Close to collinear acousto-optical interaction in TeO2 single crystal," in *Acousto-Optics and Applications* (A. Sliwinski, P. Kwiek, B. Linde, and A. Markiewicz, eds.), vol. 1844, pp. 162 – 176, International Society for Optics and Photonics, SPIE, 1992.

[169] V. Batshev, A. Machikhin, G. Martynov, V. Pozhar, S. Boritko, M. Sharikova, V. Lomonov, and A. Vinogradov, "Polarizer-Free AOTF-Based SWIR Hyperspectral Imaging for Biomedical Applications," *Sensors*, vol. 20, p. 4439, Aug. 2020.

[170] N. B. Singh, D. Kahler, D. J. Knuteson, M. Gottlieb, D. Suhre, A. Berghmans, B. Wagner, J. Hedrick, T. Karr, and J. J. Hawkins, "Operational characteristics of a long-wavelength IR multispectral imager based on an acousto-optic tunable filter, volume = 47," *Optical Engineering*, no. 1, p. 013201, 2008.

[171] D. R. Suhre, "Long-wave infrared spectral imager with an 8cm1 passband acousto-optic tunable filter," *Optical Engineering*, vol. 44, p. 094601, Sept. 2005.

[172] N. Gupta, "Acousto-optic tunable filter based visible- to near-infrared spectropolarimetric imager," *Optical Engineering*, vol. 41, p. 1033, May 2002.

[173] N. Gupta, "Hyperspectral imager development at army research laboratory," in *Infrared technology and applications XXXIV*, vol. 6940, pp. 573–582, SPIE, 2008.

[174] J. Ward, M. Farries, C. Pannell, and E. Wachman, "An acousto-optic based hyperspectral imaging camera for security and defence applications," in *Electro-Optical Remote Sensing, Photonic Technologies, and Applications IV* (G. W. Kamerman, O. Steinvall, K. L. Lewis, R. C. Hollins, T. J. Merlet, G. J. Bishop, and J. D. Gonglewski, eds.), vol. 7835, p. 78350U, International Society for Optics and Photonics, SPIE, 2010.

[175] X. Zhang, W. Liu, H. Tong, Y. Liu, X. Wang, C. Zhang, Y. Wang, H. Wang, Z. Sheng, Z. Tan, W. Qiu, X. Huang, and P. Wang, "High-Resolution Hyperspectral Microscopic Imaging With Single Acousto-Optic Tunable Filter Based on Double Filtering," *IEEE Access*, vol. 8, pp. 11570–11576, 2020.

[176] R. Abdlaty, J. Orepoulos, P. Sinclair, R. Berman, and Q. Fang, "High Throughput AOTF Hyperspectral Imager for Randomly Polarized Light," *Photonics*, vol. 5, p. 3, Jan. 2018.

[177] V. B. Voloshinov, N. V. Polikarpova, and N. F. Declercq, "Reflection of plane elastic waves in tetragonal crystals with strong anisotropy," *The Journal of the Acoustical Society of America*, vol. 125, no. 2, pp. 772–779, 2009.

[178] N. Singh, R. Hopkins, R. Mazelsky, and J. Conroy, "Purification and growth of mercurous chloride single crystals," *Journal of Crystal Growth*, vol. 75, no. 1, pp. 173–180, 1986.

[179] R. Li, G. Zhang, L. Liu, L. Zhang, P. Zhang, X. Li, Y. Hua, and X. Tao, "Origin of ultra-wide IR transmission and ultra-large birefringence of mercurous halide series with one dimensional chain-like structure: An ab initio study," *Computational Materials Science*, vol. 188, p. 110139, 2021.

[180] G. B. Brandt, N. Singh, and M. S. Gottlieb, "Mercurous halides for long time-delay Bragg cells," in *Beam Deflection and Scanning Technologies*, vol. 1454, pp. 336–343, SPIE, 1991.

[181] J.-S. Kim, S. B. Trivedi, J. Soos, N. Gupta, and W. Palosz, "Development of mercurous halide crystals for acousto-optic devices," in *Imaging Spectrometry XII*, vol. 6661, pp. 94–105, SPIE, 2007.

[182] N. Gupta, "Investigation of a mercurous chloride acousto-optic cell based on longitudinal acoustic mode," *Applied optics*, vol. 48, no. 7, pp. C151–C158, 2009.

[183] P. Tournois, "Acousto-optic programmable filters in Mercury Halides for Mid-Infrared laser pulse shaping," in *Quantum Electronics and Laser Science Conference*, p. JWA71, Optica Publishing Group, 2008.

[184] N. v. Polikarpova, M. Marunin, and I. Chizh, "IR Acousto-Optic Devices using Acoustic Reflection," in *2021 Wave Electronics and its Application in Information and Telecommunication Systems (WECONF)*, pp. 1–4, IEEE, 2021.

[185] N. Gupta, "Materials for imaging acousto-optic tunable filters," in *Image Sensing Technologies: Materials, Devices, Systems, and Applications*, vol. 9100, pp. 41–50, SPIE, 2014.

[186] P. M. Amarasinghe, J.-S. Kim, S. Trivedi, F. Jin, J. Soos, M. Diestler, S. B. Qadri, J. Jensen, N. Gupta, *et al.*, "Mercurous Bromide (Hg2Br2) Acousto-Optic Tunable Filters (AOTFs) for the Long Wavelength Infrared (LWIR) Region," *Journal of Electronic Materials*, vol. 50, no. 10, pp. 5774–5779, 2021.

[187] Č. Barta and J. Trnka, "New types of polarizers made from crystals of the calomel group," *Crystal Research and Technology*, vol. 17, no. 4, pp. 431–438, 1982.

[188] D. L. Porokhovnichenko, E. A. Dyakonov, J. Ryu, and V. I. Balakshy, "Broadband Glan-type polarization scheme based on mercury halide crystal," *Optical Engineering*, vol. 60, no. 2, p. 020501, 2021.

[189] P. M. Amarasinghe, J.-S. Kim, H. Chen, S. Trivedi, S. B. Qadri, J. Soos, M. Diestler, D. Zhang, N. Gupta, J. L. Jensen, *et al.*, "Growth of high quality mercurous halide single crystals by physical vapor transport method for AOM and radiation detection applications," *Journal of Crystal Growth*, vol. 450, pp. 96–102, 2016.

[190] H. Chen, J.-S. Kim, P. Amarasinghe, W. Palosz, F. Jin, S. Trivedi, A. Burger, J. C. Marsh, M. S. Litz, P. S. Wiejewarnasuriya, *et al.*, "Novel semiconductor radiation detector based on mercurous halides," in *Hard X-Ray, Gamma-Ray, and Neutron Detector Physics XVII*, vol. 9593, pp. 40–50, SPIE, 2015.

[191] H. Chen, J.-S. Kim, P. M. Amarasinghe, S. R. Swaminathan, J. Q. Wen, S. Kutcher, and S. Trivedi, "Activator-doped Hg2Br2 as next generation high performance scintillator for high energy physics research and other scientific and imaging applications," in *Hard X-Ray, Gamma-Ray, and Neutron Detector Physics XXIV*, vol. 12241, p. 1224102, SPIE, 2022.

[192] M. J. Weber, *Handbook of optical materials*. Boca Raton: CRC Press, 2003. OCLC: 51281488.

[193] B. E. Saleh and M. C. Teich, *Fundamentals of photonics*. john Wiley & sons, 2019.

[194] J. W. Gooch, *Cauchy's Dispersion Formula*, pp. 125–125. New York, NY: Springer New York, 2011.

[195] M. Gottlieb and N. Singh, "Elastooptic materials," in *CRC handbook of laser science and technology*, pp. 415–427, CRC Press, 2020.

[196] M. Bass, E. W. Van Stryland, D. R. Williams, and W. L. Wolfe, *Handbook of optics*, vol. 2. McGraw-Hill New York, 1995.

[197] N. Uchida and Y. Ohmachi, "Elastic and photoelastic properties of TeO2 single crystal," *Journal of Applied Physics*, vol. 40, no. 12, pp. 4692–4695, 1969.

[198] A. Pierson and C. Philippe, "Acousto-optic interaction model with mercury halides (Hg2Cl2 and Hg2Br2) as AOTF cristals," in *International Conference on Space Optics — ICSO 2018* (N. Karafolas, Z. Sodnik, and B. Cugny, eds.), (Chania, Greece), p. 219, SPIE, July 2019.

[199] N. Singh, M. Gottlieb, R. Hopkins, R. Mazelsky, W. Duval, and M. Glicksman, "Physical vapor transport growth of mercurous chloride crystals," *Progress in crystal growth and characterization of materials*, vol. 27, no. 3-4, pp. 201–231, 1993.

[200] T. H. Kim, H. T. Lee, Y.-M. Kang, G.-E. Jang, I. H. Kwon, and B. Cho, "In-depth Investigation of Hg2Br2 Crystal Growth and Evolution," *Materials*, vol. 12, no. 24, p. 4224, 2019.

[201] O. Kwon, K. Kim, S.-G. Woo, G.-E. Jang, and B. Cho, "Comparative Analysis of Hg2Br2 and Hg2BrxCl2-x Crystals Grown via PVT," *Crystals*, vol. 10, no. 12, p. 1096, 2020.

[202] L. Liu, R. Li, L. Zhang, P. Zhang, G. Zhang, S. Xia, and X. Tao, "Long wavelength infrared acousto-optic crystal Hg2Br2: Growth optimization and photosensitivity investigation," *Journal of Alloys and Compounds*, vol. 874, p. 159943, 2021.

[203] L. Liu, R. Li, Y. Bi, S.-Q. Xia, G. Zhang, and X. Tao, "Growth and Temperature-Dependent Mechanical and Thermal Properties of One-Dimensional Chain Structure Hg2Br2 Crystals for Infrared Acousto-Optic Device Application," *Crystal Growth & Design*, vol. 21, no. 12, pp. 7034–7042, 2021.

[204] O. Kwon, Y. Song, S.-G. Woo, W. Park, and B. Cho, "Physical Vapor Transport Process for Highly Purified Hg2Br2 Crystal: from Powder Purification to Crystal Growth," *Korean Journal of Metals and Materials*, vol. 60, no. 7, pp. 551–556, 2022.

[205] Y. Bi, L. Liu, Z. Yue, R. Li, G. Zhang, and X. Tao, "Single Crystal Growth and Effect of Cleavage Micro-striations on Crystallinity and Optical Properties of Mercurous Halide Single Crystals," *CrystEngComm*, 2023.

[206] L. Liu, Z. Yue, Y. Bi, S. Xia, G. Zhang, and X. Tao, "Annealing Modification and defect analysis of Hg2Br2 crystal," *Ceramics International*, 2023.

[207] P. Pata, M. Klima, J. Bednar, P. Janout, C. Barta, R. Hasal, L. Maresi, and S. Grabarnik, "OFT sectorization approach to analysis of optical scattering in mercurous chloride single crystals," *Optics Express*, vol. 23, no. 16, pp. 21509–21526, 2015.

[208] J.-S. Kim, S. B. Trivedi, J. Soos, N. Gupta, and W. Palosz, "Development of mercurous halide crystals for acousto-optic devices," in *Imaging Spectrometry XII* (S. S. Shen and P. E. Lewis, eds.), vol. 6661, p. 66610B, International Society for Optics and Photonics, SPIE, 2007.

[209] S. Valle, J. Ward, C. Pannell, and N. P. Johnson, "Acousto-optic tunable filter for imaging application with high performance in the IR region," in *Optical Components and Materials XII* (S. Jiang and M. J. F. Digonnet, eds.), vol. 9359, p. 93590E, International Society for Optics and Photonics, SPIE, 2015.

[210] S. Valle, J. Ward, C. Pannell, and N. Johnson, "Acousto-optic tunable filter for imaging application with high performance in the IR region," in *Optical Components and Materials XII*, vol. 9359, pp. 65–73, SPIE, 2015.

[211] J. D. Ward and S. Valle, "Acousto-optic devices for operation in the infrared," in *Fiber Lasers and Glass Photonics: Materials through Applications* (S. Taccheo, M. Ferrari, and J. I. Mackenzie, eds.), (Strasbourg, France), p. 76, SPIE, May 2018.

[212] D. Porokhovnichenko, J. Ryu, D. Zinkin, and V. Voloshinov, "Analysis of wide-angle acousto-optic interaction geometry in single crystal mercury bromide," in *Fourteenth School on Acousto-Optics and Applications* (I. Grulkowski, B. B. J. Linde, and M. Duocastella, eds.), (Torun, Poland), p. 12, SPIE, Nov. 2019.

[213] D. J. Knuteson, "Crystal growth, fabrication, and design of mercurous bromide acousto-optic tunable filters," *Optical Engineering*, vol. 46, p. 064001, June 2007.

[214] E. Dyakonov, D. Porokhovnichenko, J. Ryu, and V. Balakshy, "Implementation of the wide-angle acousto-optical interaction geometry in a mercury bromide single crystal," *Applied Optics*, vol. 60, no. 8, pp. 2348–2353, 2021.

[215] J. Xu and R. Stroud, *Acousto-optic devices: principles, design, and applications*. Wiley series in pure and applied optics, New York: Wiley, 1992.

[216] A. Korpel, "Acousto-optics—a review of fundamentals," *Proceedings of the IEEE*, vol. 69, no. 1, pp. 48–53, 1981.

[217] R. Dixon, "Acoustic diffraction of light in anisotropic media," *IEEE Journal of Quantum Electronics*, vol. 3, no. 2, pp. 85–93, 1967.

[218] M. Pushkareva and V. N. Parygin, "Quasi-collinear AOTF with improved resolution," in *Acousto-Optics and Applications IV*, vol. 4514, pp. 147–152, SPIE, 2001.

[219] S. Mantsevich, V. Balakshy, V. Molchanov, and K. Yushkov, "Influence of acoustic anisotropy in paratellurite on quasicollinear acousto-optic interaction," *Ultrasonics*, vol. 63, pp. 39–46, Dec. 2015.

[220] P. Tournois, "Design of acousto–optic programmable filters in mercury halides for mid-infrared laser pulse shaping," *Optics Communications*, vol. 281, pp. 4054–4056, Aug. 2008.

[221] R. Maksimenka and P. Tournois, "Mid-infrared high-frequency high-resolution reflective acousto-optic filters in mercury halides," *Optics Communications*, vol. 285, pp. 715–719, Mar. 2012.

[222] D. Kaplan and P. Tournois, "Acoustic-optical filtering method and device based on a long acousto-optical interaction," EU Patent - EP2431791B1 2012.

[223] A. O. Arellanes, V. Quintard, and A. Pérennou, "Spectral and temporal behavior of a quasi-collinear AOTF in response to acoustic pulses: simulations and experiments," *Applied optics*, vol. 61, no. 7, pp. 1687–1694, 2022.

[224] S. N. Mantsevich, V. I. Balakshy, K. B. Yushkov, V. Y. Molchanov, and S. A. Tretiakov, "Quasi-Collinear AOTF Spectral Transmission Under Temperature Gradients Aroused by Ultrasound Power Absotption," *IEEE Transactions on Ultrasonics, Ferroelectrics, and Frequency Control*, vol. 69, no. 12, pp. 3411–3421, 2022.

[225] A. P. Goutzoulis, D. R. Pape, and S. V. Kulakov, eds., *Design and fabrication of acousto-optic devices*. No. v. 41 in Optical engineering, New York: M. Dekker, 1994.

[226] J. Hough, "Polarimetry: a powerful diagnostic tool in astronomy," *Astronomy & Geophysics*, vol. 47, no. 3, pp. 3–31, 2006.

[227] A. Berdyugin, V. Piirola, and J. Poutanen, "Optical polarimetry: Methods, instruments and calibration techniques," *Astronomical Polarisation from the Infrared to Gamma Rays*, pp. 33–65, 2019.

[228] C. He, H. He, J. Chang, B. Chen, H. Ma, and M. J. Booth, "Polarisation optics for biomedical and clinical applications: a review," *Light: Science & Applications*, vol. 10, no. 1, pp. 1–20, 2021.

[229] J. Craven-Jones, M. W. Kudenov, M. G. Stapelbroek, and E. L. Dereniak, "Infrared hyperspectral imaging polarimeter using birefringent prisms," *Applied optics*, vol. 50, no. 8, pp. 1170–1185, 2011.

[230] P. Wang and Z. Zhang, "Hyperspectral imaging performance based on two TeO 2 acousto-optic tunable filters," *Applied Optics*, vol. 56, no. 6, pp. 1647–1653, 2017.

[231] J. Chamoun and S. Farhadi, "Hyperspectral imaging using a Wollaston prism," in *Optics and Photonics for Sensing the Environment*, pp. EM2C–5, Optical Society of America, 2020.

[232] D. H. Goldstein, *Polarized light*. CRC press, 2017.

[233] E. Collett, *Field guide to polarization*. Spie Bellingham, WA, 2005.

[234] G. Ghosh, "Dispersion-equation coefficients for the refractive index and birefringence of calcite and quartz crystals," *Optics communications*, vol. 163, no. 1-3, pp. 95–102, 1999.

[235] M. J. Dodge, "Refractive properties of magnesium fluoride," *Applied optics*, vol. 23, no. 12, pp. 1980–1985, 1984.

[236] H.-S. Shi, G. Zhang, and H.-Y. Shen, "Measurement of principal refractive indices and the thermal refractive index coefficients of yttrium vanadate," *Journal of Synthetic Crystals*, vol. 30, no. 1, pp. 85–88, 2001.

[237] D. Eimerl, L. Davis, S. Velsko, E. Graham, and A. Zalkin, "Optical, mechanical, and thermal properties of barium borate," *Journal of applied physics*, vol. 62, no. 5, pp. 1968–1983, 1987.

[238] L. G. DeShazer, "Improved midinfrared polarizers using yttrium vanadate," in *Polarization Analysis and Measurement IV*, vol. 4481, pp. 10–16, SPIE, 2002.

[239] A. Doblas, S. Bedoya, and C. Preza, "Wollaston prism-based structured illumination microscope with tunable frequency," *Applied Optics*, vol. 58, no. 7, pp. B1–B8, 2019.

[240] Y. Wang, Q. Yang, S. He, R. Wang, and H. Luo, "Computing Metasurfaces Enabled Broad-Band Vectorial Differential Interference Contrast Microscopy," *ACS Photonics*, 2022.

[241] A. R. Harvey and D. W. Fletcher-Holmes, "Birefringent Fourier-transform imaging spectrometer," *Optics Express*, vol. 12, no. 22, pp. 5368–5374, 2004.

[242] J. Schou, "Using birefringent elements and imaging Michelsons for the calibration of high-precision planet-finding spectrographs," *Astronomy & Astrophysics*, vol. 662, p. A119, 2022.

[243] T. Mu, C. Zhang, C. Jia, and W. Ren, "Static hyperspectral imaging polarimeter for full linear Stokes parameters," *Optics express*, vol. 20, no. 16, pp. 18194–18201, 2012.

[244] J. D. Perreault, "Triple Wollaston-prism complete-Stokes imaging polarimeter," *Optics letters*, vol. 38, no. 19, pp. 3874–3877, 2013.

[245] Q. Liu, C. Bai, J. Liu, J. He, and J. Li, "Fourier transform imaging spectropolarimeter using ferroelectric liquid crystals and Wollaston interferometer," *Optics Express*, vol. 25, no. 17, pp. 19904–19922, 2017.

[246] W. Ren, J. Ning, Z. Xu, Y. Xie, R. Zhang, and D. Wu, "Coded Apertured Snapshot Spectrapolarimetric Imager with a Wollaston Prism," in *Computational Optical Sensing and Imaging*, pp. JTh2A–37, Optical Society of America, 2020.

[247] D. Manolakis, E. Truslow, M. Pieper, T. Cooley, and M. Brueggeman, "Detection algorithms in hyperspectral imaging systems: An overview of practical algorithms," *IEEE Signal Processing Magazine*, vol. 31, no. 1, pp. 24–33, 2013.

[248] H. Deborah, N. Richard, and J. Y. Hardeberg, "A comprehensive evaluation of spectral distance functions and metrics for hyperspectral image processing," *IEEE Journal of Selected Topics in Applied Earth Observations and Remote Sensing*, vol. 8, no. 6, pp. 3224–3234, 2015.

[249] P. Pathak, C. Chalopin, L. Zick, H. Köhler, A. Pfahl, N. Rayes, I. Gockel, T. Neumuth, A. Melzer, B. Jansen-Winkeln, *et al.*, "Spectral Similarity Measures for In Vivo Human Tissue Discrimination Based on Hyperspectral Imaging," *Diagnostics*, vol. 13, no. 2, p. 195, 2023.

[250] F. Van der Meer, "The effectiveness of spectral similarity measures for the analysis of hyperspectral imagery," *International journal of applied earth observation and geoinformation*, vol. 8, no. 1, pp. 3–17, 2006.

[251] H. Deborah, S. George, and J. Y. Hardeberg, "Spectral-divergence based pigment discrimination and mapping: A case study on The Scream (1893) by Edvard Munch," *Journal of the American Institute for Conservation*, vol. 58, no. 1-2, pp. 90–107, 2019.

[252] S. Lohumi, S. Lee, H. Lee, M. S. Kim, W.-H. Lee, and B.-K. Cho, "Application of hyperspectral imaging for characterization of intramuscular fat distribution in beef," *Infrared Physics & Technology*, vol. 74, pp. 1–10, 2016.

[253] Deepthi, B. M. Devassy, S. George, P. Nussbaum, and T. Thomas, "Classification of forensic hyperspectral paper data using hybrid spectral similarity algorithms," *Journal of Chemometrics*, vol. 36, no. 1, p. e3387, 2022.

[254] L. Ramirez-Lopez, T. Behrens, K. Schmidt, R. V. Rossel, J. A. M. Demattê, and T. Scholten, "Distance and similarity-search metrics for use with soil vis–NIR spectra," *Geoderma*, vol. 199, pp. 43–53, 2013.

[255] F. A. Kruse, A. Lefkoff, J. Boardman, K. Heidebrecht, A. Shapiro, P. Barloon, and A. Goetz, "The spectral image processing system (SIPS)—interactive visualization and analysis of imaging spectrometer data," *Remote sensing of environment*, vol. 44, no. 2-3, pp. 145–163, 1993.

[256] C.-I. Chang, "An information-theoretic approach to spectral variability, similarity, and discrimination for hyperspectral image analysis," *IEEE Transactions on information theory*, vol. 46, no. 5, pp. 1927–1932, 2000.

[257] Y. Du, C.-I. Chang, H. Ren, C.-C. Chang, J. O. Jensen, and F. M. D'Amico, "New hyperspectral discrimination measure for spectral characterization," *Optical engineering*, vol. 43, no. 8, pp. 1777–1786, 2004.

[258] F. van der Meero and W. Bakker, "Cross correlogram spectral matching: application to surface mineralogical mapping by using AVIRIS data from Cuprite, Nevada," *Remote sensing of environment*, vol. 61, no. 3, pp. 371–382, 1997.

[259] O. A. De Carvalho and P. R. Meneses, "Spectral correlation mapper (SCM): an improvement on the spectral angle mapper (SAM)," in *Summaries of the 9th JPL airborne earth science workshop, JPL Publication 00-18*, vol. 9, p. 2, JPL publication Pasadena, CA, USA, 2000.

[260] S. Robila, "Using spectral distances for speedup in hyperspectral image processing," *International Journal of Remote Sensing*, vol. 26, no. 24, pp. 5629–5650, 2005.

[261] S. Padma and S. Sanjeevi, "Jeffries Matusita based mixed-measure for improved spectral matching in hyperspectral image analysis," *International journal of applied earth observation and geoinformation*, vol. 32, pp. 138–151, 2014.

[262] A. Bhattacharyya, "On a measure of divergence between two statistical populations defined by their probability distributions," *Bull. Calcutta Math. Soc.*, vol. 35, pp. 99–109, 1943.

[263] K. Koutroumbas and S. Theodoridis, *Pattern Recognition*. Elsevier Science, 2008.

[264] A. Datta, S. Ghosh, and A. Ghosh, "PCA, kernel PCA and dimensionality reduction in hyperspectral images," *Advances in Principal Component Analysis: Research and Development*, pp. 19–46, 2018.

[265] G. Chen and S.-E. Qian, "Denoising of hyperspectral imagery using principal component analysis and wavelet shrinkage," *IEEE Transactions on Geoscience and remote sensing*, vol. 49, no. 3, pp. 973–980, 2010.

[266] C. Rodarmel and J. Shan, "Principal component analysis for hyperspectral image classification," *Surveying and Land Information Science*, vol. 62, no. 2, pp. 115–122, 2002.

[267] M. P. Uddin, M. A. Mamun, and M. A. Hossain, "Effective feature extraction through segmentation-based folded-PCA for hyperspectral image classification," *International Journal of Remote Sensing*, vol. 40, no. 18, pp. 7190–7220, 2019.

[268] M. Ye, C. Ji, H. Chen, L. Lei, H. Lu, and Y. Qian, "Residual deep PCA-based feature extraction for hyperspectral image classification," *Neural Computing and Applications*, vol. 32, pp. 14287–14300, 2020.

[269] M. E. Wall, A. Rechtsteiner, and L. M. Rocha, "Singular value decomposition and principal component analysis," in *A practical approach to microarray data analysis*, pp. 91–109, Springer, 2003.

[270] S.-A. Logothetis, V. Salamalikis, S. Wilbert, J. Remund, L. F. Zarzalejo, Y. Xie, B. Nouri, E. Ntavelis, J. Nou, N. Hendrikx, *et al.*, "Benchmarking of solar irradiance nowcast performance derived from all-sky imagers," *Renewable Energy*, vol. 199, pp. 246–261, 2022.

[271] T. C. Carneiro, P. C. M. de Carvalho, H. Alves dos Santos, M. A. F. B. Lima, and A. P. d. S. Braga, "Review on photovoltaic power and solar resource forecasting: current status and trends," *Journal of Solar Energy Engineering*, vol. 144, no. 1, 2022.

[272] Y. Tang, K. Yang, S. Zhang, and Z. Zhang, "Photovoltaic power forecasting: A hybrid deep learning model incorporating transfer learning strategy," *Renewable and Sustainable Energy Reviews*, vol. 162, p. 112473, 2022.

[273] F. Lin, Y. Zhang, and J. Wang, "Recent advances in intra-hour solar forecasting: A review of ground-based sky image methods," *International Journal of Forecasting*, vol. 39, no. 1, pp. 244–265, 2023.

[274] S. Mahajan and B. Fataniya, "Cloud detection methodologies: Variants and development—A review," *Complex & Intelligent Systems*, vol. 6, pp. 251–261, 2020.

[275] M. Hasenbalg, P. Kuhn, S. Wilbert, B. Nouri, and A. Kazantzidis, "Benchmarking of six cloud segmentation algorithms for ground-based all-sky imagers," *Solar Energy*, vol. 201, pp. 596–614, 2020.

[276] S. Dev, A. Nautiyal, Y. H. Lee, and S. Winkler, "CloudSegNet: A Deep Network for Nychthemeron Cloud Image Segmentation," *IEEE Geoscience and Remote Sensing Letters*, vol. 16, no. 12, pp. 1814–1818, 2019.

[277] S. Liu, L. Zhang, Z. Zhang, C. Wang, and B. Xiao, "Automatic Cloud Detection for All-Sky Images Using Superpixel Segmentation," *IEEE Geoscience and Remote Sensing Letters*, vol. 12, pp. 354–358, Feb 2015.

[278] S. Dev, F. M. Savoy, Y. H. Lee, and S. Winkler, "High-dynamic-range imaging for cloud segmentation," *Atmospheric Measurement Techniques*, vol. 11, no. 4, pp. 2041–2049, 2018.

[279] L. Ye, Z. Cao, Y. Xiao, and Z. Yang, "Supervised Fine-Grained Cloud Detection and Recognition in Whole-Sky Images," *IEEE Transactions on Geoscience and Remote Sensing*, vol. 57, pp. 7972–7985, Oct 2019.

[280] H.-Y. Cheng and C.-L. Lin, "Cloud detection in all-sky images via multi-scale neighborhood features and multiple supervised learning techniques," *Atmospheric Measurement Techniques*, vol. 10, no. 1, pp. 199–208, 2017.

[281] W. Zhuo, Z. Cao, and Y. Xiao, "Cloud Classification of Ground-Based Images Using Texture–Structure Features," *Journal of Atmospheric and Oceanic Technology*, vol. 31, no. 1, pp. 79–92, 2014.

[282] S. Oikonomou, A. Kazantzidis, G. Economou, and S. Fotopoulos, "A local binary pattern classification approach for cloud types derived from all-sky imagers," *International Journal of Remote Sensing*, vol. 40, no. 7, pp. 2667–2682, 2019.

[283] D. Arthur and S. Vassilvitskii, "K-means++: the advantages of careful seeding," in *In Proceedings of the 18th Annual ACM-SIAM Symposium on Discrete Algorithms*, 2007.

[284] M. Blazek and P. Pata, "Colour transformations and K-means segmentation for automatic cloud detection," *Meteorologische Zeitschrift*, vol. 24, no. 5, pp. 503–509, 2015.

[285] T. Smith and J. Guild, "The C.I.E. colorimetric standards and their use," *Transactions of the Optical Society*, vol. 33, pp. 73–134, jan 1931.

[286] K. McLaren, "XIII-The Development of the CIE 1976 (L* a* b*) Uniform Colour Space and Colour-difference Formula," *Journal of the Society of Dyers and Colourists*, vol. 92, no. 9, pp. 338–341, 2008.

[287] P. Janout, M. Blažek, and P. Páta, "New generation of meteorology cameras," in *Photonics, Devices, and Systems VII* (K. Fliegel and P. Páta, eds.), vol. 10603, pp. 312 – 318, International Society for Optics and Photonics, SPIE, 2017.

[288] P. Janout, P. Páta, J. Bednář, E. Anisimova, M. Blažek, and P. Skala, "Stellar objects identification using wide-field camera," in *Photonics, Devices, and Systems VI* (P. Tománek, D. Senderáková, and P. Páta, eds.), vol. 9450, pp. 380 – 388, SPIE, 2015.

[289] W. M. Organization, ed., *International cloud atlas.* WMO [publications] ; no. 407, Geneva: Secretariat of the World Meteorological Organization, 1975.

[290] Y. Wang, M. Bellus, C. Wittmann, M. Steinheimer, F. Weidle, A. Kann, S. Ivatek-Šahdan, W. Tian, X. Ma, S. Tascu, and E. Bazile, "The Central European limited-area ensemble forecasting system: ALADIN-LAEF," *Quarterly Journal of the Royal Meteorological Society*, vol. 137, no. 655, pp. 483–502, 2011.

[291] W. Zapka, *Handbook of industrial inkjet printing: a full system approach.* John Wiley & Sons, 2017.

[292] J. Nickelson, *Fine Art Inkjet Printing: The Craft and Art of the Fine Digital Print*. Rocky Nook, Inc., 2018.

[293] S. D. Hoath, *Fundamentals of inkjet printing: the science of inkjet and droplets*. John Wiley & Sons, 2016.

[294] D. K. Chlebda, A. Rogulska, and T. Łojewski, "Assessment of hyperspectral imaging system for colour measurement," *Spectrochimica Acta Part A: Molecular and Biomolecular Spectroscopy*, vol. 185, pp. 55–62, 2017.

[295] M. Maynez-Rojas, E. Casanova-González, and J. Ruvalcaba-Sil, "Identification of natural red and purple dyes on textiles by Fiber-optics Reflectance Spectroscopy," *Spectrochimica Acta Part A: Molecular and Biomolecular Spectroscopy*, vol. 178, pp. 239–250, 2017.

[296] E. Pouyet, T. Miteva, N. Rohani, and L. de Viguerie, "Artificial Intelligence for Pigment Classification Task in the Short-Wave Infrared Range," *Sensors*, vol. 21, no. 18, p. 6150, 2021.

[297] V. Cardin, L.-I. Dion-Bertrand, F. Poirier, S. Marcet, and J. Yvon-Leroux, "Hyperspectral VIS/SWIR wide-field imaging for ink analysis," in *Hyperspectral Imaging and Applications*, vol. 11576, p. 1157609, International Society for Optics and Photonics, 2020.

[298] J. Ragai, *Scientist And The Forger, The: Insights Into The Scientific Detection Of Forgery In Paintings*. World Scientific, 2015.

Appendix A

PUBLICATIONS OF THE AUTHOR

Publications relevant to the thesis in peer-reviewed journals with Impact Factor

[A.1] L. Krauz, P. Janout, M. Blažek, and P. Páta, "Assessing Cloud Segmentation in the Chromacity Diagram of All-Sky Images," *Remote Sensing*, vol. 12, no. 11, p. 1902, 2020
Shares: **25**/25/25/25

[A.2] L. Krauz, P. Páta, J. Bednář, and M. Klíma, "Quasi-collinear IR AOTF based on mercurous halide single crystals for spatio-spectral hyperspectral imaging," *Optics Express*, vol. 29, no. 9, pp. 12813–12832, 2021
Shares: **25**/25/25/25

[A.3] L. Krauz, P. Páta, and J. Kaiser, "Assessing the Spectral Characteristics of Dye-and Pigment-Based Inkjet Prints by VNIR Hyperspectral Imaging," *Sensors*, vol. 22, no. 2, p. 603, 2022
Shares: **33**/33/33

[A.4] L. Krauz, P. Páta, J. Bednář, M. Klíma, and P. Janout, "Broadband Wollaston prism with a large output beam separation based on mercurous halides," *Optics Express*, vol. 30, no. 26, pp. 47388–47403, 2022
Shares: **20**/20/20/20/20

Other publications unrelated to the thesis in peer-reviewed journals with Impact Factor

[O.1] J. Bednář, L. Krauz, P. Páta, and P. Koten, "Meteor cluster event indication in variable-length astronomical video sequences," *Monthly Notices of the Royal Astronomical Society*, vol. 523, pp. 2710–2720, 05 2023
Shares: 25/**25**/25/25

Citations in Web of Science with excluded self-citations

Publication [A.1]

[A.1, C.1] F. Romano, "Editorial for the Special Issue: Remote Sensing of Clouds," *Remote Sensing*, vol. 12, no. 24, p. 4085, 2020

[A.1, C.2] Y. Wang, D. Liu, W. Xie, M. Yang, Z. Gao, X. Ling, Y. Huang, C. Li, Y. Liu, and Y. Xia, "Day and night clouds detection using a thermal-infrared all-sky-view camera," *Remote Sensing*, vol. 13, no. 9, p. 1852, 2021

[A.1, C.3] B. Kuang, Z. A. Rana, and Y. Zhao, "Sky and ground segmentation in the navigation visions of the planetary rovers," *Sensors*, vol. 21, no. 21, p. 6996, 2021

[A.1, C.4] L. Zhang, W. Wei, B. Qiu, A. Luo, M. Zhang, and X. Li, "A Novel Ground-Based Cloud Image Segmentation Method Based on a Multibranch Asymmetric Convolution Module and Attention Mechanism," *Remote Sensing*, vol. 14, no. 16, p. 3970, 2022

[A.1, C.5] D. Spänkuch, O. Hellmuth, and U. Görsdorf, "What Is a Cloud? Toward a More Precise Definition," *Bulletin of the American Meteorological Society*, vol. 103, no. 8, pp. E1894–E1929, 2022

Publication [A.2]

[A.2, C.1] G. N. Martynov, A. V. Gorevoy, A. S. Machikhin, and V. E. Pozhar, "On inherent spatio-spectral image distortion in AOTF-based imagers," in *Optical Measurement Systems for Industrial Inspection XII*, vol. 11782, pp. 268–277, SPIE, 2021

[A.2, C.2] P. A. Nikitin, V. V. Gerasimov, and I. S. Khasanov, "Temperature Effects in an Acousto-Optic Modulator of Terahertz Radiation Based on Liquefied SF6 Gas," *Materials*, vol. 14, no. 19, p. 5519, 2021

[A.2, C.3] A. Gorevoy, A. Machikhin, G. Martynov, and V. Pozhar, "Computational technique for field-of-view expansion in AOTF-based imagers," *Optics Letters*, vol. 47, no. 3, pp. 585–588, 2022

[A.2, C.4] A. O. Arellanes, V. Quintard, and A. Pérennou, "Spectral and temporal behavior of a quasi-collinear AOTF in response to acoustic pulses: simulations and experiments," *Applied optics*, vol. 61, no. 7, pp. 1687–1694, 2022

[A.2, C.5] Y. Bi, L. Liu, Z. Yue, R. Li, G. Zhang, and X. Tao, "Single Crystal Growth and Effect of Cleavage Micro-striations on Crystallinity and Optical Properties of Mercurous Halide Single Crystals," *CrystEngComm*, 2023

Publication [A.3]

[A.3, C.1] Y. Tang, S. Song, S. Gui, W. Chao, C. Cheng, and R. Qin, "Active and Low-Cost Hyperspectral Imaging for the Spectral Analysis of a Low-Light Environment," *Sensors*, vol. 23, no. 3, p. 1437, 2023

Appendix B

ACTIVITIES

Research projects

Czech Science Foundation

[P.1] *Meteor clusters: An evidence for fragmentation of meteoroids in interplanetary space*
2020 - 2023, GAČR, no. 20-10907S **Team member**

European Space Agency

[P.2] ESA IAPETHOS II - *Infrared Advanced Polarizer for Space Applications*
2018 - 2022 **Team member**

[P.3] ESA CALIOPE - *Calomel-Based TIR Optical AOTF Breadboarding*
2018 - 2021 **Team member**

Student Grant Agency of the Czech Technical University in Prague

[P.4] *Acquisition, processing, and display techniques for extended multidimensional imaging modalities*
2023 - 2025, no. SGS23/186/OHK3/3T/13 **Team member**

[P.5] *Modern Optical Imaging Systems with Non-linear Point Spread Function and Advanced Algorithms for Image Data Processing*
2020 - 2022, no. SGS20/179/OHK3/3T/13 **Proposer**

[P.6] *Analysis and advanced algorithms for ultra-wide imaging systems*
2018 - 2019, no. SGS18/141/OHK3/2T/13 **Team member**

Study abroad and workshops

[E.1] University of Glasgow, Scotland, UK; Erasmus+ EU programme, 2018; Topics: *Frontiers of Optics, Machine learning, Autonomous vehicles guiding systems, Radar and Electro-Optic system design*

[E.2] 6th EIROforum School on Instrumentation, European Space Agency, ESTEC, NL 2019, Topics: *Instrumentation, Artificial Intelligence, Technology Transfer*

[E.3] James Webb Space Telescope (JWST) Master Class Workshop, Prague, 2020, Topics: *JWST mission status and instruments, vailable proposal tools and end-to-end tools usage, vailable observing science modes and observing strategies*

Ad hoc reviewer for journals with impact factor

[R.1] Optics Express, *Optica Publishing Group (Optica)*, ISSN 1094-4087

[R.2] Optics Letters, *Optica Publishing Group (Optica)*, ISSN 0146-9592, 1539-4794

[R.3] Applied Optics, *Optica Publishing Group (Optica)*, ISSN 1559-128X, 2155-316

[R.4] CrystEngComm, *Royal Society of Chemistry*, ISSN 1466-8033

[R.5] Remote sensing, *Multidisciplinary Digital Publishing Institute (MDPI)*, ISSN 2072-4292

[R.6] Sensors, *Multidisciplinary Digital Publishing Institute (MDPI)*, ISSN 1424-8220

[R.7] Applied Sciences, *Multidisciplinary Digital Publishing Institute (MDPI)*, ISSN 2076-3417